VYSOKÉ UČENÍ TECHNICKÉ V BRNĚ
BRNO UNIVERSITY OF TECHNOLOGY

FAKULTA STROJNÍHO INŽENÝRSTVÍ
FACULTY OF MECHANICAL ENGINEERING

ENERGETICKÝ ÚSTAV
ENERGY INSTITUTE

IN VITRO STUDY OF THE EFFECT OF PARTICLE CHARACTERISTICS AND FLOW RATE ON REGIONAL DEPOSITION IN HUMAN AIRWAYS

IN VITRO VÝZKUM VLIVU VLASTNOSTÍ ČÁSTIC A PRŮTOKU VZDUCHU NA REGIONÁLNÍ DEPOZICI V DÝCHACÍCH CESTÁCH ČLOVĚKA

DIZERTAČNÍ PRÁCE
DOCTORAL THESIS

AUTOR PRÁCE — Ing. Miloslav Bělka
AUTHOR

ŠKOLITEL — doc. Ing. Jan Jedelský, Ph.D.
SUPERVISOR

BRNO 2018

BIBLIOGRAPHICAL REFERENCE

BĚLKA, M. In vitro výzkum vlivu vlastností částic a průtoku vzduchu na regionální depozici v dýchacích cestách člověka. Brno: Vysoké učení technické v Brně, Fakulta strojního inženýrství, 2018. 121 s. Vedoucí dizertační práce doc. Ing. Jan Jedelský, Ph.D.

Statement

I hereby declare that I have written this PhD thesis on my own according to advice of my supervisor doc. Ing. Jan Jedelský, Ph.D., and using the sources listed in references.

Brno, _____ …….

Miloslav Bělka

Acknowledgement

Foremost, I would like to express my sincere gratitude to my supervisor doc. Jan Jedelský, Ph.D. as well as the head of Department of Thermomechanics and Environmental Engineering prof. Ing. Miroslav Jícha, CSc. for their support, patience, and guidance throughout my whole doctoral study. Special thanks must go to Ing. František Lízal, Ph.D. for his help, enthusiasm and fruitful discussions. Besides, I would like to thank to all my colleagues at Department of Thermomechanics and Environmental Engineering for creating friendly and positive environment. As the topic of this thesis was multidisciplinary to some extent, I must also thank to my colleagues at the Institute of Mathematics, at the University of Veterinary and Pharmaceutical Sciences Brno, and at the Faculty of Chemistry at Brno University of Technology. Finally, I express my huge thanks to my family, my friends and to my girlfriend.

This work was created with the support of the project no. 16–23675S funded by the Czech Science Foundation and LO1202 NETME CENTRE PLUS funded by the Ministry of Education, Youth and Sports of the Czech Republic under the National Sustainability Programme I.

Abstract

Inhalation of airborne particulate matter can trigger or exacerbate pre–existing lung conditions. On the other hand, inhalation of aerosolized medicaments can be used for treatment of various respiratory or systemic diseases. In both cases, it is essential to comprehend the particle transport and subsequent deposition. The aim of this PhD thesis is to obtain new experimental data on particle deposition and elucidate the effect of particle shape and flow rate on deposition.

The deposition of porous and fibrous particles in the realistic replica of human respiratory airways was studied. The porous particles were produced by various methods, such as spray–drying or liquid–liquid interface crystallization. The produced particles were introduced into the replica and the subsequent deposition was detected using spectrophotometry. The fibrous particles were produced by crushing glass wool material. To narrow the fiber size distribution, the resulting fibers were sieved and then classified according to their length using a dielectrophoretic classifier. The fiber deposition inside the replica was detected using phase–contrast microscopy. To speed–up this analysis, an in–house software based on image processing was developed.

The results were utilized to calculate deposition characteristics. The deposition efficiency of both particle types increased with increasing Stokes number indicating a significant role of impaction. Comparing their deposition efficiency to that of spherical particles, porous particles exhibited similar deposition efficiencies, however, fibers deposited less efficiently than spherical particles having the same Stokes number. As the boundary conditions were sufficiently described and the replica is available in a digital format, the data can be also employed in validation of numerical simulations.

Keywords

Particle deposition, aerosol transport, porous particles, fibers, replica of respiratory airways

Abstrakt

Dlouhodobé vdechování částic může přispívat ke vzniku nebo zhoršení nejrůznějších plicních onemocnění. Na druhou stranu, vdechování léčiv je často používanou metodou podávání léků proti astmatu a jiným nemocem dýchacího ústrojí. V obou případech je důležité dobře porozumět mechanismům, na jejichž základě funguje pohyb částic a jejich usazování v dýchacích cestách. Cílem této disertační práce bylo získat nová experimentální data depozice částic a analyzovat vliv tvaru částic a průtoku vzduchu na depozici.

Byla studována depozice porézních a vláknitých částic v realistickém modelu dýchacích cest. Porézní částice byly vyrobeny různými metodami, např. sprejovým sušením nebo metodou krystalizace. Takto vyrobené částice byly použity při depozičních experimentech. Detekce částic byla provedena pomocí UV/VIS spektrofotometrie. Vláknitý aerosol byl vytvořen rozdrcením skelné vaty. Takto vzniklé vláknité částice byly několikrát prosety přes řadu sít a dále roztříděny podle délky pomocí klasifikátoru pracujícím na principu dielektroforézy. Následná depozice byla vyhodnocena použitím mikroskopie s fázovým kontrastem. Ke zrychlení analýzy byl vyvinut program, který dokáže na základě analýzy obrazu najít a spočítat vlákna.

Výsledky experimentu byly použity k určení depozičních charakteristik. S jejich pomocí pak byl kvantifikován vliv tvaru částic a průtoku na míru usazování. Depoziční účinnost částic rostla v závislosti na Stokesově čísle, což poukazuje na vliv setrvačnosti při usazování částic. Bylo prokázáno, že depoziční účinnost porézních částic je podobná té u částic kulových při stejném Stokesově čísle. Vláknité částice se usazovali méně efektivně v porovnání s kulovými částicemi majícími stejné Stokesovo číslo. Jelikož byly okrajové podmínky dostatečně popsány a model plic je k dispozici i v digitální podobě, je možné data použít k validaci výsledků numerických simulací.

Klíčová slova

Usazování částic, transport částic, porézní částice, vlákna, model dýchacích cest

Contents

1. Introduction

The human respiratory system is a gateway to our body. When we breathe in ambient air, we can bring air pollutants into our lungs and subsequently into our system. Air pollution exposure contributes to increase rates of asthma or worsening of existing respiratory diseases, such as chronic obstructive pulmonary disease (COPD) or lung cancer (Laumbach and Kipen, 2012). The mortality from chronic respiratory diseases is estimated to be 4 million people worldwide annually (FIRS, 2013). Moreover, inhaled nanoparticles can also translocate to other organs via bloodstream and cause additional harm (Oberdorster et al., 2004). Of course, air pollution is not the only trigger for respiratory diseases, e.g. COPD is mainly caused by cigarette smoking (Burney et al., 2015). Generally, understanding the particle transport and subsequent deposition in the respiratory tract is the first step to estimate the particle´s health hazards.

The study of particle deposition is also motivated by inhalation medicine. As inhalation of airborne particulate matter can trigger or exacerbate respiratory diseases, inhalation of aerosolized medicaments is frequently used for treatment of respiratory diseases, such as asthma or COPD. Moreover, inhalation therapy can also provide a systemic drug delivery of various therapeutic peptides and proteins as the respiratory tract is richly supplied with blood (Agu et al., 2001).

To efficiently utilize the potential of inhalation therapy or to sufficiently estimate health hazards of particulate matter, it is essential to comprehend the particle transport and subsequent deposition. Particle transport through the respiratory tract is affected mainly by breathing pattern, lung geometry and particle characteristics. The effect of various factors on deposition needs to be emphasized. Moreover, the deposition distribution is not uniform throughout the airways and therefore, study of localized deposition is of great concern. As the deposition patterns of spherical particles have been thoroughly investigated, the aim of this thesis is to analyze the effect of particle non–spherical shape and inhalation flow rate on deposition.

2. Background

2.1. Historical perspective of deposition studies

Inhalation of particles and their impact on human health has been present since humans learnt how to control fire and started cooking, and maybe earlier. The first references about negative effects of particulate matter inhalation were found in Ancient Greece where Hippocrates noticed that considerably high number of miners had difficulties with breathing during working inside the mines (Miller, 1973). In the Medieval period, the problems affected also ordinary people as the city centers were polluted mainly by sea-coal burning used during metal working and smelting (Rosner, 1984). The connection between particle inhalation and health diseases was first observed by Bernardino Ramazzini in 1705. He identified respiratory disease caused by inhalation of silica dust, silicosis, in the lungs of stonecutters.

On the other hand, people also realized the benefits of particle inhalation. The first references about inhalation therapy go back to 2000 BC in ancient India, where people smoked various herbal preparations, such as Datura species, to treat their breathing problems (Gandevia, 1975). Later, around 460 BC, Hippocrates proposed inhalation of hot vapors for treatment of sore throat and lung diseases (Miller, 1973).

Around 1200 AD, a Spanish physician Maimonides treated asthma by inhalation of vapors from throwing herbs into a fire (Smyth and Hickey, 2011). However, the great progress in inhalation therapy came only in the 19th century, when inhalation of non-volatile medicine was made possible. Auphan realized that a mist can be produced by crashing a water stream against a hard surface, e.g. a wall. He build an inhalatorium in Euzet-les-Bains, where mineral waters were splashed against walls of the room (Smyth and Hickey, 2011). In continuation, Sales-Girons constructed a small portable device in 1858 (Yernault, 1994), which people used to inhale mineral waters with various substances in their own homes instead of going to the spa. The device produced a fine mist by pumping a liquid from a reservoir through a nozzle against an impaction plate (Figure 1).

Figure 1 The nebulizer designed by Sales-Girons. (Smyth and Hickey, 2011)

The use of inhalers raised a question whether the atomized liquids penetrate into the lower airways and therefore, had any effect on human health. These were the beginnings of deposition experiments. One way to do this was to experiment on animals. Demarquay and others showed that atomized liquids

reached bronchi of rabbits (Weisz, 1995). However, it was not known how much this fact could be applied to humans. Another suggestion was to employ dummy models of respiratory airways, such as flasks and various tubes. Armand Trousseau made an analogy between atomized liquids and dust because it was already known that dust could penetrate into human respiratory system and cause various diseases or death (Weisz, 1995). Poggiale, a French chemist, was the first to experiment on human subject in 1862. He found a nurse with tracheal fistula and made her inhale a water with chemical compound. He showed that the inhaled substances reached at least the trachea and supported the assumption that atomized liquids can reach the lower respiratory airways (Anderson, 2005). In 1872, Waldenbourgh conducted series of experiments on deposition in bronchi. His results indicated that 25% of the dose deposited in mouth and larynx and approximately 30% reached beyond larynx (Bisgaard et al., 2002).

The main motivation for deposition studies shifted from the inhalation therapy to occupational hygiene, toxicology, and epidemiology in the 20th century. The most significant reason was the increasing number of people with respiratory diseases. The reason for that was mainly a decline in air quality both outside (air pollution) and inside (at home or in the workplace). Moreover, toxic weapons were used during world wars. To evaluate health risks after particle inhalation, it was essential to determine the quantity of inhaled aerosol and its penetration into the respiratory tract. The importance of particle size for respiratory tract penetration was recognized in 1916 when Watkins-Pitchford and Moir (1916) observed that over 80% of particles in the silicotic lungs of gold miners were smaller than 2 μm in diameter.

Total particle deposition and retention in the lungs has been studied by comparing fractions of inhaled and exhaled air by volunteers. Drinker et al. (1928) and Brown (1931) studied retention of zinc oxide fume, marble dust and other substances. Volunteers inhaled air containing known suspensions and exhaled through an electric precipitator afterwards. Van Wijk and Patterson (1940) experimented with dust particles and indicated that larger particles tend to be deposited in larger airways and smaller particles penetrated deeper into the respiratory tract. In 1940s, Sinclair and La Mer developed a monodisperse aerosol generator based on a principle of controlled condensation on a nuclei (Sinclair and La Mer, 1949). Wilson and La Mer (1948) then used the generator and studied total deposition of particles as a function of the particle radius during mouth breathing. Brown et al. (1950) studied alveolar deposition by separating exhalation into several fractions representing air coming from various parts of respiratory tract. Alveolar deposition was later analyzed by Altshuler et al. (1957), who also noticed mixing of tidal and residual air during breathing (Altshuler et al., 1959).

Along with the experimental works, development of mathematical models was also taking its place. In 1935, Findeisen (1935) was the first to present a mathematical model for prediction of particle deposition (Ensor, 2011). He divided the human respiratory tract from trachea to alveolar sacs into nine compartments connected in series (Figure 2). The deposition was calculated for different mechanisms including impaction, sedimentation, Brownian diffusion, and interception. The deposition efficiency was calculated for every mechanism in given compartment using approximate equations and these deposition efficiencies were summed up to get the total deposition efficiency for given compartment.

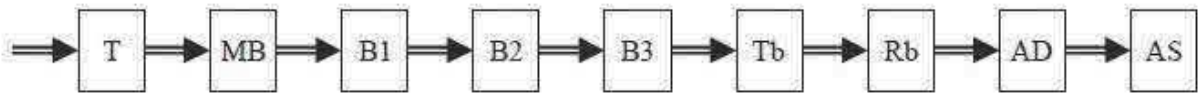

Figure 2 Findeisen's mathematical model for deposition predictions in nine compartments: T (trachea), MB (main bronchi), B1 to B3 (bronchi of order 1 to 3), Tb (terminal bronchioles), Rb (respiratory bronchioles), AD (alveolar ducts), AS (alveolar sacs). (Ensor, 2011)

The Findeisen/s model was a pioneering work and was a cornerstone for many other models. Landahl (1950) modified the model and incorporated mouth, larynx and one extra order of alveolar ducts into the model. He also added some other breathing regimes and took into account a deposition during exhalation. The work was extended by Beeckmans (1965) who included convective mixing of tidal and residual air by modifying expressions from experimental work of Altshuler (1959). The deposition model based on the aforementioned works is called Findeisen-Landahl-Beeckmans model. In 1960, the

widely used deposition model (known as the ICRP model) was developed by the Task Group on Lung Dynamics to the International Commission on Radiation Protection (Task Group on Lung Dynamics, 1966). This model contained three deposition zones: the nasopharyngeal, tracheobronchial, and pulmonary. It calculated deposition patterns for particles from 0.01 μm to 100 μm using empirical equations obtained from available experimental data. The model was intended for radiation protection, however, it was applied to other situations, such as air pollution studies. The Task Group has developed new models since that time (ICRP, 1994) incorporating new information about lung physiology, new experimental data, hygroscopic growth of particles etc.

In 1963, Weibel published a study on lung morphometry (Weibel, 1963). He described lung structure and identified 23 generations of branching in the tracheobronchial tree. The dimensions of all airways were given allowing their use in deposition models to calculate deposition on a generation-by-generation basis (Hickey, 2007). Many other deposition models have been developed since, such as the "trumpet model" (Taulbee and Yu, 1975) or multiple-path dosimetry model (Asgharian et al., 2001).

As the technology and deposition data improved, we got considerably good knowledge about total particle deposition. However, scientists dealing with inhalation therapy were looking for the way to learn more about spatial distribution of deposited particles in the lungs. In 1958, Anger reported on the development of gamma camera (Anger, 1958) to radionuclide imaging of the human body. It was initially employed in hospitals for the patient diagnosis. However, during the 1970s it was recognized that scintigraphy can be employed to assessment of drug delivery to various organs, such as the lungs (Casey et al., 1976; Meseguer et al., 1994). The radionuclide imaging methods have developed since then and can provide three-dimensional views with acceptable resolution nowadays (Newman et al., 2003). The latest tool in the field of particle deposition are computer fluid dynamics methods. With the rapid spread of computer technology, it is possible to utilize three-dimensional fluid flow and particle transport equations and calculate particle deposition with very high, submillimeter resolution (Rostami, 2009).

2.2. Overview of the respiratory airway physiology

The geometrical features of the respiratory tract are intimately linked to its function. Therefore, the knowledge of lung function and its physiology is essential for understanding the flow formation inside the respiratory airways and the subsequent particle transport and deposition. The main function of the lungs is to provide a gas exchange between bloodstream and the atmosphere, in particular transfer oxygen into the bloodstream and release carbon dioxide. Therefore, the lungs provide enormous contact area between air and bloodstream where gas exchange due to passive diffusion takes place. Secondary functions of the respiratory systems are air filtering, heating, humidification and, production of sound. The physiology of the airways has adapted to fulfill all these functions. The respiratory tract is divided into upper and lower respiratory airways. The upper respiratory airways (Figure 3) include nose and oral cavity, pharynx (throat), and larynx (voice box). The lower respiratory airways comprise trachea, main bronchi and the lungs.

Air enters the body through the nostrils as people are normally nose breathers (Yu et al., 2016). The nasal cavity includes the vestibule and main airways, which comprise three sets of meatuses. The nasal airways terminate in nasopharynx. Left and right nasal airways are separated by a cartilage known as the septum. The function of nasal airways, among others, is to filter the inhaled air from particles.

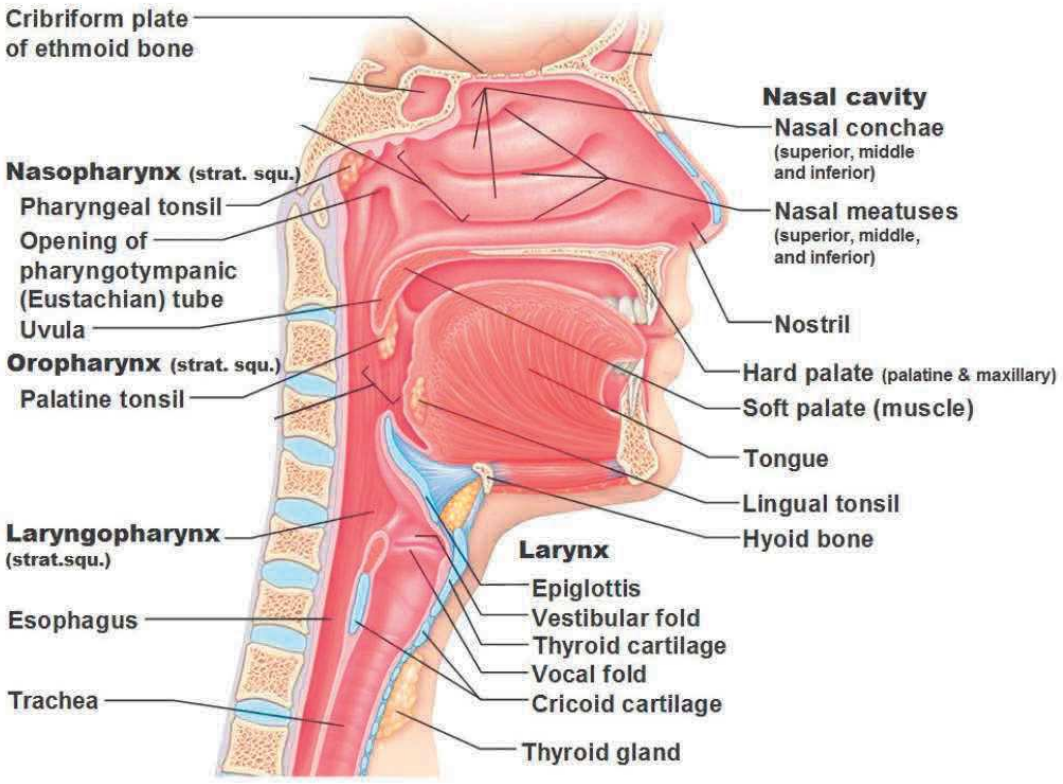

Figure 3 Upper respiratory airways. (Owlcation, 2017)

People switch to oral breathing during work or heavy exercise as the airflow resistance through the oral airways is lower compared to nasal airways. The oral cavity terminates in the oropharynx and the air undergoes a 90° bend to a pharynx/larynx area. After the passage through the oral and nasal airways, the air enters the trachea through the larynx. The larynx includes vocal cords and its function is a production of sound. The trachea is a tube that bifurcates into main bronchi that lead to the left and right lung. The airways in the lungs continue to bifurcate dichotomically (each branch divides into two smaller branches) and there are 23 generations of branching on average (Weibel, 1963). The first approximately sixteen generations form a so-called conducting zone, which ends with terminal bronchioles. The function of the conducting zone is to filter, heat, and humidify air while transporting it to a respiratory zone. The respiratory zone has an important function of gas exchange. The respiratory zone begins with respiratory bronchioles which may contain first alveoli and therefore, contribute to the total gas exchange (Figure 4). The bronchioles in respiratory zone have several generations of branching and terminate into alveolar sacs encompassing the majority of the alveoli. The total surface area of the alveoli come up to 150 m^2 in the adult human (Gehr et al., 1978).

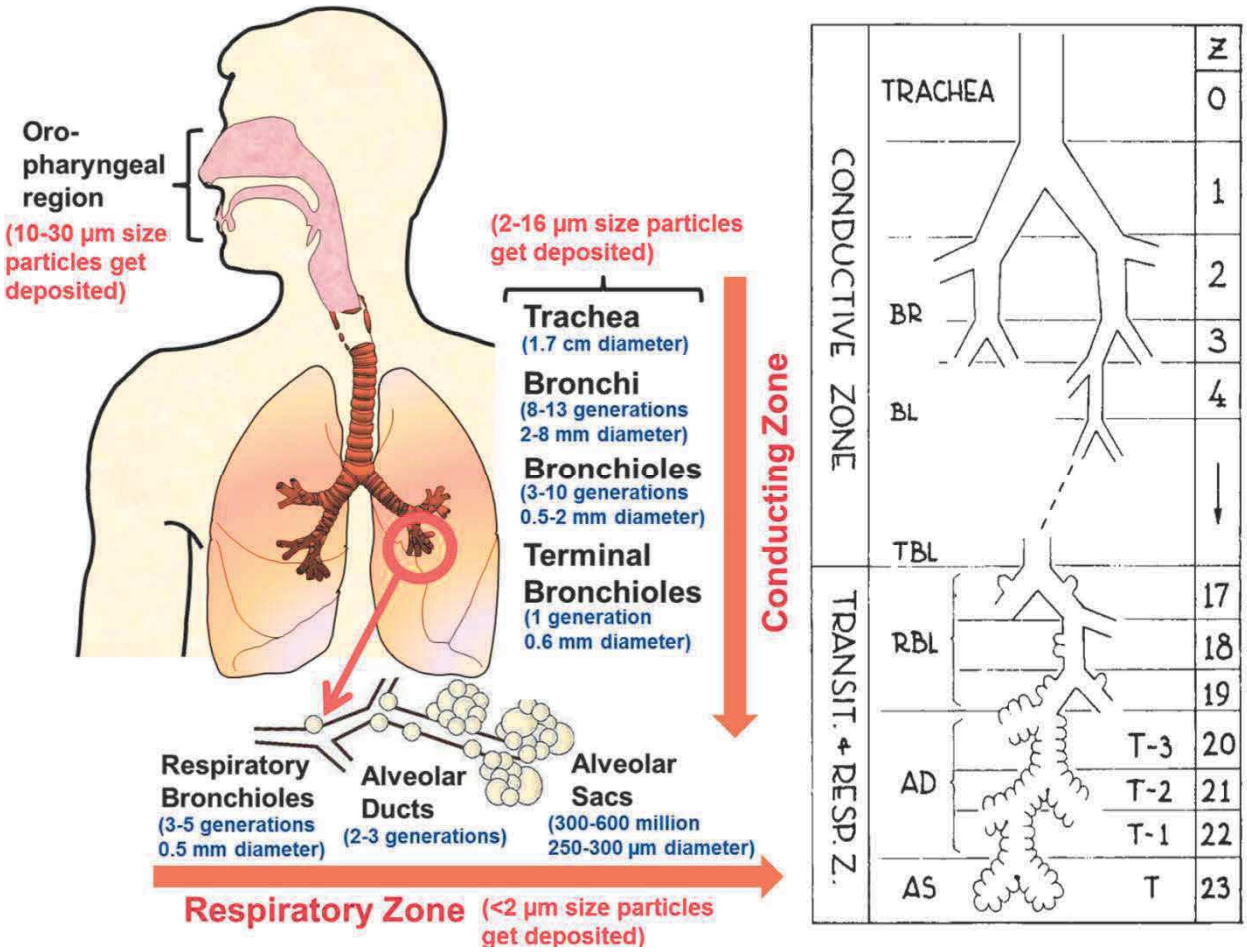

Figure 4 Respiratory tract (left) (Nahar et al., 2013); Branching of tracheobronchial tree (right). (Weibel, 1963)

The daughter-parent airway diameter ratio in the conducting zone is approximately 0.6. The change in airway diameter drops from 1.8 to 0.06 cm from trachea to terminal bronchioles (Hickey, 2007). On the other hand, the total cross-sectional area increases from 2.5 to 180 cm^2 along the way to terminal bronchioles (Hickey, 2007). The airways continue to branch in the respiratory zone, but the decrease in diameters is considerably small. Therefore, the total cross-sectional area increases rapidly from 180 to 10,000 cm^2 in the respiratory zone. With the rapid increase with the cross-sectional area, the velocity rapidly decreases as can be seen in equation 1 (equation of mass conservation for incompressible fluid).

$$Q = v \cdot A = const \qquad (1)\ ,$$

where Q is volumetric flow rate, v is average velocity and A is total cross-sectional area in given airway generation. Therefore, the air flow in the alveoli is driven entirely by diffusion.

2.3. Breathing mechanism

The air flows into the lungs because of the pressure gradient caused mainly by expansion of the thorax. During quiet inspiration, the thorax expands vertically because of the diaphragm contraction and the external intercostal muscles make the thorax expand in the anterior direction. During forced inspiration, other thoracic muscles can be employed, such as sternocleidomastoid muscle which assist with rib cage elevation. The lung deflation comes autonomically after the muscle relaxation. As the lung recoil and lung volume decreases, the pressure in the alveoli increases and becomes higher than atmospheric pressure. This pressure difference makes the air flow out of the lungs. During forced expiration, intercostal muscles lower the rib cage and abdominal wall muscles force organs to push the diaphragm upwards.

The partitioning of ventilation between various lung regions depends on driving pressure, flow resistance, lung elastic properties, and breathing regime. Assuming a pressure-induced flow, such as Poiseuille flow, in the airway, the volume flowrate is proportional to the pressure difference divided by the air flow resistance. The air flow resistance is caused by the internal and viscous properties of the air and is given by equation 2 (Kacmarek et al., 2013):

$$R_a = \frac{8 \cdot \eta \cdot L_a}{\pi \cdot {r_a}^4} \quad (2) \ ,$$

where η denotes dynamic air viscosity, L_a is the airway length, and r_a is the airway radius. It is worth noting that considerably small changes in airway radius can cause large changes of airway resistance due to the fourth power of r_a. The airway resistance can be affected by various pulmonary diseases which subsequently alter the air partitioning. For example, asthma results from inflammation which causes airway constriction in the conducting zone. These airway constrictions increase the airway resistances and thus induce breathing problems and worsen the lung function.

A static picture of lung function can be determined by measurements of lung volumes and lung capacities. These measurements involve measuring of lung vital capacity, tidal volume, inspiratory reserve volume etc. usually using spirometry. Definitions of various lung volumes and capacities together with values for healthy subjects are described in Table 1 and depicted in Figure 5. The lung volumes can be predicted based on the subject body size, age, and sex. Therefore, changes in lung volumes can be diagnosed as indication of specific pulmonary diseases.

Table 1 Lung volumes and capacities (Hickey, 2007)

Volume or capacity	Definition	Typical values (mL)	
		Female (20–30 yr)	Male (20–30 yr)
Tidal volume (V_T)	Volume of air inspired or expired during a normal breath	400	500
Inspiratory reserve volume (IRV)	Maximal volume that can be inspired after a normal tidal inspiration	1800	2700
Expiratory reserve volume (ERV)	Maximal volume that can be expired after a normal tidal expiration	1000	1600
Residual volume (RV)	Volume of air remaining in the lungs after a maximal expiratory effort	1000	1600
Inspiratory capacity (IC)	Maximal volume of air that can be inspired after a normal tidal expiration (V_T+IRV)	2200	3200
Functional residual capacity (FRC)	Volume of air remaining in the lungs after a normal tidal expiration (ERV+RV)	2000	3200
Vital capacity (VC)	Maximal volume of air that can be expired from the lungs after a maximal inspiration (IRV+V_T+ERV)	3200	4800
Total lung capacity (TLC)	Volume of air in the lungs after a maximal inspiratory effort (IRV+V_T+ERV+RV)	4200	6400

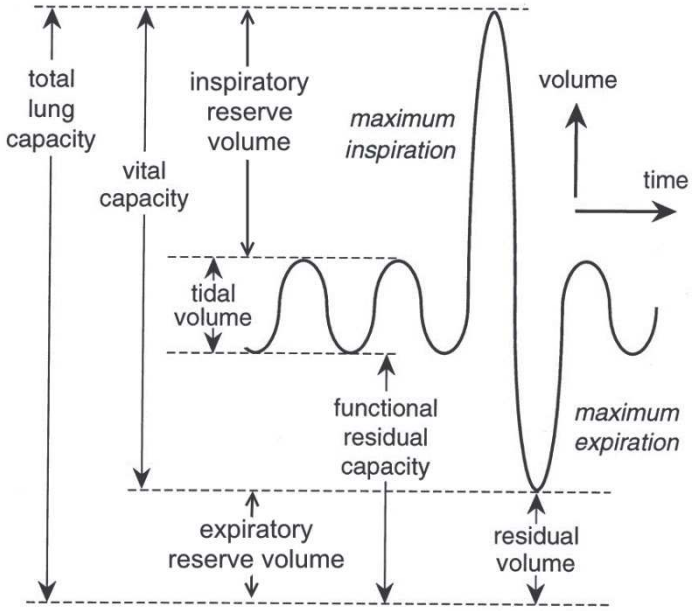

Figure 5 Lung volumes and capacities. (Rao and Verkman, 2000)

The dynamic lung function is linked to the air flow going in and out of the lungs. The basic characteristic is total ventilation (also termed minute ventilation) which represents total amount of air going into and out of the airways. Assuming respiration rate of 15 breaths/min and tidal volume of 500 mL, total ventilation would be 7500 mL/min. Another crucial characteristic is alveolar ventilation, i.e. total amount of air going into and out of the alveolar region. To determine the amount of air going into the alveoli, one must exclude the air in the conducting zone which is approximately 150 mL and is called anatomically dead space. Assuming the above-mentioned respiration rate and tidal volume, alveolar ventilation would be 5250 mL/min. Of course, total and alveolar ventilation can be greatly altered by change in respiration rate and tidal volume, such as during shallow or deep breathing. For example, respiration rate of 30 breaths/min and tidal volume 250 mL results in total ventilation of 7500 mL/min, however, the alveolar ventilation would be only 3000 mL/min (Hickey, 2007).

2.4. Aerosols

Aerosol is defined as a suspension of liquid or solid particles in the air. The term aerosol was first used by F. G. Donnan during the World War I as he was studying irritant arsenic smokes (Green et al., 1964). Aerosols are two-phase systems consisting of air and particles that are of many kinds, such as smoke particles or salt particles from ocean sprays. Particles are generated by both human activities and natural processes. Assuming that background concentration of particles is around 10^4 particles/cm^3 and adult human inhale over 10 000 liters per day, human body is exposed to trillions of particles every day. Definitions of common aerosol types can be found in Table 2.

Table 2 Definitions of common aerosol types (Anderson, 2005)

Fume	Solid-particle aerosol produced by the condensation of vapors or gaseous combustion products.
Smoke	Visible aerosol resulting from incomplete combustion; the particles can be solid or liquid.
Dust	Solid-particle aerosol formed by mechanical disintegration of a parent material.
Mist (Fog)	Liquid-particle aerosol formed by condensation of atomization.
Bioaerosol	Aerosol of biological origin.
Smog	Liquid or solid-particle aerosol originated from photochemical reactions.
Spray	Liquid-particle formed by the mechanical breakup of a liquid solution.

The particles can be divided according to their size distribution:

- Monodisperse – aerosol contains particles of uniform size
- Polydisperse – aerosol contains particles of various sizes
- Coarse – aerosol contains particles of sizes from 100 down to 1 µm
- Fine – aerosol contains particles of sizes from 1 to 0.1 µm
- Ultrafine – aerosol contains particles of sizes from 0.1 to 0.001 µm

The particle size is crucial characteristics that affect particle transport in the air and particle penetration through human respiratory system. The size of spherical particles, such as liquid particles, is determined by particle diameter (d_p). The size of irregularly-shaped particles is given by equivalent diameters. Equivalent diameters are defined as diameters of sphere having the same specific physical property. Concerning particle movement in the air, aerodynamic equivalent diameter (d_a) is usually used to determine particle size. Aerodynamic equivalent diameter is a diameter of a sphere with unit density having the same aerodynamic behavior as a particle in question. Aerodynamic diameter for irregularly-shaped particles can be calculated using equation 3, and for spheres using equation 4 (Baron and Willeke, 2005):

$$d_a = d_e \cdot \left(\frac{\rho_p}{\rho_0 \cdot \chi}\right)^{0.5} \quad (3)\ ,$$

$$d_a = d_p \cdot \left(\frac{\rho_p}{\rho_0}\right)^{0.5} \quad (4)\ ,$$

where d_e denotes equivalent volume diameter (sphere of the same volume as particle in question), χ is dynamic shape factor, ρ_p is particle density and ρ_0 is unit density. The dynamic shape factor is applied to account for the effect of shape on particle motion, for example drag force changes relative to the orientation of fibrous particle. Dynamic shape factors of some particles can be found in Table 3.

Table 3 Dynamic Shape Factors (Hinds, 1999)

	Dynamic Shape Factor (χ)			
		Axial Ratio		
Shape		2	5	10
Sphere	1.00			
Cube	1.08			
Cylinder				
Vertical axis		1.01	1.06	1.20
Horizontal axis		1.14	1.34	1.58
Orientation averaged		1.09	1.23	1.43
Sand	1.57			

The size of particles also affects the particle interaction with surrounding gas molecules which subsequently influences particle transport. This interaction is characterized by the ratio of particle size relative to the mean free path of the gas molecules (λ). The ratio is referred as Knudsen number ($Kn = \lambda/d_p$). When $Kn \gg 1$, the particle behavior follows the kinetic theory of gases. When $Kn \ll 1$, the surrounding gas molecules strike the particle surface and act as a drag force. In this case, the surrounding gas can be assumed as a fluid continuum and the drag can be calculated using the Stokes law (Tsuda et al., 2013).

2.5. Deposition mechanisms

The transport of spherical particle having diameter d_p and mass m_p in the surrounding gas can be defined by stochastic differential equation 5 (Tsuda et al., 2013) while separating the gas influence into separate effects, treating the gas as a continuum and assuming the molecular effects as random molecule collisions:

$$m_p \cdot \frac{d \cdot \vec{v}_p}{dt} = -f_{ric} \cdot \left(\vec{v}_p - \vec{v}_f\right) + m_p \cdot \vec{g} + \vec{F}(t) \qquad (5) \ .$$

This equation is a basically a form of Newton´s second law and states that the mass times acceleration (left-hand side) equals all forces which act on the particle (right-hand side). The first term on the right-hand side represents the viscous drag force which results from velocity difference between particle (particle velocity, v_p) and the surrounding fluid (fluid velocity, v_f). The second term denotes gravitational force and the third term is stochastic force that accounts for Brownian collisions of the particle with surrounding fluid molecules. The significance of individual terms is affected by particle characteristics, such as particle size. As the particle travels through the respiratory airways, it can hit the respiratory wall and stick to that place, i.e. deposit. The particle deposition is governed by several deposition mechanisms (Figure 6). The major deposition mechanisms are inertial impaction, sedimentation, and diffusion. Other deposition mechanisms, such as electrostatic deposition or interception, can play important role for specific types of particles. Turbulent diffusion can increase particle deposition in the case of turbulent flow. The deposition mechanisms are thoroughly described in (Darquenne, 2012; Hickey, 2007; Hinds, 1999; Tsuda et al., 2013). Only brief summary will be given below.

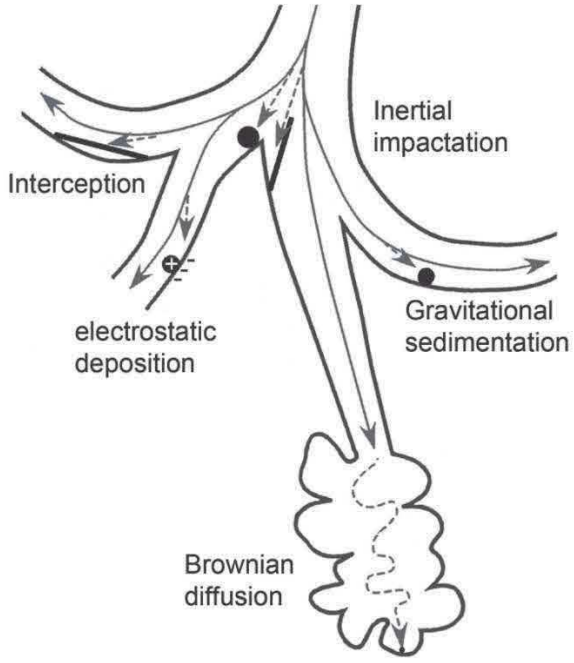

Figure 6 Deposition mechanisms (Frohlich and Salar-Behzadi, 2014)

a) Inertial Impaction

Assuming relatively large particle of interest (d_p > 0.5 μm), the last term on the right-hand side of equation 5 can be neglected. The resulting equation expresses that the particle motion is governed only by inertial, drag and gravitational force. The inertial force is proportional to a ratio of a particle stop distance to a characteristic dimension, i.e. Stokes number (Equation 6) (Tsuda et al., 2013)).

$$Stk = \frac{\rho_p \cdot d_p^2 \cdot C_s \cdot v_f}{18 \cdot \eta \cdot L} \qquad (6) \ ,$$

where C_s denotes Cunningham factor, μ is air dynamic viscosity and L is characteristic dimension (airway diameter). Friedlander (2000) indicated that inertial deposition does not occur unless critical Stokes number is reached. The critical Stokes number can be calculated as $Stk = 1/4b$, where b depends on the shape of the collector. When $Stk > Stk_{crit}$, particles deviate from curvilinear pathways due to their inertia and deposit on the airway walls. The inertial deposition takes place mainly in the large conducting airways and the highest deposition occurs in regions with high air flow curvature, such as in oropharynx or around carinas which are dividing points at the bifurcations.

b) Gravitational Sedimentation

The gravitational force plays important role in the small airways and alveolar region for micron-sized particles. The governing equation of particle motion under action of gravity is the equation for terminal settling velocity:

$$v_s = \frac{\rho_p \cdot d_p^2 \cdot \vec{g}}{18 \cdot \eta} \quad (7) \ ,$$

where g is gravitational acceleration. As can be seen, the v_s is proportional to the square of particle size for a given particle density. There are many analytical solutions of gravitational deposition in variously oriented pipes (Fuchs, 1964; Heyder and Gebhart, 1977; Pich, 1972; Wang, 1975). For example, Fuchs (1964) studied a gravitational deposition in a horizontal pipe of diameter D_p and found out that the deposition efficiency was proportional to dimensionless parameter ε.

$$\varepsilon = \frac{3 \cdot v_s \cdot L_p}{4 \cdot D_p \cdot v_f} \quad (8) \ ,$$

where L_p is pipe length. The parameter ε shows that the effect of gravitational sedimentation increases with decreasing carrier gas velocity v_f (increasing residence time of particles in given airways) which happens in the small airways. The gravitational deposition can be also increased by breath holding.

c) Brownian Diffusion

Assuming relatively small particle of interest (d_p < 0.5 μm), the gravity term in the Equation 5 may be neglected. Moreover, the acceleration term on the left-hand side of the equation can be also neglected. The particle motion is then governed by interactions with local fluid flow (velocity v_f) and impulsive Brownian motion due to random collisions with gas molecules. The particle diffusivity is given by equation 9, which is an Einstein's expression for the diffusion coefficient (Tsuda et al., 2013):

$$D_B = \frac{k_B \cdot T_{abs} \cdot C_s}{3 \cdot \pi \cdot \eta \cdot d_p} \quad (9) \ ,$$

where k_B is Boltzmann's constant and T_{abs} is absolute temperature. The particle displacement and velocity due to diffusion is then given by integrating the governing equation with respect to time. The ratio of convective and diffusive transport is given by Peclet number ($Pe = L\, v_f/D$). For example, Peclet number for the nano-sized particles is >> 1 throughout all the respiratory airways (Tsuda et al., 2013). Therefore, the transport is driven by convection rather than diffusion for these types of particles. Diffusion becomes important deposition mechanism in the small airways and alveolar regions as the dimensions in these airways are very small and particle is more likely to hit the wall.

d) Interception

Deposition mechanism by interception is significant for elongated particles, such as fibers or particle agglomerates. Even though a center of mass of these particles follows a streamline, a particle can come into contact with an airway wall and deposit. The particle orientation is crucial for occurrence of interception.

e) Electrostatic deposition

Some particles can be electrically charged during the mechanical production. While travelling through the respiratory airways, these charged particles induce image charges on an airway surface and are attracted towards it which can subsequently cause deposition. Hickey (2007) indicated that this mechanism is more important for submicron particles as they possess greater mobilities than micron particles. Charge particles also repulse like-charged inhaled particles. This repulsion drives particles from each other and can direct them at an airway wall.

f) Turbulent diffusion

Turbulent diffusion addresses particle deposition due to turbulent flow which occurs mainly in the upper respiratory tract and large conductive airways. The turbulent flows exhibit increased levels of mixing and the fluid undergoes irregular fluctuations causing rapid changes of the fluid velocity in both magnitude and direction. The particle trajectories respond to the fluid flow fluctuations which can result in particle deposition. The fluid flow can be characterized in terms of mean values and fluctuation intensities. Mean values are important for inertial impaction whereas fluctuation intensities result in turbulent deposition (Darquenne and Prisk, 2004).

3. State of the art

The particle deposition in human respiratory system can be studied using three approaches: *in vivo, in vitro* and *in silico. In vivo* methods employ human subjects in the measurements. *In vitro* methods utilized various dummy models to simulate conditions in real organisms. *In silico* methods use mathematical models or numerical simulations to predict particle transport and deposition. All the methods have their advantages and drawbacks and the choice depends on the information wanted. The studies can obtain information about total or regional deposition. Total deposition adds up particle deposition in all regions of the respiratory airways. Regional deposition provides more detailed information about the effective dose in various regions of the lungs, such as lung lobes or airway generations.

3.1. *In vivo* methods

3.1.1. Total deposition measurements

Total deposition can be easily obtained by *in vivo* measurements by comparing particle concentration of inhaled and exhaled air using various photometers. Well-controlled (prescribed breathing pattern and flow rate) inhalation of monodisperse particles results in considerably good deposition prediction related to particle size and breathing pattern. Total deposition studies have been performed for decades (Foord et al., 1978; Heyder et al., 1975; Schiller-Scotland et al., 1994; Stahlhofen et al., 1989). Heyder et al. (1975) studied total deposition of particles in the range from 0.1 to 3.2 µm while breathing by nose or mouth. Later on, Heyder et al. (1986) experimentally determined total deposition of particles in the range 0.005–15 µm. Representative data of total deposition are depicted in Figure 7 as a function of particle diameter. Since the inspiration flow rate was kept constant at 250 mL/sec during these measurements, effect of impaction remained fixed. The change in tidal volume influenced the particle residence time in the respiratory airways. It can be seen that the minimum total deposition was reported for the particle sizes around 0.4 µm as these particles are in the transition regime between nanoparticles (deposition due to Brownian motion) and microparticles (deposition due to impaction and sedimentation). The total deposition increased with increasing tidal volume, i.e. residence time. That means there was more time for the effect of sedimentation on large particle and Brownian motion on small particle fraction.

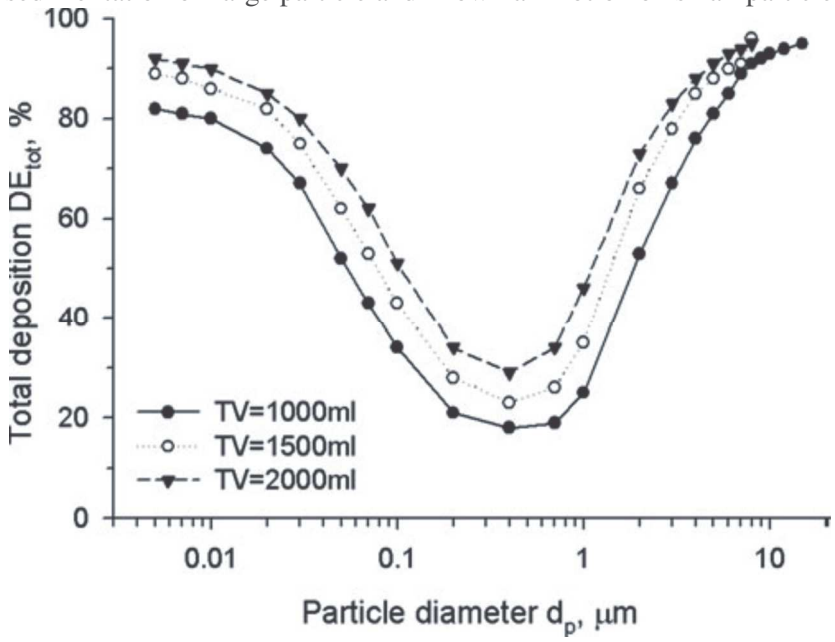

Figure 7 Total deposition as a function of particle diameter and tidal volume; the flow rate was kept constant at 250 mL/sec (Darquenne, 2012)

The available data on total deposition were extended in recent years to encompass data on ultrafine particle deposition, effect of gender on deposition, etc. (Darquenne et al., 2016; Darquenne and Prisk, 2004; Jaques and Kim, 2000; Kim and Hu, 2006; Kim and Jaques, 2004). ¨

The experimental data permit development of empirical equations for deposition predictions using various data fits. For example, Martin and Finlay (2007) made empirical fit (Figure 8) to the data of Heyder et al. (1986) and Kim and Hu (2006). Resulting equation predicts total deposition fractions (TDF_a) of micron-sized particles in adults during normal oral breathing:

$$\mathrm{TDF}_a = 0.08 + \frac{0.92}{1 + (4.09 \cdot 10^{-6}) \cdot e^{-2.06 \cdot \ln X}} \quad (10)\,,$$

where $$X = \left(\frac{C_s \cdot \rho_p \cdot {d_p}^2 \cdot Q_m}{\eta \cdot \mathrm{FRC}}\right)^{0.8} + 0.01 \cdot \left(\frac{C_s \cdot g \cdot \rho_p \cdot {d_p}^2 \cdot \mathrm{FRC}^{2/3}}{\eta \cdot Q_m}\right)^{0.4} \cdot \left(\frac{V_T}{\mathrm{FRC}}\right)^{0.8} \quad (11)\,.$$

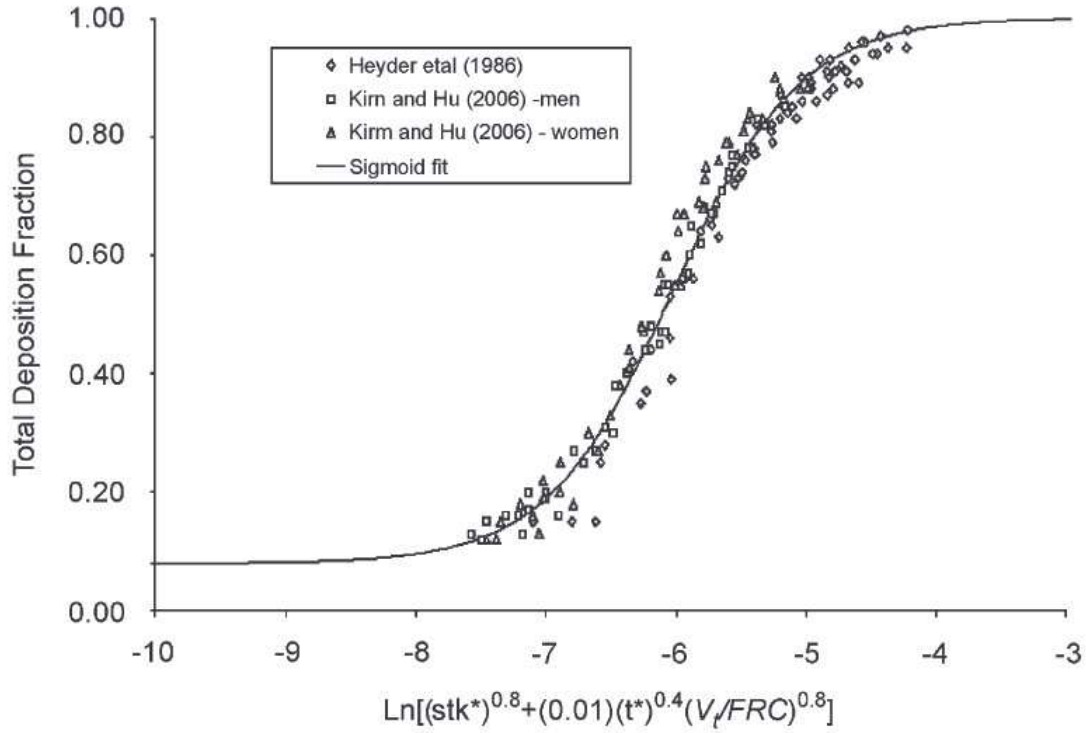

Figure 8 Empirical fit of Martin and Finlay (2007) to the experimental data; total deposition fractions measured in adults during oral breathing.

The ability to predict total deposition was compared to other special cases, such as deposition in children. The predictions were compared to the data of Schiller-Scotland et al. (1994) and good agreement was found. Empirical fits of experimental data are used very often to quickly predict total deposition fractions for various input parameters (Kim and Hu, 2006; Kim and Jaques, 2005). However, their accuracy is primarily influenced by the experimental data they are based on.

3.1.2. Aerosol bolus technique

The ratio of total particles inhaled and exhaled can be also utilized in the measurements of regional deposition using an aerosol "bolus" technique. The bolus technique can be traced back to Alshuler (1969) who described its potential in aerosol dispersion or estimating regional deposition. During this procedure, a subject breaths at regular intervals and a small bolus of particles is introduced at a predetermined point of inspiration. The point of inspiration determines how deeply the bolus penetrates the respiratory system. The depth that is reached by a bolus is usually referred as the penetration volume (V_p) and is defined as the volume of air inhaled from the mode of the bolus to the end of inspiration

(Darquenne, 2012). By delivering boluses at different points of inspiration and comparing the fractional depositions, regional deposition in various parts of the respiratory system is estimated. The first applications of this technique were reported by Muir et al. (1970). Heyder et a. (Heyder et al., 1988) employed this technique to study convective mixing in the respiratory airways. The bolus was inspired to different depths of the airways and the extent to which the aerosol spread was measured. Kim et al. (1996) assessed regional deposition in healthy nonsmoking men. Boluses of monodisperse particles (1, 3, and 5μm) were delivered to various lung depths (V_p ranged from 100 to 500 mL) in 50 mL increments and three flow rates. Representative data of deposition fraction in local volumetric regions are shown in Figure 9. The deposition fraction increased with increasing penetration volume to a peak value and then decreased with a further increase of V_p. The peak value moved to proximal airways with increasing particle size. Generally, the deposition fraction increased with decreasing flow rate.

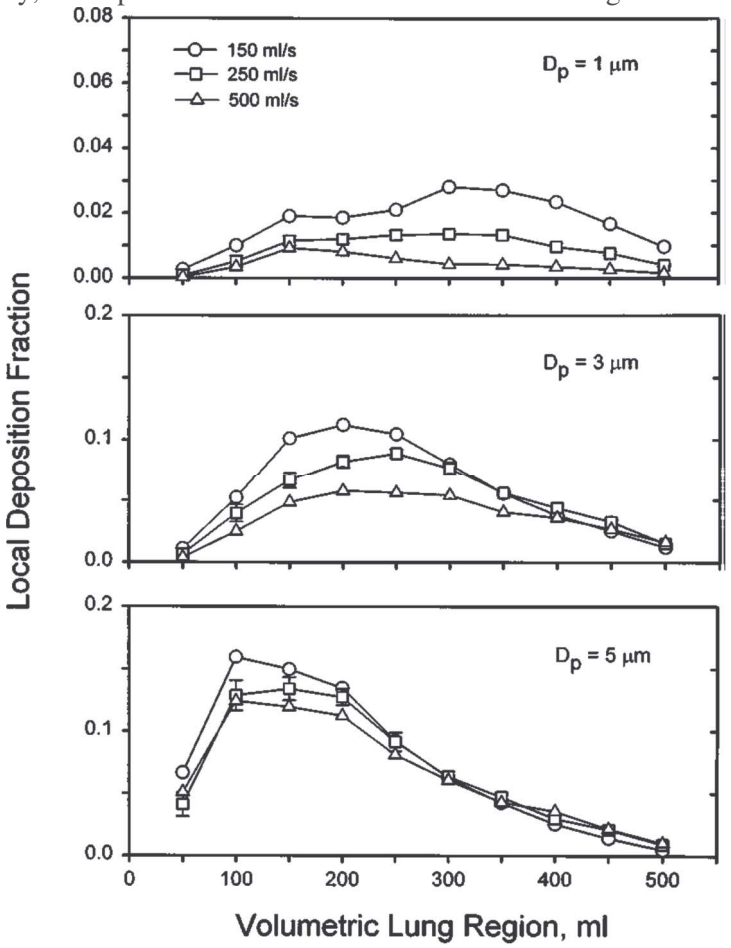

Figure 9 Deposition fraction in various volumetric lung regions as a function of particle size and flow rate (Kim et al., 1996)

Darquenne et al. (Darquenne et al., 1998) performed a bolus inhalations of 1 μm particles on the ground (1G), during parabolic flights (μG), and in 1,6 G to study the effect of sedimentation. It was shown that the deposition efficiency was not significantly different between G levels for V_p < 400 mL. For V_p > 400 mL, however, the deposition efficiency increased with increasing G level. This indicated that the sedimentation is predominant mechanism for micron-sized particle deposition in the lung periphery. The aerosol bolus technique is well established for the estimation of regional deposition and have been used in many other studies (Darquenne et al., 2000; Kim, 2009; Kim and Hu, 1998; Scheuch, 1994).

3.1.3. Radionuclide imaging methods

Another approach how to assess regional deposition of inhaled particles *in vivo* can be a use of radionuclide imaging methods. These methods label particles with various radionuclides. Subject

inhales the particles and images of lungs by one or multiple gamma cameras are taken afterwards. The advantage of this imaging is the actual picture of particle deposition in human lungs. The drawbacks include the high cost, high radiation doses and complexity of the methods. The use of these techniques is predominantly in inhalation medicine to study where the particles deposit and how quickly they are removed, i.e. lung clearance. The overview of these methods can be found elsewhere (Conway, 2012; Hickey, 2004; Nahar et al., 2013; Newman and Fleming, 2011). Only brief description will be given here.

a) Gamma Scintigraphy or Planar Imaging

Gamma scintigraphy is the most straightforward imaging technique. It utilizes a two-dimensional gamma camera that detects gamma emitting radioisotopes, usually Technetium (^{99m}Tc) (Conway, 2012). The drug is labeled by the radioisotope and administered to the patient. The image of patient´s thorax is then taken by a gamma camera. The gamma camera consists of a collimator, scintillation crystals, photodetectors multipliers, AD converter and other electronics. At first, the emitted γ-rays pass a collimator that consists of lead plates full of drilled holes. The collimator purpose it to absorb γ-rays that do not travel parallel to its plates as these would blur the final reconstructed image. The γ-rays that passed the collimator impact on a scintillation crystal. This crystal flashes after γ-ray impact and the flashes are detected by photodetectors. The light signal is amplified and converted into voltage signal. The voltage signal passes the analog-digital converter and is used for the reconstruction of the initial radioisotope distribution.

The radiolabeling of the drug with proper radioisotope is followed by validation studies which quantify the radiolabel and drug particle distribution. This is done because the radiolabel is associated with the drug but is not firmly bound to it. Because there is only physical association between the radiolabel and the drug particle, the radiolabel can dissociate from the drug particle after the deposition and be rapidly absorbed via the lung epithelium. Therefore, the gamma scintigraphy is not normally utilized to study lung clearance.

However, the gamma scintigraphy or planar imaging is frequently used to provide information on particle deposition. The information is rather on total deposition than on regional deposition as only 2D images of the lungs are obtained. It is very complicated to assess regional deposition as the respiratory tract has very complicated 3D structure. Therefore, some respiratory airways can overlap each other in the images and it can be impossible to distinguish between alveoli and conductive airways. However, many approaches have been used to divide respiratory tract into at least few regions of interest. The most common approach is to divide the lungs into a central and a peripheral region (Figure 10). Penetration index can then be defined as the ratio of these regions (Nahar et al., 2013). The index expresses an ability of the aerosol to reach the small airways and the alveolar region. The problem is that different study centers define central and peripheral regions differently and it is a big challenge to compare the results (Newman and Fleming, 2011).

The planar imaging is simple and frequently used method in the field of drug delivery studies. It provides sufficient information about total deposition and penetration of the drug through respiratory tract. However, the 2D images are an obstacle in assessing regional deposition.

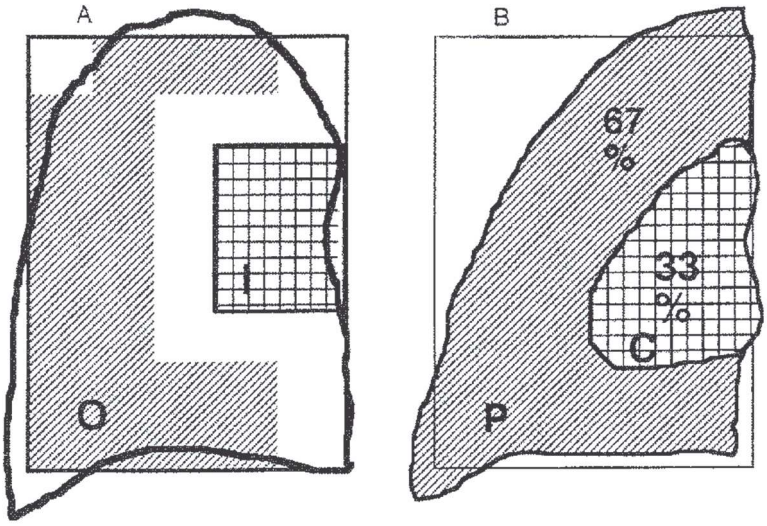

Figure 10 The lungs are frequently divided into regions of interests in gamma scintigraphy. The most common division is central (C) and peripheral (P) region, however, inner (I) and outer (O) region can be also found (Agnew, 1991)

b) Single-Photon-Emission Computed Tomography (SPECT)

The SPECT technique employs gamma camera that rotates around the patient at 360° obtaining multiple images of the thorax from different angles. These images are computationally processed and converted into 3D tomography-like reconstruction of the radiotracer distribution (usually Technetium ^{99m}Tc). This approach offers many advantages in terms of enhanced accuracy and possibility to assess deposition within the tracheobronchial tree. The resolution of SPECT is higher (8–10 mm) than that of gamma scintigraphy (10–14 mm) (Hickey, 2004). On the other hand, longer acquisition times are needed to take multiple images and therefore, higher administered doses are necessary to get high-quality data. Since the acquisition times are long, redistribution of deposited aerosol can take place because of lung clearance mechanisms or adsorption into the blood stream (Huchon et al., 1987). This complication can be addressed either by slowly absorbed or non-absorbed radionuclides, such as ^{99m}Tc-DTPA or ^{99m}Tc-colloid, or the use of "rapid" SPECT method (Chan et al., 2002; Newman and Fleming, 2011). The improvement in reduced acquisition time was brought also by newer dual- and triple-headed cameras (Hickey, 2004).

Another advantage is that SPECT images can be combined with CT scans allowing deposition distribution to be aligned with anatomical information. This is important as different body tissues attenuate gamma radiation differently. Combination with anatomical information allows better attenuation correction which leads to more uniform images. Moreover, definition of lung borders provides more convenient data interpretation. The SPECT and CT data can be obtained in different devices. However, it is more convenient to use combined SPECT/CT device (Fleming et al., 2011) as it is easier to align the acquired data.

SPECT method has been widely used to study the fate of inhaled aerosols (Dugernier et al., 2017; Fleming et al., 2011; Phipps et al., 1989; Scheuch et al., 2010; Weers et al., 2009). The information on regional data can be obtained as transverse, coronal and sagittal images, as a series of concentric shells or as the deposition fraction per airway generation (Newman and Fleming, 2011). To assess the deposition fraction per generation, various assumptions of the respiratory structure, such as number of airway generation or spatial orientation, are necessary. Illustrative example of SPECT data is depicted in Figure 11. The images taken from multiple angles (the coronal and the transverse plane) helped to distinguish deposition in various regions of interest, in particular the trachea and the main bronchi, which would overestimate the overall lung deposition in the case of planar imaging. Moreover, the SPECT data are credible to show a function of particle deposition on airway generation. Fleming (2004) employed SPECT to analyze particle deposition in a healthy subject and an asthmatic. Deposition peak

in generation 20 was observed in healthy subject inhaling fine aerosol whereas two significant deposition regions were found in asthmatic lungs, generation 4 and generation 20.

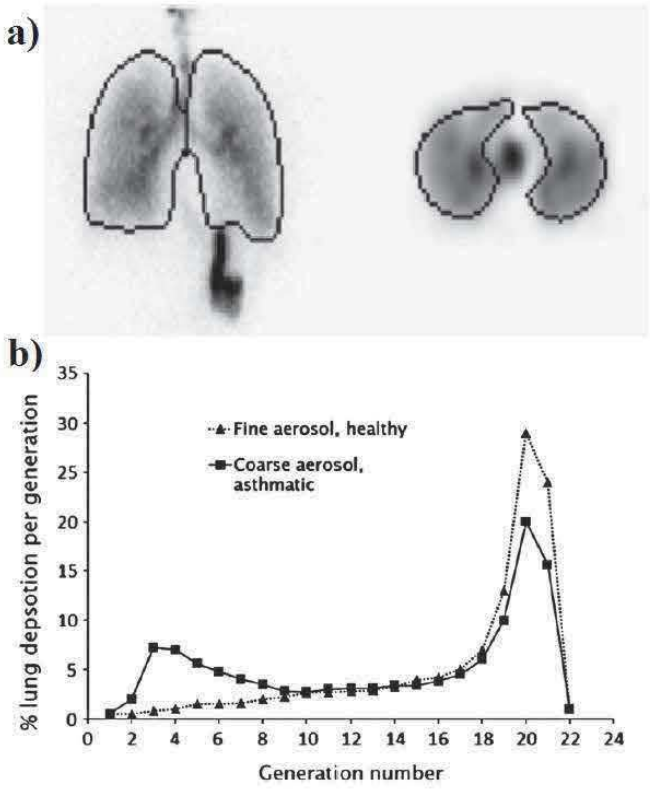

Figure 11 Illustrative example of SPECT data interpretation; a) the use of different gamma camera views in order to distinguish deposition in various regions of interest (e.g. the trachea and the lungs) (Fleming et al., 2011); b) regional deposition of a fine (mass median aerodynamic diameter of 2µm) aerosol inhaled by healthy subject and a coarse (mass median aerodynamic diameter of 6 µm) aerosol inhaled by asthmatic as a function of airway generation (Conway, 2012).

c) Positron-Emission Tomography (PET)

PET method utilizes specific scanners detecting photons that are a product of positron decay. At first, the inhaled particles are labeled with positron emitting radioisotopes, e.g. ^{11}C, ^{15}O, ^{13}N, ^{18}F (Nahar et al., 2013). The radioisotopes emit positrons that annihilate with electrons while emitting two high-energy photons at 180° to each other. These two photons are detected by a PET scanner and the exact position of the annihilation, i.e. event, is determined. All the events are recorded and a 3D image of the radionuclide distribution is reconstructed. For the proper data interpretation, the PET scanner is usually combined with a CT (Beyer et al., 2000) or an magnetic resonance imaging scanner (Judenhofer et al., 2008). Therefore, radionuclide distribution together with anatomical information is obtained while the patient remains in the same position. The resolution is better when compared to the other methods (4–6 mm) (Conway, 2012).

In the PET method, radioisotopes are incorporated into a drug molecule. This direct labeling is superior to the labeling with ^{99m}Tc as the molecule itself becomes a radiotracer. Direct labeling allows to study a regional deposition as well as the fate of the particles over time. The drawback is that the labeling process is very intricate and it can take months to validate the procedure. Moreover, the radioisotopes have very short half-life, e.g. ^{11}C and ^{18}F have a half-life of 20 and 109 min, respectively. This means that a cyclotron for production of positron emitting radioisotopes needs to be on-site or close to the research facility.

Apart from study of particle deposition, PET method is employed in nuclear medicine to reveal tumors, inflammation or infection using ^{18}F-FDG radiolabel (Basu and Alavi, 2008). Illustrative results of PET method are depicted in Figure 12. Berridge et al. (2000) analyzed pulmonary deposition of

Triamcinolone acetonide inhaled by patient using inhaler with and without a spacer. Drug absorption and clearance was observed over time.

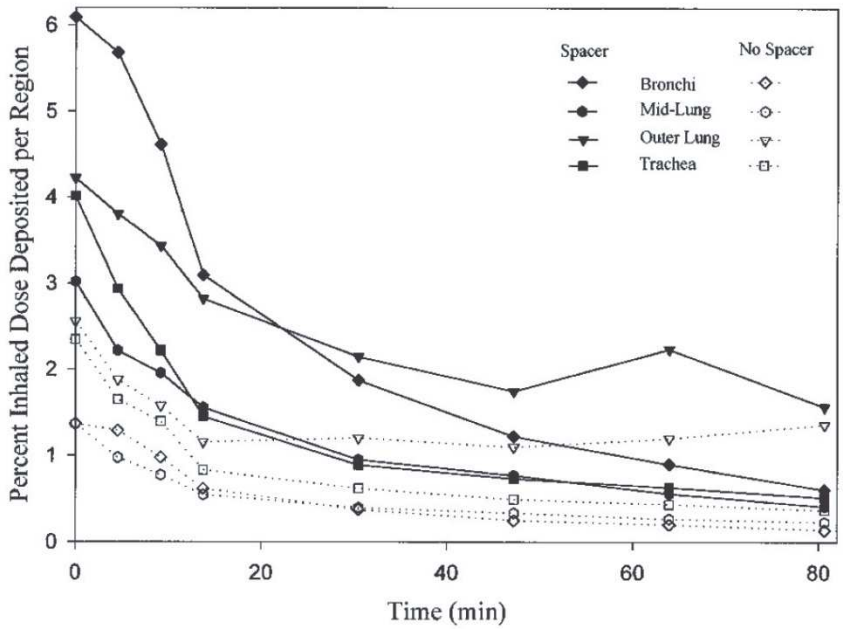

Figure 12 Deposition fraction of Triamcinolone acetonide in various regions of the respiratory tract and the effect of drug absorption and clearance (Berridge et al., 2000)

PET method provides 3D images of radioisotope distribution with great resolution and therefore, is suitable for the study of regional particle deposition and retention. However, its high costs, demands for instrumentation, and complexity make its use limited when compared to the planar imaging and SPECT.

d) Magnetic Resonance Imaging (MRI)

The previous methods involve radionuclide labeling and therefore, one must consider the problems with radiation exposure. The radiation exposure is even more dangerous for specific groups of population, such as infants, pregnant women etc. Because of this, MRI method has been previously studied as an imaging method that does not require the use of radionuclides. The overview of this method can be found elsewhere (Thompson and Finlay, 2012). Briefly, the MRI is based on Magnetic Nuclear Resonance phenomenon that uses nonionizable radiation and can distinguish between various soft tissues. The MRI scanner applies magnetic field to align proton spins in our body which creates a uniform magnetic vector. By adding additional energy to the magnetic field (e.g. radio frequency pulse), the nuclei resonate deflecting the magnetic vector. When the radiofrequency is switched off, the nuclei return to their initial state (alignment with the magnetic field) and a signal is emitted. The signal is detected by the MRI scanner and analyzed by the computer. The MRI scanner encompasses gradient coils to create gradient magnetic field and measure the spatial distribution of the source nuclei.

MRI detects signals from nuclei that have odd number of protons and/or neutrons, e.g. ^{1}H, ^{3}He, or ^{15}Na (Nahar et al., 2013). As the human body largely consists of water, most of the MRIs aim at measuring hydrogen to visualize soft tissues. The MRI is employed in revealing pathologies, such as brain tumors, torn ligaments or cancer.

MRI can be also utilized to study pulmonary deposition, however, proper contrast agent need to be used because of the large difference in susceptibility of air and tissue (Lizal et al., 2017). Sood et al. (2008) used aerosolized solutions containing contrast agent (gadopentetate dimeglumine) to study pulmonary deposition in ventilated piglets. Martin et al. (2008) measured regional lung deposition of superparamagnetic iron oxide nanoparticles in mice. Oakes et al. (2014) studied deposition of iron oxide particles in healthy and elastase-treated rats. Recently, Wang et al. (2016) published a first quantitative

map of regional deposition detected by MRI in healthy rats. Gadolinium-based contrast agent was delivered via nose and deposition in various regions, such as head, left or right lung, was studied.

The aforementioned studies showed that MRI measurements can be employed in regional deposition assessment. The benefit is that the use of MRI eliminates the risk of radiation exposure. On the other hand, the inhaled particles must exhibit sufficient magnetic susceptibility to be measured. This can be overcome using various contrast agents (Bellin, 2006), however, the amount of contrast agent that must be deposited is quite high (Thompson and Finlay, 2012).

3.2. *In vitro* methods

Aerosol regional deposition can be measured by *in vitro* methods using physical airway casts. The deposition studies using these casts can simulate realistic inhalation and deposition airway by airway can be examined. Moreover, deposition experiments can be reproduced. A series of experiments can be performed to study the effect of particle size or breathing regime on deposition under the same conditions. On the other hand, neither the available morphological data nor the technology allow production of the complete realistic lung cast. Therefore, regional deposition only in the upper respiratory tract and large airways of the tracheobronchial tree can be assessed.

The airway models have either idealized or realistic geometry. The idealized geometries were constructed with critical dimensions corresponding to available measured data of human respiratory tract or chosen aerodynamic principles (Byron et al., 2010). The casts encompass single or multiple cylindrical bifurcations made of plastic, glass, metal etc. The dimensions often correspond with dichotomous lung model of Weibel (1963). The realistic geometries are based either on casts from dental negatives and cadavers (Cheng et al., 1997) or on CT and MRI scans (Grgic et al., 2004; Tian et al., 2017).

The casts from cadavers have been developed using a following procedure (Patel et al., 2012). First, the excised lungs are dried until the parenchyma is rigid. Silicon resin is then poured into the dried lungs and allowed to solidify. When the resin “core” is solid, airway tissue is removed by dissolving in acidic solution creating a negative cast of the airways. Curable resin is applied onto the negative and allowed to become rigid. The physical airway model is obtained by dissolving the negative core. Other materials including silicone rubber, wax or metal have also been used for the cast production (Patra and Afify, 1983; Yamada et al., 1998). However, the airway casts are usually destroyed during analysis of aerosol deposition and a new model has to be created resulting in decreased reproducibility. The other method is a manufacture of a production mold representing the airway geometry. The “lost wax” technique can then be used to produce multiple hollow airway casts. Another drawback is that the resulted geometries could suffer from distortions caused by cadaveric tissue shrinkage. This problem can be overcome by obtaining CT and MRI scans *in vivo*. In addition, the anatomical data from these scans can be translated to numerical data. The same numerical data can then be utilized to manufacture identical airway casts using various methods, such as a rapid prototyping method (Lizal et al., 2012; Yamada et al., 1998).

a) The Upper respiratory airways and the tracheobronchial tree

In vitro deposition studies were pioneered by Chamberlain and Dyson (1956) who studied deposition of submicron radioactive particles in the plastic cast of human larynx and trachea. The work was extended by Martin and Jacobi (1972) who analyzed deposition patterns in an idealized model of the upper bronchial tree and observed significant role of turbulent diffusion in the trachea and bronchi. Since then, the aerodynamic behavior of particles has been widely investigated in the casts of single bifurcation (Bell and Friedlander, 1973; Kim et al., 1994; Kim and Iglesias, 1989), multiple bifurcations (Ferron, 1977; Kim and Fisher, 1999; Martonen, 1983; Oldham et al., 2000) or realistic tracheobronchial tree (Borojeni et al., 2014; Fang et al., 1993; Gurman et al., 1984; Chan and Lippmann, 1980; Robinson et al., 2006; Scheckman and McMurry, 2011; Schlesinger et al., 1977; Schlesinger et al., 1982; Smith et al., 2001).

As the reported casts mostly included airways in the upper bronchial tract, the influence of impaction on deposition was studied (Gurman et al., 1984; Kim and Fisher, 1999; Kim et al., 1994; Kim and

Iglesias, 1989; Schlesinger and Lippmann, 1972). The studies showed that the deposition efficiency in these large airways correlated reasonably well with a single deposition parameter, the Stokes number. The sites of enhanced deposition or "hot-spots" were observed, e.g. in the vicinity of bifurcation ridges, and it was found out that these sites matched the reported sites of bronchial carcinoma (Chan and Lippmann, 1980). The deposition data were employed to propose empirical deposition equation to predict deposition using mathematical models (Chan and Lippmann, 1980; Kim and Fisher, 1999). For example, Kim and Fisher (1999) analyzed deposition in multiple bifurcation casts representing 3rd to 5th generation of branching (Figure 13) at various flow rates. The casts were exposed to monodisperse oil particles ranging from 2.9 to 5.7 μm tagged with uranine. The deposition increased with increasing Stokes number. The regions with enhanced deposition were observed around bifurcations.

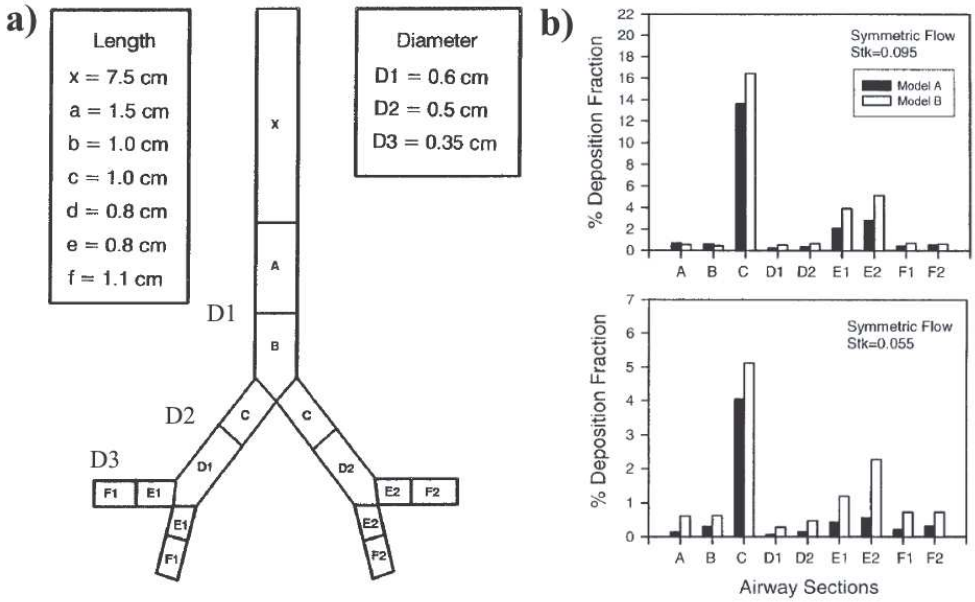

Figure 13 The study of regional deposition in the idealized multiple bifurcation tube model; a) the model geometry, branching was in-plane (model A) and out-of-plane (model B); b) the deposition fractions as the function of airway section (Kim and Fisher, 1999)

The geometrical features, such as a branching angle or a parent-daughter diameter ratio, had minor effect on deposition. Moreover, the differences in deposition between multiple bifurcation tube models and realistic casts from cadavers were considerably small (Kim and Fisher, 1999). However, the studies showed that the upstream velocity profile history is essential for proper deposition studies in the tracheobronchial tree. The early results of Chan et al. (1980) showed that the larynx increased deposition in the trachea compared to the casts without larynx. The discrepancy in results was caused by the complex larynx geometry that enhanced turbulence levels and created so-called laryngeal jet (Corcoran and Chigier, 2000). The complicated velocity profile and turbulent flow then propagated through the trachea to the main bronchi. Martonen et al. (1982) demonstrated that the laryngeal jet affected air mixing in the trachea that subsequently influenced growth of hygroscopic particles and resulted in further increase in deposition.

Therefore, the models of human respiratory tract including extrathoracic airways are necessary to provide realistic inlet conditions into the tracheobronchial tree. The realistic airway casts have been used to study deposition in both the nasal (Cheng et al., 2001; Kelly et al., 2004; Schroeter et al., 2015; Storey-Bishoff et al., 2008; Swift, 1991; Zwartz and Guilmette, 2001) and oral airways (Golshahi et al., 2012; Grgic et al., 2004; Cheng et al., 1997; Cheng et al., 1999; Lin et al., 2001; Swift, 1992). The mouth is a predominant route for drug delivery and people switch to oral breathing during heavy workload. Swift (1992) measured mass particle deposition in the mouth and throat delivered from an inhaler. Cheng et al. (1999) used a realistic airway model of human oral cavity made from dental impressions (Figure 14a) to study regional deposition of fluorescent particles. It was observed that the deposition increased with

increasing particle size and flow rate (Figure 14b). Moreover, it was suggested that the deposition in the oral cavity can be approximated to deposition in 180° curved tube of variable cross-section. Grgic et al. (2004) employed idealized geometry of mouth and throat based on CT and MRI scans to study regional deposition. The idealized geometry represented an "average" extrathoracic airway geometry and is known as Alberta Idealized Throat (DeHaan and Finlay, 2001; Stapleton et al., 2000). It was found out that the deposition in the mouth and throat was driven by impaction and was a function of Stokes and Reynolds number. Golshahi et al. (2012) studied deposition in children oropharyngeal airway casts and analyzed intra-subject variability.

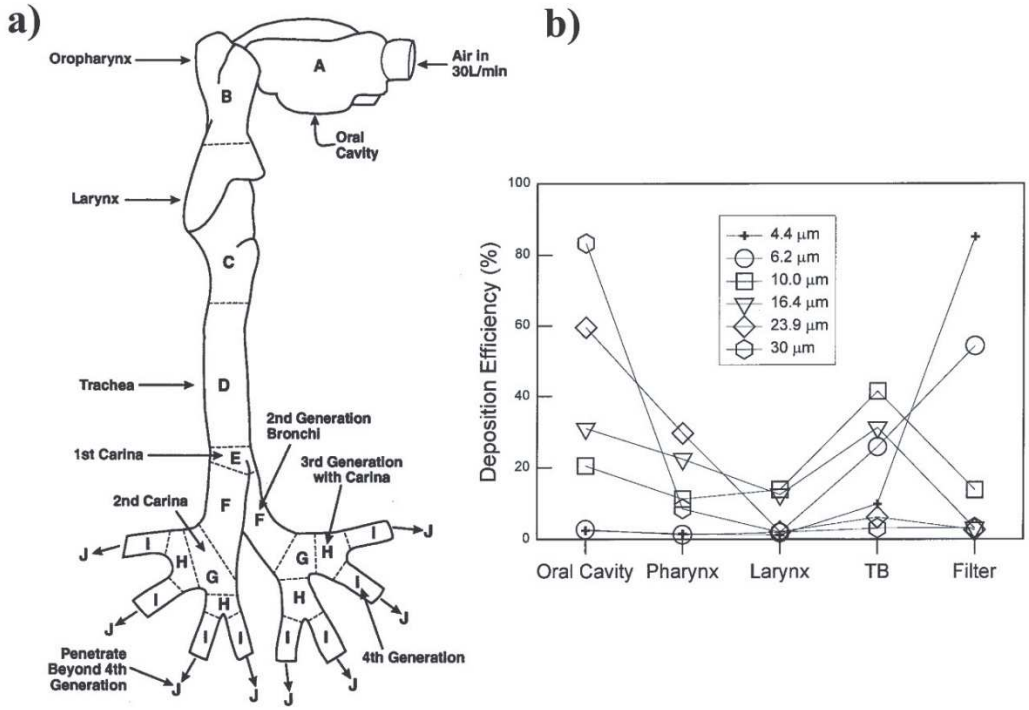

Figure 14 Results of deposition experiments in the realistic airway cast; a) the cast schematics, b) regional deposition for various particle sizes and the flow rate of 30 L/min (Cheng et al., 1999)

By combination of the upper airway and the tracheobronchial tree geometry, realistic casts of human respiratory tract have been developed (Lizal et al., 2012; Verbanck et al., 2016; Zhou and Cheng, 2005) (Figure 14). These casts allow assessment of regional deposition at rather realistic conditions, i.e. realistic inlet conditions and geometry. Zhou and Cheng (2005) investigated regional deposition of spherical particles ranging from 0.93 to 30 μm using a fluorescence method. Correlation between particle size, flow rate and deposition efficiencies was found. The deposition efficiency was higher compared to that measured by Kim and Fisher (1999) in the idealized tube model. The deposition data were employed to develop new empirical models for deposition predictions. Later, Lizal et al. (2015) studied radioactive particle deposition in the more complex airway cast encompassing respiratory airways down to the 7th generation of branching. In addition, Nordlund et al. (2017) utilized the same model to study transport of multicomponent aerosol particles simulating electronic cigarette smoke. Verbanck et al. (2016) connected idealized mouth-throat airway geometry to a realistic geometry of the tracheobronchial tree. The regional deposition corresponded reasonably well to gas flow distribution.

b) The alveolar region

The use of *in vitro* airway casts to study deposition in the alveolar region has been rather sparse to date as the geometry is complicated and the dimensions of the alveolar ducts and sacs are very small (in the order of hundreds of microns). One way to overcome the small dimensions in the acinus is to scale-up the airway models. However, it is a big challenge to match simultaneously dimensionless numbers for flow (Reynolds and Womersley number) and particles (Stokes and gravity number) (Sznitman, 2013). Therefore, the scale-up airway models have been used only for better understanding of flow patterns in

the acinus (Berg et al., 2010; Cinkotai, 1974; Karl et al., 2004; Oakes et al., 2010). Recently, microfluidic devices for simulation of various organs, so-called "organs on a chip", were developed using microfabrication techniques (Huh et al., 2007; Huh et al., 2010). These small platforms incorporate one-to-one scale idealized alveolar structures with deformable walls. Fishler et al. (2015) utilized the microfluidic devices and studied deposition of fluorescence polystyrene particles. The results showed important role of sedimentation for micro–sized particles. In addition, almost none of the particles reached distal generations independent on particle size.

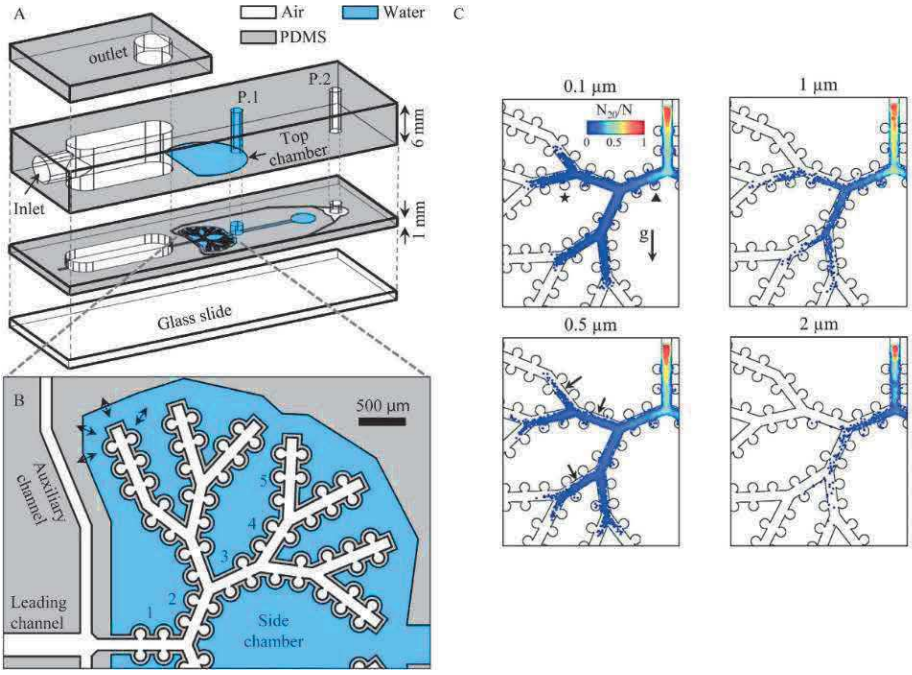

Figure 15 Acinus on a chip; A) Microfluidic acinar model; B) Schematics of the acinar tree. Airway walls are surrounded by water chambers. By applying pressure to the water chambers, the airway walls are deformed; C) Deposition results for various particle sizes. (Fishler et al., 2015)

3.3. *In silico* methods

The most significant drawback of the experimental *in vivo* data is in the limited number of tested subjects, selected breathing patterns and particle sizes. This data gap is often filled with *in silico* methods. *In silico* modelling concepts may be grouped according to the region of interest in the lung, i.e. prediction of deposition in the whole lungs (respiratory system) or prediction of deposition in selected small regions, such as airway generation, using Computational fluid dynamics approach (Hofmann, 2011).

3.3.1. Mathematical "whole lung" models

The whole lung approach simplifies the phenomena and treats the airflow, particle transport and deposition independently. The particle deposition is described by analytical deposition equations for various flow conditions. The whole lung models may be divided into five groups which will be described more thoroughly below (Hofmann, 2011; Rostami, 2009):

a) Empirical and Semi-empirical models

These models utilize available experimental data and propose equations for deposition predictions. Asgharian et al. (1995) summarized published data and constructed nomograms for estimation of deposition in the alveolar region of human, monkey, and rat. Rudolf et al. (1983; 1990) presented algebraic deposition model based on statistical analysis of data of Stahlhofen et al. (1983). Theoretical predictions were made for the regions where no data were available. The model estimated deposition in

various lung regions, such as bronchial or bronchiolar region, and included dependence of deposition on gender or age.

One of the most used semi-empirical models was proposed by the International Commission on Radiological Protection (ICRP, 1994). The purpose of the model was to estimate deposition doses of radionuclide aerosols in workers. The morphometric model encompasses four compartments (Figure 16): a) the extrathoracic compartment consisting of anterior nose (ET_1), posterior nasal passages, larynx, pharynx, and mouth (ET_2); b) the bronchial compartment (BB) consisting of the trachea and bronchi; c) the bronchiolar compartment (bb) consisting of the bronchioles and terminal bronchioles; d) the alveolar compartment (AI) consisting of respiratory bronchioles, the alveolar ducts and sacs, and the interstitial region (Rostami, 2009). Each compartment is seen as a filter with filtration efficiency for inhalation and exhalation given by equation 12 (Hofmann, 2011):

$$\mathrm{FE} = 1 - \exp(-aR^p) \qquad (12)$$

where a and p are constants and R denotes information on particle size and breathing pattern. First of all, inhalability of specific aerosol particles is calculated and is generally less than 1 (Hinds, 1999). After that, deposition in given compartment is calculated by multiplying deposition fraction (number of particles reaching given compartment) by filtration efficiency of given compartment. Particle deposition is considered as a stationary filtering process during which particles deposit in one of the compartments (filters) or pass all of them and are exhaled (Figure 16). The filtration efficiencies in given compartments are based on available experimental data in terms of fluid and particle characteristics. Therefore, the deposition patterns can be analyzed for various physical activity conditions, aerosol size distributions, body size, gender, age etc. Another benefit of the model is its simplicity and low computational costs. On the other hand, the model simplicity results in relatively low resolution of deposition and the model is not able to provide information on deposition in specific region of the lung, such as single bifurcation. Moreover, the estimation accuracy and number of exposure scenarios are limited to the range of experimental data.

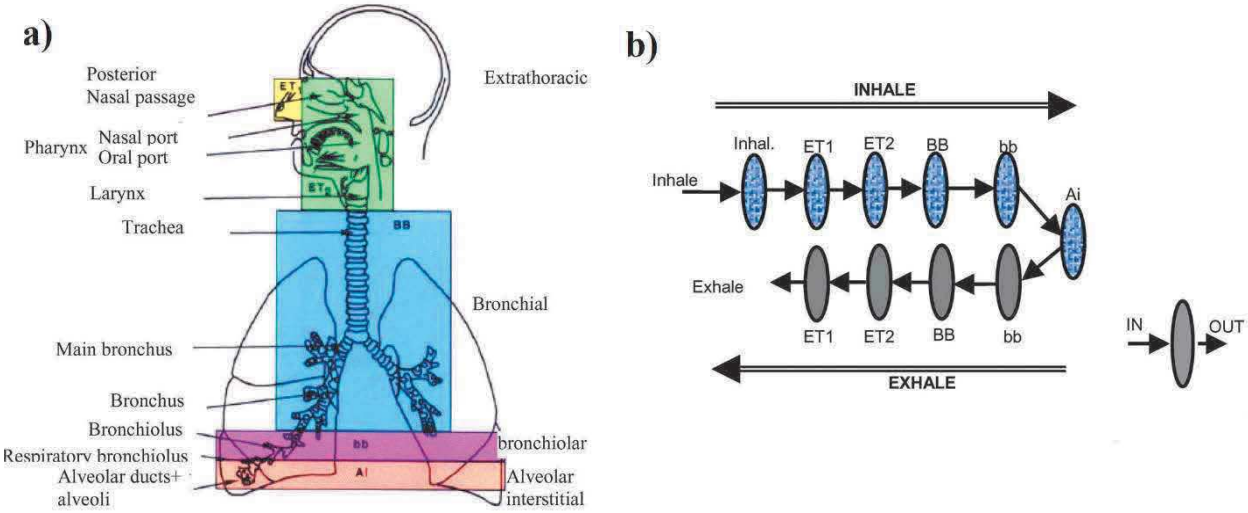

Figure 16 The ICRP dosimetry model; a) morphometric compartments; b) compartments are represented by filters with given deposition efficiency (Rostami, 2009)

b) Mechanistic one-dimensional models

Mechanistic models approximate the respiratory tract geometry to a one-dimensional, variable cross-section channel or the so-called "trumpet". As the cross-section is a function of generation number and increases sharply, it resembles trumpet-like shape (Figure 17). The trumpet model uses the lung morphology given by Weibel (1963). Aerosol concentration is calculated along the airway depth or the generation number (Rostami, 2009) using a transient transport equation (equation 12). In this equation, the use of differential length enables superposition of various deposition mechanisms and the use of differential time allows the application of any breathing pattern. As the lung morphology is one-

dimensional, the given breathing pattern and calculated aerosol concentration is considered to be the average across all the airways in the corresponding generation. Therefore, the purpose of the model is to conveniently provide average spatial aerosol concentration distribution for various scenarios.

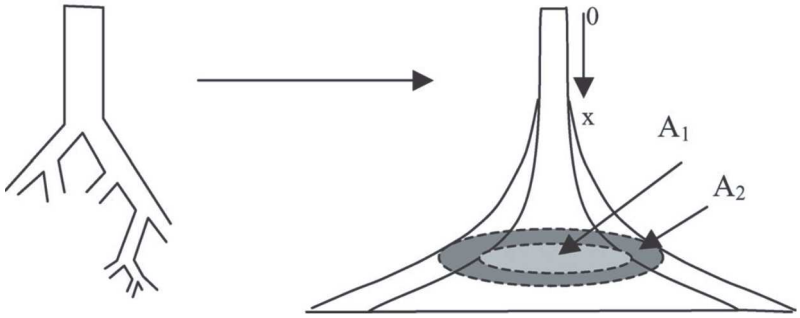

Figure 17 Illustration of the "trumpet" model (Rostami, 2009)

The "trumpet" model was developed by Taulbee and Yu (1975) and modified later by Taulbee et al. (1978). The particle concentration as a function of airway length L_a and time t is governed by transient transport equation:

$$\delta(A_1 + A_2)\frac{\partial c_a}{\partial t} = -Q\frac{\partial c_a}{\partial L_a} - Qc\lambda \qquad (13)$$

where c_a is the aerosol concentration, A_1 and A_2 are the summed cross-sectional areas, δ is an expansion factor, λ denotes a loss coefficient and Q is airflow rate. Concentration loss was considered to be the effect of deposition mechanisms of impaction, sedimentation, diffusion, and electrostatic precipitation. The model assumed monodisperse stable aerosol. As the exact solution could be found, short computational times were needed.

The model was further developed by Egan and Nixon (1985), Nixon and Egan (1987), and Darquenne and Paiva (1994) to incorporate axial diffusion and more recent transport equations. Moreover, Lazaridis et al. (2001), Robinson and Yu (2001), and Choi and Kim (2007) extended the trumpet model to include more complex particle dynamics, deposition of cigarette smoke and improved alveolar morphology. Mitsakou et al. (2005) presented deposition model with full aerosol dynamics effects encompassing hygroscopic growth and coagulation. The transient transport equation for the calculation of number concentration N_i was improved:

$$\frac{\partial}{\partial t}(A_T N_i) = \frac{\partial}{\partial x}(A_A u N_i) + \frac{\partial}{\partial x}\left(A_T D_{Ba}\frac{\partial N_i}{\partial x}\right) - v_{di}(n\pi D_a)N_i + \left(\frac{\partial}{\partial t}(A_T N_i)\right)_{growth} + \left(\frac{\partial}{\partial t}(A_T N_i)\right)_{coag} \qquad (14)$$

where A_T is cumulative cross-sectional area of all airways and alveoli, A_A denotes cross-sectional area of all convective airways, u is the air velocity, D_{Ba} is the axial diffusion coefficient, D_a denotes the diameter of given airway at distance x from trachea, and v_{di} is the deposition velocity due to impaction, sedimentation, and Brownian motion.

The illustrative results of the "trumpet" model can be seen in Figure 18. Choi and Kim (2007) calculated deposition of various particle sizes and specific breathing regime (V_T = 500 mL, Q = 250 mL/s). The estimated deposition fractions were very small in the first few generations. The deposition peaks were observed at G ≥ 15. Overall, the total deposition fractions were the lowest for the particles in the range of 0.1–1 μm as there is no major deposition mechanism for these particles.

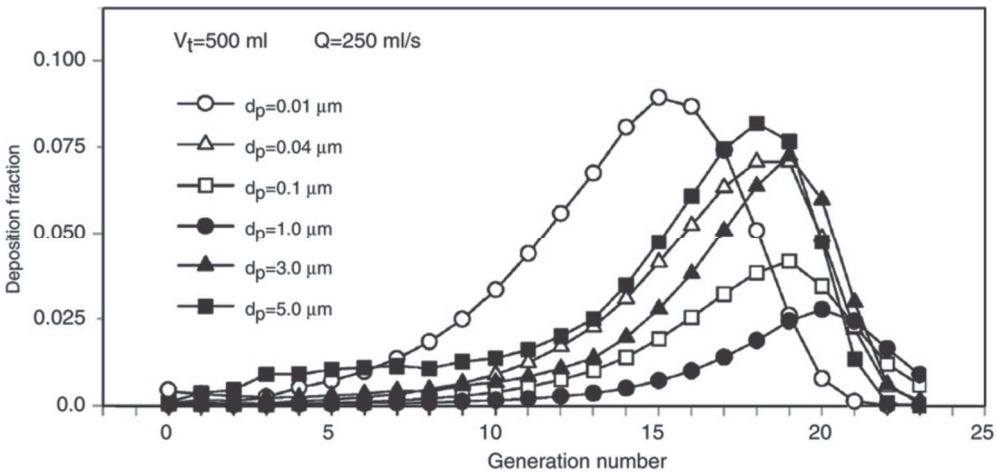

Figure 18 Generational deposition of particles in a wide range of sizes in the tracheobronchial tree (Choi and Kim, 2007)

c) Deterministic symmetric or "single-path" models

Deterministic symmetric models predict deposition in symmetrical lung geometries, such as the model A by Weibel (1963) or the model by Yeh and Schum (1980). As all airways in given generation have the same dimensions and each parent airway branch into two identical daughter airways, all the paths from the trachea to the alveolar region are identical and thus, can be represented by a single path. The deposition fractions are the same for all the airways in given generation. The deposition efficiencies in the given generation are calculated using analytical equations for various deposition mechanisms and inhalation scenarios. Many authors derived analytical equations from experimental data for deposition due to diffusion (Cohen and Asgharian, 1990; Ingham, 1984; Martonen, 1982; Yu and Cohen, 1994), impaction (Cai and Yu, 1988; Kim et al., 1994; Zhang et al., 1997), and sedimentation (Martonen, 1982; Pich, 1972; Wang, 1975). The deposition distribution throughout the respiratory tract is then calculated by multiplying deposition fraction in given airway generation by computed deposition efficiencies.

The first deterministic symmetric model was proposed by Findeisen (1935) and later extended by Landahl (1950) and Beeckmans (1965). Since then, the models improved primarily in implementation of more detailed morphometric data and more accurate analytical deposition equations (Gerrity et al., 1979; Hofmann et al., 1989; Martonen, 1982, 1993; Yeh and Schum, 1980).

Based on the model of Yeh and Schum (1980), the US National Commission on Radiological Protection proposed a new model (NCRP, 1997). Its purpose was to describe respiratory tract deposition, clearance and dosimetry of radioactive substances by workers and general public (Yeh et al., 1996). The NCRP model divides human respiratory tract into three regions: the naso-oro-pharyngolaryngeal (NOPL) region, the tracheobronchial region (TB) and the pulmonary region (P). The tracheobronchial region consists of sixteen generation of branching from trachea to terminal bronchioles. The pulmonary region consists of eight generations of airways and alveoli. The model utilizes empirical equations for the calculation of deposition in the NOPL region, however, analytical equations are employed for the calculation of deposition in the TB and the P region. Yeh et al. (1996) compared the NCRP model to the semi-empirical ICRP model for radiation protection and the results can be seen in Figure 19. The general trends of both the models agreed considerably well. However, the NCRP predicted lower NOPL deposition for particles larger than 2.5 µm. Moreover, the ICRP model predicted lower TB deposition and subsequently higher P deposition compared to the NCRP model for particles smaller than 0.1 µm.

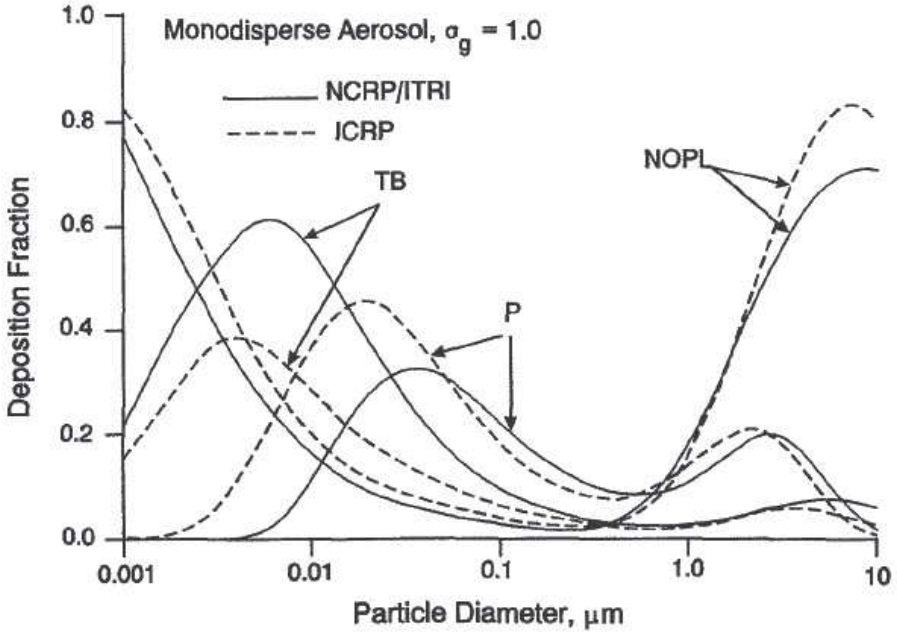

Figure 19 Comparison of deposition predictions for monodisperse particles using the NCRP and ICRP deposition model (particle density = 1 g/cm^3, tidal volume = 770 mL, breathing frequency = 13 min^{-1}, FRC = 3000 mL) (Yeh et al., 1996)

In overall, single-path models are not computational demanding because of their simple symmetric geometry and can provide fast deposition predictions of average regional or total deposition. However, the simple geometry does now allow calculation of more detailed or asymmetric deposition.

d) Deterministic "multiple-path" models

Multiple-path models implement more realistic morphological data, i.e. asymmetric branching pattern and various airway length and diameters in given airway generations, to provide more detailed deposition data. Yeh et al. (1979) was the first to study the effect of asymmetric airway branching on deposition. Two deposition models were proposed, a "single-path" model and a five-lobe model. In the five-lobe model, different single path model was described for every lobe (each lobe had different symmetrical and dichotomous branching). Therefore, each lobe had different structure. The regional and total deposition was similar for both models, however, there were significant differences for the lobar deposition results. This indicated that regional deposition predictions from single-path models were not adequate for assessment of more detailed deposition dose and subsequent lung response.

Later, Asgharian et al. (2001) presented a multiple-path model incorporating 10 different five-lobe, asymmetric human airway trees. The airway trees were constructed using a stochastic morphometric model (Koblinger and Hofmann, 1990) and were based on the morphometric data of Raabe (1976). As sufficient morphometric data for alveolar region were not available at the time of the study, identical alveolar region of Yeh et al. (1979) was connected to the tracheobronchial airway trees. The air flow in every airway was determined by the volume distal to it. The deposition efficiencies were calculated in every airway using analytical equations for deposition via sedimentation, diffusion and impaction (Anjilvel and Asgharian, 1995). Illustrative results of the multi-path model are displayed in Figure 20. The results showed that the deposition between specific lobes varied greatly and indicated the importance of multiple-path models when assessing health hazards of inhaled pollutants.

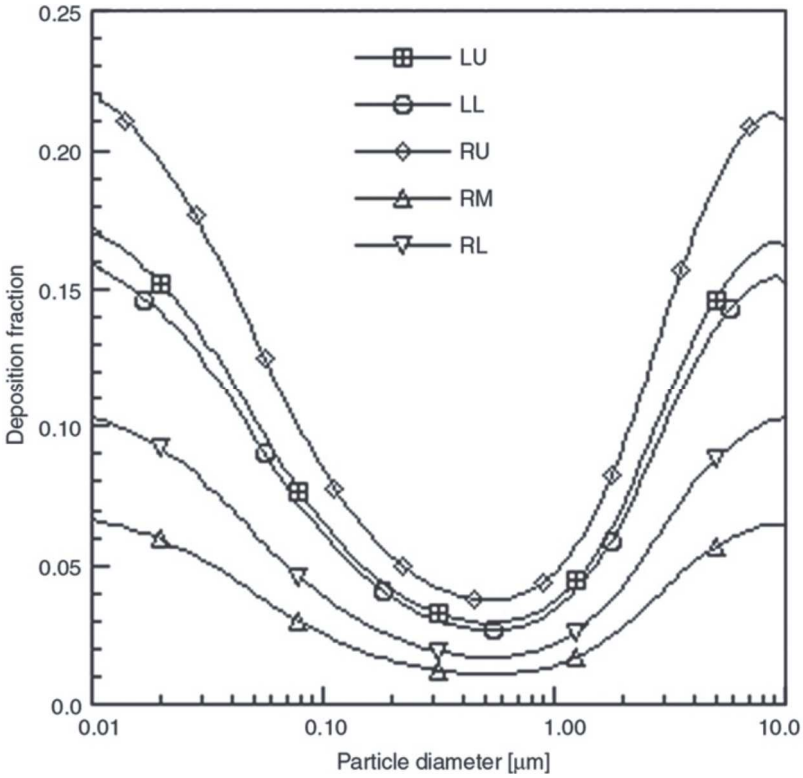

Figure 20 Total mean lobar deposition fractions of unit density particles (FRC = 3300 mL, minute ventilation = 7500 mL); LU is left upper lobe, LL is left lower lobe, RU is right upper lobe, RM is right middle lobe, and RL is right lower lobe (Hofmann, 2011).

The multiple-path models are improvements of single-path models. They incorporate realistic asymmetric lung structure with specific airway dimensions rather than symmetric lung structure with average dimensions. Therefore, they can provide more detailed deposition data. Moreover, the used lung geometries represent individual persons and can be used to determine inter-subject variability.

e) Stochastic "multiple-path" models

Stochastic multiple-path models are another way to include asymmetric lung structure into deposition predictions. In 1982, Yu and Diu (1982) introduced a probabilistic lung model for deposition studies. The model encompassed two random scaling factors to vary airway dimensions (diameter and length). The randomly calculated airway trees were used to calculate deposition and thus, emphasize the effect of inter-subject variability.

Later, alternative stochastic model IDEAL (Inhalation, Deposition and Exhalation of Aerosols in the Lung) was developed by Koblinger and Hofmann (1990) and Hofmann and Koblinger (1990, 1992). In this model, airway length and diameter together with the number of airway generations were randomly scaled using Monte Carlo method. The single particle walks step by step through a unique airway tree that is modeled by a series of randomly selected Y-shaped bifurcations. The airway dimensions are selected according to their probability density functions based on the morphometric data of Raabe (1976) and Haefelibleuer and Weibel (1988). As the path and deposition of every particle is different from all the others, order of tens or hundreds of thousands of particles are needed to calculate total or regional deposition. The deposition efficiency is calculated for every airway structure using analytical equations. The IDEAL model was extended to include deposition of charged (Majid et al., 2012) or ultrafine (Sturm, 2016) particles. Moreover, the use of Y-shaped bifurcations is suitable for comparison with in vitro experiments or numerical simulations which can lead to improvement of used deposition equations (Hofmann, 2011).

The stochastic deposition models bring valuable deposition data in the terms of inter- and intra-subject variability. However, it is worth noting that the initial information on airway dimensions is based on measurements of a few lung geometries.

3.3.2. Computational Fluid Dynamics (CFD)

CFD methods are the most recent mathematical techniques used for the study of regional deposition. Unlike whole lung models that use 1D analytical equations, CFD methods use 3D general governing transport equations for the fluid flow analysis. The fluid flow is determined by solving Navier-Stokes equations which describe the relationship of velocity, pressure, temperature, density and viscosity (Versteeg and Malalasekera, 2007). The particle deposition is then calculated using Lagrangian or Eulerian approach. The former approach tracks individual particles through the computational geometry by solving Newton´s second law equation (equation 5) (Longest and Xi, 2007). The second approach considers particles as a continuum phase and solves transport equations for aerosol concentration. The Eulerian approach is more appropriate for high concentrations and ultrafine particles for which inertia is negligible (Rostami, 2009).

During the CFD process, the airway geometry is divided into small representative elements and detailed solution of fluid flow and particle transport is calculated in each element afterwards. As the elements can have sub-millimeter sizes, CFD can provide very localized deposition patterns that are not possible to obtain by other approaches. However, the higher number of representative elements (the size and complexity of the geometry) results in higher computational times. Therefore, the CFD methods are currently employed to elucidate flow and deposition patterns in separated airway sections, such as an oral cavity, an airway bifurcation etc. The CFD model of the whole lung is not yet feasible. However, the size of the computed regions increases with increasing computational power (Longest and Holbrook, 2012).

The CFD methods are used to analyze deposition in extrathoracic airways, upper tracheobronchial tree or alveolar region. The geometries are similar to those used in the airway cast studies. Using the same geometry for both *in vitro* and *in silico* CFD approaches is convenient as the results can be easily compared. This is important because the underlying physics used in CFD methods is very intricate and the results need to be validated by experimental evidence (*in vitro* or *in vivo*).

The CFD methods have been frequently used for aerosol deposition studies. Various idealized (Zhang and Kleinstreuer, 2004) or realistic geometries (Lambert et al., 2011) were employed. Since several reviews (Cheng, 2014; Kleinstreuer et al., 2008; Longest and Holbrook, 2012; Rostami, 2009) have been published regarding this topic, only brief summary will be given here. The deposition studies will be classified according to the region of inspected deposition.

a) Extrathoracic airways

The deposition patterns have been obtained for both the nasal (Longest et al., 2011; Martonen et al., 2003; Shanley et al., 2008; Shi et al., 2006; Schroeter et al., 2011; Zamankhan et al., 2006) and the oral cavities (Paz et al., 2017) using CFD methods. As the current work aims at deposition in the oral cavity, only oral deposition will be discussed here. Deposition was computed in both idealized and realistic geometries. The purpose of the idealized models was to correctly predict the deposition patterns in conjunction with short computational time.

Kleinstreuer and Zhang (2003) developed an idealized oral/pharynx/larynx model modeled as a 180° variable cross-section tube as suggested by Cheng et al. (1999). The deposition efficiency agreed to that measured in the realistic oral cavity (Cheng et al., 1999). It was observed that turbulence, e.g. near the larynx, can enhance deposition to some extent due to turbulent dispersion. The effect was more important for smaller particles. In addition, Zhang et al. (2005) employed the same model to compute deposition for particles of various nano- and micro-sizes. The deposition of nanoparticles was more uniform than that of micro-sized particles. However, the deposition hot spots were similar across the particle sizes, in the outer bend of pharynx/larynx. Stapleton et al. (2000) analyzed deposition in the idealized mouth-throat geometry, the Alberta Idealized Throat. The CFD results agreed considerably

well with *in vitro* results for laminar flows but the used turbulence models caused poor agreement during high flow rates. In continuation, Matida et al. (2004) computed the regional deposition using Reynolds–averaged Navier–Stokes models. Good agreement was found when near-wall corrections for fluctuations were implemented. These corrections addressed the effect of turbulence anisotropy. The necessity of using near wall corrections was confirmed by Zhang et al. (2004) who proposed highly idealized mouth-throat geometry and showed that deposition patterns followed *in vivo* data considerably well. Xi and Longest (2007) quantified the effect of airway geometry simplifications on deposition using four different models. The degree of model physical realism descended from fully realistic based on CT and MRI scans to constant-diameter tube model (Figure 21). The study showed that although the regional averaged deposition agreed considerably well among the models, the deposition hot spots were sensitive to the model geometry. Therefore, realistic geometry is highly recommended while studying localized deposition.

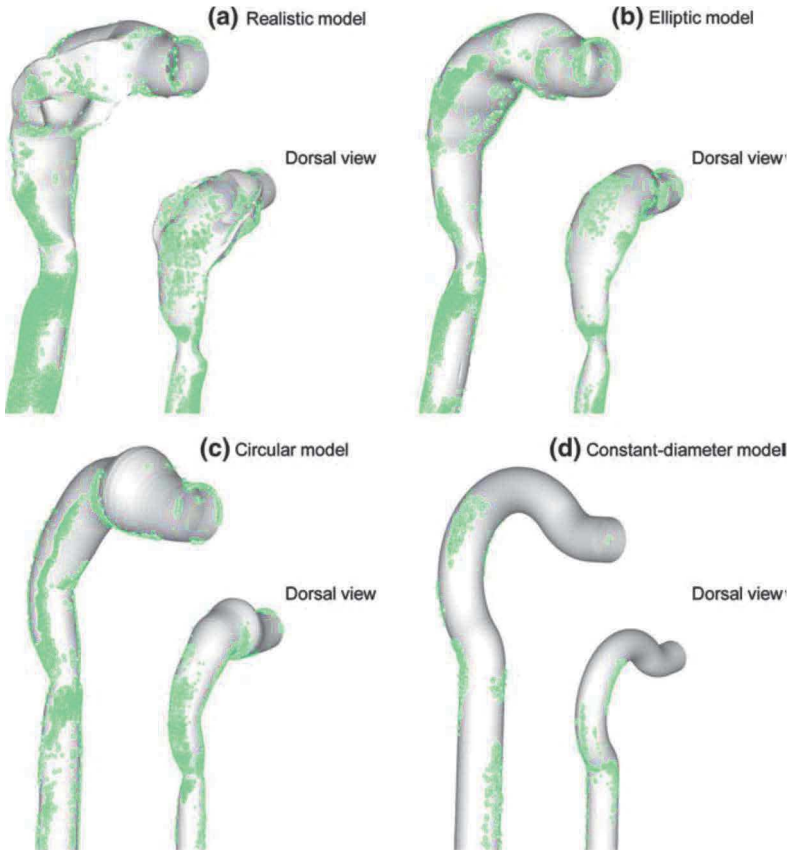

Figure 21 Deposition patterns of 6 µm particles under steady inhalation flow rate of 30 L/min for a) realistic, b) elliptic, c) circular, and d) constant-diameter model (Xi and Longest, 2007)

Sosnowski et al. (2006) developed a realistic model of human oropharynx based on CT and MRI scans. Deposition during steady and non-steady inhalation was studied. It was observed that the deposition was higher during cyclic flows compared to the steady inhalation. This could be caused by transition of the flow from laminar to turbulent and back during inhalation peak flow rates. The increased deposition in the oral cavity and oropharynx was observed in other studies emphasizing the significant particle loss in the oral cavity during drug delivery (Jayaraju et al., 2007; Takano et al., 2006). Sandeau et al. (2010) investigated the effect of using helium-oxygen during inhalation therapies. The observed deposition efficiencies with helium-oxygen mixture were lower compared to air. This was caused by the low density of helium-oxygen mixture resulting in lower pressure losses and decreased effect of turbulence.

b) Tracheobronchial tree

The ability of CFD approach to provide highly localized deposition patterns has been frequently utilized in the tracheobronchial geometries, both idealized (Isaacs et al., 2006; Soni and Aliabadi, 2013; Tian

and Ahmadi, 2012) and realistic (Rahimi-Gorji et al., 2016). The early studies analyzed deposition in idealized single or multiple bifurcation models. Hofmann et al. (1995) investigated deposition patterns in a single bifurcation model and the impact of gravity was explored by changing the model spatial orientation. Balashazy et al. (2003) computed deposition in single bifurcation models and analyzed the inhomogeneity in deposition. To quantify deposition hot spots, a deposition enhancement factor (DEF) was introduced as the ratio of local to average deposition density. Significantly high numbers of DEF were observed in the vicinity of bifurcation ridges and subsequent induction of respiratory diseases was discussed. Comer et al. (2000) studied deposition in multiple bifurcation model. The deposition results were compared to *in vitro* measurements of Kim and Fisher (1999) and good agreement was found. The deposition about the second generation was highly affected by the first bifurcation as the flow became significantly nonuniform. Therefore, the use of multiple bifurcation models was recommended when studying deposition in the tracheobronchial tree. Longest and Vinchurkar (2007b) numerically investigated deposition patterns of 10 µm particles in multiple bifurcation model representing generations G3–G5. The data showed significant impact of turbulence on deposition. Moreover, the results were compared to in vitro observations of Oldham et al. (2000) and it was concluded that inlet velocity and particle profile is important to accurately reproduce localized deposition patterns.

Zhang and Kleinstreuer (2001) analyzed the effect of particle release position on deposition patterns in an idealized triple bifurcation model that was used as a representative of upper bronchial tree (Zhang et al., 2001). As expected, inlet particle distributions (e.g. parabolic or uniform) strongly influenced the deposition efficiencies. In addition, Zhang et al. (2005) extended the model by adding an idealized extrathoracic airways and investigated deposition of nano- and microparticles in the model from mouth to G3. The maximum DEF for microparticles ranged from 40 to 500 in the oral cavity and 200 to 2400 in the bronchial tree. Deposition of nanoparticles was more uniform compared to that of microparticles. Later, deposition of nanoparticles (Zhang et al., 2008) and micro-sized particles (Kleinstreuer and Zhang, 2009) were computed in the model extending down to the G15 by decomposing the model into triple-bifurcation units with properly adjusted outlet/inlet conditions. The deposition results in these idealized models agreed very well with average regional or total deposition results of whole-lung models. However, local deposition hot spots or bifurcation-by-bifurcation deposition fractions differed significantly.

Nowak et al. (2003) conducted simulations of particle deposition in two airway geometries, an idealized one based on Weibel A model (Weibel, 1963) and a realistic one based on CT scan of a cadaver lung cast. The deposition patterns varied greatly, for example the realistic model showed higher deposition on the tubular walls. Moreover, deposition during transient inhalation differed compared to steady-state cases indicating the need of cyclic flows for accurate deposition predictions. Xi et al. (2008) studied the impact of laryngeal jet on deposition in the realistic model of tracheobronchial tree. The model was generated by digitalizing an airway cast of Cohen et al. (1990) and connecting it to the approximate model of laryngeal constriction (Xi and Longest, 2007). As can be seen in Figure 22, the inclusion of laryngeal approximation increased deposition in the trachea and subsequently reduced deposition around first bifurcation for 4 µm particles. Ma and Lutchen (2009) simulated particle deposition in a model extended from mouth to G10. Majority of the particles ranging from 1 to 30 µm deposited in the upper respiratory airways or large conductive airways. Although the ventilation was higher for the right lung, higher deposition in the left lung was observed. Lambert et al. (2011) numerically studied this phenomenon in the CT-based human airway model using large eddy simulation method. It was found that the effect of turbulent laryngeal jet together with airway asymmetry caused more particles to enter and deposit in the left lung. Recently, the realistic anatomical reference model of Schmidt et al. (2004) extending from G0 to G17 was employed in the numerical study investigating airflow (Gemci et al., 2008) and particle deposition (Islam et al., 2017). However, the number of grid cells in these studies was probably insufficient to fulfill the grid convergence criteria given by Longest and Vinchurkar (2007a) (Longest and Holbrook, 2012). Therefore, these data should be used with caution. Recently, Koullapis et al. (2017) studied the effect of various numerical approaches on the deposition in the realistic model extending from mouth down to the 7th generation of branching. The

numerical data were validated by *in vitro* measurements performed using the same geometry (Lizal et al., 2015). The results indicated significant importance of adequate mesh size and choice of turbulence model. On the other hand, inflow conditions turn out to be less important.

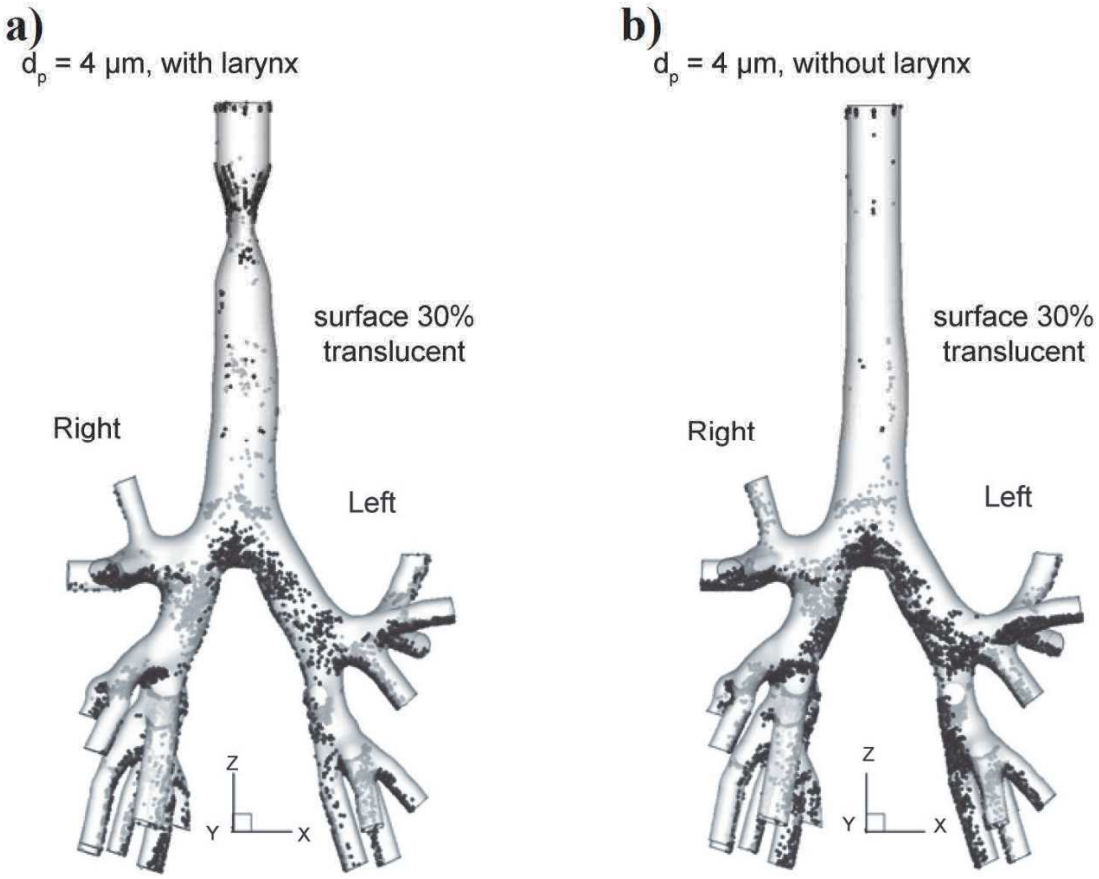

Figure 22 Deposition of 4 µm particles under sedentary conditions (Q = 15 L/min) in the model with (a) and without laryngeal approximation (b) (Xi et al., 2008)

c) Alveolar region

The use of CFD methods have contributed in understanding of mechanics responsible for particle transport and deposition in the alveolar region. This task is very difficult as the particles deposit via several deposition mechanisms, e.g. impaction, sedimentation, diffusion and convective mixing (Longest and Holbrook, 2012). Moreover, the particles exhibit chaotic nonreversible movement (Henry et al., 2002; Tsuda et al., 2008). The geometry is very complicated and one must consider wall motion which is recognized as essential for proper aerosol transport. The wall motion can be simulated by applying pressure on the exterior of the airway and subsequently coupling fluid and solid mechanics solvers (Dailey and Ghadiali, 2007). However, this method is computationally demanding, therefore, kinematic wall displacement mimicking sinusoidal breathing pattern is frequently used (Sznitman, 2013). In addition, cyclic breathing and oscillatory conditions must be taken into account when one studies particle deposition in small airways (Kojic and Tsuda, 2004). The review of mechanics governing particle transport in the pulmonary acinus has been published elsewhere (Sznitman, 2013; Tsuda et al., 2008).

The early studies aimed at particle behavior in a single alveolus. Haber et al. (2000) and later, Haber et al. (2003) studied numerically particle trajectories and deposition in the single alveolus model represented by hemispherical cavity. The studies showed that the particles undergo convective mixing and exhibit complex stochastic trajectories induced by rhythmic wall motions. Therefore, it is important to include wall motions in determining deposition. Balashazy et al. (2008) investigated deposition of particles ranging from 0.1 µm to 1 µm in the alveolus model with various orientation relative to the

direction of gravity. The deposition of small particles (0.1 µm) was driven by diffusion whereas the deposition of large particles (above 1 µm) was driven by sedimentation highly depending on the spatial orientation of the model.

Darquenne and Paiva (1996) and later Darquenne (2001) simulated 2D and 3D transport of particles within a few generations of alveolated ducts. The deposition patterns were not uniform on the alveolar walls and the <0.5 µm particles deposited mainly near the alveolus entrance. Some of the particles were not deposited neither exhaled after a single breathing cycle. These could penetrate deeper into the lung during subsequent inhalation. Lee and Lee (2003) compared particle transport in a straight tube and an alveolated duct. The velocity profile became blunter in the presence of the alveolus as opposed to a parabolic profile in the straight tube. The dispersion of particles was correlated to Strouhal number. Sznitman et al. (2009) numerically simulated transport of micro-sized particles (1 and 3 µm) in a simple alveolated duct and in an asymmetric acinar tree. The 3 µm particles yielded trajectories characteristic for gravitational sedimentation and deposited within a single inhalation phase. On the other hand, 1 µm particles exhibited complicated trajectories influenced by the coupling of flow reversal, gravity and intricate alveoli geometry. Moreover, some of 1 µm particles remained airborne for several breathing cycles before depositing. The study also implied that the use of simplified models, such as a single alveolus or an alveolated duct, is not adequate in order to comprehend complicated mechanics.

Ma and Darquenne (2011) developed idealized multigenerational model of alveolated airways with various bifurcation angles and spherical alveolar shapes. Deposition of 1 and 3 µm particles was investigated under the effect of gravity and without. Total deposition was 33 and 75% for 1 and 3 µm particles under normal gravity, respectively, as opposed to total deposition of 2–5% for both particles sizes under zero gravity indicating important role of gravitational sedimentation. Khajeh-Hosseini-Dalasm and Longest (2015) generated a space-filling model of the acinus region based on 14-hedron elements to study micron-sized particle deposition. The majority of particles deposited in the first three generations of alveolated ducts indicating no need to simulate micro-sized particle deposition in the models including more than 3 generations. Moreover, the gravity angle had minor effect on total deposition, although the effect on local deposition patterns had been demonstrated earlier (Ma and Darquenne, 2012). Hofemeier and Sznitman (2015) further investigated deposition of particles in the range from 0.001 to 10 µm in the polyhedral alveolar duct structures (Figure 23). The results showed that particles with sizes around $d_p \approx 0.5$ µm reached deepest into the acinar structure. On the other hand, particles with $d_p < 0.1$ µm or $d_p > 1$ µm deposited in the proximal generations. In addition, Katan et al. (2016) employed similar models encompassing polyhedral elements and modified them to capture lung development from 3 month-old infant to a 3-year child. The significant effect of age (alveolar geometry) and particle size on deposition was observed.

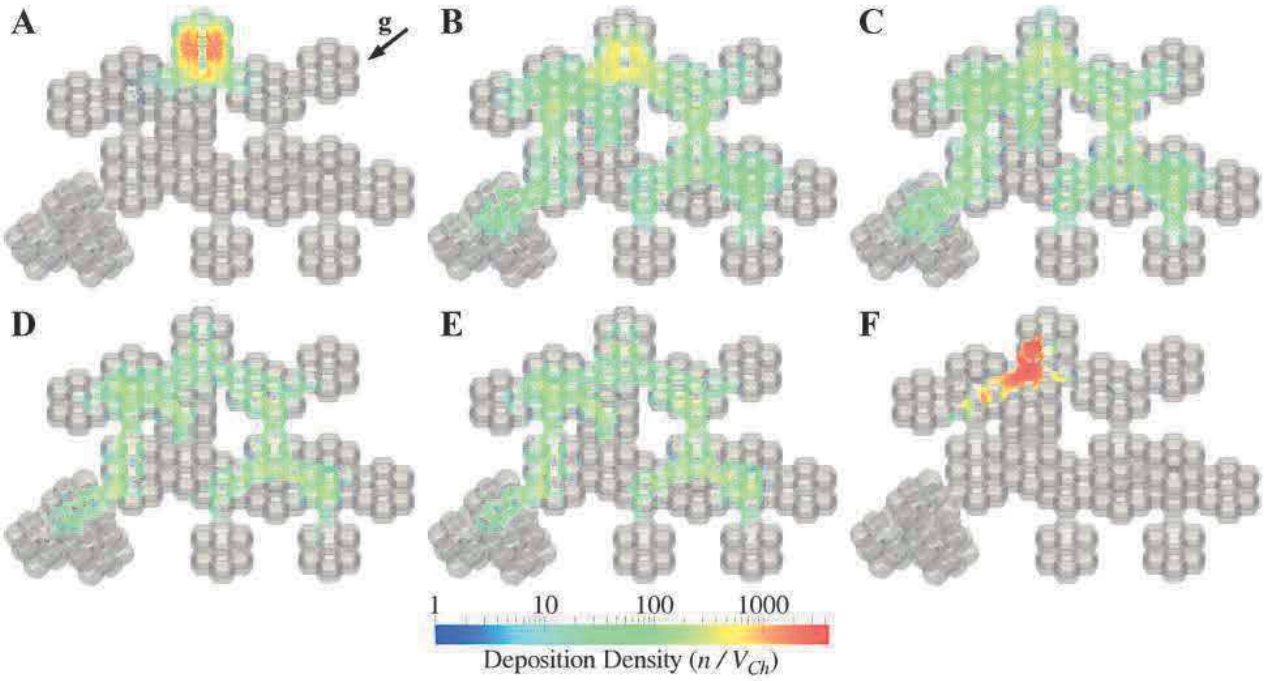

Figure 23 Deposition densities of particles with diameters of 0.01 µm (A), 0.05 µm (B), 0.1 µm (C), 0.5 µm (D), 1 µm (E), and 5 µm (F) in the alveolar region model; deposition density represented number of particles depositing within the radius of 100 µm around any given particle (Hofemeier and Sznitman, 2015)

In conclusion, the CFD methods have been widely used to contribute in understanding of aerosol transport and deposition in the respiratory airways. They provide detailed information about fluid mechanics and localized deposition patterns. However, due to their complexity and computational demands they are more suitable to analyze separate airway sections, such as the oral cavity or upper bronchial tree. Moreover, the CFD results need to be validated by other methods which can be very challenging.

3.4. Special cases affecting particle transport and deposition

The particle transport and subsequent deposition is generally affected by several factors, e.g. respiratory tract geometry, breathing pattern and particle characteristics (Kleinstreuer and Feng, 2013). As can be seen from the literature survey above, deposition of particles under normal conditions, i.e. deposition of spherical particles in human adult lungs under various breathing regimes, has been widely studied and can be accurately predicted by various methods. However, special cases, such as deposition of non-spherical particles in diseased or infant lungs has not been fully understood. Some of the examples will be discussed here.

3.4.1. Analysis of fiber deposition

Although most studies were performed using spherical particles, naturally occurring particles usually have non-spherical shapes. Fibrous particles are of great interest because exposure to fibrous particles may result in various health problems. For example, exposure to asbestos fibers can lead to onset of asbestosis or lung cancer (Su and Cheng, 2009). The pathogenicity of fibers is determined by the three Ds: dosage, durability, and dimension (DeVuyst et al., 1995). The dosage is expressed by the fiber quantity deposited in given airway region. Durability implies fiber capability to resist lung defensive mechanisms. Dimension largely affects fiber transport and deposition throughout the respiratory tract.

Fiber aerodynamic behavior is different than that of spherical particles. Fibers tend to align with its main axis parallel to the air flow direction causing their effective aerodynamic diameter to closely approximate fiber diameter (Baron, 2001). Because of this phenomenon, fibers react to changes of flow

direction more easily compared to spherical particles and their deposition patterns are different. During fiber motion through the respiratory airways, fibers occasionally rotate. The frequency of rotation depends on the fiber aspect ratio and local velocity gradients (Feng and Kleinstreuer, 2013). Since the fibers are hazardous to human health, experiments using human volunteers are unethical and strictly forbidden. Therefore, the total and regional deposition of fibrous aerosol have been analyzed only via *in vitro* and *in silico* approaches.

The number of experimental studies on fiber deposition to date is rather sparse. One of the obstacles during *in vitro* experiments is a complicated generation of monodisperse fiber aerosol. Therefore, polydisperse fibers have been usually employed during the experiments and the deposition of fibers having specific diameter or length was determined by means of optical or electron microscopy afterwards. Myojo (1987) and Myojo (1990) studied deposition of polydisperse glass fibers in the bifurcation model at several steady inhalation flow conditions. The model was inspected using scanning electron microscopy after the exposition. Deposition fractions of various fiber groups according to their length (10–20 μm, 20–40 μm, and 40–80 μm) were obtained. The fibers deposited mostly around bifurcation ridges and the deposition fraction increased with increasing flow rate and dimensions. Sussman et al. (1991) examined deposition of crocidolite fibers in a realistic cast of tracheobronchial tree made from cadaver. The fibers were aerodynamically classified having diameters from 1.5 to 2.5 μm and various lengths. It was observed that both the length and flow rate affected deposition. Moreover, the deposition fractions were higher around bifurcations than along the airways. Comprehensive study of fiber deposition in two realistic airway casts was presented by Su and Cheng (2005, 2006, 2009) and Zhou et al. (2007). Regional deposition of various fiber types, such as carbon or glass, was examined by optical microscopy. Deposition hot spots were found in the oropharynx and around bifurcation ridges (Figure 24). The deposition fractions increased with increasing flow rate and dimensions (diameter and length) and was represented by a single parameter, Stokes number for randomly oriented fibers. The regional deposition differed between the models indicating significant effect of local geometrical features on deposition. The fiber deposition fractions were compared to those of spherical particles in the same geometry (Zhou and Cheng, 2005) and it was found that fiber deposited less than spherical particles having the same aerodynamic diameter. Later, Su and Cheng (2015) investigated deposition of size classified fiber nanotubes in the same airway cast. The majority of fibers penetrated the model extending from mouth to 4th generation of branching. These fibers would continue deeper into the respiratory tract and possibly deposit there.

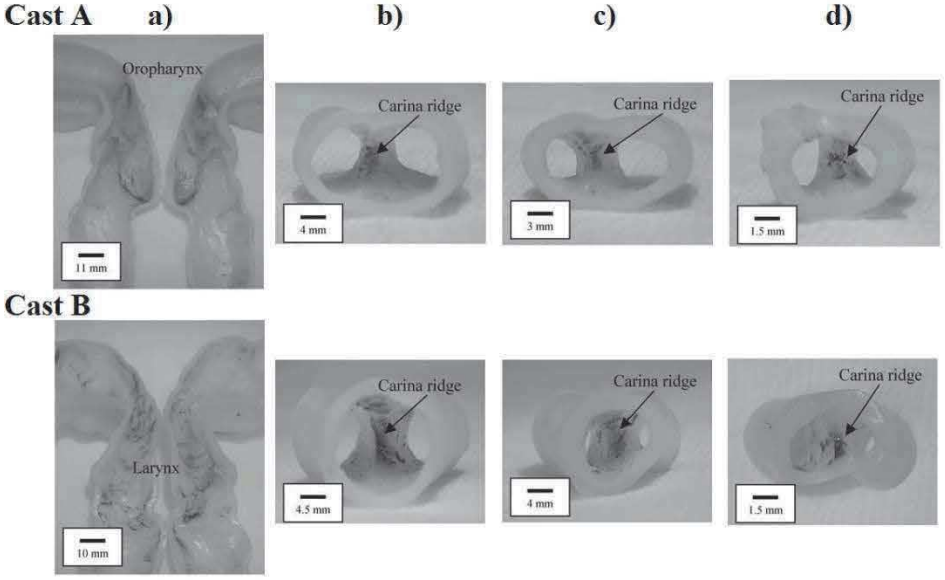

Figure 24 The deposition hot spots in the two realistic airway casts for steady inhalation of 43.5 L/min: a) oral cavity and throat, b) 1st bifurcation, c) 2nd bifurcation, c) 3rd bifurcation (Su and Cheng, 2006)

When studying regional and total fiber deposition using *in silico* methods, one needs to mathematically describe a complex fiber movement, both translation and rotation, in the fluid flow and take into account several deposition mechanisms including interception. Many theoretical or empirical models (Myojo and Takaya, 2001) for deposition estimations have been presented in the past. One of the first studies on fiber motion was published by Jeffery (1922). He investigated fiber transport in linear shear flow and observed fiber rotation. The rotation was a function of fiber aspect ratio and flow shear rate. Later, Beeckmans (1970) used equations for deposition prediction of spherical particles and modified them to estimate fiber deposition. However, this approach turned out to be not adequate. Other studies treated deposition mechanisms separately and derived equations for some of them while neglecting others. Harris and Fraser (1976) and later Asgharian and Yu (1989) presented theoretical equations for deposition caused by interception while neglecting inertia. The equations could be applied in small airways with low velocities and laminar flow. It was shown that interception was a function of fiber aspect ratio and initial fiber orientation. Cai and Yu (1988) derived formulas for inertial and interceptional deposition of fibers in bifurcation model based on the concept of particle stopping distance. Chen and Yu (1991) proposed deposition correlations for fiber sedimentation rates in a horizontal circular duct assuming parabolic flow field. In addition, Asgharian and Anjilvel (1995b) derived equations for translation and rotation movement under the effect of gravity in horizontal and inclined airway ducts. Both the studies showed that the effect of sedimentation decreased with increasing aspect ratio.

Asgharian and Anjilvel (1995a) employed expressions for fluid dynamic torque given by Jeffery (1922) and incorporated it in the Euler equations of motion to obtain expressions about a fiber orientation in a shear flow. They concluded that the fiber orientation was influenced by initial orientation, aspect ratio and other parameters, such as fiber diameter, fluid viscosity and flow velocity gradient. Moreover, the effect of inertia was significant for fibers having diameter larger than 1 µm. Fan and Ahmadi (1995) developed a sublayer model to predict fiber deposition from turbulent flows. They employed Euler´s four parameters (quaternions) to describe fiber transport and orientation. The effect of fiber dimensions, gravity and particle-to-fluid density on deposition was investigated.

With the increase in computational power, the derived equations got employed in numerical analysis of fiber deposition in the respiratory airways. Zhang et al. (1996) numerically calculated fiber deposition in equal-diameter bifurcation model. Equations for fiber trajectories given by Asgharian and Anjilvel (1995b) together with the Navier-Stokes equations were solved. The majority of fibers deposited around the bifurcation ridge via impaction and interception. Shanley and Ahmadi (2011) implemented the same equations into a CFD solver and studied fiber transport and deposition in a horizontal pipe. The empirical expressions were proposed to predict fiber sedimentation rates under various flow conditions. Later, Shanley et al. (2016) analyzed fiber transport and deposition in a realistic model of the nasal airways. Tian et al. (2012) employed the numerical model of Fan and Ahmadi (1995) and studied fiber transport in low Reynolds number flows using computational modelling. Later, Tian and Ahmadi (2013) investigated fiber transport and deposition in a multiple bifurcation model. The absence of larynx was approximated by an equivalent turbulence generator. The study showed that fibers travelled aligned with the main air flow stream and occasionally exhibited impulsive rotation behavior that enhanced deposition by interception. The fibers deposited by impaction around bifurcation ridges mainly in the 1st bifurcation (Figure 25). Moreover, the fiber aspect ratio enhanced deposition indicating significant role of inertia. Feng and Kleinstreuer (2013) studied fiber deposition in a realistic human respiratory model encompassing respiratory airways from mouth to the 4th generation of bronchial branching. Generally, the deposition of slender (high-aspect ratio) fibers was lower than that of thicker fibers indicating that these fibers plentifully penetrate the large airways. Inthavong et al. (2013) investigated carbon and glass fiber deposition in the realistic model extending from the nasal cavity to the main bronchi. Instead of solving equations describing fiber transport and orientation, an empirically defined drag coefficient was applied to account for the random fiber behavior. Generally, longer carbon (> 100 µm) and glass (> 50 µm) fibers were trapped in the nose or in the larynx area. Shorter fibers penetrated the model and would continue to the right and left lung (Figure 26).

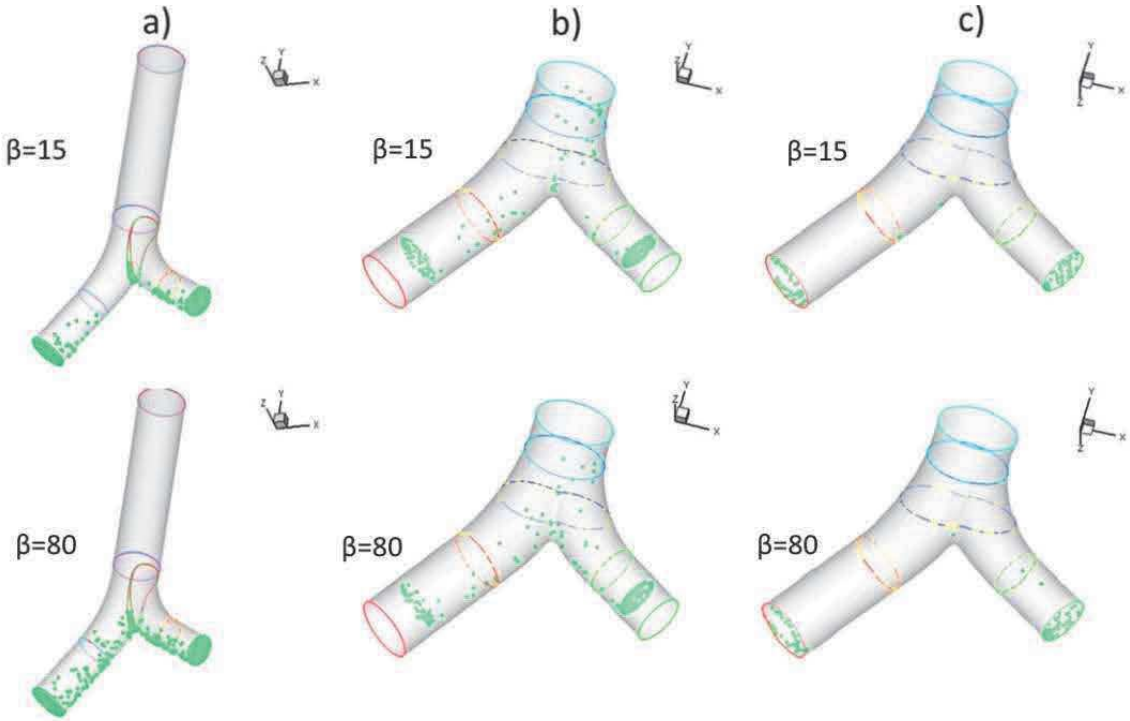

Figure 25 Deposition patterns of carbon fibers (d = 3.66 µm) with various aspect ratios in the first three bifurcation of the tracheobronchial tree under the flow rate of 40 L/min; a) trachea and 1st bifurcation, b) 2nd bifurcation, c) 3rd bifurcation (Tian and Ahmadi, 2013)

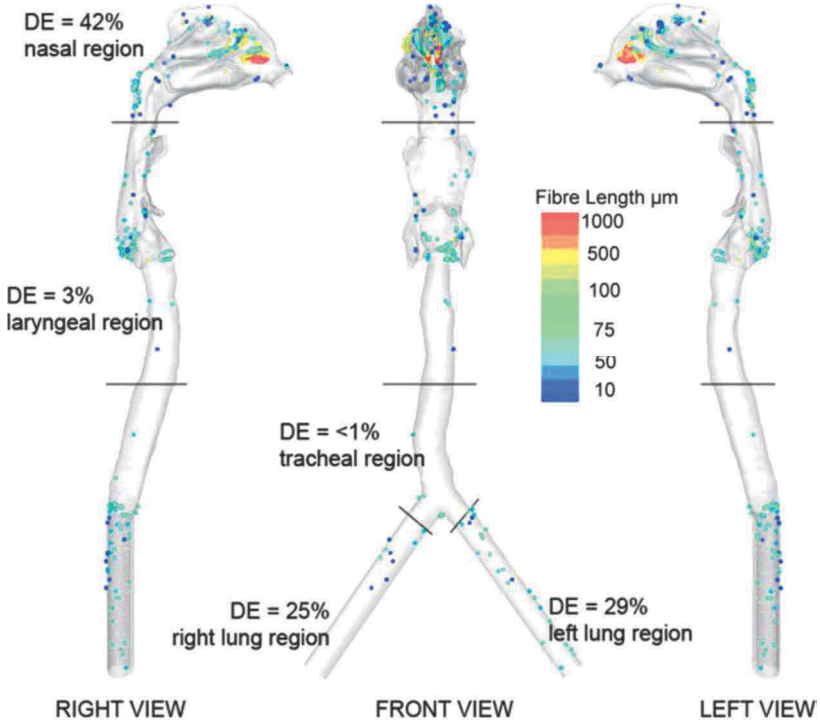

Figure 26 Deposition patterns of carbon fibers under the flow rate of 15 L/min (Inthavong et al., 2013)

Both the *in vitro* and *in silico* method have been employed in the studies of fiber deposition. However, the number of studies is limited compared to studies investigating the fate of spherical particles. An intricate way of producing monodisperse fiber aerosol and subsequent time-consuming and tedious sample analysis using microscopy is an obstacle for experimental studies. On the other hand,

complex fiber movement including translation and rotation makes it difficult to simulate fiber deposition with CFD solvers. As the inhaled fibers are potentially hazardous for human health, more work should be done to fully understand their transport and deposition in the human respiratory airways.

3.4.2. Analysis of porous particle deposition

Presence and deposition of particles in the respiratory tract does not always result in possible health hazards. The respiratory route is also frequently used for delivery of aerosolized medicaments. Inhalation of the medicine is commonly utilized for treatment of respiratory diseases, such as chronic obstruction pulmonary disease (COPD). However, it can also provide a systemic drug delivery of various therapeutic peptides and proteins via air-blood barrier (Pirozynski and Sosnowski, 2016).

For systemic drug delivery, a penetration into respiratory zone of the lungs is necessary and therefore, the optimum aerodynamic size of particles ranges between 1 and 3 µm (Edwards et al., 1997). Following the basic aerodynamic concept given by equation 4, the optimum size can be achieved by unit density particles in the range of 1–3 µm or by larger particles with lower density. Nowadays, large porous particles are a very promising platform. They are characterized by large size (> 5 µm, up to 30 µm) and low density (usually < 0.4 g/cm^3) (Gharse and Fiegel, 2016).

The relatively large size provides the porous particles with some key advantages compared to small nonporous micro-sized ones. One of the advantages is a good deagglomeration. Particle agglomerates are not suitable for drug delivery as the agglomerates have high inertia and deposit mostly in the upper respiratory airways due to impaction. To deagglomerate the particles, shear force caused by the flowing airstream has to overcome the effects of van der Waals cohesive forces that attract particles to each other. Since the van der Waals forces are proportional to particle geometric particle diameter d_p and the shear force is proportional to d_p^2 (Li et al., 1996), it is easier to separate large particles compared to small ones (Gharse and Fiegel, 2016). Another benefit of the large size particles is the resistance to pulmonary defense mechanisms. In the alveolar region, macrophages engulf and digest exogenous particles in a process called phagocytosis. This process is most effective for particles with geometric diameter ranging from 1 to 2 µm. The more the particle geometric diameter deviates from this range (to nano or few micron-sized particles) the less significant is the effect of phagocytosis (Makino et al., 2003). Therefore, the porous particles can avoid phagocytic clearance and are ideal for delivery of slowly absorbing drugs and controlled release systems (Edwards et al., 1997).

Porous particles can be formulated by various methods, such as spray drying, spray freeze drying, crystallization, supercritical fluid technologies etc. The review of the methods can be found elsewhere (Gradon and Sosnowski, 2014; Shoyele and Cawthome, 2006). The focus will be given only to spray drying here as it is the most frequent method for porous particle formulation (Rosenberg et al., 1990). The benefit of this method is a relatively uniform particle size and shape distribution which is convenient in inhalation medicine. The principle of this technique includes several steps: atomization, liquid-to-particle conversion, and particle collection (Nandiyanto and Okuyama, 2011) (Figure 27). The first step is to prepare a precursor which is a liquid mixture of an inorganic solution (material of the porous particles), template and a solvent. The precursor is atomized using a two-fluid nozzle (or other type of atomizer) to create small droplets. The droplets are carried to a tubular reactor where the solvent is evaporated. The evaporation creates composite particles of inorganic material containing spaces filled with template material. The template material is then eradicated by heating and porous particles made of desired material remain. Highly porous or hollow particles can be fabricated this way.

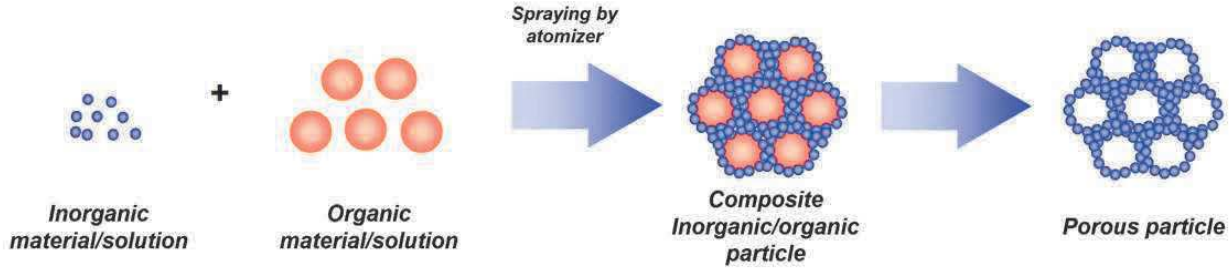

Figure 27 The schematics of porous particle formulation using spray drying process (Nandiyanto and Okuyama, 2011)

The porous particles are formulated for medical purposes and, as other forms of aerosolized medicine, they are administered via inhalers. The assessment of drug delivery systems is performed following U.S or European Pharmacopeias instructions (Mitchell and Nagel, 2003). These instructions recommend a use of cascade impactor to measure an aerodynamic particle size distribution and mass median aerodynamic diameter (MMAD). Limited information about deposition is then based on the given particle size distribution. Fine particle fraction (FPF) is determined as having the mass median aerodynamic diameter less than 5 µm (Council of Europe, 2007) and it is assumed that the FPF penetrates the upper respiratory airways and reaches the lungs. Many studies concerning porous particles have employed this procedure to assess the fate of the particles in the lungs (Dellamary et al., 2000; Gervelas et al., 2007; Nolan et al., 2009; Vanbever et al., 1999). However, these attempts to connect aerodynamic particle size distributions and respiratory tract deposition are not adequate as the deposition is affected by many other factors than only particle size (Mitchell et al., 2007).

Other methods, such as *in vivo* or *in silico*, have been employed to provide more realistic and more detailed information about regional deposition of porous particles. In some of the studies, the aerodynamic particle size distribution measured by a cascade impactor was utilized as an input parameter into the whole-lung deposition models. For example, Dunbar et al. (2002) measured sizes of large porous particle placebo formulations (MMAD of 3 and 5 µm) using multistage liquid impinger. The extrathoracic and lung deposition was then calculated using the ICRP model. The percentage of 3 µm and 5 µm particles that would reach the lungs was estimated as 60% and 45%, respectively. Musante et al. (2002) employed a developed mathematical model and predicted deposition of large porous particles and aerodynamically similar but geometrically smaller particles. The results indicated that small submicron particles had higher deposition efficiency in the lower respiratory airways compared to porous particles because of the effect of diffusion. Other studies have employed *in vivo* methods, in particular a gamma scintigraphy method. Hirst et al. (2002) investigated deposition of Pulmosphere™ porous particles and conventional micronized particles in nine nonsmoking subjects. It was found out that the oropharyngeal deposition fraction of porous particles was lower compared to conventional particles (42.6±9% vs. 72±8%) and the total lung deposition was approximately double in the case of porous particles (28.5±11.3% vs 14.5±8.1%). The difference could be caused by the fact that large porous particles aggregate less compared to smaller conventional particles. Dunbar et al. (2002) obtained regional deposition of 3 and 5 µm porous particles in several healthy subjects (Figure 28). The lung deposition for 3 and 5 µm particles was 59% and 37.3% on average, respectively. The *in vivo* results were compared to those obtained by a cascade impactor in combination with ICRP model. It was concluded that the ICRP model overpredicted the deposition for larger particles and the intersubject variability was not captured by the ICRP model.

In general, porous or hollow particles are a promising tool in drug delivery. From the point of deposition, they are frequently characterized only by measuring aerodynamic particle size distribution using cascade impactors. The results of *in vivo* and *in silico* studies indicate that porous particles deposit less in the oropharyngeal area compared to conventional spherical particles and thus, are able to penetrate deeper into the respiratory tract. This difference is usually related to the higher surface–to–volume ratio of porous particles and thus, less frequent aggregation.

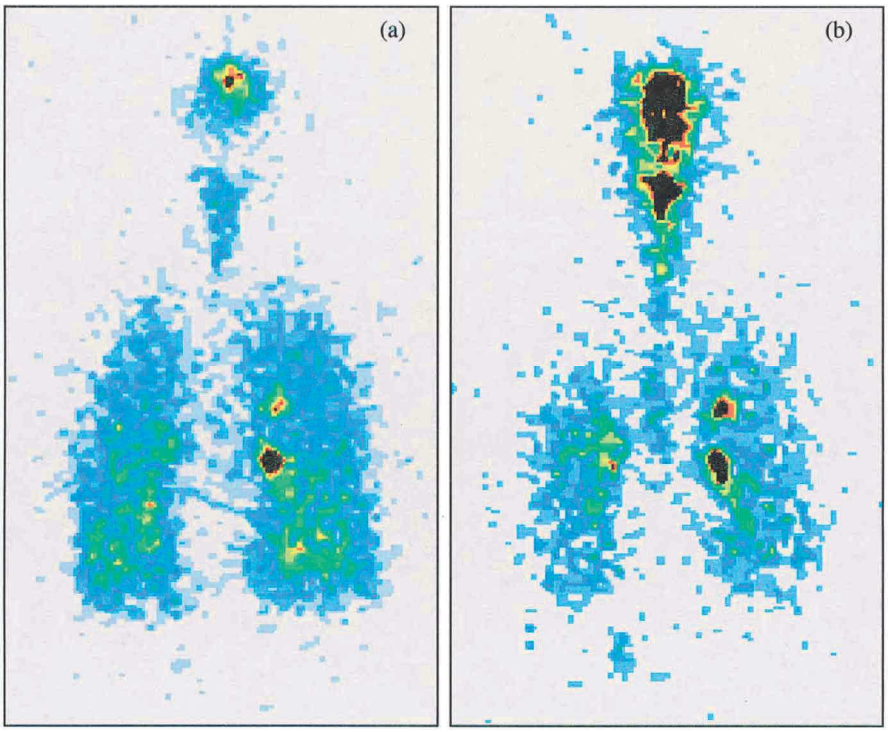

Figure 28 Deposition of 3 (a) and 5 (b) µm porous particles in healthy subjects obtained via scintigraphy method (Dunbar et al., 2002)

4. Aims of the thesis

The study of particle deposition is very complex and highly investigated topic. Generally, the *in vivo* methods and the "whole-lung" *in silico* models are frequently used to predict deposition of spherical particles during normal conditions in the entire respiratory system. The use of CFD methods in conjunction with *in vitro* methods can be utilized for special cases, such as non–spherical particles, or to predict localized deposition in specific parts of the respiratory tract.

The aim of this research is to study the effect of particle shape and inspiratory conditions on regional deposition in the replica of human respiratory airways that was developed at our department. The deposition data may be used to elucidate the complicated transport mechanisms of non-spherical particles, such as fibers. Moreover, experimental data are crucial for validation of CFD methods, which have become a convenient tool for study of particle transport and deposition in human respiratory airways. The objectives of this research were determined at the state doctoral examination and are listed below:

- Analysis of porous particle deposition.
    - Generation of porous particles.
    - Choice of proper method for deposition detection.
    - Carrying out of deposition experiments.
    - Analysis of the results.

- Analysis of fiber deposition
    - Generation of monodisperse fiber aerosol.
    - Choice of proper method for deposition detection.
    - Carrying out of deposition experiments.
    - Analysis of the results.

4.1. Scientific question

How is the deposition efficiency or fraction of non–spherical particles related to that of spherical particles?

4.2. Hypotheses

- *It is expected that the deposition efficiency of porous particles throughout the respiratory airways is similar to that of spherical particles having the same aerodynamic diameter.*
- *It is expected that fibers deposit less effectively than spherical particles having the same aerodynamic diameter.*

5. Results

5.1. Objective 1 - Deposition of porous particles

The objective was to determine a deposition of porous particles. To do this, porous particles of suitable size and density had to be produced. The produced porous particles were supposed to be introduced into the replica and deposit there. Proper detection method had to be found to quantify the regional particle deposition.

5.1.1. Porous particle generation

Gharse and Fiegel (2016) stated that porous particles typically have density around 0.4 g/cm^3. The particle size should be larger than 5 µm and can go up to 30 µm. There are many techniques how to produce porous particles. Given the instruments and experimental setup available, spray–freeze drying, spray drying, and liquid–liquid interfacial crystallization method were tested.

a) Spray-freeze drying

In a cooperation with the University of Veterinary and Pharmaceutical Sciences Brno, a spray-freeze drying method was employed to precipitate chitosan porous particles. The spray-freeze drying method is a two-step technology that consists of rapid freezing of atomized droplets and subsequent sublimation of a solvent under low pressure and temperature. Chitosan is a low toxicity polysaccharide that is biocompatible, biodegradable and thus, widely studied as a possible drug carrier (He et al., 1999). All the results of this study were presented in Halodova S. (2015) and only a short summary will be given here.

The precursor was prepared by dissolving 2% aqueous solution of chitosan in a 1% acetic acid solution. An Y–jet atomizer with nozzle diameter of 1 mm was utilized to spray the precursor into a thermally insulated 10-liter freezing chamber (Figure 29). The atomization medium was air at pressure of 120 kPa. The precursor container was situated 1 m above the effervescent atomizer and thus, spontaneous supply of the precursor was achieved. Spherical valve was placed downstream the precursor container to allow precursor flow regulation. Liquid nitrogen (-196 °C) was poured into the freezing chamber up to the height of 10 cm above the chamber bottom.

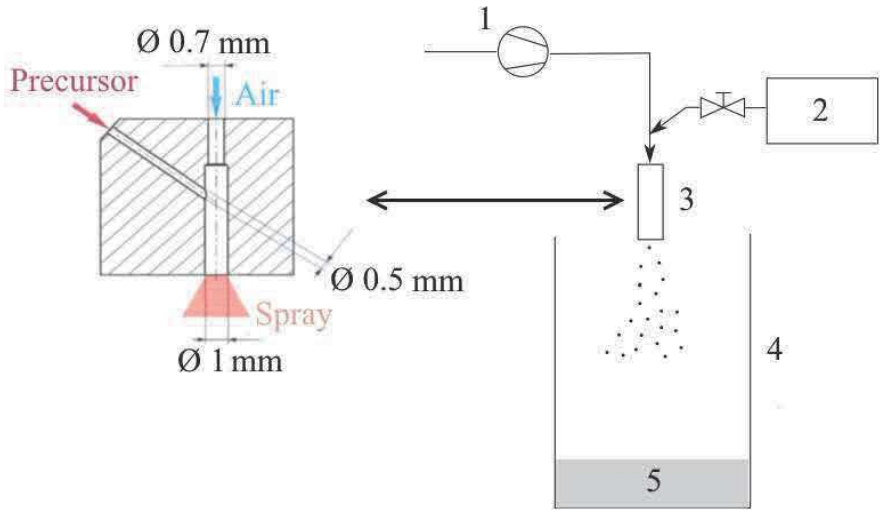

Figure 29 Experimental setup for spray-freeze drying procedure; 1 – air for atomization, 2 – precursor container, 3 – effervescent atomizer, 4 – freezing chamber, 5 – liquid nitrogen

The precursor was sprayed into the chamber for approximately 10 minutes. After that, the solution of liquid nitrogen and frozen droplets was poured into 200-ml beakers. The beakers were placed into a laboratory freeze dryer Alpha 1-2 LD (Christ, Osterode am Harz, Germany). The temperature inside the freezer was set to -25 °C and the pressure was kept at 0.15 kPa using a vacuum pump. The lyophilization

lasted for 144 hours during which the solvent sublimed and a porous structure was obtained. As the particles were not completely dry after the lyophilization, they were transferred to a desiccator and left there for another 168 hours.

The resulting porous particles were analyzed using optical microscopy. Images of particles were taken by a CCD camera DFK 72AUCO2 (The imaging Source, Bremen, Germany) attached to a microscope E200 (Nikon, Tokyo, Japan). The particle images were analyzed in a software package NIS-Elements (Nikon, Tokyo, Japan) in the terms of equivalent area diameter (diameter of a circle having the same area as a given particle), sphericity etc.

The bulk density was determined by adding a known mass of the porous material into a graduated cylinder and reading its volume. The tapped density was obtained by reading a change in volume after 2500 tappings of the graduated cylinder filled with the porous material. The characteristics of porous particles are presented in Table 4. The created porous particles were also examined using scanning electron microscope (SEM) VEGA (Tescan, Brno, the Czech Republic) and the SEM particle images can be seen in Figure 30.

Table 4 The characteristics of produced porous particles; the values represent mean values ± standard deviations

Equivalent area diameter (μm)	Sphericity (–)	Bulk density (g/cm^3)	Tapped density (g/cm^3)
21.2±23.4	0.4±0.3	0.09	0.11

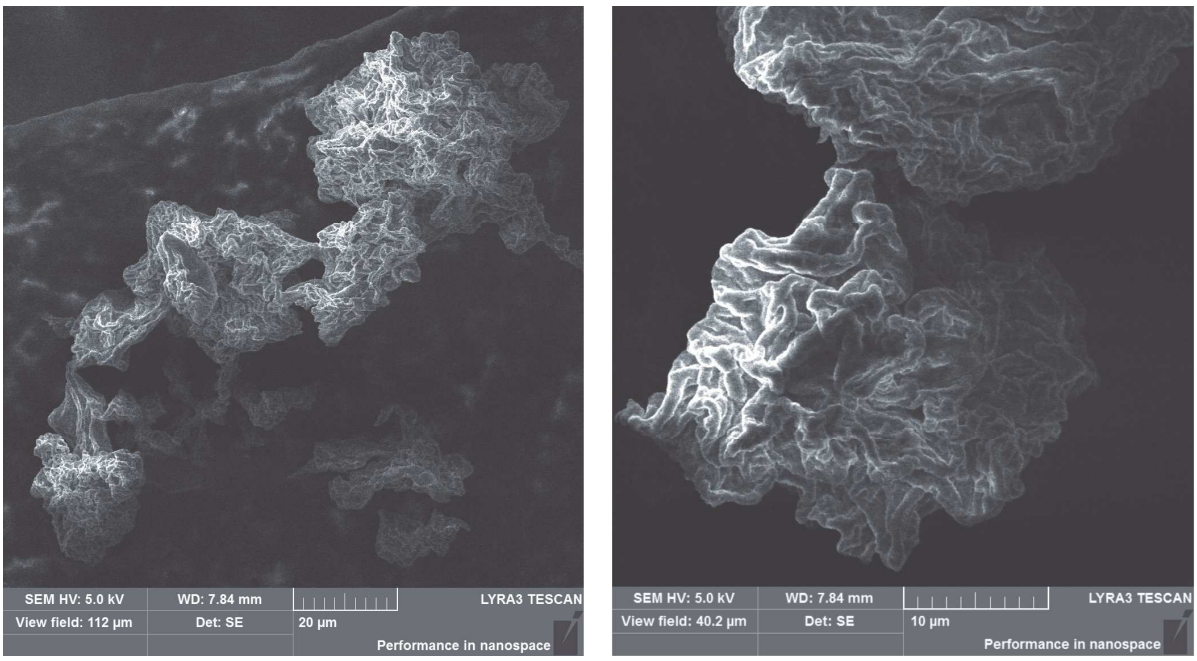

Figure 30 The SEM images of porous particle produced by spray-freeze drying technique

During the analysis, it was found out that the porous particles created large agglomerates. Various approaches were performed to deagglomerate the particle clusters. The porous material was immersed into 96% ethanol (Dr. Kulich Pharma, the Czech Republic) and IKA T 25 ULTRA-TURRAX® disperser (IKA, NC, USA) was used for deagglomeration. The disperser exhibits high rotation speeds up to 3000 rpm that create high shear and thrust forces acting on the particles. It was observed that the forces acting on the particles were too high and the porous particles were destroyed during the dispersion process. Another approach was a use of an ultrasonic bath. The porous material was immersed into 96% ethanol (Dr. Kulich Pharma, s.r.o., the Czech Republic) and this solution was sonicated in an ultrasonic bath RK 106 (Bandelin, Berlin, Germany) for 30 min. This step partially helped to break the agglomerates. However, some of the particles were destroyed and some agglomerates were still present.

There were also attempts to reduce the number of agglomerates during the lyophilization process. However, as the agglomeration probably had taken place in the freezing chamber during the spraying process, these attempts were not sufficiently successful.

b) Spray drying

In a cooperation with University of Veterinary and Pharmaceutical Sciences Brno, a spray drying method was employed to precipitate the porous particles. The spray-drying method is widely used because of its simplicity and reliability to generate porous particles with rather uniform size. During this technique, a precursor is atomized and a solvent is evaporated in a heated chamber.

The precursor was prepared by dissolving 2% aqueous solution of chitosan in a 1% acetic acid solution. A spray dryer SD-06 (Labplant, North Yorkshire, UK) with a nozzle diameter of 0.5 mm was utilized to spray the precursor (Figure 31). The characteristics of the spray drying process were similar to those used by He et al. (1999). The precursor was fed into a two-fluid atomizer via peristaltic pump at flow rate of 10 mL/min. The atomization medium was compressed air at air flow of 8 L/min. The inlet temperature was set to 160 °C. The atomized droplets were dried in a drying chamber. After that, they were separated from the exhaust flow in a cyclone and collected in a sample collection bottle.

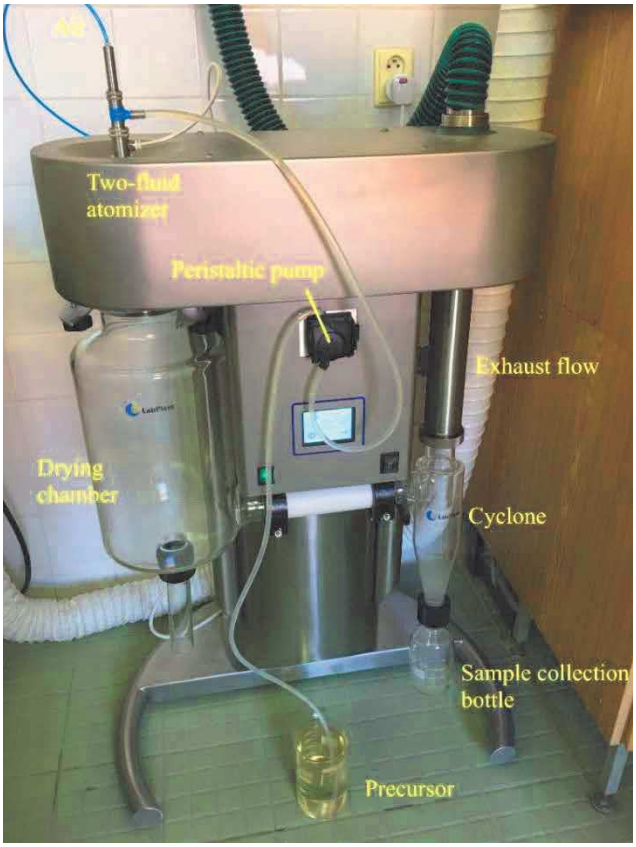

Figure 31 A spray-drying setup

The produced particles were analyzed in the terms of particle size. The particle size was observed using scanning electron microscope Lyra 3 (Tescan, Brno, the Czech Republic). The SEM images can be seen in Figure 32. As the aerodynamic particle diameter is more important than geometric particle diameter, the particles were also analyzed using a TSI Aerodynamic Particle Sizer (APS) 3321 (TSI, Shoreview, USA). To do that, the porous particles were first dispersed using a Small-Scale Powder Disperser (SSPD) 3433 (TSI, Shoreview, USA). The outlet of the SSPD was connected to the inlet of the APS that measured particle aerodynamic characteristics using the "time of flight" principle. The count median aerosol diameter (CMAD) was 3.1 µm. The particle bulk and tapped density were not measured as the total volume of produced particles was too small to be determined.

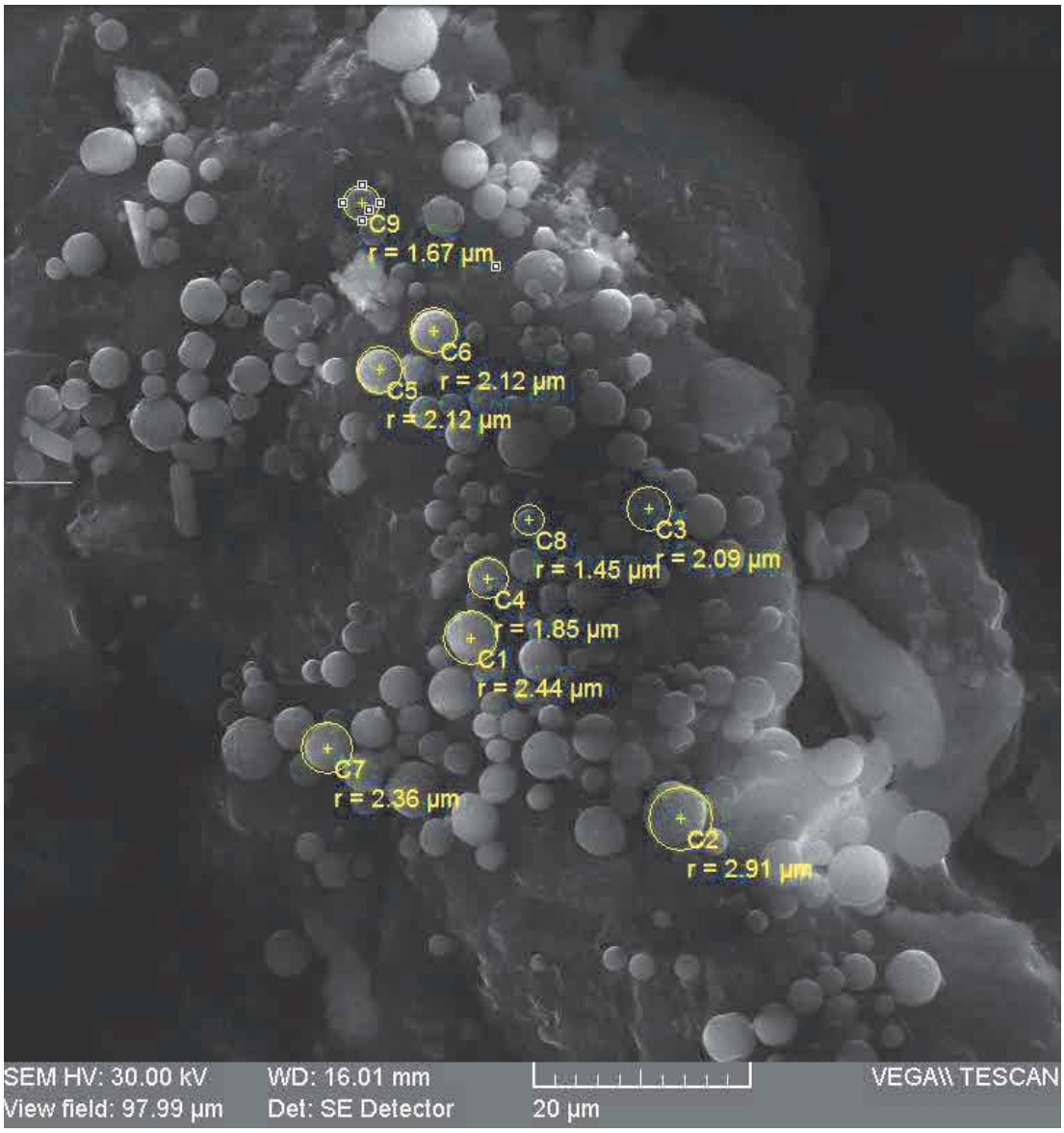

Figure 32 SEM image of porous particles produced by spray drying technique; *r* represents particle radius

c) Liquid–liquid interfacial crystallization

In cooperation with the Faculty of Chemistry at Brno University of Technology, a liquid–liquid interfacial crystallization method was tested as a suitable tool for porous particle production. In this technique, a solute dissolved in a solvent can be crystallized by adding an antisolvent. Because the solute has a poor solubility in the antisolvent, a solubility in the whole solution is decreased and crystallization occurs (Kitayama et al., 2009). In a system of aqueous solution and organic antisolvent, the interfacial area becomes supersaturated which leads to nucleation and crystal growth (Tanaka et al., 2011). The interfacial area shape corresponds to the shape of the precipitated particles. A spherical shape of the interfacial area results in spherical particles. The crystallization technique can be operated at room temperature and the size of the precipitated particles can be changed by changing the contact time or concentration of the solute.

NaCl material was chosen as a solute (Tanaka et al., 2011). NaCl aqueous solutions with molar concentration of 2, 4, and 6 mol/L were prepared. These solutions were sprayed via airbrush Fengda BD-138 atomizer into an isopropanol bath that served as an antisolvent (Figure 33). The nozzle diameter was 0.8 mm and the atomization medium was air at pressure of 120 kPa. The nozzle was situated at the

top of a 1–liter beaker that contained 200 ml of isopropanol. As the crystallization takes time, the atomization was performed in a series of pulses. The time between the pulses was approximately 180 s.

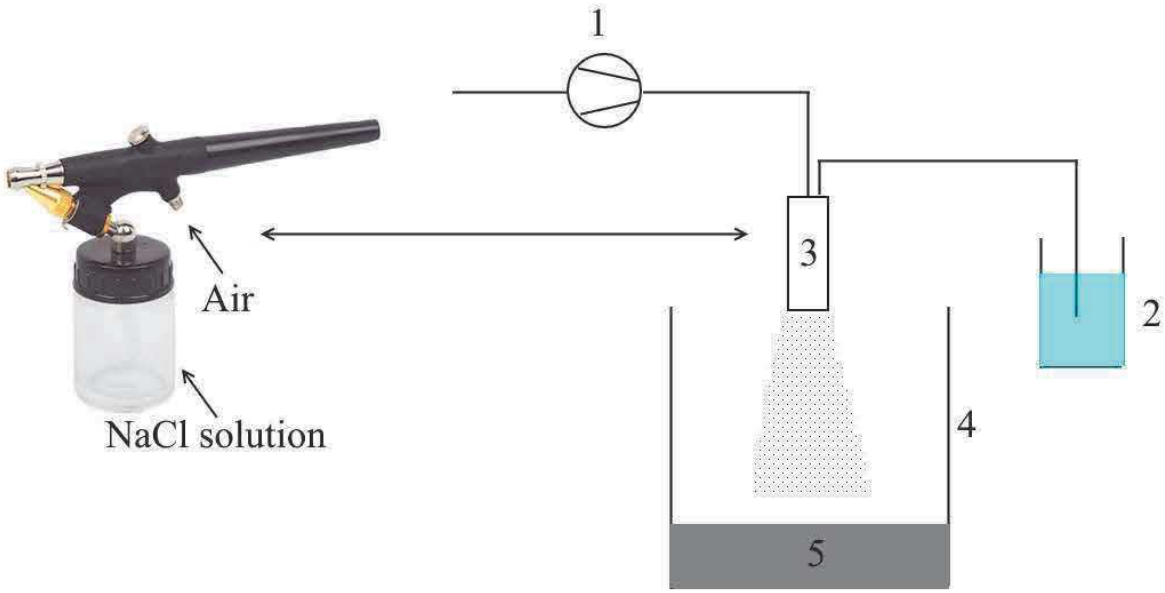

Figure 33 The experimental setup for porous particles production via crystallization; 1 – compressed air, 2 –NaCl solution reservoir, 3 – airbrush Fengda BD-138 atomizer, 4 – a beaker with isopropanol, 5 – isopropanol

The precipitated particles were analyzed by scanning electron microscope Lyra 3 (Tescan, Brno, the Czech Republic) and they can be seen in Figure 34. The crystallization technique created porous and hollow spherical particles made of NaCl crystals. The particle porosity increased with decreasing molar concentration. The particle sizes were in the order of tens of micrometers. The bulk and tapped density of the 4 mol/L concentration case was 0.37 and 0.48 g/cm^3, respectively.

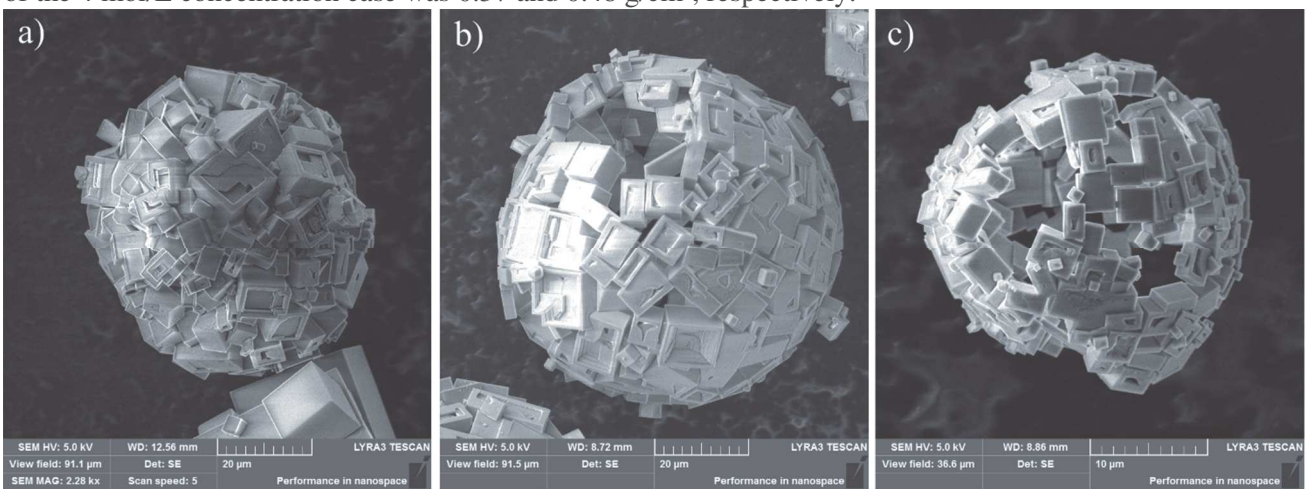

Figure 34 Porous NaCl particles; the molar concentration of the atomized solution was: a) 6 mol/L, b) mol/L, c) 2 mol/L

Since the NaCl particles were too large to be used in the deposition experiments, $CuSO_4 \cdot 5H_2O$ material was tested as a solute instead. A saturated aqueous solution having the molar concentration of 1.27 mol/L was prepared. The solution was sprayed using the Fengda BD-138 atomizer into a 4–liter bowl (Figure 35). The bowl was used because it was wider than the beaker and thus, fewer droplets were lost on the walls during the spraying process. The atomization medium was compressed air at pressure

of 120 kPa. The spraying was performed in a series of pulses. The time between pulses was approximately 60 s.

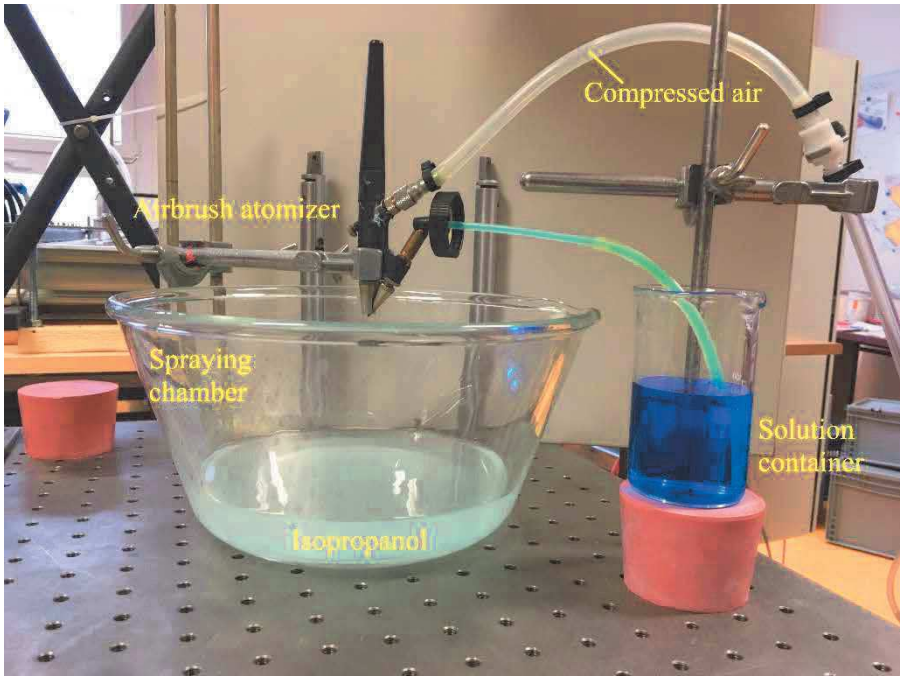

Figure 35 The experimental setup for the precipitation of $CuSO_4 \cdot 5H_2O$

The produced particles were analyzed by scanning electron microscope Lyra 3 (Tescan, Brno, the Czech Republic) and they can be seen in Figure 36a. The microscope included a focused ion beam (FIB) technology that can be used for a sample modification. The ion beam was utilized to cut the particles in half to observe particle inner structure. As can be seen in Figure 36b, the particles were porous with hollow centers. This was suitable as the hollow centers together with the porous structure resulted in low density particles. The bulk and tapped density of the $CuSO_4$ porous particles were 0.42 and 0.54 g/cm^3, respectively. The particle size distribution was measured by the APS 3321 as in the previous cases. The CMAD was 1.9±1.9 µm and the MMAD was 7.4±1.7 µm.

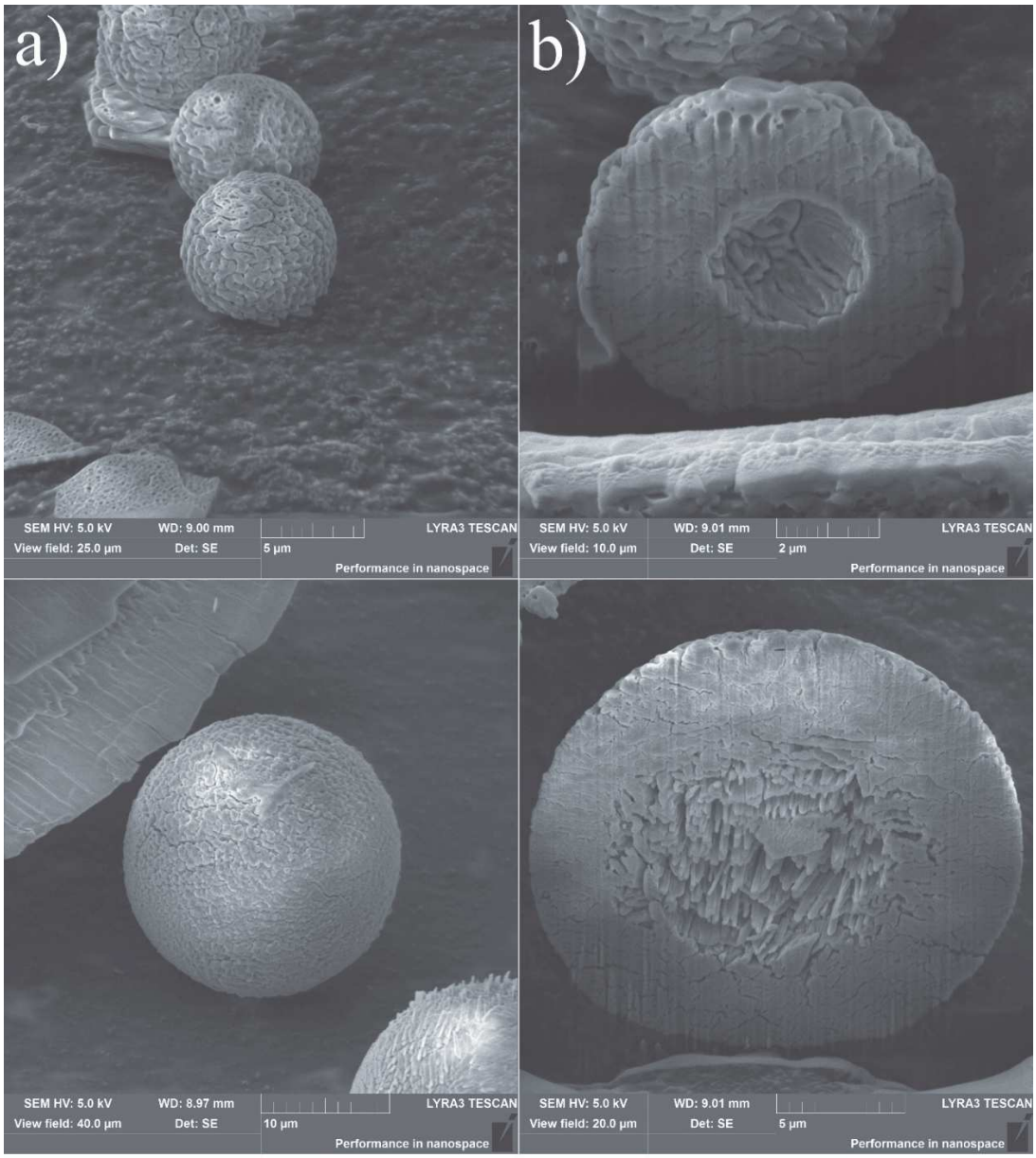

Figure 36 SEM images of the $CuSO_4$ particles; a) whole particle, b) particle halves

d) Market screening

Market screening was performed to see if there is an existing product that would fulfil our needs. However, the porous particles produced for the purpose of inhalation medicine are either very expensive or they are not commercially available at all. The only possibility was to buy porous particles that are utilized for other purposes, such as porous silica particles used in high-performance liquid chromatography. These porous particles are used in liquid chromatography columns for separation of various compounds. POLYGOSIL 1000-7 particles (MACHEREY-NAGEL, Düren, Germany) were obtained and analyzed in the terms of particle size. The particle size was analyzed either by scanning electron microscope Vega (Tescan, Brno, the Czech Republic) and the resulting image is depicted in Figure 37. The particles were also measured by APS 3321 and the aerodynamic diameter can be found in Table 5. The bulk density was given by the manufacturer.

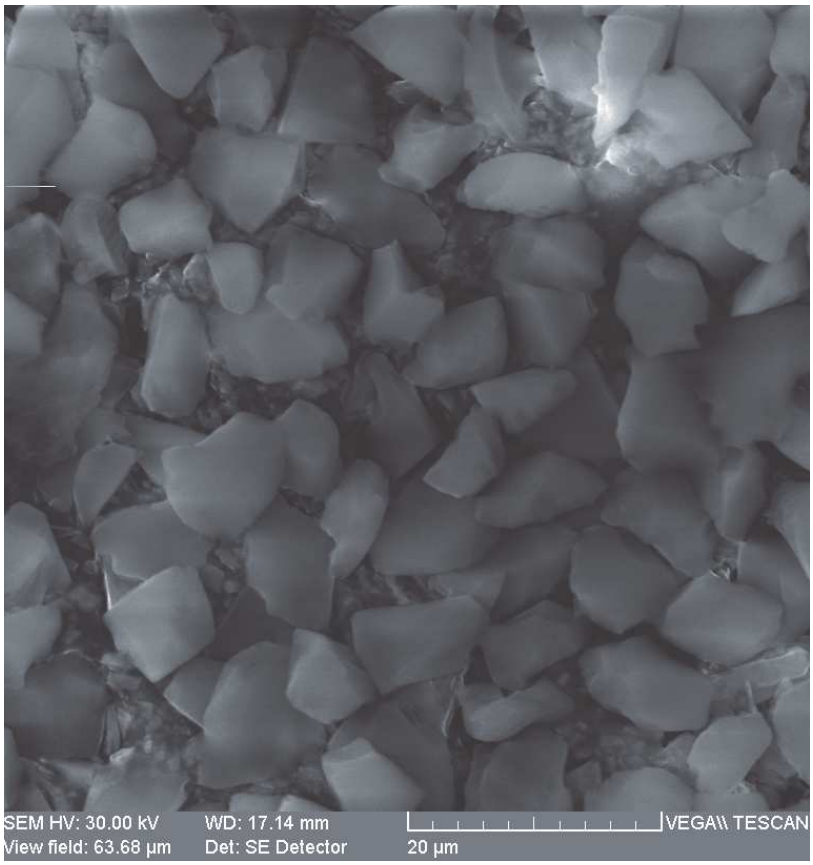

Figure 37 Porous particles used for high-performance liquid chromatography

Table 5 Characteristics of silica porous particles

CMAD (µm)	Bulk density (g/cm^3)
4.1±2.2	0.45

e) Porous particle generation – Summary

Several methods were tested to produce particles with porous structure. A market screening was performed to obtain porous particles with suitable properties. All the particles were analyzed in the terms of density and size and the results can be found in Table 6.

The spray–freeze drying method and crystallization of NaCl produced particles that were large with diameters in the order of tens of micrometers. As the maximum recommended particle size is 30 µm, these particles were not suitable for the use in deposition experiments. In the case of spray–freeze drying there was a problem with agglomeration. The particles agglomerated during particle spraying and the proper solution for particle deagglomeration was not found. On the other hand, the density of the particles produced by the spray–freeze drying method was the lowest from all the produced particles. The crystallization of the NaCl also produced low density particles and it was indicated that the porosity of the particles increased with decreasing molar concentration.

The particles produced by spray drying method or crystallization of $CuSO_4 \cdot 5H_2O$ had suitable sizes (d_p < 30 µm). The aerodynamic size distribution of these particles can be seen in Figure 38 together with size distribution of commercially obtained particles (the silica particles). Relative counts were used for an easy comparison. The narrowest size distribution had silica particles. Spray drying method produced particles with narrower size distribution (lower standard deviation) compared to the crystallization method. Comparing the mass median aerodynamic diameters, the MMAD of particles produced by crystallization method was rather high indicating that significant number of large particles was produced

by this method. The bulk density of $CuSO_4$ particles only slightly exceeded the recommended value of 0.4 g/cm^3. The density of the chitosan particles produced by spray–drying method was not determined as the process was not optimized at the time and the output volume was too low.

The most suitable particles in the terms of sizes and density were silica particles. However, given the financial sources it would not be possible to obtain enough particles for deposition experiments. The spray drying method produced particles with narrowest size distribution which is needed for deposition experiments. However, the output was too low. That is why the $CuSO_4$ particles were chosen to be used in the deposition experiments.

Table 6 Characteristics of the produced porous particles

Particle type	Particle size (μm)	Tapped density (g/cm^3)	Bulk density (g/cm^3)
Freeze–spray drying (chitosan)	Equivalent diameter of 21.2±23.4	0.11	0.09
Spray drying (chitosan)	CMAD of 3.5±1.8 MMAD of 5.9±1.6	–	–
Crystallization (NaCl)	–	0.48	0.37
Crystallization ($CuSO_4 \cdot 5H_2O$)	CMAD of 1.9±1.9 MMAD of 7.4±1.7	0.54	0.42
Silica porous particles	CMAD of 4.1±2.2 MMAD of 4.7±1.3	–	0.45

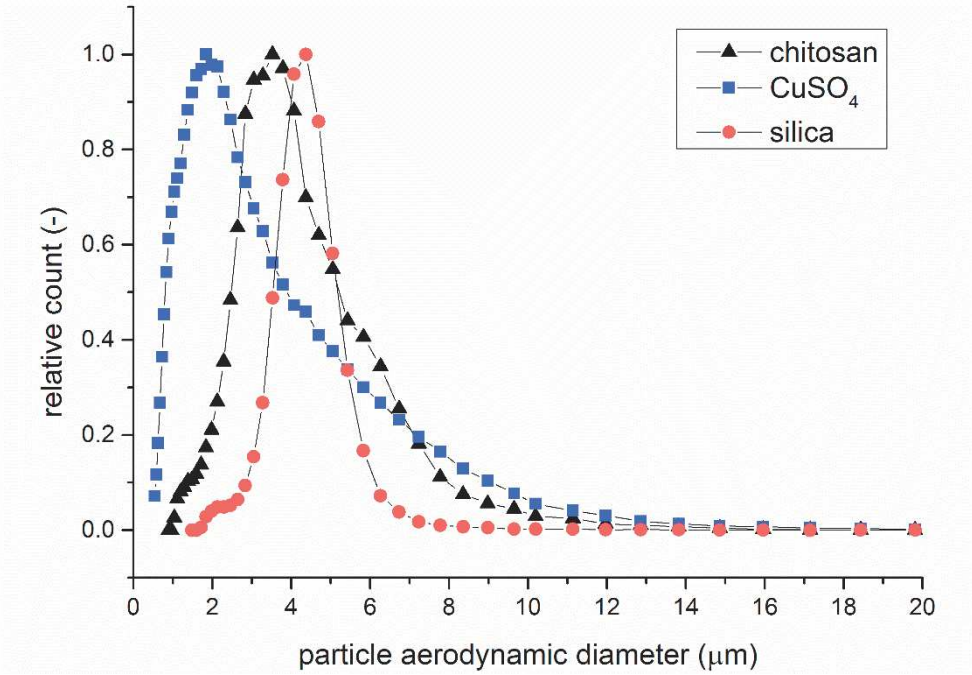

Figure 38 Aerodynamic size distribution of silica, chitosan and $CuSO_4$ particles

5.1.2. Detection of deposited porous particles

To perform the deposition experiments, it was essential that the employed porous particles are detectable by any available method, such as gravimetry, optical microscopy, fluorometry, etc. The gravimetry was the simplest method and could be applied to any kind of particles. However, as the porous particles have low densities, large amount of powder would be needed to deposit in the model to reliably determine the mass of the deposited particles. Moreover, an application of silicon oil on the model inner walls prior to the experiment had to be considered.

To detect particles using optical microscopy, the particle would need to be transferred from the model onto filters and count manually afterwards. However, particles must be large enough to be reliably found

and counted. In the case of our laboratory microscope Nikon E200 (Nikon, Tokyo, Japan), the particle size should be at least 10 µm in diameter and thus, it was not possible to employ optical microscopy to detect the obtained porous particles.

Another option was to use a chemical analysis. Chitosan or silica particles could be detected for example by gas chromatography–mass spectrometry method, however, this method is very expensive. A cheaper option was to utilize ultraviolet visible (UV/VIS) spectroscopy to detect $CuSO_4$ particles. The UV/VIS spectroscopy works on the principle of measuring ultraviolet or visible light absorption. When a molecule is exposed to a light having the energy that matches the electron transition energy, the electron is excited to a higher orbital while absorbing energy. Various compounds absorb maximum energies at different wavelengths depending on a type of electron transition that occurs, e.g. $CuSO_4$ absorbs maximum light energy in the region around 810 nm. The determination of the solution molar concentration is given by the Lamber–Beer law (Figure 39):

$$Absorbance = -\log\frac{I}{I_0} \quad (15)\,,$$

$$Absorbance = \varepsilon \cdot l \cdot c_m \quad (16)\,,$$

where I_0 is intensity of light before it passes a sample, I is intensity of light after it passes a sample, ε denotes molar absorption coefficient, l is a width of the sample and c is the molar concentration of the solution. Using the equations 15 and 16, the amount of absorbed light can be correlated to a solution concentration as the molar absorption coefficient and width of the sample are known constants. Molar absorption coefficient of $CuSO_4$ at 810 nm was 14.85 L/mol/cm as can be seen in Figure 40.

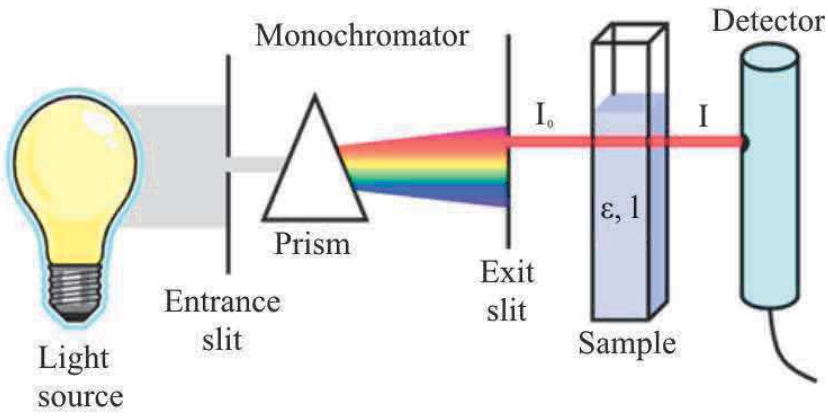

Figure 39 Principle of a UV/VIS spectrophotometer (Concordia College, 2015)

At first, correlation between absorbance and concentration had to be determined. Aqueous solutions with known concentration of $CuSO_4$ (0.005, 0.01, 0.05, and 0.1 mol/L) were prepared. The absorbance was measured using a Spectrophotometer U-3900H (Hitachi, Tokyo, Japan). The method proved to be adequate for determining concentration of $CuSO_4$ as a linear relationship between absorbance and molar concentration of $CuSO_4$ (R^2=0.99) was observed (Figure 40). The relationship is given by equation 17:

$$A = 14.85 \cdot c \quad (17)\,.$$

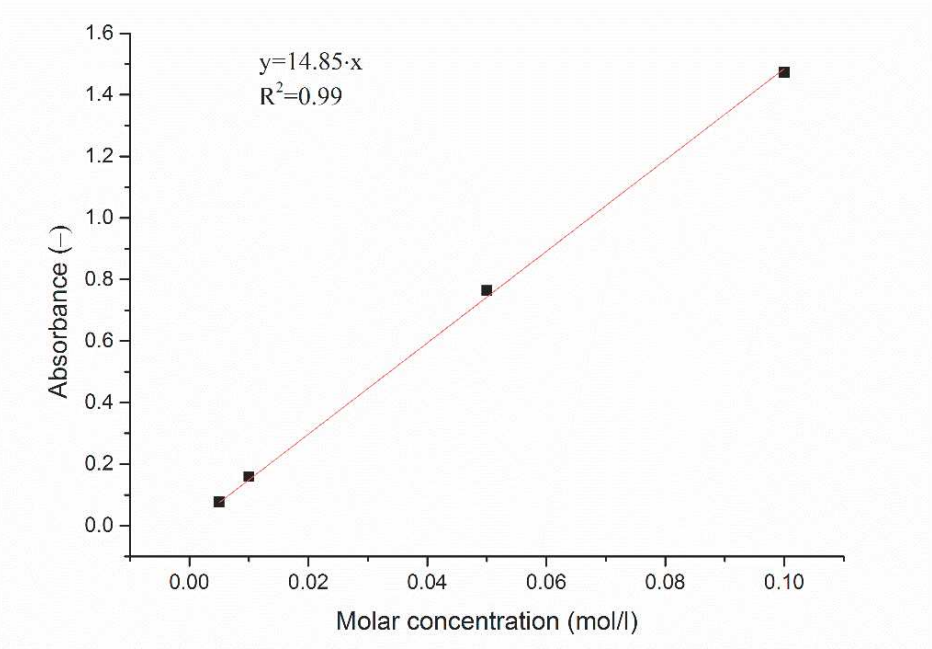

Figure 40 Absorbance of $CuSO_4$ as a function of molar concentration

5.1.3. Deposition measurements of porous particles

Deposition experiments were carried out using a realistic replica of human respiratory airways (Figure 41). The replica encompasses respiratory airways from the mouth to the 7th generation of bronchial branching (Lizal et al., 2012). The geometry was created by combining the tracheobronchial tree from the reference model of Schmidt et al. (2004) and the oral cavity from the Lovelace Respiratory Research Institute (Albuquerque, NM, USA (Cheng et al., 1997)). The resulting geometry was divided into 22 segments to permit regional deposition measurements. The numbering went from top to bottom starting with the oral cavity as number 1 and the trachea as number 2. At the model outlets, funnel–shaped segments were created to facilitate connection of the model to the rest of the experimental setup. These segments were numbered from 23 to 32 since the model had 10 outlets. To allow reassemble of the model, flanges with screw or bayonet joints were created between the segments. The replica was manufactured on a Viper Si2 stereolithographic prototyping system (3D Systems, Rock Hill, SC) and the material used was WaterShed XC 11122 (DSM, Heerlen, Netherlands). The accuracy of the machine was 7.6 µm and the layer thickness was 25 µm.

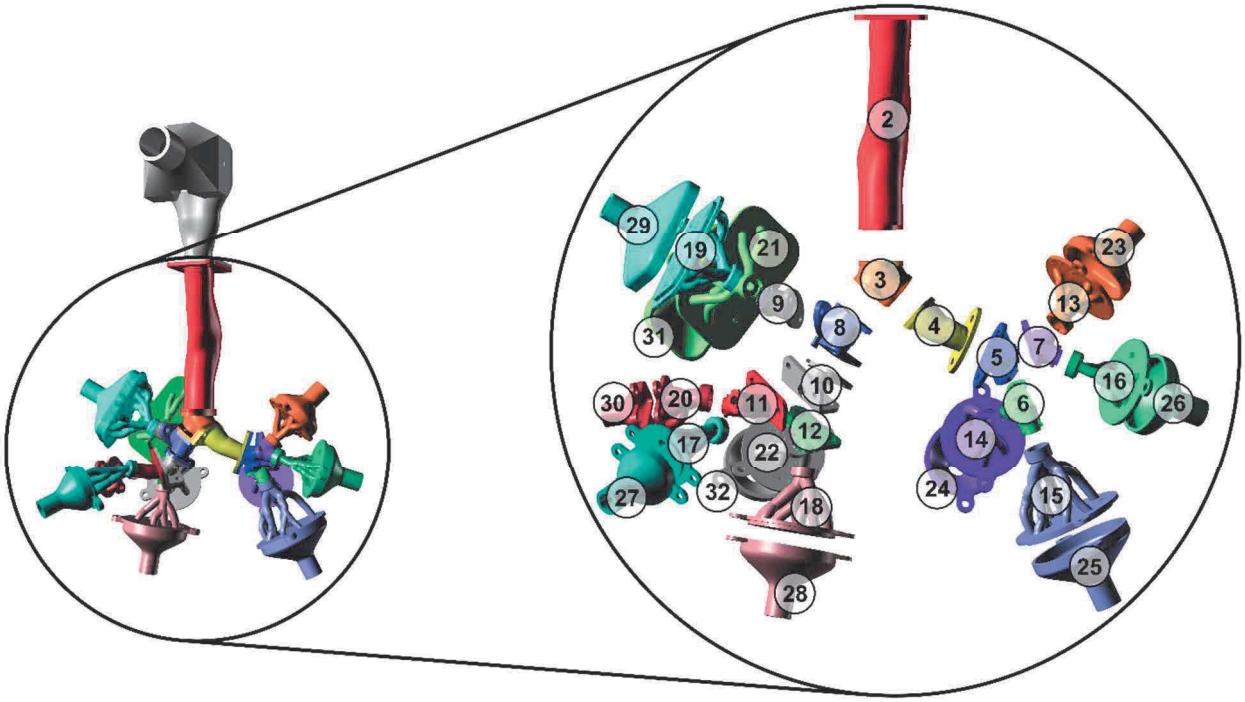

Figure 41 The replica of the respiratory airways (Lizal et al., 2015)

Leak test was performed prior to the deposition experiment because the replica consisted of multiple segments. Any leaks found, mostly between the flanges, were sealed with a small layer of silicone sealant. After that, silicon oil (550 Fluid, Dow Corning) was poured into the replica and then dried out for 24 hours. Thus, a thin layer of silicon oil was created on the inner walls of the model to prevent resuspension of the deposited particles.

The experimental setup can be seen in Figure 42. The TSI SSPD 3433 was utilized to disperse the porous particles. The particles then flew through a dilutor where the air from the SSPD was mixed with additional filtered air to reach a desirable flow rate through the replica (the inspiratory flow rate was 30 L/min). After the dilutor, particles passed through the replica. Some of the particles deposited in the replica and the rest of them was collected on the output filters downstream of the model. The air through the replica was driven by the vacuum pump and the flow distribution through the individual branches was set via rotameters. The flow rates through the output segments are listed in Table 7. The model exposition took 30 hours to deposit enough particles inside the replica.

The drawback of the method was that the output particle concentration from the SSPD was very low and a lot of particles deposited inside the SSPD or in the dilutor (Figure 43). The considerably high deposition in the dilutor also indicated that the particle size distribution measured during the particle production was different from the particle size distribution entering the replica. That is why the particle size distribution at the dilutor output was measured using the APS 3321. The measured CMAD was 1.41±2.1 μm and the MMAD was 8.15±1.6 μm. These values were used in the particle deposition calculations.

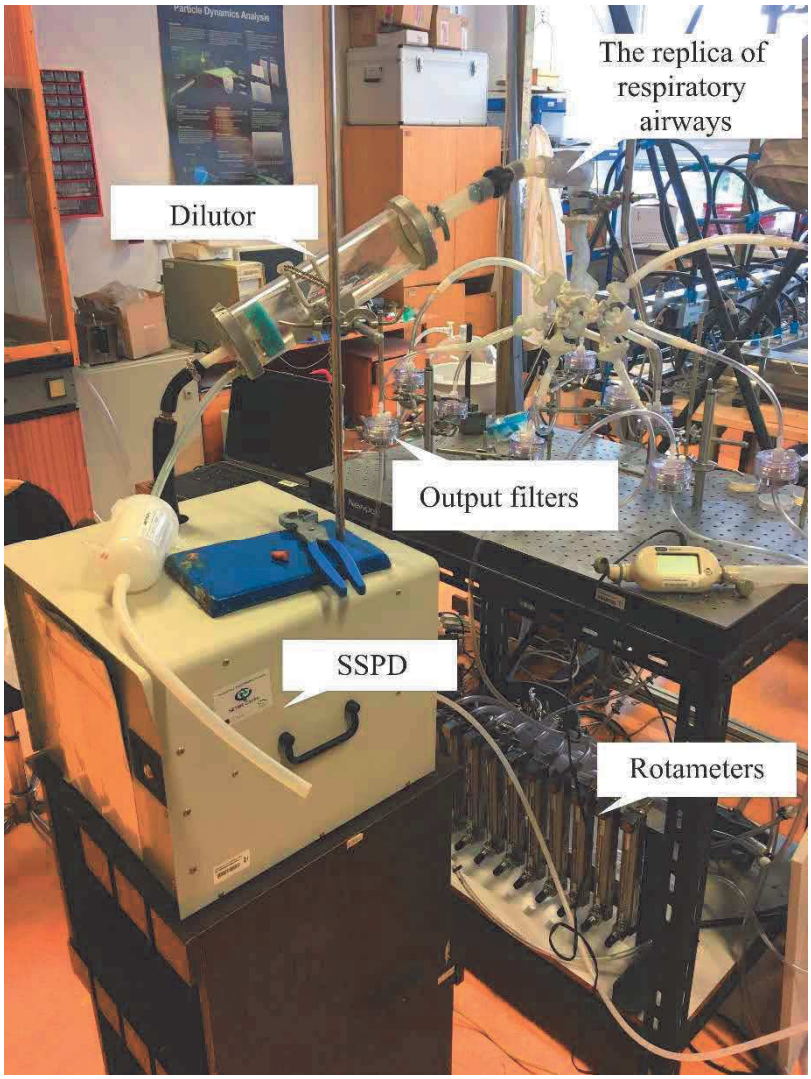

Figure 42 The experimental setup for deposition experiments

Table 7 The flow rates through output model segments

Output segment number	13	14	15	16	17	18	19	20	21	22	Total
Flow rate (L/min)	1.4	1.6	4	1.9	3.6	4.6	3.8	3.1	3	3	30

Figure 43 Particle deposition throughout the experimental setup; a) the expansion cone inside the SSPD, b) the dilutor

After the deposition experiment, the replica was disassembled and each segment was rinsed with a known volume of distilled water. The required volume to rinse a segment depended on the size and shape of the segment. The resulting solutions were poured into plastic containers and these were placed into a sample box. The samples were analyzed using a Spectrophotometer U-3900H (Hitachi, Tokyo, Japan) and values of absorbance for each solution was obtained. The molar concentration of $CuSO_4$ in each sample was calculated using equation 17. The actual mass of $CuSO_4$ deposited in each segment was calculated as

$$m = c_m \cdot V \cdot M \quad (18)\,,$$

where V is volume of distilled water used for segment rinsing and M is molar mass of $CuSO_4$ (M = 249.686 g/mol).

5.1.4. Results of porous particle deposition

Deposited mass in each segment was used for calculation of deposition characteristics, such as deposition fraction or deposition efficiency. Deposition fraction (DF) and deposition efficiency (DE) are given by equations 19 and 20:

$$\mathrm{DF} = \frac{deposited\ mass\ in\ a\ specific\ region}{total\ particle\ mass\ entering\ the\ oral\ airways} \quad (19)\,,$$

$$\mathrm{DE} = \frac{deposited\ mass\ in\ a\ specific\ region}{total\ particle\ mass\ entering\ this\ region} \quad (20)\,.$$

The deposition fraction represents a deposition distribution in the respiratory airways as a part of a total inhaled dose. The fractional deposition was calculated for every segment of the replica and the results can be seen in Figure 44. The deposition fractions at the outputs of the replica represent deposited mass downstream of the replica, i.e. in the output funnel-shaped segments, in the tubing, and on the filters. Deposited particles in the output parts of the experimental setup penetrated the replica and would continue deeper into the lungs. However, the deposition fractions in these output parts were very low, under 1% in all cases. Most of the particles deposited within the lung replica, in particular in the oral cavity (62.6%) and the trachea (9.8%). Significant deposition was also around the first bifurcation and in the segments with the highest output flow rates (segments 15 and 18). The results indicated that the large porous particles were not able to follow the streamlines and deposited either in the oral cavity or around bifurcation of large respiratory airways. This was somehow expected as the porous particles had quite high MMAD (8.15 µm).

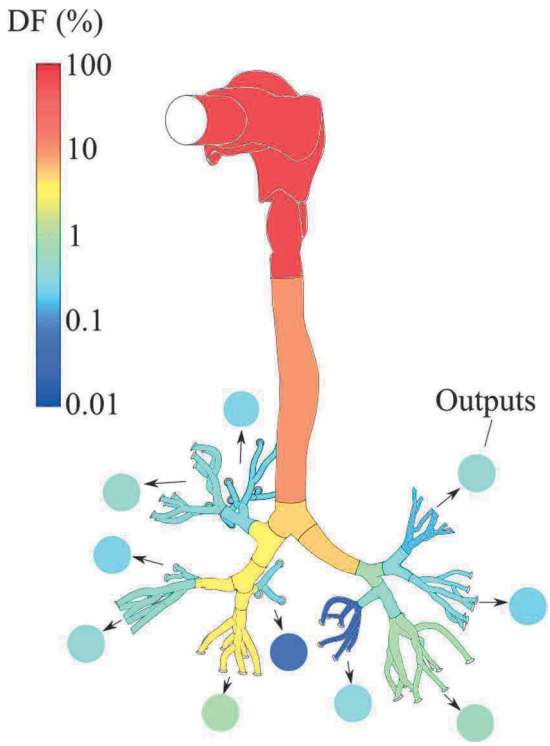

Figure 44 Deposition fractions in the replica; the output circles represent deposited mass in the output funnel-shaped segments, in the tubing and on the filters.

Deposition fraction as a function of segment number can be seen in Figure 45. The results of the current study were compared to the results of CFD simulation that was done on the same geometry (Koullapis et al., 2017). Koullapis et al. (2017) performed a large eddy simulation (LES) using a dynamic Smagorinsky turbulence model and implicit Euler particle tracking. The particle size was 10 µm with density of 0.914 g/cm^3. Using the equation 4, the aerodynamic diameter of these particles was 8.4 µm. The inspiratory flow rate was the same as in the experiment (30 L/min). The deposition patterns observed in the experimental results agreed to those predicted by the numerical simulations quite well. However, the deposition fraction differed slightly. The deposition in the oral cavity and in the trachea was higher during the experiment compared to the results of simulation. As most of the particles deposited in the upper respiratory airways, less particles reached the lower respiratory airways which caused lower deposition fraction in this part of the replica during experiment. This could be caused by the inlet velocity pattern. Turbulent inflow conditions were set in the simulation. However, it is impossible to say if these inlet conditions matched the conditions during the experiment without proper velocity measurements. Other reason for the deposition over prediction in the upper respiratory airways could be the particle size distribution. The porous particles were polydisperse which could result in significant deposition of large particles (larger than MMAD) in the oral cavity and the trachea and thus, very high deposition fraction. The advantage of numerical simulations is that all the particles have uniform size which is difficult to accomplish during experiments.

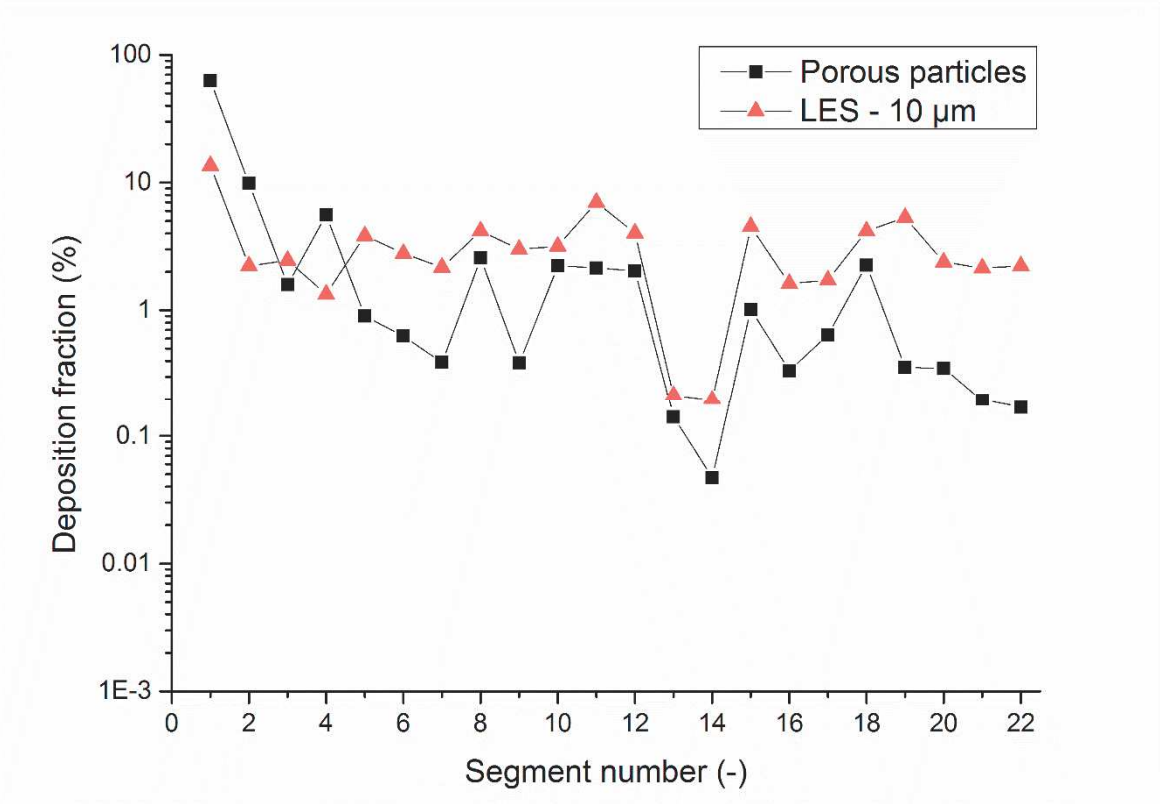

Figure 45 Comparison of deposition fraction as a function of segment number between experiment and numerical simulation

The particles did not deposit evenly in the respiratory airways but created so–called deposition hot spots. The deposition hot spots in the upper respiratory airways are depicted in Figure 46a. For the clarity, the mean velocity field in the exact lung replica numerically investigated by Koullapis et al. (2017) is depicted in Figure 46b. The numerical simulation was done for the inhalation flow rate of 60 L/min. However, it is assumed that the flow field for the case of 30 L/min would differ only in velocity magnitudes. As the impaction was the main deposition mechanism, the deposition was highly affected by the flow field. The deposition hot spots were observed in the regions where the air turned rapidly, such as on the tongue, on the posterior wall of the oral cavity and larynx, and in the trachea. The deposition hot spots around the 1st bifurcation are depicted in Figure 47. A significant deposition was spotted on the carina of the bifurcation. The effect of the cartilage rings was observed in the main bronchi. The particles deposited in the protruding surfaces of the rings and created a "striped" deposition pattern. This effect was more significant after the bifurcation which was also observed in the study of Russo et al. (2008). In the smaller airways, deposition hot spots were mostly observed around carinas of the bifurcation (Figure 48). This trend went down to the 6th and 7th generation in which deposition around bifurcations was still noticeable (Figure 49).

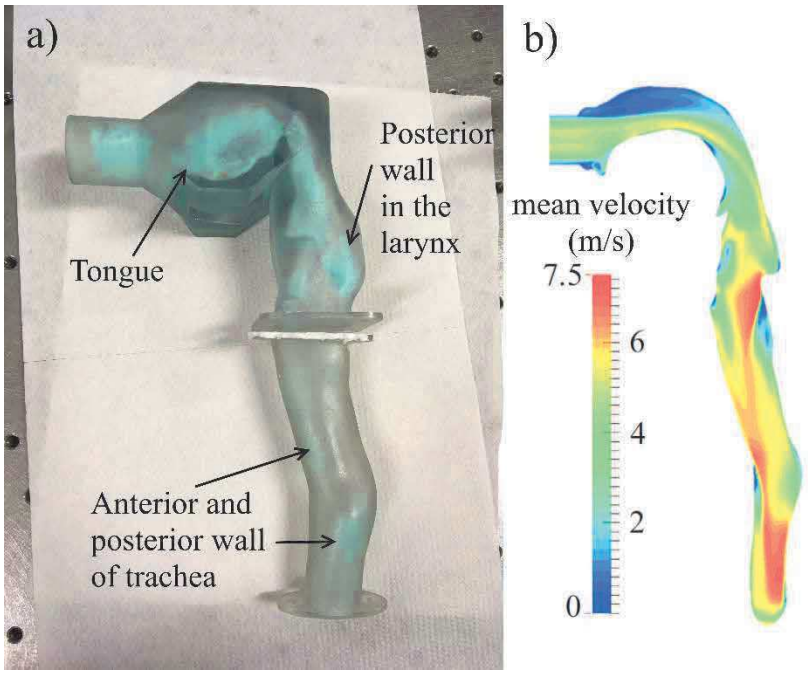

Figure 46 Deposition hot spots in the upper respiratory airways (a) and their agreement to flow field (b) at the inspiratory flow rate of 60 L/min (Koullapis et al., 2017)

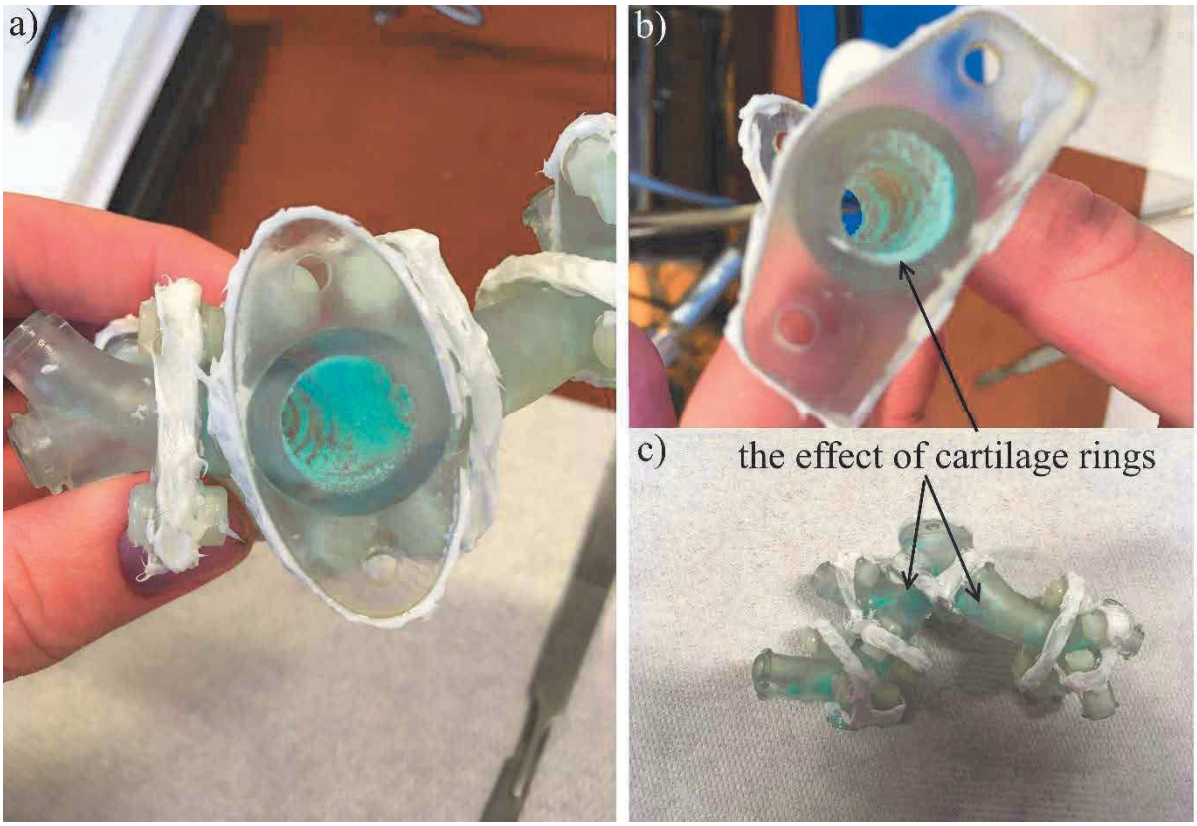

Figure 47 Deposition around the 1st bifurcation (a) and the effect of cartilage rings in the main bronchi (b, c)

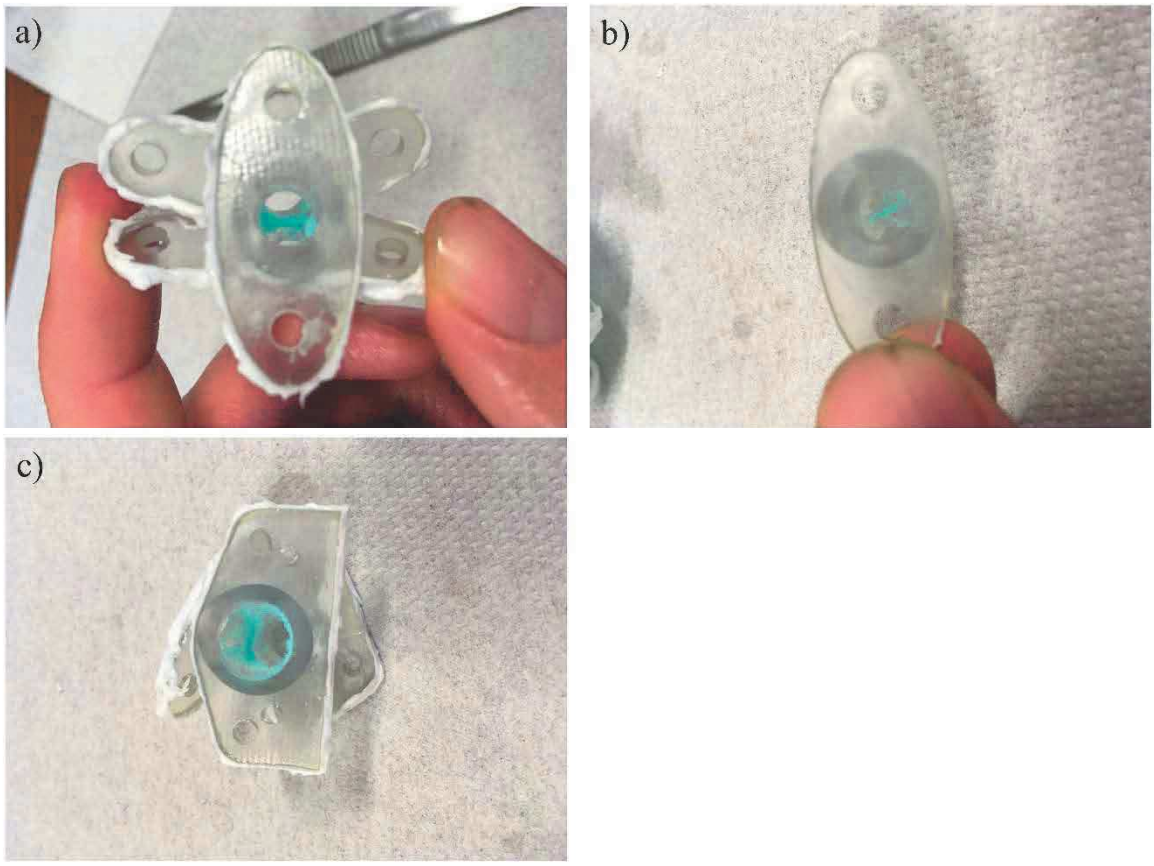

Figure 48 Deposition hot spots in the segments encompassing bifurcation in the 2nd to 4th generation

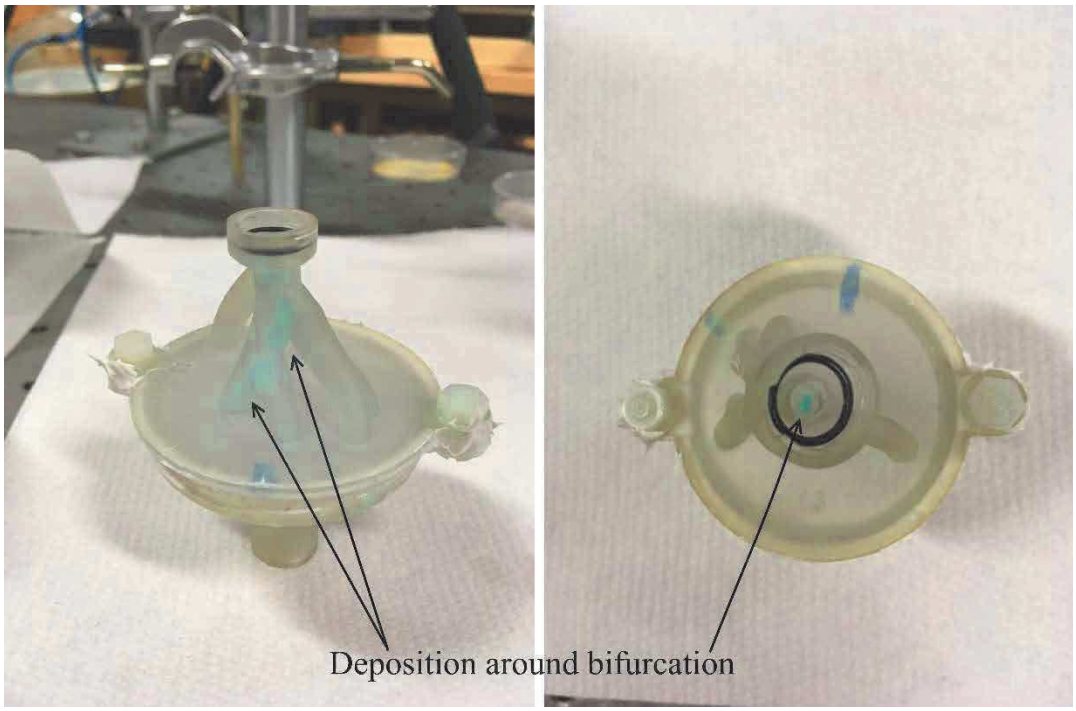

Figure 49 Deposition hot spots in the multigeneration segments encompassing approximately 4th to 7th bronchial generation

Deposition efficiency as opposed to deposition fraction describes the ability of a given region to collect or filter particles. As the impaction mechanism has an important role in the upper respiratory

tract and large conductive airways, deposition efficiency is frequently given as a function of impaction parameter ($d_a^2 Q$) or Stokes number. Stokes number can be calculated using equation 21:

$$\mathrm{Stk} = \frac{\rho_0 \cdot d_a^2 \cdot v_i}{18 \cdot \eta \cdot D_i} \qquad (21)\,,$$

where d_a is MMAD of the porous particles. When calculating the Stokes number for particles flowing through the tracheobronchial tree, v_i represents the mean velocity in the trachea (segment 2) or the parent airway of the bifurcation (segment 3 to 12), and D_i is the mean diameter of the trachea or parent airway of the bifurcation. When calculating the Stokes number for aerosol flowing through the segment with multiple generations (segments 13–22), an output equivalent diameter was first calculated as an average of all output cross–sections from the given segment. Then, the average of input airway diameter and the output equivalent diameter were used as a mean diameter D_i. The mean velocity v_i in the given segment was calculated as the flow rate through the segment divided by its mean diameter D_i.

Deposition efficiency in the oral cavity as a function of impaction parameter is given in Figure 50. The deposition data of spherical particles from the study of Cheng et al. (1999) are presented for comparison. Our measurement showed higher deposition compared to the data from the other study. As in the previous chapters, this discrepancy could be caused either by the inlet conditions or polydispersity of porous particles. The polydispersity of particles is represented by a GSD. As GSD increases, the fraction of particles with diameter smaller than MMAD increases. On the other hand, the fraction of particles with diameter larger than MMAD also increases. Musante (2002) indicated, that for larger MMAD increasing GSD resulted in enhanced deposition in the tracheobronchial tree and decreased deposition in the pulmonary region. As the deposition in the oral cavity is driven by the same mechanisms as the deposition in the tracheobronchial tree, it can be assumed that deposition increases with increasing GSD in this region.

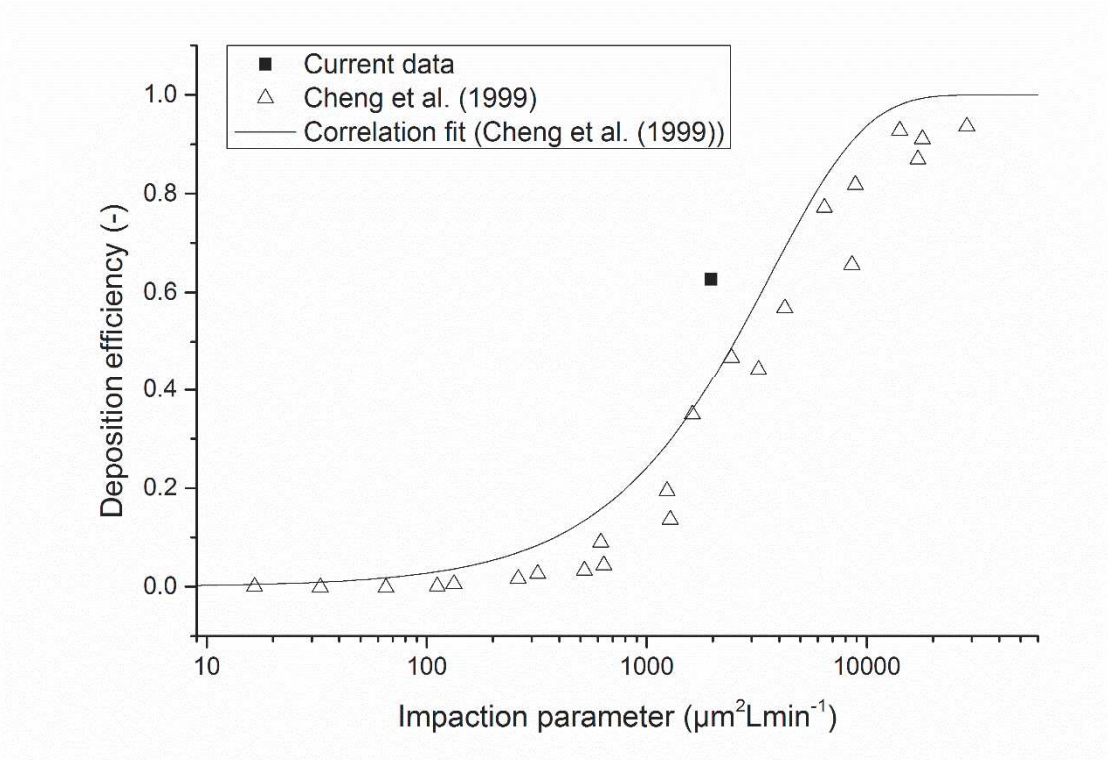

Figure 50 Deposition efficiency as a function of impaction parameter.

Deposition efficiency in the tracheobronchial tree as a function of Stokes number is depicted in Figure 51. The deposition efficiency increased with increasing Stokes number confirming the important role of impaction. The current data were compared to the data on spherical particle deposition measured by Chan and Lippmann (1980) and Zhou and Cheng (2005). Zhou and Cheng (2005) proposed empirical

models for deposition of spherical particles in bifurcations from 1st to 4th generation of branching. These models are given by equation 22:

$$\mathrm{DE} = 1 - \exp(-5.39 \cdot F \cdot \mathrm{Stk}^{1.34}) \qquad (22)\,,$$

where F is the function of the bifurcation angle and the ratio of parent and daughter tube diameters. The values of F for various bifurcation were between values of 0.485 and 1.326 (solid lines in Figure 51). Our data agreed to the data from other studies quite well. Some of the data in the multigeneration segments overpredicted the deposition. This could be caused by the fact that "average" Stokes number had to be calculated for the segments encompassing several generation. Other reason can be the UV/VIS spectrometry method. As very low amount of particles deposited in the small airways and on the output filters, the resulting concentrations were close to the detection limit of the method.

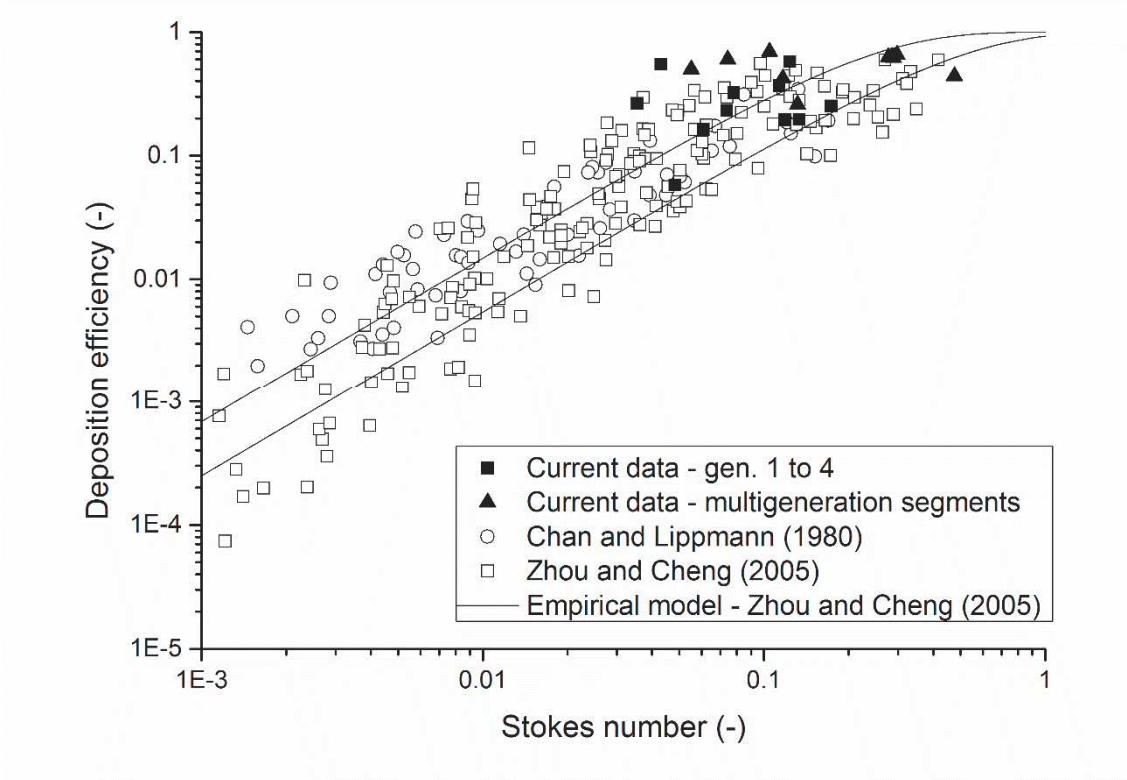

Figure 51 Deposition efficiency in the tracheobronchial tree as a function of Stokes number

The deposition of porous particles in the human airway replica was measured. The porous particles had rather high MMAD and thus, deposited significantly in the upper respiratory tract via impaction. When compared to other studies investigating deposition of spherical particles, the deposition characteristics agreed very well except the oral cavity. This indicated that porous particles deposited according to the aerodynamic diameter concept and the deposition is comparable to that of spherical particles. However, the effect of polydispersity on deposition should be studied in more detail.

5.2. Objective 2 - Deposition of fibrous particles

This chapter deals with fibrous particle deposition. It is composed of two papers that were published in journals with impact factor. The deposition of glass fibers in the replica of respiratory airways was studied. Glass fibers with uniform diameter were classified by length using dielectrophoretic classifier. The classified fibers were introduced into the replica and deposition at three steady inhalation flow rates was analyzed. The replica was rinsed after each experiment and the fibers were transferred onto membrane filters. Automatic method based on image processing was utilized to count all the fibers on the filters. These fiber counts were then used to calculate deposition characteristics. The results were compared to results of other studies regarding fiber deposition as well as other studies regarding deposition of spherical particles.

The first paper includes details about the image analysis method. The software was developed and optimized in collaboration with the institute of Mathematics. The second paper deals with the experimental setup, sample preparation and a fiber deposition analysis.

AEROSOL SCIENCE AND TECHNOLOGY
2016, VOL. 50, NO. 4, 353–362
http://dx.doi.org/10.1080/02786826.2016.1151858

Application of image analysis method to detection and counting of glass fibers from filter samples

Miloslav Belka[a], Frantisek Lizal[a], Jan Jedelsky[a], Pavel Starha[a], Hana Druckmullerova[a], Philip K. Hopke[b], and Miroslav Jicha[a]

[a]Department of Thermodynamics and Environmental Engineering, Faculty of Mechanical Engineering, Brno University of Technology, Brno, Czech Republic; [b]Center for Air Resources Engineering and Science, Clarkson University, New York, New York, USA

ABSTRACT

Man-made vitreous fibers (MMVFs) are noncrystalline substances made of glass, rock or slag and are widely used as thermal or acoustic insulation materials. There is continued concern about their potential health impacts and thus, their dosimetry and behavior in the environment still require study using filters to collect fiber samples. After deposition or exposure measurements of MMVFs it is often necessary to analyze the filters with deposited fibers. This task is tedious, time-consuming, and requires skill. Therefore, many researchers have tried to simplify or automatize fiber detection and quantification. This article describes features of our in-house software, which automatically detects and counts fibers in images of filter samples. The image analysis is based on the use of a histogram equalization and an adaptive radial convolution filter that enhances fiber contrast and thus, improves the fiber identification. The accuracy of the software analysis was verified by comparison with manual counting using ordinary phase-contrast microscopy method. The correlation between the methods was very high (coefficient of determination was 0.977). However, there were some discrepancies caused by false identifications, which led to implementation of manual corrective functions.

ARTICLE HISTORY
Received 17 October 2015
Accepted 28 January 2016

EDITOR
Tiina Reponen

1. Introduction

Man-made vitreous fibers (MMVFs) are fibers of various compositions that are widely used in buildings as a thermal or acoustic insulation material. MMVFs are noncrystalline substances made mainly of glass, rock, slag or other minerals. Health concerns from exposure to MMVFs come from their physical similarities to asbestos. They have similar aerodynamic characteristics, which causes their penetration into the human respiratory system. Oberdorster (2000) described pathogenicity of fibers with three parameters, in particular fiber dose, dimension, and durability. Fiber dose is generally expressed as particle mass deposited in the lungs, but with respect to fibrous aerosols particle number is also accepted. Fiber dimensions, in particular fiber length and diameter, determine deposition hot spots and affect the retention time of fibers in human respiratory tract. Fiber durability or fiber biopersistence means the overall retention capability of fibers in the lungs, which is influenced, e.g., by resistance to mechanical breakdown or chemical dissolution (DeVuyst et al. 1995). It is well known that exposure to asbestos leads to malignancies such as mesothelioma or lung carcinoma (IARC 2012). However, such results were not confirmed for MMVFs. The International Agency for Research on Cancer classified MMVFs as noncarcinogenic, because there is inadequate evidence for carcinogenicity in humans (IARC 2002). This finding may result from their lower biopersistence compared to asbestos, e.g., the MMVFs are more soluble and they tend to decompose transversely compared to tangential breakage of asbestos (DeVuyst et al. 1995; Hesterberg et al. 1996). Despite the lower risk of MMVFs, there are recommendations for occupational exposure limits for MMVFs in the range of 1–3 fibers/ml depending on the fiber type (SCOEL 2012).

Thus, it remains important to obtain additional information from both lung deposition and exposure measurements. The outputs of such measurements are membrane filters onto which the fibers deposited. Each filter has to be inspected and the individual fibers have to be counted to obtain the fiber concentrations. Several analytical methods were established to determine airborne concentrations of fibers, including NIOSH 7400

CONTACT Miloslav Belka belka@fme.vutbr.cz Department of Thermodynamics and Environmental Engineering, Faculty of Mechanical Engineering, Brno University of Technology, Technicka 2896/2, Brno 616 69, Czech Republic.

methodology developed for asbestos and other fibers using phase-contrast microscopy (PCM method) (NIOSH 1994). Drawbacks of these methods are their poor consistency and reproducibility. Manual fiber counting is very time consuming and requires high skill in the analyst such as visual acuity, concentration while counting, care for adjusting a microscope, experience in counting fiber bundles etc. Aforementioned flaws can cause fiber counts for the same samples to vary greatly between different analysts and laboratories (Pang 2000).

Many groups have tried to simplify or automate counting practices and decrease the influence of human factor on the results largely focused on filters with asbestos fibers. Lundgren et al. (1995) connected a microscope to a Macintosh computer with special video card and software. An analyst was able to mark fibers with a mouse on a screen and the software displayed total fiber counts. Other groups tried to automate the counting mostly using various image analysis methods (IAMs). One of the earliest works was proposed by Manchester University's Asbestos fiber-counting Program (MAP) (Kenny 1984). Their software called Magiscan gave reasonable agreement with manual counts, but it was not consistent for all types of samples. It produced precise results at lower counts, but undercounted fibers on heavily loaded filters. This bias was a result of the software development, which was done primarily on filters with low fiber numbers (Baron and Shulman 1987). The most frequent errors of Magiscan were missed fibers, broken fibers, and false identification of nonfibrous particles. Inoue et al. (Inoue et al. 1998) introduced Asbestos Fibers Automatic Counting System (AFACS), which was a home-made software written in C language. The AFACS was capable of post-processing, such as restoration of broken fibers according to their orientation and thickness. The accuracy of AFACS was verified and compared with counting facilities. The AFACS counts were similar to manual counts and were considered to be equivalent, although the AFACS counted some fibers that were missed by manual counters and *vice versa*.

Cho et al. (2011) focused mainly on improvement of image acquisition part of their IAM. They described High Through-put Microscopy method for counting asbestos fibers, which employed a charge couple device (CCD) camera and a robotic stage to quickly scan the entire filter area processing up to 300 images in 5 min. In another study (Cho et al. 2013) they tagged fibers with a fluorescent protein and analyzed them with fluorescence microscopy (FM) to enhance the detection limit for small and thin fibers. The freeware image processing software ImageJ with appropriate plugins was used for image analysis. However, the counting rules were not implemented into the software so it was not possible to count overlapping or crossed fibers, fiber bundles or differentiate oval-shaped particles. Further use of FM was made by Alexandrov et al. (2015). They used Asbester Counter Software for the image analysis. Although the application of FM should have eliminated nonfibrous particles with only asbestos fibers being visible in the FM images, some dust particles were still found. These particles caused discrepancies, especially for low concentration samples, because their edges were misidentified as fibers. Other IAMs for fiber counting were presented in Theodosiou et al. (2010), Ishizu et al. (2008), and Moriguchi et al. (2009). However, they did not get further than to testing and preliminary results. One of the problems of these IAMs was the occurrence of air bubbles from sample preparation (Ishizu et al. 2010), which biased the total fiber counts. As it can be seen, development of fully automatic IAM for fiber counting with sufficient accuracy is a very difficult task not completely solved yet.

As an output of *in vitro* deposition experiments we obtained a set of several hundreds of filter samples with deposited fibers, which needed to be analyzed. Since manual inspection and counting of fibers is very time consuming, tedious and sensitive to subjective errors, it would be valuable to use an IAM for fiber counting. Because all the methods that have been reported to date are inaccurate, expensive or not freely available, we developed our own software. By doing so, it is possible to easily adjust its features for different types of particles in future experiments. This article describes the main features of our software and presents a comparison with manual PCM method results.

2. Experimental setup

2.1. *The phase-contrast microscopy method*

2.1.1. *Sample preparation*

Millipore AAWP02500 nitrocellulose membrane filters (Merck Millipore, Billerica, MA, USA) were used as part of an *in vitro* deposition measurements in the model of human respiratory tract (Belka et al. 2013). The model consisted of upper respiratory airways and several generations of the tracheobronchial tree (Lizal et al. 2012). The filters were situated as output filters from each branch of the bronchus to collect particles passing through the model. We used glass fibers, processed by crushing of glass wool. The glass fibers were classified according to their length causing the mean fiber length to be approximately 15 μm and the mean diameter to be 1 μm (Wang et al. 2005). After the filters were loaded with fibers an acetone-immersion method was applied to clear the filter (NIOSH 1994). The filters were mounted on clean glass slides and made transparent using a Quick

fix acetone vaporizer (EMS Inc., Charleston, USA). The slides with filters were then kept in a desiccator for sufficient amount of time to dry. The samples featured generally low amount of dust and other nonfibrous particles. The fiber area density varied from 100 to 1300 fiber/mm^2. Ten representative samples with various fiber loads were chosen from the set to optimize the software development and to validate its results.

2.1.2. *Manual counting*

The manual counting was conducted using PCM, which is fast and requires less skill than electron microscopy. Moreover, the speed of PCM was suitable for the software development, which required a lot of tests, such as taking images with various camera settings. Each glass slide with a filter from the 10 samples was manually placed on a stage of Nikon Eclipse E200 microscope (Nikon, Tokyo, Japan) equipped with a nominal 10× eyepiece and a nominal 40× phase contrast objective. The microscope was focused on the fibers and Walton-Beckett graticule was used for sizing the fibers. The graticule consists of a circle with projected diameter of 300 μm (area of about 0.07 mm^2). Manual counting was conducted by four practiced analysts using NIOSH 7400 counting B rules, e.g., only fibers longer than 5 μm, with diameter less than 3 μm and with length to width ratio greater or equal to 5:1 were to be counted. The only significant modification of the methodology was that 20 fields were inspected on each filter rather than to fulfill a minimal fiber count rule. Moreover, the entire filter area was used for counting instead of cutting a wedge as recommended by the standard methodology. Because different parts of the filter were inspected by the analysts, it was necessary to compare property of the whole filter, such as total fiber number or fiber area density. Since the total fiber numbers were in the order of hundred thousands, fiber densities were calculated for their better readability. The fiber area density is calculated by dividing average fiber count per graticule field by the graticule field area. Fiber area density for every filter was calculated as:

$$E_i = \frac{\frac{F_i}{n_f}}{A_f}, \qquad [1]$$

where F_i is total fiber count on the sample i, n_f denotes the number of inspected fields per sample and A_f is the graticule field area. Since four analysts performed manual counting, geometric averages of the fiber area densities with geometric standard deviations were calculated for every sample. These average densities were considered as the "right" densities and were used for optimization of the software.

2.2. *The image analysis method*

2.2.1. *Image acquisition*

An IR-UV light filter and a monochrome camera Atik 314E (Atik cameras, Norwich, UK) were attached to the microscope to acquire a set of filter images. The nonuniformity in fiber distribution on a filter could cause discrepancies in the results, because only a part of each filter was inspected. This problem was partly solved by changing a 40× phase contrast objective to a 10× objective. Because the glass fibers with diameter of 1 μm were used, it was possible to decrease the magnification and, thus increase the examined filter area while keeping the visibility of the fibers at sufficient level. Resolution of the camera was 1619 × 1219 pixels and image area was 0.34 mm^2. The camera was connected to a computer with Artemis/ATK capture software. Sixteen images of each filter were taken and their analysis was executed afterward.

2.2.2. *Image processing*

The novel software uses several steps to correct and change the fiber contrast to improve their detection by thresholding (Figure 1). Even though the camera was properly adjusted and enough illumination was used, the brightness of original images was not sufficient. Some of the fibers did not have sufficient contrast and their visibility was very poor (Figure 1a). To enhance the fiber contrast the Adaptive Contrast Control (ACC) method was applied. This method is based on method by Zhu et al. (1999). It increases the contrast of an object with respect to its size, which can be used for brightness enhancement of poorly visible objects such as thin fibers. The ACC method calculates an equalization function using pixel brightness values from the respective neighborhood of each pixel. Application of this function creates a new calibrated image. Let $I_{m\times n} = (P[i,j])$ be the image brightness matrix of pixel P and its rectangular neighborhood $N^P{}_{w\times h}(i,j)$, where w and h are neighborhood dimensions. The equalization function $\phi^P{}_{wh}$ can be calculated using following formulas for each l in $[0; L_{max}]$, where L_{max} is maximum pixel value in this field.

$$\phi^P_{wh}(i,j,l) = Z\left(\frac{F_{ij}(l)}{wh} L_{max}\right), \qquad [2]$$

$$Z(x) = y \text{ for } x \in (\mathrm{y}-0.5; \mathrm{y}+0.5), \mathrm{y} \in \mathrm{Z}, \qquad [3]$$

where $F_{ij}(l)$ is cumulative density function of pixel brightness values and Z is a rounding function. The

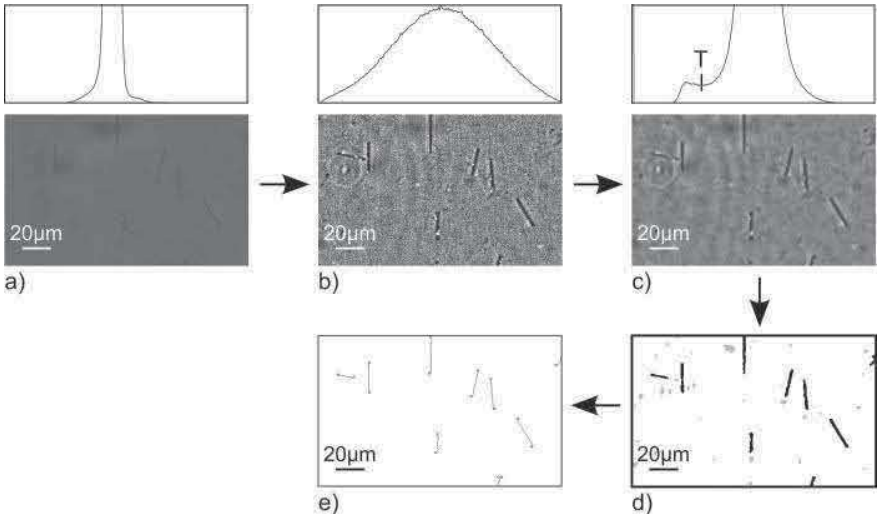

Figure 1. Image analysis process: (a) original image and its histogram; (b) image and histogram after ACC application; (c) image and histogram after adaptive radial convolution, *T* denotes threshold; (d) segmented image; (e) image with identified fibers.

rounding function provides round numbers at the output of equalization function. This is desirable, because image brightness values are round numbers. Moreover, the use of round numbers reduces computational time and memory demand. The size of the pixel neighborhood used for the equalization function influences the contrast change for objects of different size. Therefore, the equalization functions were tested with various sizes of the pixel neighborhood to find the best settings. The final image brightness matrix I^C of the new calibrated image was created by linear combination of three matrices, I^7, I^{15}, I^{31} with their respective square neighborhoods $N^P{}_{7\times7}$, $N^P{}_{15\times15}$, and $N^P{}_{31\times31}$:

$$I^C = 0.25I^7 + 0.5I^{15} + 0.25I^{31}. \quad [4]$$

The ACC method increased contrast of the fibers in the image, but also of any additive noise. The additive noise was not separated in brightness from the fibers, which can be seen from the image histogram with unimodal distribution (Figure 1b). It is required to have bimodal distribution to correctly identify individual fibers by thresholding.

To do this, an adaptive radial convolution filter was applied. Detailed mathematical description and derivation can be found in Starha et al. (2013). A classical Gaussian radial convolution filter used as a low-pass filter attenuates high spatial frequencies in a convolution function. The convolution function $h(\alpha,\beta)$ for the radial convolution filter is defined as

$$h(\alpha,\beta) = \frac{1}{2\pi\varsigma_\alpha\varsigma_\beta}\exp\left(-\frac{(\alpha-\alpha_0)^2}{2\varsigma_\alpha^2} - \frac{(\beta-\beta_0)^2}{2\varsigma_\beta^2}\right), \quad [5]$$

where α_0, β_0, ς_α and ς_β are constants. If this classical radial convolution filter was used, all of the additive noise, as well as fiber edges, would be suppressed and the fiber detection by thresholding would be still biased. This problem can be solved by addition of a weight function, which causes the radial filter to prefer certain directions more than others. This method recognizes directions of fiber edges by application of the stochastic approach. The fiber edge is defined as a change of the image from dark to bright, particularly the variance of image values is much higher in the direction of a fiber edge than in the absence of an edge. Because of this, the radial filter with its weight function recognizes fiber edges and adapts its properties to different parts of the image. Application of the adaptive radial filter caused suppression of noise while the fiber contrast was preserved. As it can be seen in Figure 1c, the image histogram presented a bimodal distribution and the image could be segmented by means of thresholding. The threshold T was set close to a minimum value between the two modes.

2.2.3. *Object classification and fiber counting*

Objects identified by thresholding were not only fibers, but also other objects, such as dust particles (Figure 1d).

For this reason it was necessary to classify all the objects and choose only those that fulfilled certain rules, i.e., fibers. Fiber recognition was done by the moment method, which is based on the fact that shape of every object can be described by moment invariants (Ming-Kuei 1962). The fiber moments were described by this method and all particles, which did not fit into this group, were excluded from the selection.

It was also essential to know the fiber dimensions to correctly count all of the fibers, because only fibers longer than 5 μm were to be counted. Additionally, it allowed the verification of the proper functioning of the electrical diffusion-phoretic fiber classifier (Wang et al. 2005) that was employed to separate the fibers according to their length. Fiber lengths were obtained by an erosion method using digital line structuring. This method calculates fiber core-line, which is a line of one pixel width defined by starting and end points. The fiber length is then expressed from the calculated core-line and known size of the pixel. Since the core-line is only one pixel wide, its length depends on the distances between adjacent pixels. If the pixels are adjoined vertically or horizontally, the distance between them equals the size of a pixel. If the pixels are adjoined diagonally, the distance between them equals the pixel diagonal. The total fiber length is a sum of distances between all the pixels of the core-line. Figure 1e depicts final image after object classification and transformation of fibers into digital lines.

The identified fibers were counted afterward. A Walton-Beckett graticule is employed in PCM method to help size the fibers and better identify the fibers, which occur on the edge of counting area. Fibers with only one end point lying in the counting area are counted as $\frac{1}{2}$ of a fiber. An elliptical field with area of 0.167 mm^2 was created in the software in order to follow this feature of the PCM method (Figure 2). This step was necessary for the determination of the actual size of all counted fibers. If the whole image was used for counting, only part of the fibers lying at the edge would be visible and the calculation of their actual sizes would be biased. The elliptical shape of the field has several advantages compared to rectangular field. There is lower probability that the fiber lies with both ends outside the field and its center inside the field, such as at the corners. Moreover, it is less likely that the fiber lies right on the edge of elliptical field compared to rectangular one. The software counted all the end points of fibers lying in the counting area and the number of end points was divided by two to get the final fiber count.

This procedure was applied to all filter images and respective fiber counts were acquired. Equation 1 was used for the calculation of fiber area densities for all

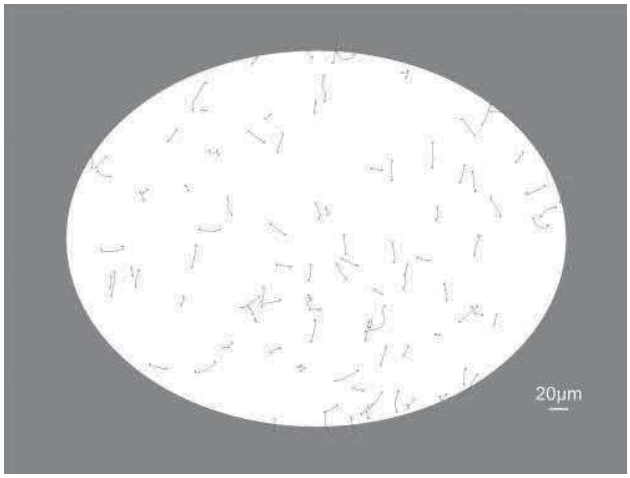

Figure 2. The use of elliptical field to correctly determine the actual size of all counted fibers; dimensions of semimajor and semiminor axis are 0.266 and 0.2 mm (area of about 0.167 mm^2).

samples, where F_i denotes total fiber count on the sample i calculated by the software, n_f is number of images per sample and A_f is counting area (area of the elliptical field). The results of the automatic method were validated by the PCM method afterward. The manual method contains several uncertainties caused by the methodology, such as the choice of inspected fields. By comparing the properties of entire filters, such as fiber area densities, it can be seen how the methods agree amongst themselves including all the limitations.

2.2.4. *Manual corrections*

The software allows it to be used in "correction" mode to assist the analysts to reject false identifications or restore broken fibers during postprocessing. The software interface can be seen in Figure 3 with first five windows representing different steps of image analysis. The results of the analysis are displayed in the sixth window in the bottom right corner. The selected portion of the filter can be displayed by the analyst and compared across the various stages of the IAM process. This combination of different steps of IAM simplifies the corrections, because, e.g., the visibility of particles is the highest after ACC application, but the particle origins are best determined in the original image. In cases of filters with high fiber area densities, it is very complicated to orientate and localize a particle of interest in the different windows. Therefore, a yellow circle cursor was integrated to improve orientation by defining the current position in all the windows. All of the corrections and the identified particles are highlighted in the segmented image (left bottom corner). Object identification and fiber counting can be launched

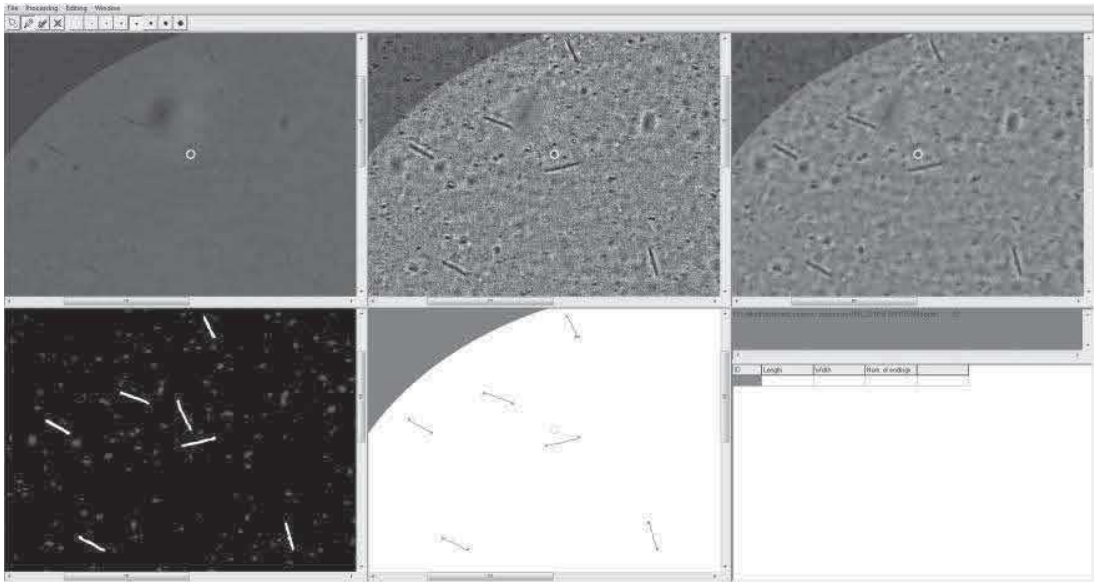

Figure 3. The software interface with six primary windows, the first five windows represent different steps of the IAM, the last window in the bottom right corner displays the results of the analysis.

after the corrections are made and a corrected fiber count is displayed.

3. Results and discussion

3.1. *The PCM method*

The results from the four analysts were compared and are listed in Table 1. The fiber area densities of test samples varied from 100 to 800 fibers/mm^2. The coefficient of variation (COV) among analysts ranged from 8 to 16%. The coefficient of variation is defined as the ratio of standard deviation to the average value and represents probability distribution. The differences between manual counts are generally caused by the sensitivity of the method to operator judgment, which can be influenced by not counting fibers with low contrast or counting one fiber twice in high area density samples. Moreover, fibers were not distributed uniformly on the filters with higher fiber area densities being found towards the filter center. Since every analyst inspected only 20 randomly chosen fields, the choice of the inspected fields could cause a slight difference in fiber counts even if fibers were counted properly.

3.2. *Validation of the IAM*

The collected images of the fibers had very low contrast and also contained nonfibrous particles. While the human eye is able to adapt to different background brightness, suppress additive noise and ignore dust particles, IAMs require various image modifications to successfully detect the particles. We found that the application of the ACC and the adaptive radial convolution filter enhanced the fiber contrast while the contrast of the background noise remained low. This process improved the detection limit of the IAM, and thus, very thin and low contrast fibers were detected. The moment method was then applied to restrict counting nonfibrous particles.

Table 1. Fiber area densities given by analysts for ten samples; SD denotes standard deviation and COV is coefficient of variation.

	S 1	S 2	S 3	S 4	S 5	S 6	S 7	S 8	S 9	S 10
Analyst 1 (f/mm^2)	457.1	410.0	90.4	568.9	403.2	222.1	577.9	185.4	585.4	158.6
Analyst 2 (f/mm^2)	355.4	471.1	111.1	802.1	493.2	250.7	588.2	224.6	480.4	181.1
Analyst 3 (f/mm^2)	373.9	512.9	118.2	890.4	525.4	279.6	624.6	262.9	611.4	219.6
Analyst 4 (f/mm^2)	300.7	390.4	140.7	833.6	432.9	238.6	499.3	233.6	510.4	186.1
Average (f/mm^2)	371.8	446.1	115.1	773.8	463.7	247.8	572.5	226.6	546.9	186.3
SD (f/mm^2)	56.2	48.7	18.0	122.4	48.2	21.0	45.7	27.7	53.4	21.8
COV (—)	0.15	0.11	0.16	0.16	0.10	0.08	0.08	0.12	0.10	0.12

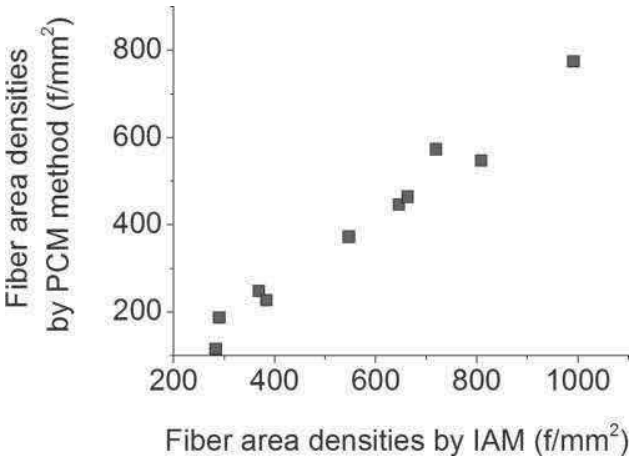

Figure 4. Correlation between the PCM method and the IAM.

Results of the software were validated by comparison with the results of PCM method. Both methods were employed to acquire fiber area densities on ten filter samples. The correlation between the methods is depicted in Figure 4. Although the coefficient of determination was very high ($R^2 = 97.7\%$), there were some discrepancies between the methods and the IAM appears to have overestimated the fiber area densities in all samples.

The main causes of this trend were false object identifications, particularly misidentified particles, and broken fibers. The moment method was applied to select fibers from all of the objects present in the image. This method is, just like NIOSH methodology, unable to distinguish between fibers and elongated particles. Therefore, dust particles resembling fibers are considered to be fibers. Moreover, our IAM falsely identified edges of large dust particles as elongated particles and counted them as fibers.

Another problem in object identification was caused by circular particles or so-called bubbles (Figure 5). Ishizu et al. (2010) indicated that these bubbles could be created during specimen preparation. The bubbles were located in a different plane than the fibers and were out of focus during image acquisition. This mismatch in focal plane produced halos around the bubbles. During the image processing the halo contrast was enhanced by the ACC and resembled large circular particles. In addition, the edges of these false particles were sometimes identified as objects during thresholding and could be selected as fibers. This problem was caused by the moment method settings. The moment method exclude nonfibrous particle from the final selection based on their geometric properties. The settings of the moment method were rather universal, but with the knowledge of the moment invariants of various nonfibrous particles, such as bubbles, microorganisms or membrane particles, it would be possible to adjust the method for specific cases.

Apart from false object identification, fibers were sometimes split into shorter objects during thresholding (Figure 6) caused by the drop in contrast along the fiber, such as in the case of fiber crossing. The upper fiber was identified as one piece, but fiber underneath was split into two separate objects and misinterpreted as different fibers. This problem could be solved in postprocessing step using information from the moment method. The fibers could be restored based on their orientation, thickness and mutual distance. However, this feature will require further tests and optimization for high area density samples.

3.3. *Corrected IAM*

The software allows manual corrections of the false object identifications. To validate this approach the results of the IAM were corrected by an analyst using the software feature and the resulting fiber area densities were compared to the PCM method again. As can

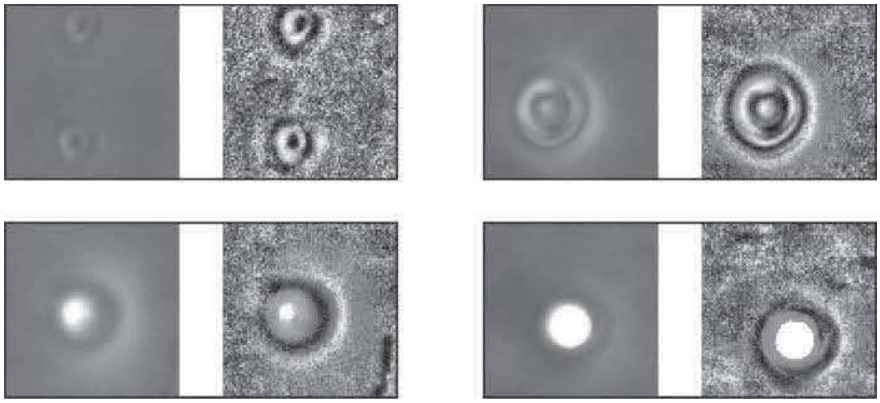

Figure 5. Enhancement of bubble contrast during ACC application; particle image size is 32 × 32 μm.

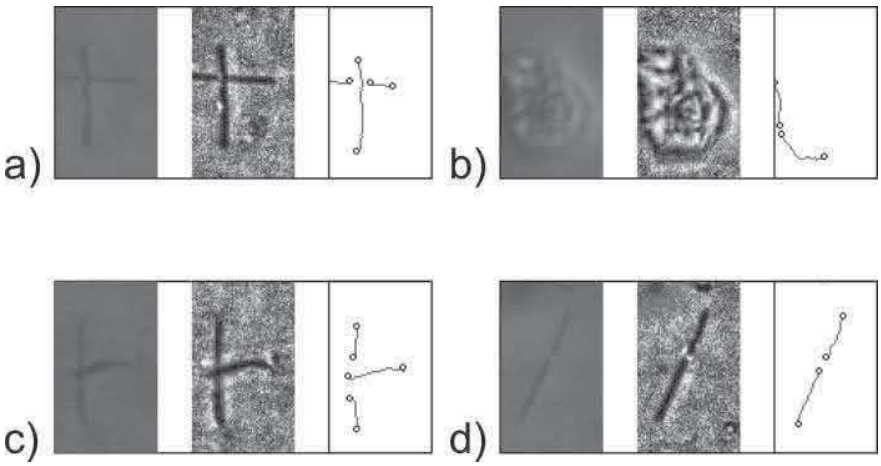

Figure 6. Examples of false identification in three steps of IAM: Original image, application of ACC, fiber identification; (a) crossed fibers, (b) dust particle, (c) crossed fibers, (d) single fiber; particle image size is 24 × 40 μm.

be seen in Figure 7, the IAM accuracy was improved and differences between methods decreased. The coefficient of determination increased from 97.7 to 98.5%. Moreover, average coefficient of variation decreased from 56 to 10% after the corrections. These results show that the accuracy of the corrected IAM is as high as the accuracy of the PCM method. The discrepancies between the corrected IAM and the PCM method can be caused by the sensitivity of both methods to the choice of inspected fields. Although the lower magnification was used for the automatic method, the software algorithms compensated for this drawback and even thin and low contrast fibers were counted.

Even though the software is not yet ready to be used in the fully automatic mode, it can be reliably used with manual corrections. Since the corrected images are stored, they can be opened and examined repeatedly. This way the software can be used for educational purposes and analysts who are not skilled and experienced can learn to analyze fiber samples. Moreover, as stated by Lundgren et al. (1995), fiber counting using a computer is more user-friendly and less exhausting than counting using a microscope. Apart from that, the errors in identification and counting of certain kinds of particles were observed and their future solution can bring more precise results and development of the fully automatic fiber counting instrument. Current version of the software can be found and downloaded at http://www.energetickeforum.cz/ext/2pf/software/.

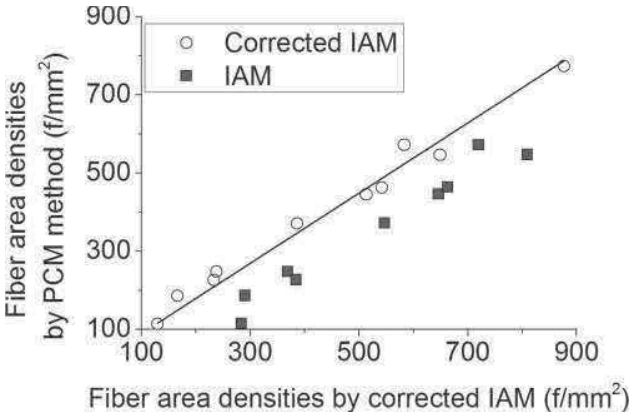

Figure 7. Correlation between the PCM and the corrected IAM.

4. Conclusions

This article presents an in-house software intended for automatic fiber counting using image analysis. The software was developed and optimized on filters with deposited glass fibers, which were obtained during *in vitro* deposition measurements. However, the software can be used for counting of various kinds of fibers. The analyzed images are saved on a hard-drive and can be checked or examined repeatedly. The software is able to identify fiber shape and determine its length, which is the most important parameter for fiber counting and determination of fiber pathogenicity. It is worth noting that the software was used to analyze images from PCM at total magnification of 100×. Although this magnification was sufficient for the analysis of MMVFs, the analysis of some kinds of asbestos fibers, such as chrysotile fibers, can be biased. However, this limitation could be overcome by the change of the magnification and adjustment of the software settings.

We found that the use of histogram equalization and adaptive radial convolution filter can enhance the fiber

contrast while additive noise remained suppressed. This way the software is able to localize and identify even very thin and short fibers. Results of the software were validated by comparison with the manual PCM method indicating some shortcomings in the IAM. The software overestimated the fiber counts, which was mostly caused by broken fibers or misidentification of particle edges as fibers. Therefore, it is desirable to check every analyzed image and correct false identifications with software corrective functions. The time efficiency of the automatic method is reduced due to this step, however, it is still more convenient and less exhausting than the PCM method.

Despite these minor limitations, the software can be used for fiber counting analysis, because it can help the analyst with fiber localization and summation of all fibers. Moreover, the present errors of the counting were observed and analyzed. Future work should, therefore, concentrate on improvement of fiber identification and restoration of broken fibers using postprocessing functions. The program can be obtained by contacting the first author.

Funding

Authors greatly acknowledge support from the projects FCH/FSI-J-14–2479 and LO1202 NETME CENTRE PLUS funded by the Ministry of Education, Youth and Sports of the Czech Republic under the National Sustainability Programme I and projects no. 105/11/1339 and 16–23675S funded by the Czech Science Foundation.

References

Alexandrov, M., Ichida, E., Nishimura, T., Aoki, K., Ishida, T., Hirota, R., Ikeda, T., Kawasaki, T., and Kuroda, A. (2015). Development of an Automated Asbestos Counting Software Based on Fluorescence Microscopy. *Environ. Monit. Assess.*, 187:4166

Baron, P. A., and Shulman, S. A. (1987). Evaluation of the Magiscan Image Analyzer for Asbestos Fiber Counting. *Am. Ind. Hyg. Assoc. J.*, 48:39–46.

Belka, M., Lizal, F., Jedelsky, J., and Jicha, M. (2013). Analysis of Fiber Deposition Using Automatic Image Processing Method. *Epj. Web. Conf.*, 45. doi: 10.1051/epjconf/20134501011.

DeVuyst, P., Dumortier, P., Swaen, G. M. H., Pairon, J. C., and Brochard, P. (1995). Respiratory Health Effects of Man-Made Vitreous (Mineral) Fibres. *Eur. Respir. J.*, 8:2149–2173.

Hesterberg, T. W., Miiller, W. C., Musselman, R. P., Kamstrup, O., Hamilton, R. D., and Thevenaz, P. (1996). Biopersistence of Man-Made Vitreous Fibers and Crocidolite Asbestos in the Rat Lung Following Inhalation. *Fund. Appl. Toxicol.*, 29:267–279.

Cho, M. O., Chang, H. M., Lee, D., Yu, Y. G., Han, H., and Kim, J. K. (2013). Selective Detection and Automated Counting of Fluorescently-Labeled Chrysotile Asbestos Using a Dual-Mode High-Throughput Microscopy (DM-HTM) Method. *Sensors*, 13:5686–5699.

Cho, M. O., Yoon, S., Han, H., and Kim, J. K. (2011). Automated Counting of Airborne Asbestos Fibers by a High-Throughput Microscopy (HTM) Method. *Sensors*, 11:7231–7242.

IARC. (2002). Monographs on the Evaluation of Carcinogenic Risks to Humans, in *Man-Made Vitreous Fibers*. International Agency for Research on Cancer, Lyon, France.

IARC. (2012). Monographs on the Evaluation of Carcinogenic Risks to Humans, in *Arsenic, Metals, Fibres, and Dusts*. International Agency for Research on Cancer, Lyon, France, pp. 219-310.

Inoue, Y., Kaga, A., Yamaguchi, K., and Kamoi, S. (1998). Development of an Automatic System for Counting Asbestos Fibers Using Image Processing. *Part. Sci. Technol.*, 16:263–279.

Ishizu, K., Takemura, H., and Kawabata, K. (2010). Automatic Counting Robot Development Supporting Qualitative Asbestos Analysis: Asbestos, Air Bubbles, and Particles Classification Using Machine Learning. *J. Robot. Mechatron.*, 22: 506–513.

Ishizu, K., Takemura, H., Kawabata, K., Asama, H., Mishima, T., and Mizoguchi, H. (2008). Image Processing of Particle Detection for Asbestos Qualitative Analysis Support Method—Particle Counting System Based on Classification of Background Area, in *10th International Conference on Control Automation Robotics & Vision: Icarv 2008*, IEEE, New York, NY, pp. 868–873.

Kenny, L. C. (1984). Asbestos Fiber Counting by Image-Analysis—The Performance of the Manchester Asbestos Program on Magiscan. *Ann. Occup. Hyg.*, 28:401–415.

Lizal, F., Elcner, J., Hopke, P. K., Jedelsky, J., and Jicha, M. (2012). Development of a Realistic Human Airway Model. *Proc. Inst. Mech. Eng. H*, 226:197–207.

Lundgren, L., Lundstrom, S., Laszlo, I., and Westling, B. (1995). Modern Fiber Counting—A Technique with the Phase-Contrast Microscope Online to a Macintosh Computer. *Ann. Occup. Hyg.*, 39:455–467.

Ming-Kuei, H. (1962). Visual pattern recognition by moment invariants. *Inf. Theory, IRE Trans.*, 8:179–187.

Moriguchi, Y., Hotta, K., and Takahashi, H. (2009). Asbestos Detection from Microscope Images Using Support Vector Random Field of Local Color Features, in *Advances in Neuro-Information Processing*, Pt Ii, ed., Springer-Verlag, Berlin, Berlin, pp. 344–352.

National Institute for Occupational Safety and Health (NIOSH). (1994). NIOSH Manual of Analytical Methods; ASBESTOS and OTHER FIBERS by PCM 7400, 4th ed., in DHHS (NIOSH) Publication No. 94-113, U.S. Department of Health and Human Services, Cincinnati, Ohio, USA.

Oberdorster, G. (2000). Determinants of the Pathogenicity of Man-Made Vitreous Fibers (MMVF). *Int. Arch. Occ. Env. Hea.*, 73:S60–S68.

Pang, T. W. S. (2000). Precision and Accuracy of Asbestos Fiber Counting by Phase Contrast Microscopy. *Aihaj.*, 61:529–538.

Scientific Committee on Occupational Exposure Limits (SCOEL). (2012). Recommendation from the Scientific

Committee on Occupational Exposure Limits for Man Made-Mineral Fibres (MMMF) in SCOEL/SUM/88, European Commission. Employment, Social Affairs and Inclusion.

Starha, P., Druckmüllerová, H., Belka, M., Lizal, F., and Jedelsky, J. (2013). Application of Adaptive Radial Convolutional Filter, in *19th International Conference on Soft Computing*, MENDEL 2013, Brno, pp. 357–362.

Theodosiou, Z., Tsapatsoulis, N., Bujak-Pietrek, S., Szadkowska-Stanczyk, I., and Ieee (2010). Airborne Asbestos Fibers Detection in Microscope Images using re-initialization free Active Contours, in *32nd Annual International Conference of the IEEE Engineering-in-Medicine-and-Biology-Society* (EMBC 10), Ieee, Buenos Aires, ARGENTINA, pp. 4785–4788.

Wang, Z., Hopke, P. K., Baron, P. A., Ahmadi, G., Cheng, Y.-S., Deye, G., and Su, W.-C. (2005). Fiber Classification and the Influence of Average Air Humidity. *Aerosol Sci. Technol.*, 39:1056–1063.

Zhu, H., Chan, F. H. Y., and Lam, F. K. (1999). Image Contrast Enhancement by Constrained Local Histogram Equalization. *Comput. Vis. Image Und.*, 73:281–290.

Journal of Aerosol Science 117 (2018) 149–163

Contents lists available at ScienceDirect

Journal of Aerosol Science

journal homepage: www.elsevier.com/locate/jaerosci

Deposition of glass fibers in a physically realistic replica of the human respiratory tract

Miloslav Belka[a,*], Frantisek Lizal[a], Jan Jedelsky[a], Jakub Elcner[a], Philip K. Hopke[b], Miroslav Jicha[a]

[a] Faculty of Mechanical Engineering, Brno University of Technology, Technicka 2, Brno 61669, the Czech Republic
[b] Center for Air Resources Engineering and Science, Clarkson University, USA

ARTICLE INFO

Keywords:
Fiber deposition
Human respiratory airways
Glass fibers
Experiments
Deposition measurement

ABSTRACT

Regional deposition of glass fibers was investigated in a physically realistic, human respiratory tract replica. The replica begins with the oral cavity and includes the airways up to the 7th generation of the tracheobronchial tree. Uniform diameter glass fibers were classified by length using a dielectrophoretic classifier and introduced into the replica at three steady-state flow rates (15, 30, and 50 LPM). A novel automatic image processing method was utilized to speed up the sample analysis and make it more reproducible. Fractional deposition was high in the oral cavity and the upper respiratory airways. Deposition density was higher in the first few generations of the tracheobronchial tree. Deposition efficiencies were compared with published data and good agreement was obtained. Our data confirmed that the deposition efficiency increased with increasing Stokes number indicating that impaction was the main deposition mechanism. The experimental data were used to propose new empirical models predicting fiber deposition in the tracheobronchial tree.

1. Introduction

Since the discovery of the toxicity of asbestos, there has been ongoing interest in inhalable fibers (Baron, 2001). The use of asbestos has been strictly regulated or banned altogether in the past. However, these restrictions led to increased production of substitute materials, such as man-made vitreous fibers (MMVFs). MMVFs have some physical similarities to asbestos that provide them with comparable aerodynamic characteristics and thus, the ability to penetrate into the human respiratory system. This capability naturally raised the question of their toxicity. Although the International Agency for Research on Cancer has classified glass, rock, and slag wool as non-carcinogenic to humans, and ceramic fibers as possibly carcinogenic to humans (IARC, 2002), MMVFs remain a concern. Recommended occupational exposure limits (OEL) of 1 fiber/ml have been established in the countries of European Union (SCOEL, 2012).

Most prior studies regarding particle transport and deposition in human respiratory airways involved spherical particles (Chan & Lippmann, 1980; Lizal, Belka, Adam, Jedelsky, & Jicha, 2015; Zhou & Cheng, 2005). However, it is not possible to extrapolate these results to fibrous aerosols. Fibers exhibit different aerodynamic behavior than spherical particles, causing different deposition patterns. This difference occurs because of the complicated motion of fibers that undergo both translation and rotation. After inhalation, fibers tend to align with the air stream causing their effective aerodynamic diameter to closely approximate its diameter with length having a negligible influence (Baron, 2001). During translation motion, fibers occasionally rotate, which temporarily changes the

* Corresponding author.
E-mail address: belka@fme.vutbr.cz (M. Belka).

https://doi.org/10.1016/j.jaerosci.2017.11.006
Received 3 February 2017; Received in revised form 16 October 2017; Accepted 15 November 2017
Available online 21 November 2017
0021-8502/

particle's drag force (Kleinstreuer & Feng, 2013). The frequency of fiber rotation in the flow depends on the fiber aspect ratio and the position in the airways. Fibers rotate more frequently with a decreasing aspect ratio, and near the walls in high shear flow (Feng & Kleinstreuer, 2013; Tian, Ahmadi, Wang, & Hopke, 2012).

Only a few studies of fiber deposition in human respiratory airways have been reported. Controlled experiments on human subjects are potentially hazardous and thus, unethical. Therefore, experimental methods using airway replicas and numerical simulations are required. Myojo and coworkers (Myojo & Takaya, 2001; Myojo, 1990) experimentally investigated glass fiber deposition in bifurcating airway models. The two models consisted of single bifurcations from the 2nd to 3rd and the 3rd to 4th generations of tracheobronchial branching of a Weibel A lung model (Weibel, 1963), respectively. Preferred sites of deposition or "hot spots" were found around the carinal ridges, and the orientation of deposited fibers was parallel to the air stream. Sussman, Cohen, and Lippmann (1991) performed experiments with an upper tracheobronchial tree replica to study the influence of fiber length and diameter on deposition distribution. A mechanical larynx was connected to the model to simulate the influence of upper respiratory airways. Deposition hot spots were identified around carinas as well as on the upper dorsal wall of the trachea. Deposition in the trachea was caused by a jet that formed at the larynx constriction and directed the air towards the trachea wall (Chan & Schreck, 1980). Su and coworkers (Su & Cheng, 2006a, 2006b, 2009) and Zhou, Su, and Cheng (2007) experimentally studied fiber deposition in two realistic replicas consisting of human airways from the oral cavity to the 4th branch generation. Various fiber types with different densities were employed including carbon, TiO_2, and glass fibers. High inertia fibers deposited extensively in oropharynx and larynx in both the replicas. However, low inertia fibers mostly traversed the replicas. Comparing the two replicas, the exact location of deposition hot spots differed slightly indicating that the differences in geometry caused small changes in the flow field and the resulting changes in deposition.

Computational studies of particle deposition in realistic human airway models are difficult because the underlying physics that must be captured is highly complex. Moreover, the complex coupled rotational and translational fiber motion must be addressed. Therefore, many studies have been conducted on idealized geometries using simplified cases where an analytical solution was employed or simple shear flows were used. For example, Cai and Yu (1988) predicted fiber deposition in bifurcating airways. Fan and Ahmadi (1995) presented fiber equations of motion in a sublayer model evaluating the fiber deposition in turbulent streams. Zhang, Asgharian, and Anjilvel (1996) studied the fiber deposition numerically in an equal diameter bifurcating airway model for various fiber sizes and bifurcation angles. Balashazy, Martonen, and Hofmann (1990, 2005) tested an equivalent diameter concept and predicted fiber deposition in the bifurcating model for the three fiber orientations; parallel, perpendicular and random with respect to the streamlines.

Recently, numerical simulations of fiber deposition in realistic geometries have been reported. Tian et al. (2012) introduced a computational model for predicting the fiber transport and deposition in low Reynolds number flows. Later, Tian and Ahmadi (2013) employed the model to study fiber deposition in bronchial airways from the trachea to the 3rd bronchial generation. The absence of a larynx was addressed by prescribing turbulence intensities at the trachea inlet. The results showed that turbulence enhances deposition, emphasizing the importance of larynx and upper respiratory airways for a proper study of deposition patterns. Feng and Kleinstreuer (2013) investigated transport and deposition of ellipsoidal particles in a similar geometry of human respiratory airways as those used by Su and Cheng (2006b). The deposition efficiencies in these studies were compared and acceptable agreement was found. Deposition of particles with various aspect ratios was then studied. It was observed that the particles with higher aspect ratios have higher probabilities of penetrating deeper into the lungs compared to lower aspect ratio particles, e.g. spherical particles. Additionally, the deposition efficiency per generation of these high aspect ratio fibers increased slightly from trachea to the fourth generation, indicating interception driven by secondary flows can influence the deposition in higher branch generations. Inthavong, Mouritz, Dong, and Tu (2013) studied the transport of airborne fibers through the nostrils into the respiratory system using empirically defined drag coefficient for the fiber motion. Dastan, Abouali, and Ahmadi (2014) extended the work of Fan and Ahmadi (1995) and employed the equations for fiber motion to study fiber deposition in human nasal cavities. Shanley and Ahmadi (2011) developed a computational model to account for the motion of ellipsoidal particles in viscous shear flows. Shanley, Ahmadi, Hopke, and Cheng (2016) employed this model to numerically analyze fiber deposition in human nasal cavity.

The use of proper computational models that account for the fiber motion in conjunction with the computational fluid dynamics methods is essential in fiber deposition studies. The crucial step on the way to routinely and reliably use CFD calculations is a proper validation with experimental data, either acquired in vivo or on human replicas. However, the number of experimental data regarding fiber deposition is rather sparse. That is the reason why we experimentally investigated glass fiber deposition in our human airway replica. The replica geometry extends from the oral cavity to the 7th bronchial generation (Lizal, Elcner, Hopke, Jedelsky, & Jicha, 2012). The fibers were classified using dielectrophoresis to yield uniform length particles. A novel automatic image processing method was utilized to speed up the sample analysis, make it more convenient and more reproducible (Belka et al., 2016). The results of this study also provide the first measurements of deposition beyond the 4th generation. The current replica has been employed in other experimental works (Jedelsky, Lizal, & Jicha, 2012; Lizal et al., 2015; Nordlund et al., 2017) and thus, the results on fiber deposition presented in this paper further extend the data set for experimental validation. Recent progress in simulations performed on the current replica has been documented by Koullapis et al. (2017) and Frederix et al. (2018). The digital geometry of the airways is available upon request.

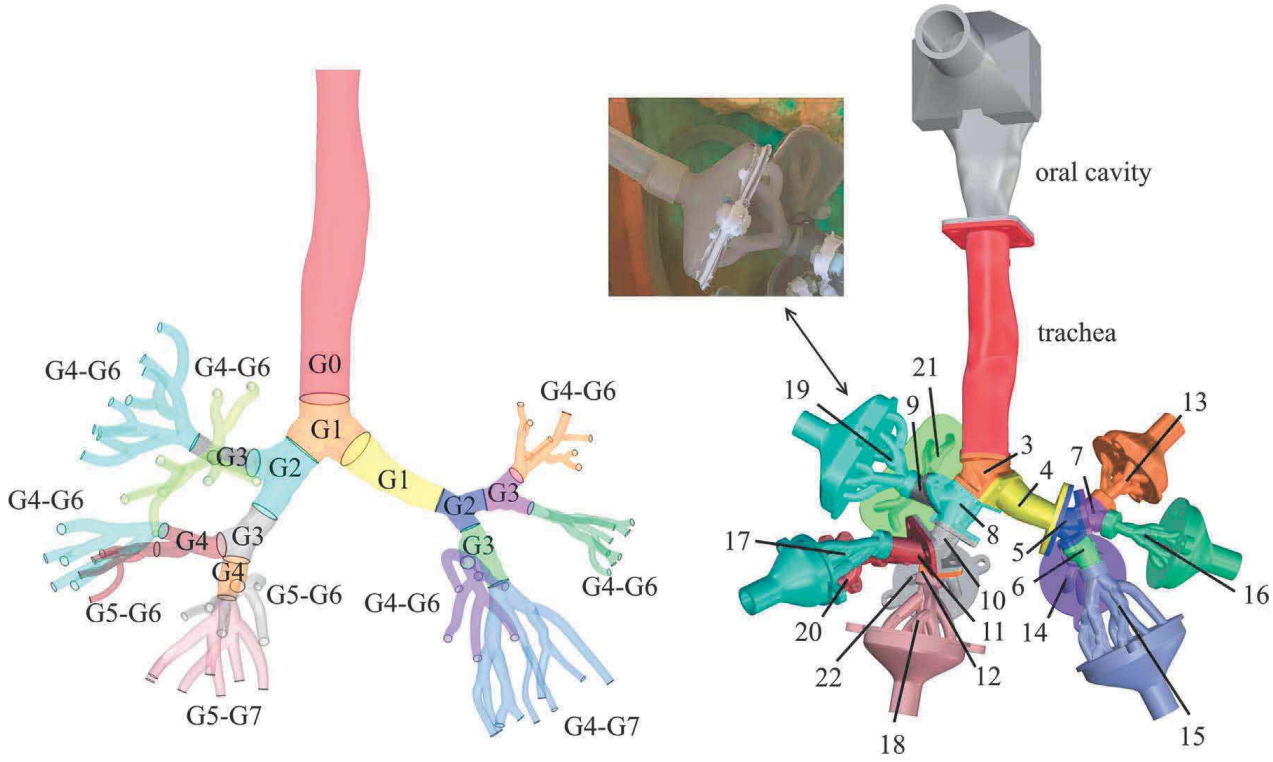

Fig. 1. The geometry of respiratory airways with generations of bronchial branching for individual segments (left); segmented replica for deposition experiments (right) with the photo of connection to the rest of the experimental setup.

2. Experimental setup

2.1. Replica of respiratory airways

A realistic replica of the human airways from the oral cavity to the 7th bronchial generation (Fig. 1) was developed by Lizal et al. (2012). The oral cavity was chosen because it is the predominant way of breathing during light or heavy work (Cheng, Zhou, & Chen, 1999). The geometry of the replica originates from two sources. The bronchial tree is based on the reference model of Schmidt et al. (2004), which was derived from CT images of a male adult free from pathological alterations. The oral cavity was acquired from the Lovelace Respiratory Research Institute (Albuquerque, NM, USA, Cheng, Cheng, Yeh, & Swift, 1997). These two geometries were converted into the stereolithographic format (STL) and imported into the software package Rhinoceros 4.0 (McNeel, Seattle, WA, USA). The program connected the geometries and a 3 mm-thick envelope was added on the top of the final geometry to permit the manufacture of a replica suitable for experimental studies. The geometry was divided into individual segments to facilitate regional deposition measurements. Flanges with screw or bayonet joints were created between the segments to allow easy assembly and disassembly of the replica.

The replica consisted of 32 segments, and the numbering of the segments increases from the top to the bottom starting with the oral cavity as number 1 and the trachea as number 2. The upper respiratory airways and a few bifurcations with relatively large dimensions were isolated into individual segments. The branches from the 4th to 7th generation, which have smaller airway dimensions, were combined into complex multigenerational segments numbered from 13 to 22. Following these complex segments, ten output segments with “funnel-like” shapes numbered from 23 to 32 were created to facilitate connection of the replica to the rest of

Table 1
Comparison of model geometries (Lizal et al., 2012).

Generation number	Present model Diameter (mm)		Weibel Diameter (mm)		Zhou and Cheng (cast A) Diameter (mm)	
	Left	Right	Left	Right	Left	Right
Trachea 0	16.3		18		15.8	
1	10.2	12.6	12.2		7.1	12.3
2	6.5	8.3	8.3		6.0	7.8
3	5.6	5.9	5.6		5.9	6.5
4	3.8	4.4	4.4			5.6
5	2.8	3.9	3.5			

the experimental setup. The summary of diameters in given airway generations together as well as comparison with other replica geometries (Weibel, 1963; Zhou & Cheng, 2005) are given in Table 1.

The replica was manufactured on a Viper Si2 stereolithographic prototyping system (3D Systems, Rock Hill, SC) using WaterShed XC 11122 (DSM, Heerlen, the Netherlands). The layer thickness was 25 μm and the accuracy of the build was 7.6 μm. Since the replica consisted of multiple segments, leak tests were performed prior to each experiment. Leaks, mostly between flanges, were sealed with a small layer of silicone sealant. Silicon oil (550 Fluid, Dow Corning) was carefully applied to the inner walls of the replica to prevent resuspension of deposited fibers and to simulate the mucus layer (Su & Cheng, 2015; Zhou, Xi, Simpson, Irshad, & Cheng, 2013). The replica was filled with silicone oil and then dried for sufficient time (approximately 12 h) to produce a thin wall layer. Thus, all inner surfaces were covered with silicone.

2.2. Experimental setup

Fiber generation and classification was performed with the system described by Wang et al. (2005). The methodology for fiber production was the same as that of Wang, Hopke, Ahmadi, Cheng, & Baron (2008). Glass wool (Johns Manville JM 100/475) was crushed and sieved to produce glass fibers with a density of 2.56 g/cm^3 and fiber diameter of 1.03 ± 0.45. The fibers were mixed with glass beads (Ballotini Impact Beads, Potters Industries Inc.). The mixture of fibers and glass beads was loaded into a hopper connected to a fiber generator via a rotary feeder (Fig. 2). The rotary feeder speed determined the number of generated and subsequently classified fibers. The fiber generator used a high-speed orbital shaker.

Airstream A_1 at 20 °C, which had passed through a humidifier to produce a relative humidity of 40%, delivered polydisperse fibers from the fiber generator into an aging chamber. The chamber was 9 cm-wide, 90 cm-long, and provided a sufficient contact time between the fibers and air humidity. The chamber also damped flow pulsations from reaching the classifier. Polonium 210 ionizers (Staticmaster, Amstat Industries, USA) were used to produce charge equilibrium on the particles before entering the classifier.

The classifier works on the principle of dielectrophoretic separation (Lipowicz & Yeh, 1989) and has been described elsewhere (Baron, Deye, & Fernback, 1994; Deye, Gao, Baron, & Fernback, 1999). The classifier consists of two concentric cylinders. The outer cylinder was grounded and the inner one was connected to a high voltage AC generator oscillating between ± 4 kV at 50 Hz. The

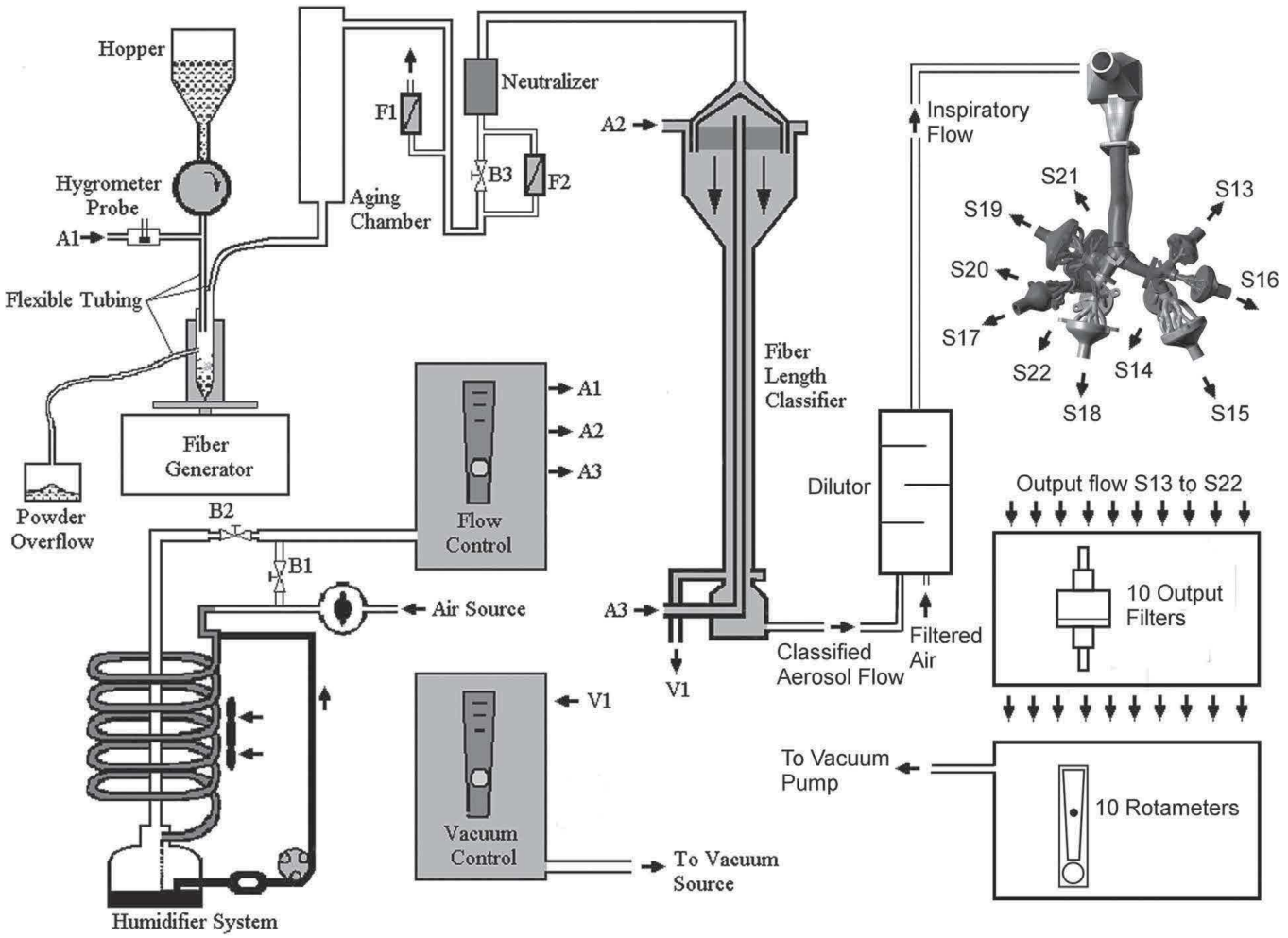

Fig. 2. The experimental setup, which includes the fiber generator, the classifier, the replica of respiratory airways, etc., modified with permission from Wang et al. (2005).

Table 2
Flow rates through the classifier.

Airstream name	Sheath flow A_2	Sheath flow A_3	Fiber flow A_1	Dump flow V_1	Classified Aerosol flow
Flow rate (LPM)	4	4	1	8	1

alternating electric field eliminates electrophoresis, which is dependent on electric field polarity. The separated dipolar charges induced within neutral particles flowing through the classifier permit them to move toward the inner electrode by dielectrophoresis.

A fiber-laden flow was introduced at the top of the classifier surrounded by clean humidified sheath flows A_2 and A_3. The classifier dimensions were such that the velocities of all flows were the same and the flow through the classifier was laminar. The flow was split at the bottom of the classifier to the classified aerosol flow containing classified fibers, and the dump flow V_1 with the rest of the fibers. The flow rates were checked by rotameters (Cole-Palmers, IL, USA). The flow values can be found in Table 2.

The classified aerosol flow continued to a dilutor where it was mixed with filtered air to produce the desired inspiratory flow rate through the replica (Fig. 2). The inspiratory flow rates of 15, 30, and 50 LPM were used to simulate steady inhalation for people under normal, light, and heavy activity, respectively. The flow through the replica was induced by a vacuum pump situated below the replica. The flow distribution through the individual branches was accomplished by adding rotameters with regulated valves between the replica and the vacuum pump. The flow was split between the left and the right lung with a ratio of 30:70; the flow rates through the individual segments of the replica can be found in Table 3 together with various segment characteristics. Since the flow rates were set for the outlet segments, the flow rates for the rest of the replica were calculated using Fig. 1. The flow distribution comes from prior measurements.

The replica was exposed to fibers for 4 h. Since this replica did not include the entire lungs, some fibers passed through the replica and were collected on output filters (AAWP02500 nitrocellulose membrane filters, Merck Millipore). The output filters were changed every 30 min to prevent overfilling. Three experiments were performed under each flow rate condition to allow calculation of statistical errors, such as standard deviations.

2.3. Sample preparation

Phase contrast microscopy was used for the sample analysis (Su & Cheng, 2005; Wang, Hopke, Ahmadi, Cheng, & Baron, 2008). The fibers deposited in the replica needed to be transferred to filters (AAWP02500 nitrocellulose membrane filters, Merck Millipore) to permit counting. The replica was disassembled and each segment was put into a beaker with isopropanol (2-propanol, Fisher Scientific). The beaker with a segment was inserted into an ultrasonic bath and sonicated for one minute to release the fibers from the replica into the isopropanol. The resulting suspension was filtered through a membrane filter using a vacuum filtration unit. The filters were placed in a desiccator to dry. Dry filters were placed on glass microscope slides and made transparent using an acetone vaporizer (QuickFix, EMS, USA). Each segment was rinsed twice. The quantity of extracted fibers in the second rinse was negligible so

Table 3
Airway segment characteristics.

Segment number	Flow rate (LPM)			Airway generation	Surface area (cm^2)
1	15	30	50	Oral cavity	174.2
2	15	30	50	G0	60.2
3	15	30	50	G1	9.7
4	4.5	8.9	14.8	G1	9.2
5	4.5	8.9	14.8	G2	3.6
6	2.8	5.6	9.3	G3	5.7
7	1.7	3.3	5.5	G3	4.0
8	10.6	21.1	35.2	G2	8.6
9	3.4	6.9	11.4	G3	6.0
10	7.1	14.3	23.8	G3	4.9
11	3.3	6.7	11.1	G4	6.1
12	3.8	7.6	12.7	G4	4.1
13	0.7	1.4	2.3	G4–G6	10.1
14	0.8	1.6	2.7	G4–G6	16.1
15	2.0	4.0	6.7	G4–G7	25.2
16	1.0	1.9	3.2	G4–G6	10.7
17	1.8	3.6	5.9	G5–G6	14.4
18	2.3	4.7	7.8	G5–G7	17.7
19	1.9	3.8	6.3	G4–G6	21.9
20	1.6	3.1	5.2	G4–G6	5.9
21	1.5	3.1	5.1	G4–G6	21.0
22	1.5	3.0	4.9	G5–G6	10.6
Inspiratory flow rate (LPM)	15	30	50		

this step was discontinued. The output filters were made transparent using the same procedure and all the filters were stored in filter boxes.

2.4. Sample analysis

An automatic image analysis method was employed to speed up the analysis, make it more convenient and more reproducible. A monochrome camera Atik 314E (Atik cameras, Norwich, UK) was attached to a microscope Nikon Eclipse E200 (Nikon, Tokyo, Japan) to take images of the filters. Twenty images of each filter were taken. As only a part of each filter was inspected this way, the counted numbers of fibers were then increased proportionally to account for the entire filter area. The images were analyzed with an in-house software Fiber Analyzer, which is able to identify and count fibers in filter images following the methodology for manual counting NIOSH 7400 (Belka et al., 2016). The image analysis is based on the use of a histogram equalization and adaptive radial convolution filtering. The steps of the image analysis process are depicted in the Supplementary material (Fig. S1). These steps enhance particle contrasts and facilitate their identification during segmentation. The software identifies particles present in the image (fibers, dust, etc.) and calculates their sizes and other characteristics describing the particle shapes, such as area, perimeter, moments, elongation, shape factor etc. These characteristics are used to exclude non-fibrous particles from the final selection. Therefore, only fibers fulfilling the specifications are counted. Although the software uses various steps to count fibers properly, images with particularly high numbers of non-fibrous particles tend to bias the final fiber counts since the dust and other particles can resemble fibers.

The output filters (majority of the filters) contained a low amount of non-fibrous particles and were suitable for automatic analysis by the software. However, the filters created by rinsing of the replica parts contained many non-fibrous particles. The debris may have been produced by sonication of the replica segments releasing small pieces of its material into the isopropanol together with the fibers. Dust may have also deposited on the outside of the replica during the experiments and may have been released into the isopropanol solution while rinsing the segments. Therefore, the filters created by rinsing of the replica were analyzed manually by an analyst.

The software used for the output filters was validated by manual counting. Fibers in two hundred images were counted manually and with the software. The results were compared using the Paired Sample T-test in the software Origin 9 (OriginLab Corporation, MA, USA). It was shown that the differences between the fiber counts were statistically significant at the level of significance of 0.05. The fiber counts given by the software were slightly lower than those resulting from manual counting executed by an analyst. Some fibers, such as fibers in fiber bundles, were split up into smaller groups and these were subsequently identified as small particles. These fibers were excluded from the selection. Therefore, the software fiber counts were underestimated. That is the reason for which a linear regression model was used to determine the relationship between the automated and manual counts. A very good fit was found with coefficient of determination (R^2) of 0.997 (Fig. S2). Therefore, the results from the software were recalculated using Eq. (1):

$$Correct\ fiber\ count = 1.11 \cdot fiber\ count\ given\ by\ the\ software. \tag{1}$$

2.5. Calculation of local deposition

Fiber numbers were used to calculate deposition parameters, such as deposition efficiency or deposition fraction, in different parts of the replica. Deposition efficiency (DE) and deposition fraction (DF) can be expressed using Eqs. (2) and (3), respectively:

$$DE = \frac{number\ of\ deposited\ fibers\ in\ a\ specific\ region}{number\ of\ fibers\ entering\ this\ region}, \tag{2}$$

$$DF = \frac{number\ of\ deposited\ fibers\ in\ a\ specific\ region}{number\ of\ fibers\ entering\ the\ oral\ airways}. \tag{3}$$

The branching in the tracheobronchial tree and alveolar region is asymmetric. Consequently, airways dimensions, such as airway length or diameter, differ among subjects. Since the deposition fraction is dependent on the dimensions of the specific deposition region, Hofmann, Winkler-Heil, and Balashazy (2006) propose using deposition density. The deposition density is the ratio of deposition fraction to the relevant surface area and is expressed in units of cm^{-2}. To predict a particle dose per surface area, the deposition density is multiplied by the number of inhaled particles and expressed in units of particles/cm^2. The deposition density for a given segment of the replica was calculated using Eq. (4).

$$DD = \frac{deposition\ fraction}{surface\ area\ of\ the\ given\ airway\ segment}, \tag{4}$$

In upper respiratory airways, deposition is driven largely by impaction, and many empirical equations for prediction of deposition have been reported (Cheng et al., 1999; Grgic, Finlay, Burnell, & Heenan, 2004; Stahlhofen, Rudolf, & James, 1989). These equations often contain the impaction parameter $d_{ae}^2 Q$, where Q denotes the flow rate in the given respiratory segment, and d_{ae} is particle aerodynamic equivalent diameter. The aerodynamic diameter of a fiber can be calculated by Eq. (5) given by Stöber (1972) while neglecting the slip correction:

$$d_{ae} = d_{ve}\cdot\left(\frac{\rho_p}{\rho_0\cdot\chi}\right)^{\frac{1}{2}}, \tag{5}$$

where d_{ve} is a volume equivalent diameter, ρ_p is fiber density, ρ_0 is density of water and χ denotes a dynamic shape factor. This correction factor accounts for the effect of shape on the particle motion and is affected by particle properties and its orientation in a flow field. For simplification, the dynamic shape factor of a fiber can be approximated by a dynamic shape factor of a prolate spheroid. It can be calculated for a prolate spheroid moving with its main axis parallel, perpendicular, or randomly oriented to a flow field using Eqs. (6)–(8) (Baron & Willeke, 2001), respectively.

$$\chi_{\parallel} = \frac{\frac{4}{3}(\beta^2-1)\beta^{-\frac{1}{3}}}{((2\beta^2-1)/\sqrt{\beta^2-1})\ln(\beta+\sqrt{\beta^2-1})-\beta}, \tag{6}$$

$$\chi_{\perp} = \frac{\frac{8}{3}(\beta^2-1)\beta^{-\frac{1}{3}}}{((2\beta^2-3)/\sqrt{\beta^2-1})\ln(\beta+\sqrt{\beta^2-1})+\beta}, \tag{7}$$

$$\frac{1}{\chi_r} = \frac{1}{3\chi_{\parallel}} + \frac{2}{3\chi_{\perp}}, \tag{8}$$

where β is a fiber aspect ratio.

Many empirical models use the Stokes number to predict deposition. The Stokes number is a more appropriate metric since it contains information regarding the respiratory airway geometry. This feature is important because lung geometry is one of the factors strongly affecting particle deposition (Hofmann, 2011). The Stokes number is given by:

$$Stk = \frac{\rho_0\cdot d_{ae}^2\cdot U_i}{18\cdot\mu\cdot D_i}, \tag{9}$$

where U_i is an equivalent mean velocity in the given airway, μ is dynamic air viscosity, and D_i defines an equivalent mean diameter of the given airway.

The mean velocity in the oral cavity ($U_i = 4Q/\pi D_{mean}^2$) and the equivalent mean diameter ($D_i = 2^*(V/\pi L)^{0.5}$, where V is the volume of the oral cavity and L is length of the centerline path from mouth to throat) were used to calculate the Stokes number for the segment 1, i.e. the oral cavity (Grgic et al., 2004; Su & Cheng, 2009). When calculating the Stokes number for particles flowing through the tracheobronchial tree, U_i represents the mean velocity in the trachea (segment 2) or the parent airway of the bifurcation (segment 3–12), and D_i is the mean diameter of the trachea or parent airway of the bifurcation (Zhou & Cheng, 2005). When calculating the Stokes number for aerosol flowing through the segment with multiple generations (segments 13–22), an output equivalent diameter was first calculated as an average of all output cross–sections from the given segment. Then, the average of input airway diameter and the output equivalent diameter were used as a mean diameter D_i. The mean velocity U_i in the given segment was calculated as the flow rate through the segment divided by its mean diameter D_i.

3. Results and discussion

The fiber quantities for various regions of the respiratory tract replica were used to calculate deposition characteristics, such as deposition fraction, density, or efficiency. The results of this study were then compared to those of Su and Cheng (2009, 2015), Myojo and Takaya (2001), and Zhou et al. (2007).

3.1. Fiber lengths

The length distributions for all experiments were measured and mean lengths together with standard deviations are presented in Table 4. The length distributions differed slightly for some experiments and are shown in Fig. S3. These differences were caused by the apparatus, which had to be readjusted prior to every experiment, or whenever a new batch of fibers was prepared. However, fiber lengths were important only for the calculation of aerodynamic diameter. The aerodynamic diameter was determined primarily by fiber diameter rather than length. Changes in fiber length resulted in negligible changes in the aerodynamic diameter for randomly oriented fibers as calculated with Eqs. (5)–(8). The fiber diameter was 1.03 ± 0.45 μm and the fiber density was 2.56 g/cm^3.

Table 4
Fiber dimensions and aerodynamic diameters during the experiments.

Inspiratory flow rate	15 LPM			30 LPM			50 LPM		
Run	1	2	3	1	2	3	1	2	3
Mean diameter					1.03 ± 0.45				
Mean length (μm)	17 ± 3.6	17 ± 3.2	20.9 ± 4.5	21.7 ± 6.3	21.2 ± 6.5	19.2 ± 5.1	22.1 ± 5.9	23.2 ± 6.7	27 ± 9.2
Aerodynamic diameter (μm)	3.4	3.4	3.5	3.6	3.5	3.6	3.6	3.6	3.7

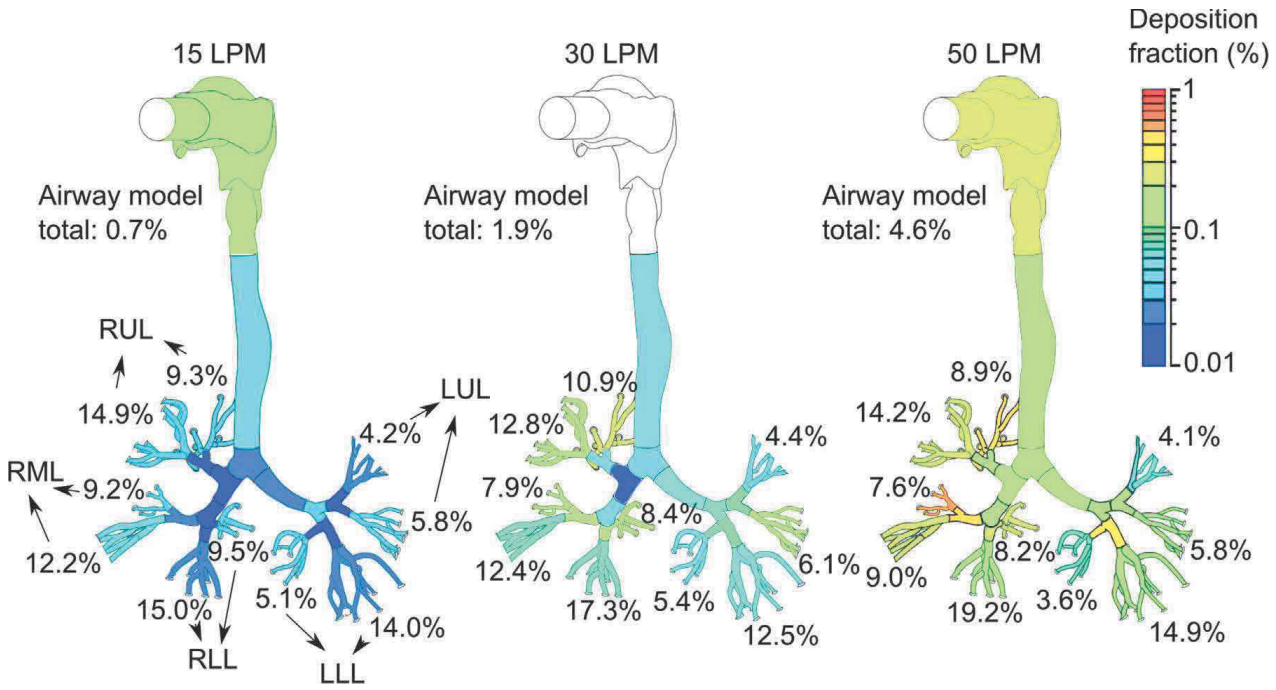

Fig. 3. Regional deposition fractions in the replica as a function of flow rate; the values around the replica represent deposition fractions in the parts of the experimental setup downstream of the replica (the funnel-shaped output segments, the tubing, and the filters); the data for the oral cavity during 30 LPM study were excluded from the analysis.

3.2. Deposition fractions and densities

The deposition fraction represents an initial dose of inhaled aerosol, which deposits at the given site. This dose is important to assess the potential hazards (Hinds, 1999). A fractional deposition was calculated for every segment of the replica. The regional deposition fractions in the replica for the measured flow rates are shown in Fig. 3. The graph with deposition fractions as a function of segment number can be found in the Supplementary Material (Fig. S4). Deposition fractions at the replica outlets represent fractional depositions in the parts of the experimental setup downstream of the replica, i.e. funnel-like shaped segments, tubing and filters. Fibers deposited in these parts of the experimental setup penetrated the replica and would continue deeper into the lung. Only a few fibers actually deposited in the replica. The deposition fraction increased with an increasing flow rate, and the total deposition fractions in the replica were 0.7%, 1.9% and 4.6% for the inspiratory flow rates of 15, 30, and 50 LPM, respectively. A slightly higher deposition fraction was detected in the oral cavity and in the complex segments. Moreover, segments in the right lung that encompassed a bifurcation in the fourth generation (segments 11 and 12) had a noticeably higher deposition fraction for higher inspiratory flow rates. By contrast, the complex segments downstream of the segments 11 and 12 had lower deposition fraction for higher inspiratory flow rate. This result indicated the role of impaction as the fibers were not able to follow streamlines into these complex segments and deposited near the carinal ridges.

Deposition densities in the replica for the measured flow rates are depicted in Fig. 4. The graph of deposition densities as a function of segment number can be found in the Supplementary Material (Fig. S5). If the effect of segment size is accounted for, the lowest deposition density can be observed in the first two segments including the oral cavity, oropharynx, larynx, and trachea. The deposition densities in the complex segments were lower compared to the rest of the replica. The exception was segment 20 that contains several small length generations so their surface areas were very small.

The replica has a realistic geometry with irregular dichotomy, i.e. every branch in tracheobronchial tree divides into two smaller daughter branches differing in length and diameter. Weibel (1963) defined the number of these divisions, or the so-called generations, that are similar across the population. Therefore, if the prediction of deposition is extrapolated to the population and not to the individual person, it is more convenient to consider deposition to be a function of airway generation. The deposition fraction and density as a function of airway generation are presented in Fig. S6. The deposited fiber dose increased with an increasing airway generation number and inspiratory flow rate. Clearly, the deposition of fibers was driven primarily by impaction. The increasing velocity (flow rate) and decreasing airway dimensions (increasing airway generation number) made it more difficult for the fibers to follow the air streamlines. Our replica has only two separate bifurcations in the 4th generation and it was difficult to extract deposition information for the individual generations in the complex multigenerational segments.

3.3. Deposition efficiency in the oral airways

Deposition efficiency as opposed to deposition fraction describes the ability of a given airway region to collect particles. The upper respiratory tract removes foreign particles from the flow. Generally, particle penetration through the nasal airways is lower than that

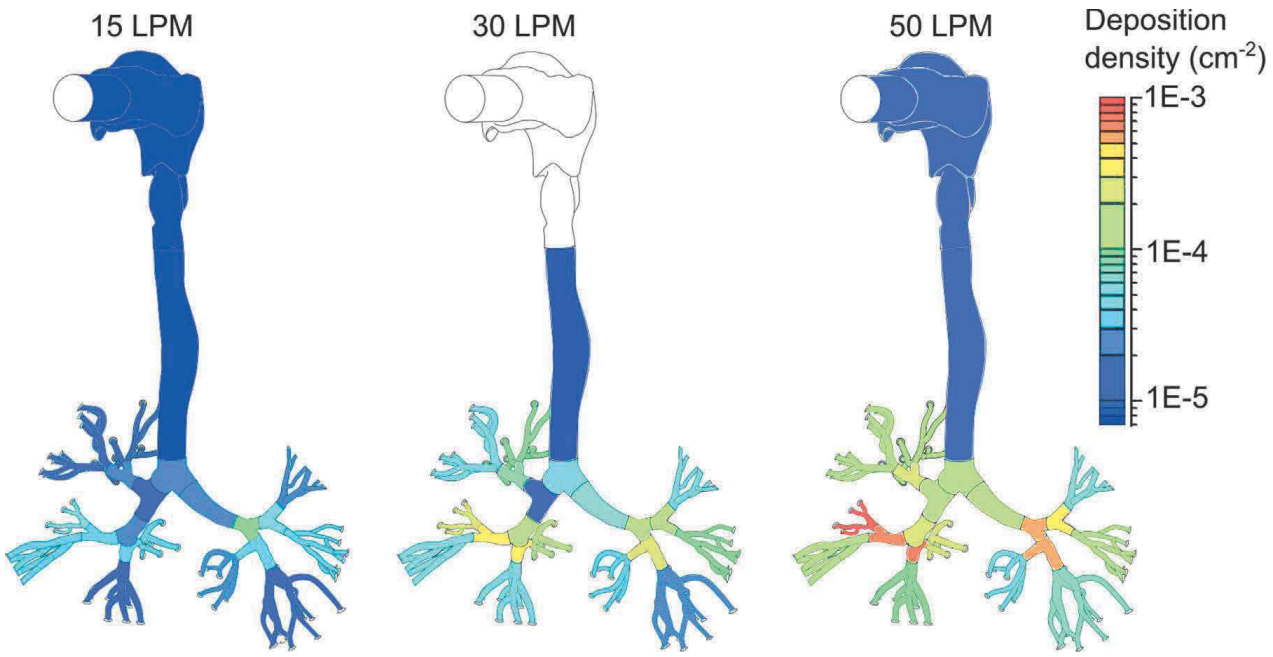

Fig. 4. Deposition densities in the replica as a function of flow rate.

of the oral airways (Ruzer & Harley, 2013). However, resistance to flow through the nasal airways is higher. Therefore, most people switch to oral breathing during work or heavy exercise (Cheng, Su, Yeh, & Swift, 1993). To penetrate the oral cavity, particles need to avoid the tongue and undergo a 90° bend to the pharynx/larynx area. The flow becomes turbulent after the constriction caused by the soft palate. These turbulence levels are reduced afterwards and enhanced again in the glottis (Kleinstreuer & Zhang, 2003).

The deposition efficiency in the oral cavity as a function of impaction parameter is shown in Fig. 5 and compared to the results of Su and Cheng (2015) (nanotubes and spherical particles were excluded). Only the 15 and 50 LPM results for the current replica are shown. The deposition at 30 LPM was excluded because parts of the replica wall were released into isopropanol together with the fibers. This debris obscured the fibers on the filters leading to an underestimation of the fiber quantities. This problem only existed for the oral cavity because it was the largest segment with the highest quantity of released debris. The deposition experiments for 30 LPM were performed first, using filters with diameter of 25 mm. Larger filters, 50 mm in diameter, reduced the problem for the

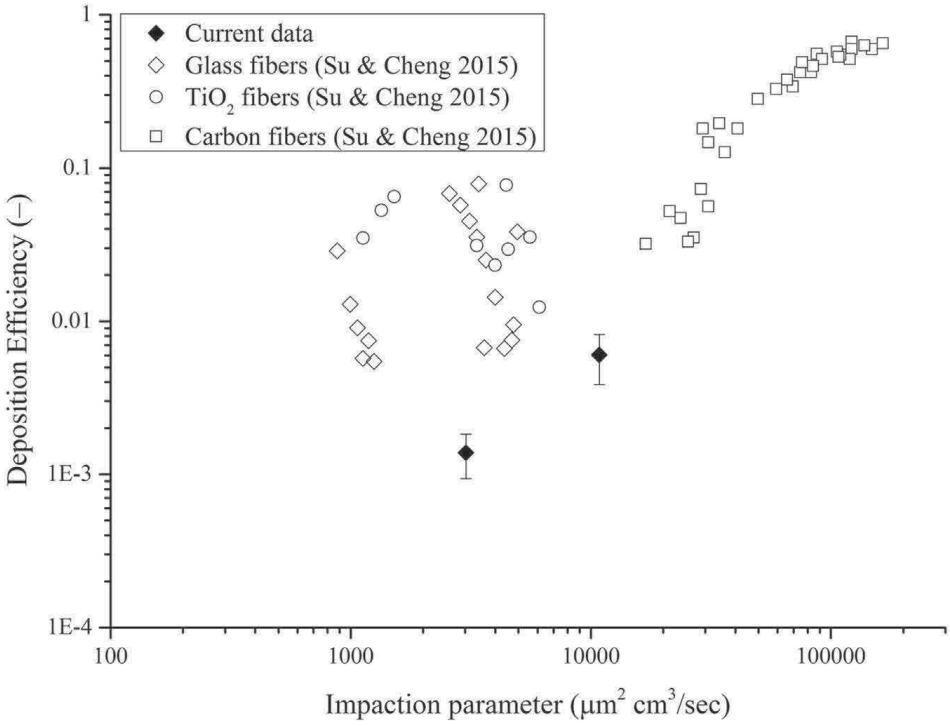

Fig. 5. Deposition efficiency in the oral airway as a function of impaction parameter; the error bars represent standard deviations.

experiments with inspiration flow rates of 15 and 50 LPM. Given financial and time limitations, it was not possible to repeat the experiments at 30 LPM using the larger filters.

In general, the deposition efficiencies in the oral cavity were less than 1% even for the highest flow rate. Thus, most fibers penetrated through the oral airways and would likely deposit in lower airways even during heavy activity. The deposition efficiency increased with increasing impaction parameter indicating impaction as the dominant deposition mechanism. The deposition efficiencies observed in the current respiratory airway replica are lower than those measured by Su and Cheng (2015). Although the replicas were manufactured by different methods, the effect of surface roughness or material was expected to be negligible since the inner walls were covered with a silicon oil. The problem with released debris during sonication could be responsible for the discrepancy. Small portions of the filters were obscured by the debris and some of the fibers could remain hidden and hence undetected despite the use of larger filters. Therefore, the current deposition data for the oral cavity should be considered as a lower bound estimate.

3.4. Deposition efficiencies in the tracheobronchial airways

After passage through oral airways, the fibers enter the trachea through the larynx. Martonen, Zhang, and Lessmann (1993) reported that the flow in the trachea and subsequent generation of branching is strongly influenced by the complicated larynx geometry. This geometry, particularly the restriction of vocal cords, enhances local turbulence levels and creates the so-called laryngeal jet of accelerated particles. This jet is shifted to the back side of trachea in our geometry (Elcner, Lizal, Jedelsky, Jicha, & Chovancova, 2016) increasing deposition of large (> 1 μm) particles. The jet effect is reduced throughout the trachea and it is not noticeable beyond the first generation (Lin, Tawhai, McLennan, & Hoffman, 2007). However, the flow disturbances may be enhanced by bifurcations.

Fiber deposition efficiencies in the trachea and in the first generation as a function of Stokes number are presented in Fig. 6. The measured data were compared with those reported by Su and Cheng (2009) (casts A and B). It can be seen that the deposition efficiency in both regions increased with the increasing Stokes number indicating the important role of impaction. The measured data were in good agreement with the literature results.

Empirical models were suggested to relate an average Stokes number in each given region to the average deposition efficiency in that region. Chan and Schreck (1980) proposed a model for prediction of deposition in the trachea

$$DE_{trachea} = a \cdot Stk^{b}, \tag{10}$$

where a and b are constants. Kim and Fisher (1999) proposed an empirical model for predicting deposition in bifurcations using sequentially bifurcating tube models. A modified logistic function was suggested.

$$DE_{gen.\ number} = 1 - \frac{1}{a \cdot Stk^{b} + 1}, \tag{11}$$

where a and b are constants. Su and Cheng (2009) employed these models and found the best fits for deposition in the trachea (a = 0.67, b = 0.89) and the first generation (a = 4.2, b = 1.4). As seen in Fig. 6, the current data showed a slightly lower deposition efficiency compared to the reported data. Moreover, the proposed models slightly overestimated the deposition for low Stokes numbers.

Turbulence levels caused by the larynx are reduced throughout the trachea. However, they are enhanced again at bifurcations. Therefore, the turbulence can persist into the first few generation branches even at low Reynolds numbers (Zhang & Kleinstreuer, 2004). Velocity patterns are complicated and are influenced by the upstream flows and secondary vortices appearing in daughter

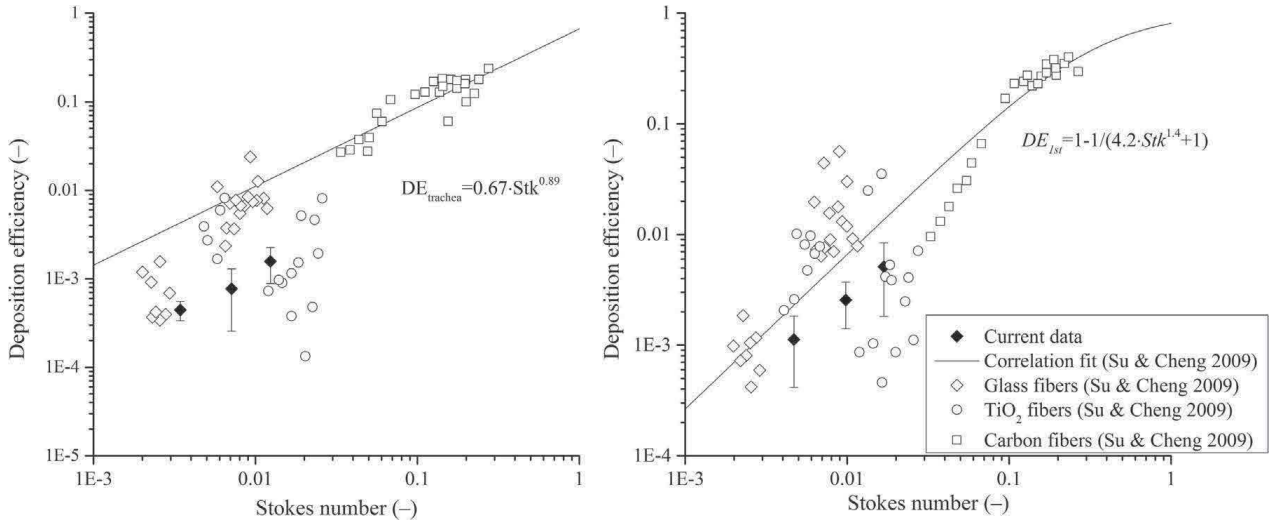

Fig. 6. Deposition efficiency in the trachea (left) and 1st generation (right) as a function of Stokes number; the error bars represent standard deviations.

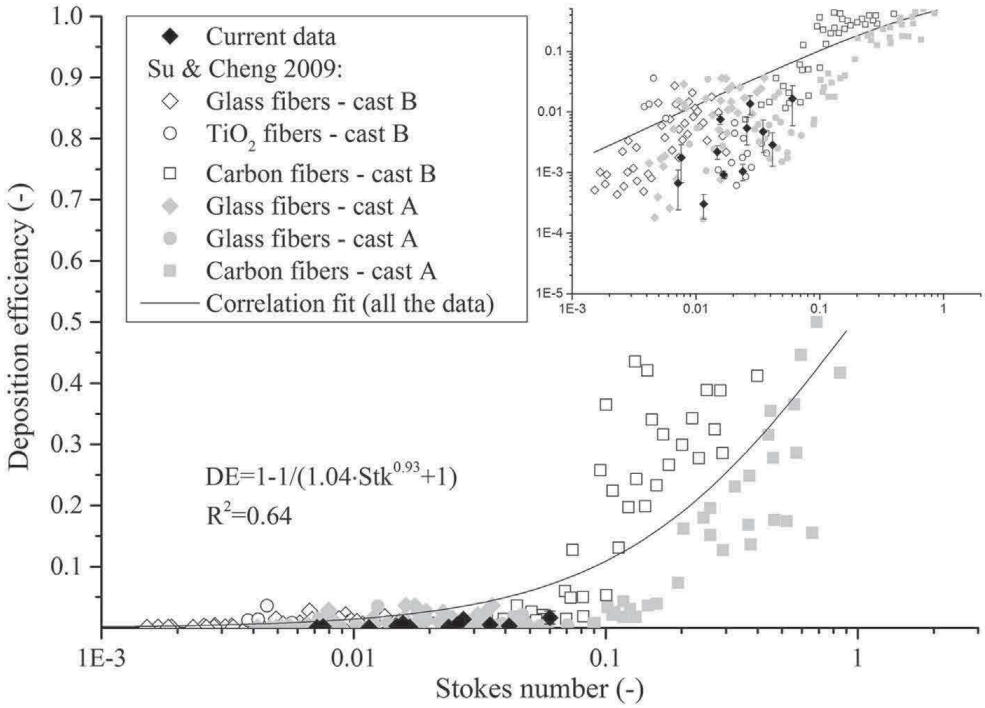

Fig. 7. Deposition efficiency in the 3rd generation as a function of Stokes number; the error bars represent standard deviations.

branches. The particles tend to deposit on the carinal ridges by impaction and near the carinas because of secondary flows (Kleinstreuer, Zhang, & Li, 2008).

Deposition efficiency in the 3rd generation is shown in Fig. 7. Deposition efficiency in the 2nd generation is presented in Fig. S7. The graphs are displayed with both linear and logarithmic scales. The trend was the same as in the previous cases; deposition efficiency increased as the Stokes number increased. Good agreement between the current and previously reported results was observed. However, there was significant variability. Differences were observed when comparing among the different geometries or different branches in any specific generation of a given geometry. These differences can be caused by the dependence of the flow on the upstream velocity fields and geometry. Local geometric features could influence the airflow, such as velocity patterns, magnitudes

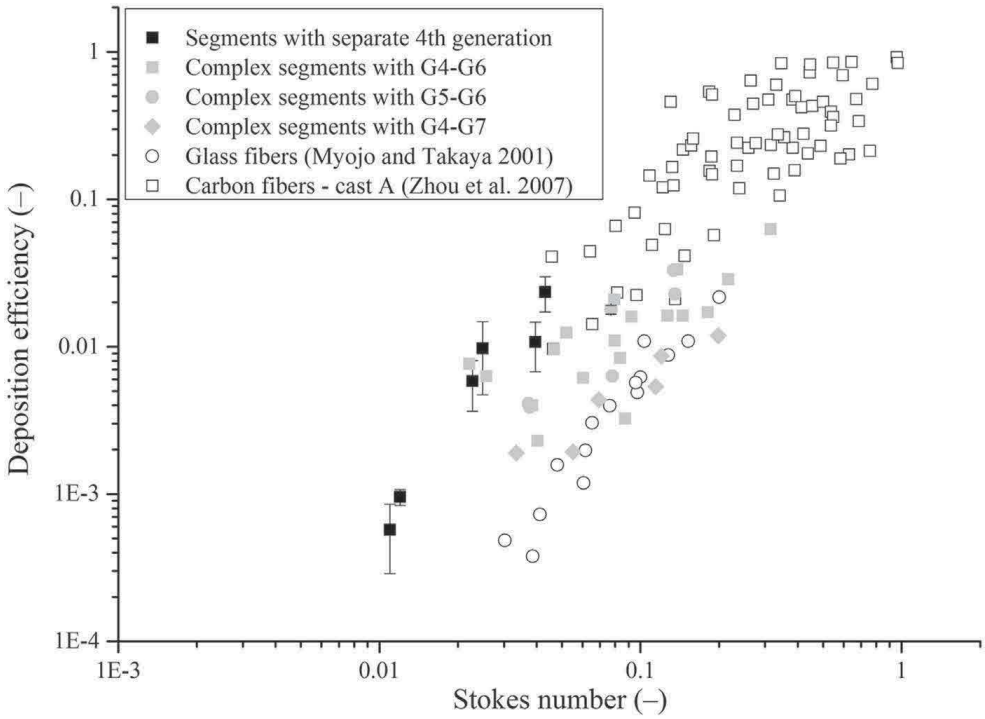

Fig. 8. Deposition efficiency in the 4th to 7th generation as a function of Stokes number; the error bars represent standard deviations.

and local turbulence structures, which are induced by the sequential airway branching resulting in different deposition patterns at specific locations or branches in the same generation.

Although the deposition data in the 2nd and 3rd generation showed large variations and were difficult to interpret, the empirical model suggested by Kim and Fisher (1999) was employed to obtain the empirical equations. OriginPro 9 (OriginLab Corporation, MA, USA) was used to obtain the best curve fit ($a_2 = 0.35$, $b_2 = 0.68$, $a_3 = 1.04$ and $b_3 = 0.93$). Fig. 7 shows that the empirical curve overestimated the deposition for low Stokes numbers (Stk < 0.1). This discrepancy was caused by a large variation of deposition efficiency for high Stokes numbers. Therefore, it would be useful to acquire more deposition data using high momentum fibers.

In the medium-sized airways, such as the 4th or the 6th generations, the flow becomes laminar, but it is still not fully developed. Zhang et al. (2008) numerically investigated the airflow in the tracheobronchial tree made of symmetric triple-bifurcation units down to the 16th generation. They showed that the flow patterns around the 6th generation were still skewed and the secondary flows were very strong.

Deposition in the 4th to 7th generation in the current respiratory airway replica can be seen in Fig. 8. The 4th generation was incomplete and included only two bifurcations which were assumed to represent all the bifurcations in the 4th generation. The deposition efficiency increased with the increasing Stokes number even in the 4th generation. The measured data were also compared with the results of Myojo and Takaya (2001) and Zhou et al. (2007). Zhou et al. (2007) presented deposition of carbon fibers with a higher Stokes number than those in our study. However, our data followed the same trend. The deposition efficiencies reported by Myojo and Takaya (2001) were lower compared to the other studies. The deposition was measured in only one idealized bifurcation in their study. The smooth idealized walls together with the absence of upstream flow history likely caused the lower fiber deposition.

The other bifurcations in the 4th generation were part of the complex segments that extended down to the 6th or 7th generation. It was not possible to extract deposition per generation in these segments. Therefore, deposition efficiency for several generations as a function of average Stokes number is shown in Fig. 8. Substantial variability was reported in the complex segments that included the same airway generations. This result indicated that the deposition was influenced by the upstream velocity fields and the individual segment geometry. The deposition efficiencies increased with increasing Stokes number, however, the increase was not that significant as in the case of more proximal generations. This result could be caused by the diminishing effect of impaction with increasing generation number. However, the use of average Stokes number is not ideal for this analysis and comparison with CFD results could provide additional insights.

3.5. Deposition of fibers and spherical particles

Deposition of fibers was compared to that of spherical particles. Lizal et al. (2015) carried out deposition experiments with radioactive spherical particles using the same airway replica. The Stokes numbers for the spherical particles were calculated using Eq. (9). The linear empirical model of Chan and Lippmann (1980) was also applied to the spherical particles data, and the fits for the data from first four generations were calculated. The same empirical model was used to calculate the fits for the fibrous particles. The

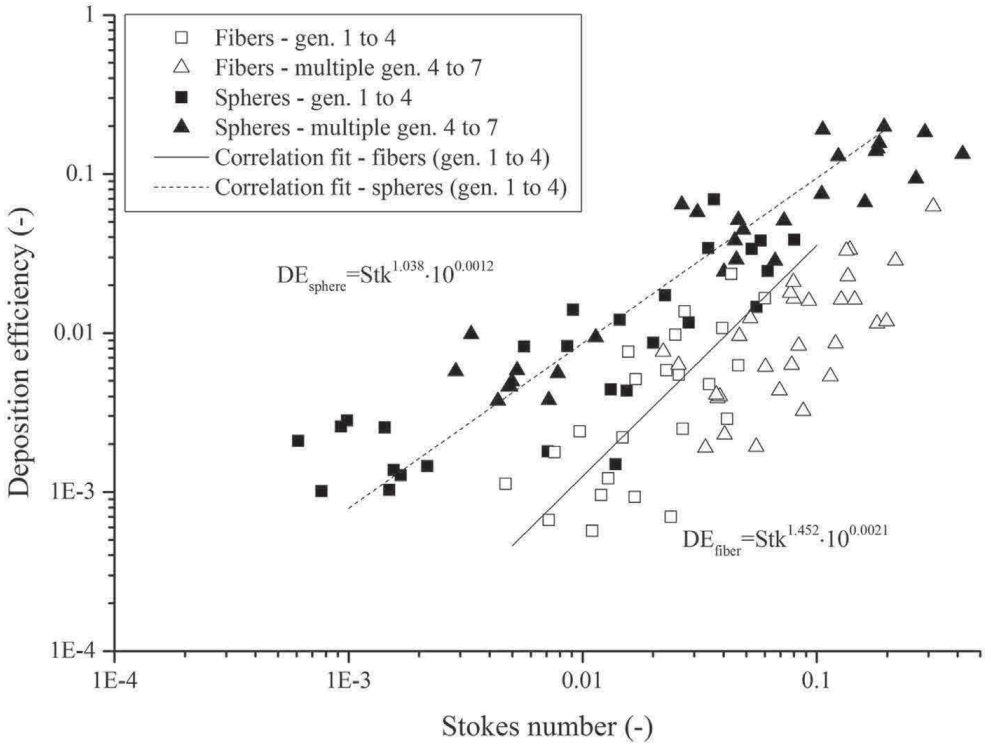

Fig. 9. Deposition efficiency of fibrous and spherical particles as a function of Stokes number.

deposition in the replicas was represented by Eqs. (12) (R^2 = 0.97) and (13) (R^2 = 0.98), respectively.

$$DE_{spheres} = Stk^{1.038} \cdot 10^{0.0012}, \quad (12)$$

$$DE_{fibers} = Stk^{1.452} \cdot 10^{0.0021}. \quad (13)$$

A comparison of particle deposition in the tracheobronchial tree together with the correlations are presented in Fig. 9. Deposition of both particle types was driven by impaction since the deposition efficiency increased with the increasing Stokes number. Generally, deposition efficiency is higher for spherical particles than for the fibers having the same Stokes number. This result can be caused by the ability of fibers to align themselves with the airflow.

4. Conclusions

Deposition measurements of length classified glass fibers in a realistic human airway replica were performed. In-house software was employed to analyze filters from the experiments and speed up the process. Deposition characteristics in various regions of the replica were investigated with respect to the inspiratory flow rate afterwards.

It was found that the deposition fraction increased with increasing inspiratory flow rate. However, the total deposition fraction in the replica did not exceed 5% implying that the vast majority of fibers passed through the replica and would reach the lower respiratory airways. Although a considerably high deposition fraction was found in the oral cavity and the segment including several generations, deposition density appeared to be low in these regions. Deposition density was higher in the main bronchi compared to the oral cavity.

Deposition efficiencies in the oral cavity and the tracheobronchial tree were compared with other reported data and good agreement was found except for the oral cavity. It was observed that the deposition efficiency was strongly correlated with the Stokes number, indicating the role of impaction. Empirical models that have been suggested for different regions of the respiratory airways down to the 3rd branch generation of branching are reasonably useful for fiber deposition prediction in these regions. The next step should be to obtain more deposition data for fibers with Stokes numbers in the range of 0.1–1.

Deposition of fibers was compared to that of spherical particles. This comparison confirmed that fibers deposit less effectively than spherical particles of the same Stokes number. This result was likely due to the ability of fibers to align with the flow.

Conflict of interest

The authors have no conflict of interest.

Funding

The authors greatly acknowledge support from the projects FSI-S-17–4444 funded by the Ministry of Education, Youth and Sports of the Czech Republic and project no. GA16–23675S funded by the Czech Science Foundation.

Appendix A. Supporting information

Supplementary data associated with this article can be found in the online version at http://dx.doi.org/10.1016/j.jaerosci.2017.11.006.

References

Balashazy, I., Martonen, T. B., & Hofmann, W. (1990). Fiber Deposition in Airway Bifurcations. *Journal of Aerosol Medicine-Deposition Clearance and Effects in the Lung, 3*(*4*), 243–260. http://dx.doi.org/10.1089/jam.1990.3.243.

Balashazy, I., Moustafa, M., Hofmann, W., Szoke, R., El-Hussein, A., & Ahmed, A. R. (2005). Simulation of fiber deposition in bronchial airways. *Inhalation Toxicology, 17*(*13*), 717–727. http://dx.doi.org/10.1080/08958370500224565.

Baron (2001). Measurement of airborne particles-review. *Industrial Health*. Retrieved from 〈http://202.241.32.9/en/indu_hel/pdf/IH39_08.pdf〉 website:.

Baron, P. A., & Willeke, K. (2001). *Aerosol Measurement : Principles, Techniques, and Application* (2nd ed.). New York: Wiley.

Baron, P. A., Deye, G. J., & Fernback, J. (1994). Length separation of fibers. *Aerosol Science and Technology, 21*(*2*), 179–192. http://dx.doi.org/10.1080/02786829408959707.

Belka, M., Lizal, F., Jedelsky, J., Starha, P., Druckmullerova, H., Hopke, P. K., & Jicha, M. (2016). Application of image analysis method to detection and counting of glass fibers from filter samples. *Aerosol Science and Technology, 50*(*4*), 353–362. http://dx.doi.org/10.1080/02786826.2016.1151858.

Cai, F. S., & Yu, C. P. (1988). Inertial and interceptional deposition of spherical-particles and fibers in a bifurcating airway. *Journal of Aerosol Science, 19*(*6*), 679–688. http://dx.doi.org/10.1016/0021-8502(88)90003-1.

Dastan, A., Abouali, O., & Ahmadi, G. (2014). CFD simulation of total and regional fiber deposition in human nasal cavities. *Journal of Aerosol Science, 69*, 132–149. http://dx.doi.org/10.1016/j.jaerosci.2013.12.008.

Deye, G. J., Gao, P., Baron, P. A., & Fernback, J. (1999). Performance evaluation of a fiber length classifier. *Aerosol Science and Technology, 30*(*5*), 420–437. http://dx.doi.org/10.1080/027868299304471.

Elcner, J., Lizal, F., Jedelsky, J., Jicha, M., & Chovancova, M. (2016). Numerical investigation of inspiratory airflow in a realistic model of the human tracheobronchial airways and a comparison with experimental results. *Biomechanics and Modeling in Mechanobiology, 15*(*2*), 447–469. http://dx.doi.org/10.1007/s10237-015-0701-1.

Fan, F. G., & Ahmadi, G. (1995). A sublayer model for wall deposition of ellipsoidal particles in turbulent streams. *Journal of Aerosol Science, 26*(*5*), 813–840. http://dx.doi.org/10.1016/0021-8502(95)00021-00024.

Feng, Y., & Kleinstreuer, C. (2013). Analysis of non-spherical particle transport in complex internal shear flows. *Physics of Fluids, 25*(*9*), http://dx.doi.org/10.1063/1.

4821812.
Frederix, E. M. A., Kuczaj, A. K., Nordlund, M., Belka, M., Lizal, F., Jedelsky, J., … Geurts, B. J. (2018). Simulation of size-dependent aerosol deposition in a realistic model of the upper human airways. *Journal of Aerosol Science, 115* (Supplement C), 29–45. https://dx.doi.org/10.1016/j.jaerosci.2017.10.007.
Grgic, B., Finlay, W. H., Burnell, P. K. P., & Heenan, A. F. (2004). In vitro intersubject and intrasubject deposition measurements in realistic mouth-throat geometries. *Journal of Aerosol Science, 35*(*8*), 1025–1040. http://dx.doi.org/10.1016/j.jaerosci.2004.03.003.
Hinds, W. C. (1999). *Aerosol technology: properties, behavior, and measurement of airborne particles* (2nd ed.). New York; Chichester: Wiley.
Hofmann, W. (2011). Modelling inhaled particle deposition in the human lung—A review. *Journal of Aerosol Science, 42*(*10*), 693–724. http://dx.doi.org/10.1016/j.jaerosci.2011.05.007.
Hofmann, W., Winkler-Heil, R., & Balashazy, I. (2006). The effect of morphological variability on surface deposition densities of inhaled particles in human bronchial and acinar airways. *Inhalation Toxicology, 18*(*10*), 809–819. http://dx.doi.org/10.1080/08958370600753851.
Chan, T. L., & Lippmann, M. (1980). Experimental measurements and empirical modeling of the regional deposition of inhaled particles in humans. *American Industrial Hygiene Association Journal, 41*(*6*), 399–408. http://dx.doi.org/10.1080/15298668091424942.
Chan, T. L., Schreck, R. M., & Lippmann, M. (1980). Effect of the laryngeal jet on particle deposition in the human trachea and upper bronchial airways. *Journal of Aerosol Science, 11*(*5–6*), 447. http://dx.doi.org/10.1016/0021-8502(80)90117-2.
Cheng, K. H., Cheng, Y. S., Yeh, H. C., & Swift, D. L. (1997). Measurements of airway dimensions and calculation of mass transfer characteristics of the human oral passage. *Journal of Biomechanical Engineering-Transactions of the ASME, 119*(*4*), 476–482. http://dx.doi.org/10.1115/1.2798296.
Cheng, Y. S., Su, Y. F., Yeh, H. C., & Swift, D. L. (1993). Deposition of thoron progeny in human head airways. *Aerosol Science and Technology, 18*(*4*), 359–375. http://dx.doi.org/10.1080/02786829308959610.
Cheng, Y. S., Zhou, Y., & Chen, B. T. (1999). Particle deposition in a cast of human oral airways. *Aerosol Science and Technology, 31*(*4*), 286–300. http://dx.doi.org/10.1080/027868299304165.
IARC International Agency for Research on Cancer (2002). Working Group on the Evaluation of Carcinogenic Risks to Humans., World Health Organization. *Man-made vitreous fibres*. Lyon, France.
Inthavong, K., Mouritz, A. P., Dong, J. L., & Tu, J. Y. (2013). Inhalation and deposition of carbon and glass composite fibre in the respiratory airway. *Journal of Aerosol Science, 65*, 58–68. http://dx.doi.org/10.1016/j.jaerosci.2013.07.003.
Jedelsky, J., Lizal, F., & Jicha, M. (2012). Characteristics of turbulent particle transport in human airways under steady and cyclic flows. *International Journal of Heat and Fluid Flow, 35*, 84–92. http://dx.doi.org/10.1016/j.ijheatfluidflow.2012.01.003.
Kim, C. S., & Fisher, D. M. (1999). Deposition characteristics of aerosol particles in sequentially bifurcating airway models. *Aerosol Science and Technology, 31*(*2–3*), 198–220. http://dx.doi.org/10.1080/027868299304255.
Kleinstreuer, C., & Feng, Y. (2013). Computational analysis of non-spherical particle transport and deposition in shear flow with application to lung aerosol dynamics-A review. *Journal of Biomechanical Engineering-Transactions of the ASME, 135*(*2*), http://dx.doi.org/10.1115/1.4023236.
Kleinstreuer, C., & Zhang, Z. (2003). Laminar-to-turbulent fluid-particle flows in a human airway model. [article]. *International Journal of Multiphase Flowing, 29*(*2*), 271–289. http://dx.doi.org/10.1016/S0301-9322(02)00131-3.
Kleinstreuer, C., Zhang, Z., & Li, Z. (2008). Modeling airflow and particle transport/deposition in pulmonary airways. *Respiratory Physiology & Neurobiology, 163*(*1–3*), 128–138. http://dx.doi.org/10.1016/j.resp.2008.07.002.
Koullapis, P., Kassinos, S. C., Muela, J., Perez-Segarra, C., Rigola, J., Lehmkuhl, O., & Nicolaou, L. (2017). Regional aerosol deposition in the human airways: The SimInhale benchmark case and a critical assessment of in silico methods. *European Journal of Pharmaceutical Sciences*. http://dx.doi.org/10.1016/j.ejps.2017.09.003.
Lin, C., Tawhai, M., McLennan, G., & Hoffman, E. (2007). Characteristics of the turbulent laryngeal jet and its effect on airflow in the human intra-thoracic airways. [Article]. *Respiratory Physiology & Neurobiology, 157*(*2–3*), 295–309. http://dx.doi.org/10.1016/j.resp.2007.02.006.
Lipowicz, P. J., & Yeh, H. C. (1989). Fiber dielectrophoresis. *Aerosol Science and Technology, 11*(*3*), 206–212. http://dx.doi.org/10.1080/02786828908959313.
Lizal, F., Belka, M., Adam, J., Jedelsky, J., & Jicha, M. (2015). A method for in vitro regional aerosol deposition measurement in a model of the human tracheo-bronchial tree by the positron emission tomography. *Proceedings of the Institution of Mechanical Engineers Part H-Journal of Engineering in Medicine, 229*(*10*), 750–757. http://dx.doi.org/10.1177/0954411915600005.
Lizal, F., Elcner, J., Hopke, P. K., Jedelsky, J., & Jicha, M. (2012). Development of a realistic human airway model. *Proceedings of the Institution of Mechanical Engineers Part H-Journal of Engineering in Medicine, 226*(*H3*), 197–207. http://dx.doi.org/10.1177/0954411911430188.
Martonen, T. B., Zhang, Z., & Lessmann, R. C. (1993). Fluid-dynamics of the human larynx and upper tracheobronchial airways. *Aerosol Science and Technology, 19*(*2*), 133–156. http://dx.doi.org/10.1080/02786829308959627.
Myojo, T. (1990). The effect of length and diameter on the deposition of fibrous aerosol in a model lung bifurcation. *Journal of Aerosol Science, 21*(*5*), 651–659. http://dx.doi.org/10.1016/0021-8502(90)90120-M.
Myojo, T., & Takaya, M. (2001). Estimation of fibrous aerosol deposition in upper bronchi based on experimental data with model bifurcation. *Industrial Health, 39*(*2*), 141–149. http://dx.doi.org/10.2486/indhealth.39.141.
Nordlund, M., Belka, M., Kuczaj, A. K., Lizal, F., Jedelsky, J., Elcner, J., & Hoeng, J. (2017). Multicomponent aerosol particle deposition in a realistic cast of the human upper respiratory tract. *Inhalation Toxicology, 29*(*3*), 113–125. http://dx.doi.org/10.1080/08958378.2017.1315196.
Ruzer, L. S., & Harley, N. H. (2013). *Aerosols handbook: measurement, dosimetry, and health effects* (2nd ed.). Boca Raton: Taylor & Francis.
SCOEL Scientific Committee on Occupational Exposure Limits (2012). *Recommendation from the Scientific Committee on Occupational Exposure Limits for man made-mineral fibres (MMMF)*: European Commission. Employment, Social Affairs and Incusion.
Shanley, K. T., & Ahmadi, G. (2011). A numerical model for simulating the motions of ellipsoidal fibers suspended in low reynolds number shear flows. *Aerosol Science and Technology, 45*(*7*), 838–848. http://dx.doi.org/10.1080/02786826.2011.566293.
Shanley, K. T., Ahmadi, G., Hopke, P. K., & Cheng, Y.-S. (2016). Simulated airflow and rigid fiber behavior in a realistic nasal airway model. *Particulate Science and Technology,* 1–10. http://dx.doi.org/10.1080/02726351.2016.1208694.
Schmidt, A., Zidowitz, S., Kriete, A., Denhard, T., Krass, S., & Peitgen, H. O. (2004). A digital reference model of the human bronchial tree. *Computerized Medical Imaging and Graphics, 28*(*4*), 203–211. http://dx.doi.org/10.1016/j.compmedimag.2004.01.001.
Stahlhofen, W., Rudolf, G., & James, A. C. (1989). Intercomparison of experimental regional aerosol deposition data. *Journal of Aerosol Medicine, 2*(*3*), 285–308. http://dx.doi.org/10.1089/jam.1989.2.285.
Stöber, W. (1972). Dynamic shape factors of nonspherical aerosol particles. *Assesment of Airborne Particles,* 249–289.
Su, W. C., & Cheng, Y. S. (2005). Deposition of fiber in the human nasal airway. *Aerosol Science and Technology, 39*(*9*), 888–901. http://dx.doi.org/10.1080/02786820500295685.
Su, W. C., & Cheng, Y. S. (2006aa). Deposition of fiber in a human airway replica. *Journal of Aerosol Science, 37*(*11*), 1429–1441. http://dx.doi.org/10.1016/j.jaerosci.2006.01.015.
Su, W. C., & Cheng, Y. S. (2006bb). Fiber deposition pattern in two human respiratory tract replicas. *Inhalation Toxicology, 18*(*10*), 749–760. http://dx.doi.org/10.1080/08958370600748513.
Su, W. C., & Cheng, Y. S. (2009). Deposition of man-made fibers in human respiratory airway casts. *Journal of Aerosol Science, 40*(*3*), 270–284. http://dx.doi.org/10.1016/j.jaerosci.2008.11.003.
Su, W. C., & Cheng, Y. S. (2015). Estimation of carbon nanotubes deposition in a human respiratory tract replica. *Journal of Aerosol Science, 79*, 72–85. http://dx.doi.org/10.1016/j.jaerosci.2014.09.005.
Sussman, R. G., Cohen, B. S., & Lippmann, M. (1991). Asbestos fiber deposition in a human tracheobronchial cast. I. Experimental. *Inhalation Toxicology, 3*(*2*), 145–160. http://dx.doi.org/10.3109/08958379109145281.
Tian, L., & Ahmadi, G. (2013). Fiber transport and deposition in human upper tracheobronchial airways. *Journal of Aerosol Science, 60*, 1–20. http://dx.doi.org/10.1016/j.jaerosci.2013.02.001.

Tian, L., Ahmadi, G., Wang, Z., & Hopke, P. K. (2012). Transport and deposition of ellipsoidal fibers in low Reynolds number flows. *Journal of Aerosol Science, 45*, 1–18. http://dx.doi.org/10.1016/j.jaerosci.2011.09.001.

Wang, Z., Hopke, P. K., Ahmadi, G., Cheng, Y.-S., & Baron, P. A. (2008). Fibrous particle deposition in human nasal passage: The influence of particle length, flow rate, and geometry of nasal airway. *Journal of Aerosol Science, 39*(*12*), 1040–1054. http://dx.doi.org/10.1016/j.jaerosci.2008.07.008.

Wang, Z., Hopke, P. K., Baron, P. A., Ahmadi, G., Cheng, Y.-S., Deye, G., & Su, W.-C. (2005). Fiber classification and the influence of average air humidity. *Aerosol Science and Technology, 39*(*11*), 1056–1063. http://dx.doi.org/10.1080/02786820500380198.

Weibel, E. R. (1963). *Morphometry of the human lung.* Berlin: [s.n.].

Zhang, L., Asgharian, B., & Anjilvel, S. (1996). Inertial and interceptional deposition of fibers in a bifurcating airway. *Journal of Aerosol Medicine-Deposition Clearance and Effects in the Lung, 9*(*3*), 419–430. http://dx.doi.org/10.1089/jam.1996.9.419.

Zhang, Z., & Kleinstreuer, C. (2004). Airflow structures and nano-particle deposition in a human upper airway model. *Journal of Computational Physics, 198*(*1*), 178–210. http://dx.doi.org/10.1016/j.jcp.2003.11.034.

Zhang, Z., Kleinstreuer, C., & Kim, C. S. (2008). Airflow and nanoparticle deposition in a 16-generation tracheobronchial airway model. *Annals of Biomedical Engineering, 36*(*12*), 2095–2110. http://dx.doi.org/10.1007/s10439-008-9583-z.

Zhou, Y., & Cheng, Y. (2005). Particle deposition in a cast of human tracheobronchial airways. *Aerosol science and Technology, 39*, 492–500.

Zhou, Y., Su, W. C., & Cheng, Y. S. (2007). Fiber deposition in the tracheobronchial region: Experimental measurements. *Inhalation Toxicology, 19*(*13*), 1071–1078. http://dx.doi.org/10.1080/08958370701626634.

Zhou, Y., Xi, J. X., Simpson, J., Irshad, H., & Cheng, Y. S. (2013). Aerosol deposition in a nasopharyngolaryngeal replica of a 5-year-old child. *Aerosol Science and Technology, 47*(*3*), 275–282. http://dx.doi.org/10.1080/02786826.2012.749341.

5.3.Summary

The deposition results of both porous and fibrous particles were analyzed. The results indicated that porous particles deposited as effectively as spherical particles. On the other hand, fibers deposited less effectively. Both formulated hypotheses were confirmed.

The deposition efficiencies of porous and fibrous particles as a function of Stokes number are depicted in Figure 52. The deposition results of spherical particles measured on the same airway replica are presented as well (Lizal et al., 2015). The empirical model used by Zhou et al. (2005) was employed to obtain empirical equations for various particles. OriginPro 9 (OriginLab Corporation, MA, USA) was utilized for this purpose. Only the deposition data measured in the segments encompassing single generation (gen. 1 to 4 of the replica) were employed for the curve fitting. The best curve fits for spherical and porous particles, and fibers are represented by equations 23 ($R^2 = 0.45$) and 24 ($R^2 = 0.486$), respectively:

$$\mathrm{DE}_{sphere,porous\ p.} = 1 - \exp(-5.14 \cdot \mathrm{Stk}^{1.3}) \quad (23)\ ,$$

$$\mathrm{DE}_{fibers} = 1 - \exp(-0.66 \cdot \mathrm{Stk}^{1.31}) \quad (24)\ .$$

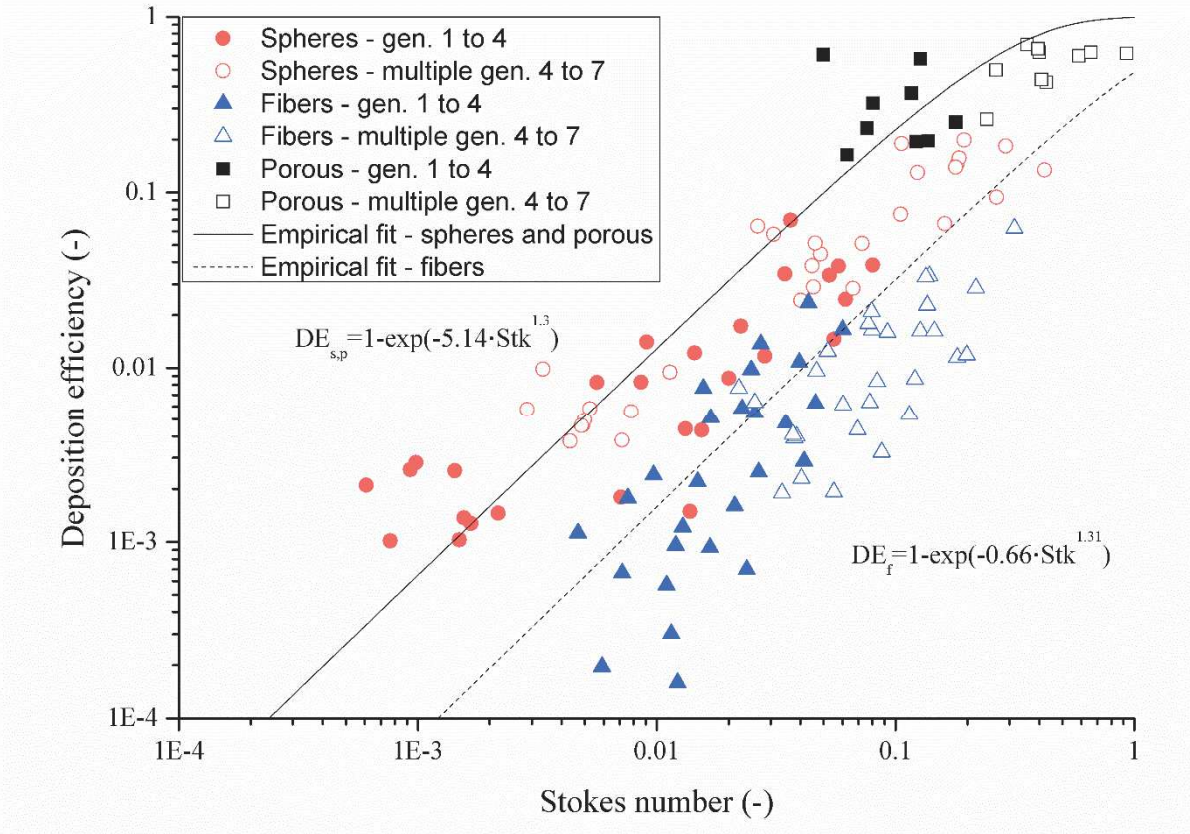

Figure 52 Deposition efficiencies of various particles as a function of Stokes number

Conclusions

Particle transport and deposition is highly studied topic nowadays. As the main attention of researchers has been deposition of spherical particles during normal breathing, this PhD thesis deals with regional deposition of non–spherical particles. The main goal was to analyze deposition of porous and fibrous particles.

The first objective was to study deposition of porous particles that have a big potential in inhalation therapy. Several methods for porous particle production were tested. The most suitable particles in the terms of size were obtained using spray–drying and liquid–liquid interface crystallization method. Chitosan particles with rather monodisperse size were produced by the spray–drying method. However, the total particle volume output was low and therefore, density measurements were not carried out. The crystallization method produce polydisperse particles made of $CuSO_4$ with sufficiently low density and porous structure. The mass median aerodynamic diameter of these particles was 8.15±1.6 μm and the bulk density was 0.42 g/cm^3. The $CuSO_4$ particles were utilized in deposition experiment at steady inhalation flow rate of 30 L/min. The deposition detection was performed using spectrophotometry.

As the MMAD of the particles was in micrometer scale, the deposition was driven mainly by impaction. This resulted in significant deposition fraction in the oral cavity (62,6%), the trachea (10%) and the main bronchi (7,2%). Comparing the deposition data to other studies using spherical particles, the deposition agreed very well except the oral cavity. The deposition of porous particles in the oral cavity was higher than that of spherical particles. This could be caused by the polydispersity of the particles.

The other objective was to study deposition of fibrous particles that are potentially hazardous for human health after inhalation. The glass fibers with density of 2.56 g/cm^3 and uniform diameter of 1.03±0.45 μm were classified according to their length using a dielectrophoretic classifier. After that, the fibers were introduced into the replica of respiratory airways at three steady inhalation flow rates (15, 30, and 50 L/min). The deposition detection was performed using phase–contrast microscopy. As the use of this method is very time–consuming and demanding for operator´s concentration, an automatic counting software based on the image processing was developed.

The deposition fraction of fibers was very low in the respiratory airway replica. The total deposition fractions were 0.7, 1.9, and 4.6% for inhalation flow rates of 15, 30, and 50 L/min, respectively. The deposition data agreed considerably well to available studies except the oral cavity. This time, the problem occurred during the sample preparation. The replica segments were sonicated to release the deposited fibers that were subsequently transferred onto filters. During the sonication, parts of the replica walls were released into the solution and these replica debris caused discrepancies during image analysis. This problem was observed only in the case of oral cavity as it was the largest segment with most released debris. Comparing the fiber deposition to that of spherical particles, fibers deposited less efficiently than spherical particles having the same Stokes number.

The current thesis contains original experimental results of non–spherical particles in the realistic replica of human respiratory airways from the oral cavity to 7th generation of branching. The amount of such a data in the literature is rather scarce and for example, fiber deposition beyond 4th generation has not been experimentally measured before. The deposition data confirmed that porous particles deposit as efficiently as spherical particles. On the other hand, fibers deposited less efficiently indicating that their aerodynamic behavior is of great importance. The formulated hypotheses of this thesis were confirmed.

The future research in this area can be aimed at measuring deposition of fibers having large Stokes numbers, i.e. fibers made of materials with higher density than glass or very long glass fibers having length approximately 100 μm. Further research can be aimed at deposition of polydisperse particles and their impact on deposition characteristics. The polydispersity is essential for inhalation therapy as the pharmaceutical aerosols are polydisperse. Experimental measurement using realistic breathing pattern for inhalation maneuver can be valuable.

References

Agnew, J. E. (1991). Characterizing Lung Aerosol Penetration. *Journal of Aerosol Medicine-Deposition Clearance and Effects in the Lung, 4*(3), 237-249. doi: DOI 10.1089/jam.1991.4.237

Agu, R. U., Ugwoke, M. I., Armand, M., Kinget, R., & Verbeke, N. (2001). The lung as a route for systemic delivery of therapeutic proteins and peptides. *Respiratory Research, 2*(4), 198-209.

Altshuler, B. (1969). Behaviour of Airborne Particles in the Respiratory Tract *Ciba Foundation Symposium - Circulatory and Respiratory Mass Transport* (pp. 215-235): John Wiley & Sons, Ltd.

Altshuler, B., Palmes, E. D., Yarmus, L., & Nelson, N. (1959). Intrapulmonary Mixing of Gases Studied with Aerosols. *Journal of Applied Physiology, 14*(3), 321-327.

Altshuler, B., Yarmus, L., Palmes, E. D., & Nelson, N. (1957). Aerosol deposition in the human respiratory tract. I. Experimental procedures and total deposition. *AMA Arch Ind Health, 15*(4), 293-303.

Anderson, P. J. (2005). History of aerosol therapy: liquid nebulization to MDIs to DPIs. *Respir Care, 50*(9), 1139-1150.

Anger, H. O. (1958). Scintillation Camera. *Review of Scientific Instruments, 29*(1), 27-33. doi: Doi 10.1063/1.1715998

Anjilvel, S., & Asgharian, B. (1995). A Multiple-Path Model of Particle Deposition in the Rat Lung. *Fundamental and Applied Toxicology, 28*(1), 41-50. doi: DOI 10.1006/faat.1995.1144

Asgharian, B., & Anjilvel, S. (1995a). The Effect of Fiber Inertia on Its Orientation in a Shear-Flow with Application to Lung Dosimetry. *Aerosol Science and Technology, 23*(3), 282-290. doi: Doi 10.1080/02786829508965313

Asgharian, B., & Anjilvel, S. (1995b). Movement and Deposition of Fibers in an Airway with Steady Viscous-Flow. *Aerosol Science and Technology, 22*(3), 261-270. doi: Doi 10.1080/02786829408959745

Asgharian, B., Hofman, W., & Bergmann, R. (2001). Particle deposition in a multiple-path model of the human lung. *Aerosol Science and Technology, 34*(4), 332-339. doi: Doi 10.1080/02786820151092478

Asgharian, B., Wood, R., & Schlesinger, R. B. (1995). Empirical Modeling of Particle Deposition in the Alveolar Region of the Lungs - a Basis for Interspecies Extrapolation. *Fundamental and Applied Toxicology, 27*(2), 232-238. doi: DOI 10.1006/faat.1995.1128

Asgharian, B., & Yu, C. P. (1989). A Simplified Model of Interceptional Deposition of Fibers at Airway Bifurcations. *Aerosol Science and Technology, 11*(1), 80-88. doi: Doi 10.1080/02786828908959301

Balashazy, I., Hofmann, W., Farkas, A., & Madas, B. G. (2008). Three-dimensional model for aerosol transport and deposition in expanding and contracting alveoli. *Inhalation Toxicology, 20*(6), 611-621. doi: 10.1080/08958370801915291

Balashazy, I., Hofmann, W., & Heistracher, T. (2003). Local particle deposition patterns may play a key role in the development of lung cancer. *Journal of Applied Physiology, 94*(5), 1719-1725. doi: 10.1152/japplphysiol.00527.2002

Baron. (2001). Measurement of airborne particles-review. *Industrial Health*. Retrieved from http://202.241.32.9/en/indu_hel/pdf/IH39_08.pdf website:

Baron, P. A., & Willeke, K. (2005). *Aerosol measurement : principles, techniques, and applications* (2nd ed. ed.). Hoboken, N.J.: Wiley-Interscience.

Basu, S., & Alavi, A. (2008). Unparalleled Contribution of F-18-FDG PET to Medicine Over 3 Decades. *Journal of Nuclear Medicine, 49*(10), 17n-+.

Beeckmans, J. M. (1965). Deposition of Aerosols in Respiratory Tract .I. Mathematical Analysis and Comparison with Experimental Data. *Canadian Journal of Physiology and Pharmacology, 43*(1), 157-+.

Beeckmans, J. M. (1970). The deposition of asbestos particles in the human respiratory tract. *International Journal of Environmental Studies, 1*(1-4), 31-34. doi: 10.1080/00207237008709392

Bell, K. A., & Friedlander, S. K. (1973). Aerosol deposition in models of a human lung bifurcation. *Staub-Reinhalt. Luft., 33*, 178-182.

Bellin, M. F. (2006). MR contrast agents, the old and the new. *European Journal of Radiology, 60*(3), 314-323. doi: 10.1016/j.ejrad.2006.06.021

Berg, E. J., Weisman, J. L., Oldham, M. J., & Robinson, R. J. (2010). Flow field analysis in a compliant acinus replica model using particle image velocimetry (PIV). *J Biomech, 43*(6), 1039-1047. doi: 10.1016/j.jbiomech.2009.12.019

Berridge, M. S., Lee, Z., & Heald, D. L. (2000). Pulmonary distribution and kinetics of inhaled [C-11]triamcinolone acetonide. *Journal of Nuclear Medicine, 41*(10), 1603-1611.

Beyer, T., Townsend, D. W., Brun, T., Kinahan, P. E., Charron, M., Roddy, R., . . . Nutt, R. (2000). A combined PET/CT scanner for clinical oncology. *Journal of Nuclear Medicine, 41*(8), 1369-1379.

Bisgaard, H., O'Callaghan, C., & Smaldone, G. C. (2002). *Drug delivery to the lung*. New York: Dekker.

Borojeni, A. A. T., Noga, M. L., Vehring, R., & Finlay, W. H. (2014). Measurements of total aerosol deposition in intrathoracic conducting airway replicas of children. *Journal of Aerosol Science, 73*, 39-47. doi: DOI 10.1016/j.jaerosci.2014.03.005

Brown, C. E. (1931). Quantitative measurements of the inhalation, retention, and exhalation of dusts and fumes by man. II. Concentrations below 50 mg per cubic meter. *J. Ind. Hyg. Toxicol, 13*, 285-291.

Brown, J. H., Cook, K. M., Ney, F. G., & Hatch, T. (1950). Influence of Particle Size upon the Retention of Particulate Matter in the Human Lung. *American Journal of Public Health and the Nations Health, 40*(4), 450-480.

Burney, P. G. J., Patel, J., Newson, R., Minelli, C., & Naghavi, M. (2015). Global and regional trends in COPD mortality, 1990-2010. *European Respiratory Journal, 45*(5), 1239-1247. doi: 10.1183/09031936.00142414

Byron, P. R., Hindle, M., Lange, C. F., Longest, P. W., McRobbie, D., Oldham, M. J., . . . Finlay, W. H. (2010). In vivo-in vitro correlations: predicting pulmonary drug deposition from pharmaceutical aerosols. *J Aerosol Med Pulm Drug Deliv, 23 Suppl 2*, S59-69. doi: 10.1089/jamp.2010.0846

Cai, F. S., & Yu, C. P. (1988). Inertial and Interceptional Deposition of Spherical-Particles and Fibers in a Bifurcating Airway. *Journal of Aerosol Science, 19*(6), 679-688. doi: Doi 10.1016/0021-8502(88)90003-1

Casey, D. L., Beihn, R. M., Digenis, G. A., & Shambhu, M. B. (1976). Method for Monitoring Hard Gelatin Capsule Disintegration Times in Humans Using External Scintigraphy. *Journal of Pharmaceutical Sciences, 65*(9), 1412-1413. doi: DOI 10.1002/jps.2600650941

Cinkotai, F. F. (1974). Fluid-Flow in a Model Alveolar Sac. *Journal of Applied Physiology, 37*(2), 249-251.

Cohen, B. S., & Asgharian, B. (1990). Deposition of Ultrafine Particles in the Upper Airways - an Empirical-Analysis. *Journal of Aerosol Science, 21*(6), 789-797. doi: Doi 10.1016/0021-8502(90)90044-X

Cohen, B. S., Sussman, R. G., & Lippmann, M. (1990). Ultrafine Particle Deposition in a Human Tracheobronchial Cast. *Aerosol Science and Technology, 12*(4), 1082-1091. doi: Doi 10.1080/02786829008959418

Comer, J. K., Kleinstreuer, C., Hyun, S., & Kim, C. S. (2000). Aerosol transport and deposition in sequentially bifurcating airways. *Journal of Biomechanical Engineering-Transactions of the Asme, 122*(2), 152-158. doi: Doi 10.1115/1.429636

Concordia College. (2015). Determination of Caffeine and Benzoic Acid in Soft Drinks by Multicomponent UV Analysis. *Analytical Chemistry Lab Manual*, from http://sites.cord.edu/chem-330-lab-manual/experiments/uv-vis

Conway, J. (2012). Lung imaging - two dimensional gamma scintigraphy, SPECT, CT and PET. *Adv Drug Deliv Rev, 64*(4), 357-368. doi: 10.1016/j.addr.2012.01.013

Corcoran, T., & Chigier, N. (2000). Characterization of the laryngeal jet using phase Doppler interferometry. [Article]. *Journal of Aerosol Medicine-Deposition Clearance and Effects in the Lung, 13*(2), 125-137. doi: 10.1089/089426800418659

Council of Europe (2007). *European Pharmacopoeia: Published in Accordance with the Convention on the Elaboration of a European Pharmacopoeia (European Treaty Series No. 50)*: Council of Europe.

Dailey, H. L., & Ghadiali, S. N. (2007). Fluid-structure analysis of microparticle transport in deformable pulmonary alveoli. *Journal of Aerosol Science, 38*(3), 269-288. doi: 10.1016/j.jaerosci.2007.01.001

Darquenne, C. (2001). A realistic two-dimensional model of aerosol transport and deposition in the alveolar zone of the human lung. *Journal of Aerosol Science, 32*(10), 1161-1174. doi: Doi 10.1016/S0021-8502(01)00047-7

Darquenne, C. (2012). Aerosol Deposition in Health and Disease. *Journal of Aerosol Medicine and Pulmonary Drug Delivery, 25*(3), 140-147. doi: DOI 10.1089/jamp.2011.0916

Darquenne, C., Lamm, W. J., Fine, J. M., Corley, R. A., & Glenny, R. W. (2016). Total and regional deposition of inhaled aerosols in supine healthy subjects and subjects with mild-to-moderate COPD. *Journal of Aerosol Science, 99*, 27-39. doi: 10.1016/j.jaerosci.2016.01.019

Darquenne, C., & Paiva, M. (1994). One-Dimensional Simulation of Aerosol Transport and Deposition in the Human Lung. *Journal of Applied Physiology, 77*(6), 2889-2898.

Darquenne, C., Paiva, M., & Prisk, G. K. (2000). Effect of gravity on aerosol dispersion and deposition in the human lung after periods of breath holding. *Journal of Applied Physiology, 89*(5), 1787-1792.

Darquenne, C., & Paiva, N. (1996). Two- and three-dimensional simulations of aerosol transport and deposition in alveolar zone of human lung. *Journal of Applied Physiology, 80*(4), 1401-1414.

Darquenne, C., & Prisk, G. K. (2004). Aerosol deposition in the human respiratory tract breathing air and 80 : 20 heliox. *Journal of Aerosol Medicine-Deposition Clearance and Effects in the Lung, 17*(3), 278-285. doi: DOI 10.1089/jam.2004.17.278

Darquenne, C., West, J. B., & Prisk, G. K. (1998). Deposition and dispersion of 1-mu m aerosol boluses in the human lung: effect of micro- and hypergravity. *Journal of Applied Physiology, 85*(4), 1252-1259.

DeHaan, W. H., & Finlay, W. H. (2001). In vitro monodisperse aerosol deposition in a mouth and throat with six different inhalation devices. *Journal of Aerosol Medicine-Deposition Clearance and Effects in the Lung, 14*(3), 361-367. doi: Doi 10.1089/089426801316970321

Dellamary, L. A., Tarara, T. E., Smith, D. J., Woelk, C. H., Adractas, A., Costello, M. L., . . . Weers, J. G. (2000). Hollow porous particles in metered dose inhalers. *Pharmaceutical Research, 17*(2), 168-174. doi: Doi 10.1023/A:1007513213292

DeVuyst, P., Dumortier, P., Swaen, G. M. H., Pairon, J. C., & Brochard, P. (1995). Respiratory health effects of man-made vitreous (mineral) fibres. *European Respiratory Journal, 8*(12), 2149-2173. doi: Doi 10.1183/09031936.95.08122149

Drinker, P., Thomson, R. M., & Finn, J. L. (1928). Quantitative Measurements of the Inhalation, Retention and Exhalation of Dusts and Fumes by Man : I. Concentrations of 50 to 450 mg. per Cubic Meter. *Journal of Industrial Hygiene, 10*, 13-25.

Dugernier, J., Hesse, M., Vanbever, R., Depoortere, V., Roeseler, J., Michotte, J. B., . . . Reychler, G. (2017). SPECT-CT Comparison of Lung Deposition using a System combining a Vibrating-mesh Nebulizer with a Valved Holding Chamber and a Conventional Jet Nebulizer: a Randomized Cross-over Study. *Pharmaceutical Research, 34*(2), 290-300. doi: 10.1007/s11095-016-2061-7

Dunbar, C., Scheuch, G., Sommerer, K., DeLong, M., Verma, A., & Batycky, R. (2002). In vitro and in vivo dose delivery characteristics of large porous particles for inhalation. *International Journal of Pharmaceutics, 245*(1-2), 179-189. doi: 10.1016/s0378-5173(02)00349-6

Edwards, D., Hanes, J., Caponetti, G., Hrkach, J., BenJebria, A., Eskew, M., . . . Langer, R. (1997). Large porous particles for pulmonary drug delivery. [Article]. *Science, 276*(5320), 1868-1871. doi: 10.1126/science.276.5320.1868

Egan, M. J., & Nixon, W. (1985). A Model of Aerosol Deposition in the Lung for Use in Inhalation Dose Assessments. *Radiation Protection Dosimetry, 11*(1), 5-17.

Ensor, D. (2011). *Aerosol Science and Technology: History and Reviews.* : RTI Press.

Fan, F. G., & Ahmadi, G. (1995). A Sublayer Model for Wall Deposition of Ellipsoidal Particles in Turbulent Streams. *Journal of Aerosol Science, 26*(5), 813-840. doi: Doi 10.1016/0021-8502(95)00021-4

Fang, C. P., Wilson, J. E., Spektor, D. M., & Lippmann, M. (1993). Effect of Lung Airway Branching Pattern and Gas-Composition on Particle Deposition in Bronchial Airways .3. Experimental

Studies with Radioactively Tagged Aerosol in Human and Canine Lungs. *Experimental Lung Research, 19*(3), 377-396. doi: Doi 10.3109/01902149309064353
Feng, Y., & Kleinstreuer, C. (2013). Analysis of non-spherical particle transport in complex internal shear flows. *Physics of Fluids, 25*(9). doi: Artn 091904
10.1063/1.4821812
Ferron, G. A. (1977). Deposition of polydisperse aerosols in two glass models representing the upper human airways. *Journal of Aerosol Science, 8*(6), 409-427. doi: http://dx.doi.org/10.1016/0021-8502(77)90035-0
Findeisen, W. (1935). Über das Absetzen kleiner, in der Luft suspendierter Teilchen in der menschlichen Lunge bei der Atmung. *Pflügers Archiv European Journal of Physiology, 236*(1), 367-379. doi: 10.1007/BF01752351
FIRS Forum of International Respiratory Societies, (2013). *Respiratory diseases in the world : realities of today - opportunities for tomorrow*.
Fishler, R., Hofemeier, P., Etzion, Y., Dubowski, Y., & Sznitman, J. (2015). Particle dynamics and deposition in true-scale pulmonary acinar models. *Scientific Reports, 5*. doi: ARTN 14071
10.1038/srep14071
Fleming, J. (2004). Measuring drug deposition by airway generation in humans,. In R. Dalby, P. Byron, J. Peart, J. Suman & S. Farr (Eds.), *Respiratory Drug Delivery IX* (pp. 187-193). River Grove: Davis Healthcare International.
Fleming, J., Conway, J., Majoral, C., Tossici-Bolt, L., Katz, I., Caillibotte, G., . . . Apiou-Sbirlea, G. (2011). The Use of Combined Single Photon Emission Computed Tomography and X-ray Computed Tomography to Assess the Fate of Inhaled Aerosol. *Journal of Aerosol Medicine and Pulmonary Drug Delivery, 24*(1), 49-60. doi: DOI 10.1089/jamp.2010.0843
Foord, N., Black, A., & Walsh, M. (1978). Regional deposition of 2.5–7.5 μm diameter inhaled particles in healthy male non-smokers. *Journal of Aerosol Science, 9*(4), 343-357. doi: http://dx.doi.org/10.1016/0021-8502(78)90037-X
Friedlander, S. K. (2000). *Smoke, dust, and haze : fundamentals of aerosol dynamics* (2nd ed. ed.). New York: Oxford University Press.
Frohlich, E., & Salar-Behzadi, S. (2014). Toxicological Assessment of Inhaled Nanoparticles: Role of in Vivo, ex Vivo, in Vitro, and in Silico Studies. *International Journal of Molecular Sciences, 15*(3), 4795-4822. doi: 10.3390/ijms15034795
Fuchs, N. A. (1964). *Mechanics of Aerosols* (revised and enlarged edition. ed.). [S.l.]: Pergamon Press.
Gandevia, B. (1975). Historical Review of Use of Parasympatholytic Agents in Treatment of Respiratory Disorders. *Postgraduate Medical Journal, 51*, 13-20.
Gehr, P., Bachofen, M., & Weibel, E. R. (1978). The normal human lung: ultrastructure and morphometric estimation of diffusion capacity. *Respir Physiol, 32*(2), 121-140.
Gemci, T., Ponyavin, V., Chen, Y., Chen, H., & Collins, R. (2008). Computational model of airflow in upper 17 generations of human respiratory tract. *Journal of Biomechanics, 41*(9), 2047-2054. doi: 10.1016/j.jbiomech.2007.12.019
Gerrity, T., Lee, P., Hass, F., Marinelli, A., Werner, P., & Lourenco, R. (1979). CALCULATED DEPOSITION OF INHALED PARTICLES IN THE AIRWAY GENERATIONS OF NORMAL SUBJECTS. [Article]. *Journal of Applied Physiology, 47*(4), 867-873.
Gervelas, C., Serandour, A. L., Geiger, S., Grillon, G., Fritsch, P., Taulelle, C., . . . Tsapis, N. (2007). Direct lung delivery of a dry powder formulation of DTPA with improved aerosolization properties: Effect on lung and systemic decorporation of plutonium. *Journal of Controlled Release, 118*(1), 78-86. doi: 10.1016/j.jconrel.2006.11.027
Gharse, S., & Fiegel, J. (2016). Large Porous Hollow Particles: Lightweight Champions of Pulmonary Drug Delivery. *Current Pharmaceutical Design, 22*(17), 2463-2469. doi: 10.2174/1381612822666160128145356
Golshahi, L., Noga, M. L., & Finlay, W. H. (2012). Deposition of inhaled micrometer-sized particles in oropharyngeal airway replicas of children at constant flow rates. *Journal of Aerosol Science, 49*, 21-31. doi: 10.1016/j.jaerosci.2012.03.001
Gradon, L., & Sosnowski, T. R. (2014). Formation of particles for dry powder inhalers. *Advanced Powder Technology, 25*(1), 43-55. doi: DOI 10.1016/j.apt.2013.09.012

Green, H. L., Lane, & Lane, W. R. (1964). *Particulate Clouds: dusts, smokes and mists ... Second edition*. London: E. & F. N. Spon.
Grgic, B., Finlay, W. H., & Heenan, A. F. (2004). Regional aerosol deposition and flow measurements in an idealized mouth and throat. *Journal of Aerosol Science, 35*(1), 21-32. doi: Doi 10.1016/S0021-8502(03)00387-2
Gurman, J. L., Lioy, P. J., Lippmann, M., & Schlesinger, R. B. (1984). Particle Deposition in Replicate Casts of the Human Upper Tracheobronchial Tree under Constant and Cyclic Inspiratory Flow .2. Empirical-Model. *Aerosol Science and Technology, 3*(3), 253-257. doi: Doi 10.1080/02786828408959013
Haber, S., Butler, J. P., Brenner, H., Emanuel, I., & Tsuda, A. (2000). Shear flow over a self-similar expanding pulmonary alveolus during rhythmical breathing. *Journal of Fluid Mechanics, 405*, 243-268. doi: Doi 10.1017/S0022112099007375
Haber, S., Yitzhak, D., & Tsuda, A. (2003). Gravitational deposition in a rhythmically expanding and contracting alveolus. *Journal of Applied Physiology, 95*(2), 657-671. doi: 10.1152/japplphysiol.00770.2002
Haefelibleuer, B., & Weibel, E. R. (1988). Morphometry of the Human Pulmonary Acinus. *Anatomical Record, 220*(4), 401-414. doi: DOI 10.1002/ar.1092200410
Halodova S. (2015). *Zavádění metody přípravy porézních částic pomocí sprejové lyofilizace.* Master´s, University of Veterinary and Pharmaceutical Sciences Brno.
Harris, R. L., & Fraser, D. A. (1976). Model for Deposition of Fibers in Human Respiratory System. *American Industrial Hygiene Association Journal, 37*(2), 73-89. doi: Doi 10.1080/0002889768507416
He, P., Davis, S. S., & Illum, L. (1999). Chitosan microspheres prepared by spray drying. *International Journal of Pharmaceutics, 187*(1), 53-65. doi: Doi 10.1016/S0378-5173(99)00125-8
Henry, F. S., Butler, J. P., & Tsuda, A. (2002). Kinematically irreversible acinar flow: A departure from classical dispersive aerosol transport theories. *Journal of Applied Physiology, 92*(2), 835-845.
Heyder, J., Armbruster, L., Gebhart, J., Grein, E., & Stahlhofen, W. (1975). Total deposition of aerosol particles in the human respiratory tract for nose and mouth breathing. *Journal of Aerosol Science, 6*(5), 311-328. doi: http://dx.doi.org/10.1016/0021-8502(75)90020-8
Heyder, J., Blanchard, J. D., Feldman, H. A., & Brain, J. D. (1988). Convective mixing in human respiratory tract: estimates with aerosol boli. *J Appl Physiol (1985), 64*(3), 1273-1278.
Heyder, J., & Gebhart, J. (1977). Gravitational deposition of particles from laminar aerosol flow through inclined circular tubes. *Journal of Aerosol Science, 8*(4), 289-295. doi: http://dx.doi.org/10.1016/0021-8502(77)90048-9
Heyder, J., Gebhart, J., Rudolf, G., Schiller, C. F., & Stahlhofen, W. (1986). Deposition of particles in the human respiratory tract in the size range 0.005–15 μm. *Journal of Aerosol Science, 17*(5), 811-825.
Hickey, A. J. (2004). *Pharmaceutical inhalation aerosol technology* (2nd ed., rev. and expanded. ed.). New York: Marcel Dekker.
Hickey, A. J. (2007). *Inhalation aerosols : physical and biological basis for therapy* (2nd ed. ed.). New York ; London: Informa Healthcare.
Hinds, W. C. (1999). *Aerosol technology : properties, behavior, and measurement of airborne particles* (2nd ed. ed.). New York ; Chichester: Wiley.
Hirst, P. H., Pitcairn, G. R., Weers, J. G., Tarara, T. E., Clark, A. R., Dellamary, L. A., . . . Newman, S. P. (2002). In vivo lung deposition of hollow porous particles from a pressurized metered dose inhaler. *Pharmaceutical Research, 19*(3), 258-264. doi: Doi 10.1023/A:1014482615914
Hofemeier, P., & Sznitman, J. (2015). Revisiting pulmonary acinar particle transport: convection, sedimentation, diffusion, and their interplay. *Journal of Applied Physiology, 118*(11), 1375-1385. doi: 10.1152/japplphysiol.01117.2014
Hofmann, W. (2011). Modelling inhaled particle deposition in the human lung—A review. *Journal of Aerosol Science, 42*(10), 693-724. doi: 10.1016/j.jaerosci.2011.05.007
Hofmann, W., Balashazy, I., & Koblinger, L. (1995). The Effect of Gravity on Particle Deposition Patterns in Bronchial Airway Bifurcations. *Journal of Aerosol Science, 26*(7), 1161-1168. doi: Doi 10.1016/0021-8502(95)00044-D

Hofmann, W., & Koblinger, L. (1990). Monte-Carlo Modeling of Aerosol Deposition in Human Lungs .2. Deposition Fractions and Their Sensitivity to Parameter Variations. *Journal of Aerosol Science, 21*(5), 675-688. doi: Doi 10.1016/0021-8502(90)90122-E

Hofmann, W., & Koblinger, L. (1992). Monte-Carlo Modeling of Aerosol Deposition in Human Lungs .3. Comparison with Experimental-Data. *Journal of Aerosol Science, 23*(1), 51-63. doi: Doi 10.1016/0021-8502(92)90317-O

Hofmann, W., Martonen, T. B., & Graham, R. C. (1989). Predicted Deposition of Nonhygroscopic Aerosols in the Human Lung as a Function of Subject Age. *Journal of Aerosol Medicine, 2*(1), 49-68. doi: 10.1089/jam.1989.2.49

Huh, D., Fujioka, H., Tung, Y. C., Futai, N., Paine, R., Grotberg, J. B., & Takayama, S. (2007). Acoustically detectable cellular-level lung injury induced by fluid mechanical stresses in microfluidic airway systems. *Proceedings of the National Academy of Sciences of the United States of America, 104*(48), 18886-18891. doi: 10.1073/pnas.0610868104

Huh, D., Matthews, B. D., Mammoto, A., Montoya-Zavala, M., Hsin, H. Y., & Ingber, D. E. (2010). Reconstituting Organ-Level Lung Functions on a Chip. *Science, 328*(5986), 1662-1668. doi: 10.1126/science.1188302

Huchon, G. J., Montgomery, A. B., Lipavsky, A., Hoeffel, J. M., & Murray, J. F. (1987). Respiratory Clearance of Aerosolized Radioactive Solutes of Varying Molecular-Weight. *Journal of Nuclear Medicine, 28*(5), 894-902.

Chamberlain, A. C., & Dyson, E. D. (1956). The Dose to the Trachea and Bronchi from the Decay Products of Radon and Thoron. *British Journal of Radiology, 29*(342), 317-325.

Chan, H. K., Eberl, S., Daviskas, E., Constable, C., & Young, I. (2002). Changes in lung deposition of aerosols due to hygroscopic growth: A fast SPECT study. *Journal of Aerosol Medicine-Deposition Clearance and Effects in the Lung, 15*(3), 307-311. doi: Doi 10.1089/089426802760292654

Chan, T. L., & Lippmann, M. (1980). EXPERIMENTAL MEASUREMENTS AND EMPIRICAL MODELING OF THE REGIONAL DEPOSITION OF INHALED PARTICLES IN HUMANS. *American Industrial Hygiene Association Journal, 41*(6), 399-408. doi: 10.1080/15298668091424942

Chan, T. L., Schreck, R. M., & Lippmann, M. (1980). EFFECT OF THE LARYNGEAL JET ON PARTICLE DEPOSITION IN THE HUMAN TRACHEA AND UPPER BRONCHIAL AIRWAYS. *Journal of Aerosol Science, 11*(5-6), 447-&. doi: 10.1016/0021-8502(80)90117-2

Chen, Y. K., & Yu, C. P. (1991). Sedimentation of Fibers from Laminar Flows in a Horizontal Circular Duct. *Aerosol Science and Technology, 14*(3), 343-347. doi: Doi 10.1080/02786829108959496

Cheng, K. H., Cheng, Y. S., Yeh, H. C., & Swift, D. L. (1997). An experimental method for measuring aerosol deposition efficiency in the human oral airway. *American Industrial Hygiene Association Journal, 58*(3), 207-213. doi: Doi 10.1202/0002-8894(1997)058<0207:Aemfma>2.0.Co;2

Cheng, Y. S. (2014). Mechanisms of pharmaceutical aerosol deposition in the respiratory tract. *AAPS PharmSciTech, 15*(3), 630-640. doi: 10.1208/s12249-014-0092-0

Cheng, Y. S., Holmes, T. D., Gao, J., Guilmette, R. A., Li, S., Surakitbanharn, Y., & Rowlings, C. (2001). Characterization of nasal spray pumps and deposition pattern in a replica of the human nasal airway. *Journal of Aerosol Medicine-Deposition Clearance and Effects in the Lung, 14*(2), 267-280. doi: Doi 10.1089/08942680152484199

Cheng, Y. S., Zhou, Y., & Chen, B. T. (1999). Particle deposition in a cast of human oral airways. *Aerosol Science and Technology, 31*(4), 286-300. doi: Doi 10.1080/027868299304165

Choi, J. I., & Kim, C. S. (2007). Mathematical analysis of particle deposition in human lungs: An improved single path transport model. *Inhalation Toxicology, 19*(11), 925-939. doi: Doi 10.1080/08958370701513014

ICRP. (1994). Human respiratory tract model for radiological protection. A report of a Task Group of the International Commission on Radiological Protection. *Ann ICRP, 24*(1-3), 1-482.

Ingham, D. B. (1984). Diffusion of Aerosols from a Stream Flowing through a Short Cylindrical Pipe. *Journal of Aerosol Science, 15*(5), 637-641. doi: Doi 10.1016/0021-8502(84)90025-9

Inthavong, K., Mouritz, A. P., Dong, J. L., & Tu, J. Y. (2013). Inhalation and deposition of carbon and glass composite fibre in the respiratory airway. *Journal of Aerosol Science, 65*, 58-68. doi: 10.1016/j.jaerosci.2013.07.003

Isaacs, K. K., Schlesinger, R. B., & Martonen, T. B. (2006). Three-dimensional computational fluid dynamics simulations of particle deposition in the tracheobronchial tree. *Journal of Aerosol Medicine-Deposition Clearance and Effects in the Lung, 19*(3), 344-352. doi: DOI 10.1089/jam.2006.19.344

Islam, M. S., Saha, S. C., Sauret, E., Gemci, T., & Gu, Y. T. (2017). Pulmonary aerosol transport and deposition analysis in upper 17 generations of the human respiratory tract. *Journal of Aerosol Science, 108*, 29-43. doi: 10.1016/j.jaerosci.2017.03.004

Jaques, P. A., & Kim, C. S. (2000). Measurement of total lung deposition of inhaled ultrafine particles in healthy men and women. *Inhalation Toxicology, 12*(8), 715-731.

Jayaraju, S. T., Brouns, M., Verbanck, S., & Lacor, C. (2007). Fluid flow and particle deposition analysis in a realistic extrathoracic airway model using unstructured grids. *Journal of Aerosol Science, 38*(5), 494-508. doi: 10.1016/j.jaerosci.2007.03.003

Jeffery, G. B. (1922). The Motion of Ellipsoidal Particles Immersed in a Viscous Fluid. [10.1098/rspa.1922.0078]. *Proceedings of the Royal Society of London. Series A, 102*(715), 161.

Judenhofer, M. S., Wehrl, H. F., Newport, D. F., Catana, C., Siegel, S. B., Becker, M., . . . Pichler, B. J. (2008). Simultaneous PET-MRI: a new approach for functional and morphological imaging. *Nature Medicine, 14*(4), 459-465. doi: 10.1038/nm1700

Kacmarek, R. M., Stoller, J. K., Heuer, A. J., & Egan, D. F. (2013). *Egan's fundamentals of respiratory care* (10th ed.). St. Louis, Mo.: Elsevier/Mosby.

Karl, A., Henry, F. S., & Tsuda, A. (2004). Low Reynolds number viscous flow in an alveolated duct. *Journal of Biomechanical Engineering-Transactions of the Asme, 126*(4), 420-429. doi: 10.1115/1.1784476

Katan, J. T., Hofemeier, P., & Sznitman, J. (2016). Computational Models of Inhalation Therapy in Early Childhood: Therapeutic Aerosols in the Developing Acinus. *Journal of Aerosol Medicine and Pulmonary Drug Delivery, 29*(3), 288-298. doi: 10.1089/jamp.2015.1271

Kelly, J. T., Asgharian, B., Kimbell, J. S., & Wong, B. A. (2004). Particle deposition in human nasal airway replicas manufactured by different methods. Part I: Inertial regime particles. *Aerosol Science and Technology, 38*(11), 1063-1071. doi: 10.1080/027868290883360

Khajeh-Hosseini-Dalasm, N., & Longest, P. W. (2015). Deposition of particles in the alveolar airways: Inhalation and breath-hold with pharmaceutical aerosols. *Journal of Aerosol Science, 79*, 15-30. doi: 10.1016/j.jaerosci.2014.09.003

Kim, C. S. (2009). Deposition of aerosol particles in human lungs: in vivo measurement and modelling. *Biomarkers, 14 Suppl 1*, 54-58. doi: 10.1080/13547500902965286

Kim, C. S., & Fisher, D. M. (1999). Deposition characteristics of aerosol particles in sequentially bifurcating airway models. *Aerosol Science and Technology, 31*(2-3), 198-220. doi: 10.1080/027868299304255

Kim, C. S., Fisher, D. M., Lutz, D. J., & Gerrity, T. R. (1994). Particle Deposition in Bifurcating Airway Models with Varying Airway Geometry. *Journal of Aerosol Science, 25*(3), 567-581. doi: Doi 10.1016/0021-8502(94)90072-8

Kim, C. S., & Hu, S. C. (1998). Regional deposition of inhaled particles in human lungs: comparison between men and women. *Journal of Applied Physiology, 84*(6), 1834-1844.

Kim, C. S., & Hu, S. C. (2006). Total respiratory tract deposition of fine micrometer-sized particles in healthy adults: empirical equations for sex and breathing pattern. *Journal of Applied Physiology, 101*(2), 401-412. doi: 10.1152/japplphysiol.00026.2006

Kim, C. S., Hu, S. C., DeWitt, P., & Gerrity, T. R. (1996). Assessment of regional deposition of inhaled particles in human lungs by serial bolus delivery method. *Journal of Applied Physiology, 81*(5), 2203-2213.

Kim, C. S., & Iglesias, A. J. (1989). Deposition of Inhaled Particles in Bifurcating Airway Models: I. Inspiratory Deposition. *Journal of Aerosol Medicine, 2*(1), 1-14. doi: 10.1089/jam.1989.2.1

Kim, C. S., & Jaques, P. A. (2004). Analysis of total respiratory deposition of inhaled ultrafine particles in adult subjects at various breathing patterns. *Aerosol Science and Technology, 38*(6), 525-540. doi: Doi 10.1080/02786820490465513

Kim, C. S., & Jaques, P. A. (2005). Total lung deposition of ultrafine particles in elderly subjects during controlled breathing. *Inhalation Toxicology, 17*(7-8), 387-399. doi: 10.1080/08958370590929493

Kitayama, A., Yamanaka, S., Kadota, K., Shimosaka, A., Shirakawa, Y., & Hidaka, J. (2009). Diffusion behavior in a liquid-liquid interfacial crystallization by molecular dynamics simulations. *Journal of Chemical Physics, 131*(17). doi: Artn 174707
10.1063/1.3254517

Kleinstreuer, C., & Feng, Y. (2013). Computational Analysis of Non-Spherical Particle Transport and Deposition in Shear Flow With Application to Lung Aerosol Dynamics-A Review. *Journal of Biomechanical Engineering-Transactions of the Asme, 135*(2). doi: Artn 021008
Doi 10.1115/1.4023236

Kleinstreuer, C., & Zhang, Z. (2003). Laminar-to-turbulent fluid-particle flows in a human airway model. [Article]. *International Journal of Multiphase Flow, 29*(2), 271-289. doi: 10.1016/S0301-9322(02)00131-3

Kleinstreuer, C., & Zhang, Z. (2009). An Adjustable Triple-Bifurcation Unit Model for Air-Particle Flow Simulations in Human Tracheobronchial Airways. *Journal of Biomechanical Engineering-Transactions of the Asme, 131*(2). doi: Artn 021007
10.1115/1.3005339

Kleinstreuer, C., Zhang, Z., & Li, Z. (2008). Modeling airflow and particle transport/deposition in pulmonary airways. *Respiratory Physiology & Neurobiology, 163*(1-3), 128-138. doi: DOI 10.1016/j.resp.2008.07.002

Koblinger, L., & Hofmann, W. (1990). Monte-Carlo Modeling of Aerosol Deposition in Human Lungs .1. Simulation of Particle-Transport in a Stochastic Lung Structure. *Journal of Aerosol Science, 21*(5), 661-674. doi: Doi 10.1016/0021-8502(90)90121-D

Kojic, M., & Tsuda, A. (2004). A simple model for gravitational deposition of non-diffusing particles in oscillatory laminar pipe flow and its application to small airways. *Journal of Aerosol Science, 35*(2), 245-261. doi: 10.1016/j.jaerosci.2003.08.005

Koullapis, P., Kassinos, S. C., Muela, J., Perez-Segarra, C., Rigola, J., Lehmkuhl, O., . . . Nicolaou, L. (2017). Regional aerosol deposition in the human airways: The SimInhale benchmark case and a critical assessment of in silico methods. *European Journal of Pharmaceutical Sciences*. doi: https://doi.org/10.1016/j.ejps.2017.09.003

Lambert, A. R., O'Shaughnessy, P., Tawhai, M. H., Hoffman, E. A., & Lin, C. L. (2011). Regional deposition of particles in an image-based airway model: large-eddy simulation and left-right lung ventilation asymmetry. *Aerosol Sci Technol, 45*(1), 11-25. doi: 10.1080/02786826.2010.517578

Landahl, H. (1950). On the removal of air-borne droplets by the human respiratory tract: I. The lung. *Bulletin of Mathematical Biology, 12*(1), 43-56. doi: 10.1007/BF02477345

Laumbach, R. J., & Kipen, H. M. (2012). Respiratory health effects of air pollution: Update on biomass smoke and traffic pollution. *Journal of Allergy and Clinical Immunology, 129*(1), 3-13. doi: 10.1016/j.jaci.2011.11.021

Lazaridis, M., Broday, D. M., Hov, O., & Georgopoulos, P. G. (2001). Integrated exposure and dose modeling and analysis system. 3. Deposition of inhaled particles in the human respiratory tract. *Environmental Science & Technology, 35*(18), 3727-3734. doi: Doi 10.1021/Es001545w

Lee, D. Y., & Lee, J. W. (2003). Characteristics of particle transport in an expanding or contracting alveolated tube. *Journal of Aerosol Science, 34*(9), 1193-1215. doi: 10.1016/s0021-8502(03)00097-1

Li, W. I., Perzl, M., Heyder, J., Langer, R., Brain, J. D., Englemeier, K. H., . . . Edwards, D. A. (1996). Aerodynamics and aerosol particle deaggregation phenomena in model oral-pharyngeal cavities. *Journal of Aerosol Science, 27*(8), 1269-1286. doi: Doi 10.1016/0021-8502(96)00046-8

Lin, T. C., Breysse, P. N., Laube, B. L., & Swift, D. L. (2001). Mouthpiece diameter affects deposition efficiency in cast models of the human oral airways. *Journal of Aerosol Medicine-Deposition Clearance and Effects in the Lung, 14*(3), 335-341. doi: Doi 10.1089/089426801316970295

Lizal, F., Belka, M., Adam, J., Jedelsky, J., & Jicha, M. (2015). A method for in vitro regional aerosol deposition measurement in a model of the human tracheobronchial tree by the positron emission

tomography. *Proceedings of the Institution of Mechanical Engineers Part H-Journal of Engineering in Medicine, 229*(10), 750-757. doi: 10.1177/0954411915600005
Lizal, F., Elcner, J., Hopke, P. K., Jedelsky, J., & Jicha, M. (2012). Development of a realistic human airway model. *Proceedings of the Institution of Mechanical Engineers Part H-Journal of Engineering in Medicine, 226*(H3), 197-207. doi: 10.1177/0954411911430188
Lizal, F., Jedelsky, J., Morgan, K., Bauer, K., Llop, J., Cossio, U., . . . Schnabel, C. (2017). Experimental methods for flow and aerosol measurements in human airways and their replicas. *European Journal of Pharmaceutical Sciences*. doi: https://doi.org/10.1016/j.ejps.2017.08.021
Longest, P. W., & Holbrook, L. T. (2012). In silico models of aerosol delivery to the respiratory tract - development and applications. *Adv Drug Deliv Rev, 64*(4), 296-311. doi: 10.1016/j.addr.2011.05.009
Longest, P. W., Tian, G., & Hindle, M. (2011). Improving the lung delivery of nasally administered aerosols during noninvasive ventilation-an application of enhanced condensational growth (ECG). *J Aerosol Med Pulm Drug Deliv, 24*(2), 103-118. doi: 10.1089/jamp.2010.0849
Longest, P. W., & Vinchurkar, S. (2007a). Effects of mesh style and grid convergence on particle deposition in bifurcating airway models with comparisons to experimental data. *Med Eng Phys, 29*(3), 350-366. doi: 10.1016/j.medengphy.2006.05.012
Longest, P. W., & Xi, J. X. (2007). Effectiveness of direct Lagrangian tracking models for simulating nanoparticle deposition in the upper airways. *Aerosol Science and Technology, 41*(4), 380-397. doi: 10.1080/02786820701203223
Longest, W. P., & Vinchurkar, S. (2007b). Validating CFD predictions of respiratory aerosol deposition: effects of upstream transition and turbulence. *J Biomech, 40*(2), 305-316. doi: 10.1016/j.jbiomech.2006.01.006
Ma, B., & Lutchen, K. R. (2009). CFD simulation of aerosol deposition in an anatomically based human large-medium airway model. *Ann Biomed Eng, 37*(2), 271-285. doi: 10.1007/s10439-008-9620-y
Ma, B. S., & Darquenne, C. (2011). Aerosol deposition characteristics in distal acinar airways under cyclic breathing conditions. *Journal of Applied Physiology, 110*(5), 1271-1282. doi: 10.1152/japplphysiol.00735.2010
Ma, B. S., & Darquenne, C. (2012). Aerosol bolus dispersion in acinar airways-influence of gravity and airway asymmetry. *Journal of Applied Physiology, 113*(3), 442-450. doi: 10.1152/japplphysiol.01549.2011
Majid, H., Madl, P., Hofmann, W., & Alam, K. (2012). Implementation of Charged Particles Deposition in Stochastic Lung Model and Calculation of Enhanced Deposition. *Aerosol Science and Technology, 46*(5), 547-554. doi: 10.1080/02786826.2011.645957
Makino, K., Yamamoto, N., Higuchi, K., Harada, N., Ohshima, H., & Terada, H. (2003). Phagocytic uptake of polystyrene microspheres by alveolar macrophages: effects of the size and surface properties of the microspheres. *Colloids and Surfaces B-Biointerfaces, 27*(1), 33-39. doi: Pii S0927-7765(02)00042-5
Doi 10.1016/S0927-7765(02)00042-5
Martin, A. R., & Finlay, W. H. (2007). A general, algebraic equation for predicting total respiratory tract deposition of micrometer-sized aerosol particles in humans. *Journal of Aerosol Science, 38*(2), 246-253. doi: 10.1016/j.jaerosci.2006.11.002
Martin, A. R., Thompson, R. B., & Finlay, W. H. (2008). MRI Measurement of Regional Lung Deposition in Mice Exposed Nose-Only to Nebulized Superparamagnetic Iron Oxide Nanoparticles. *Journal of Aerosol Medicine and Pulmonary Drug Delivery, 21*(4), 335-341. doi: DOI 10.1089/jamp.2008.0698
Martin, D., & Jacobi, W. (1972). Diffusion Deposition of Small-Sized Particles in Bronchial Tree. *Health Physics, 23*(1), 23-+. doi: Doi 10.1097/00004032-197207000-00003
Martonen, T. B. (1982). Analytical Model of Hygroscopic Particle Behavior in Human Airways. *Bulletin of Mathematical Biology, 44*(3), 425-442. doi: Doi 10.1007/Bf02462290
Martonen, T. B. (1983). Measurement of Particle Dose Distribution in a Model of a Human Larynx and Tracheobronchial Tree. *Journal of Aerosol Science, 14*(1), 11-22. doi: Doi 10.1016/0021-8502(83)90080-0

Martonen, T. B. (1993). Mathematical-Model for the Selective Deposition of Inhaled Pharmaceuticals. *Journal of Pharmaceutical Sciences, 82*(12), 1191-1199. doi: DOI 10.1002/jps.2600821202
Martonen, T. B., Bell, K. A., Phalen, R. F., Wilson, A. F., & Ho, A. (1982). Growth-Rate Measurements and Deposition Modeling of Hygroscopic Aerosols in Human Tracheobronchial Models. *Annals of Occupational Hygiene, 26*(1-4), 93-108. doi: DOI 10.1093/annhyg/26.1.93
Martonen, T. B., Zhang, Z. Q., Yue, G., & Musante, C. J. (2003). Fine particle deposition within human nasal airways. *Inhalation Toxicology, 15*(4), 283-303. doi: 10.1080/08958370390168265
Matida, E. A., Finlay, W. H., Lange, C. F., & Grgic, B. (2004). Improved numerical simulation of aerosol deposition in an idealized mouth-throat. *Journal of Aerosol Science, 35*(1), 1-19. doi: 10.1016/s0021-5802(03)00381-1
Meseguer, G., Gurny, R., & Buri, P. (1994). In-Vivo Evaluation of Dosage Forms - Application of Gamma-Scintigraphy to Non-Enteral Routes of Administration. *Journal of Drug Targeting, 2*(4), 269-288. doi: Doi 10.3109/10611869409015908
Miller, W. F. (1973). Aerosol Therapy in Acute and Chronic Respiratory-Disease. *Archives of Internal Medicine, 131*(1), 148-155. doi: DOI 10.1001/archinte.131.1.148
Mitchell, J., Newman, S., & Chan, H. K. (2007). In Vitro and In Vivo Aspects of Cascade Impactor Tests and Inhaler Performance: A Review. *Aaps Pharmscitech, 8*(4).
Mitchell, J. P., & Nagel, M. W. (2003). Cascade impactors for the size characterization of aerosols from medical inhalers: Their uses and limitations. *Journal of Aerosol Medicine-Deposition Clearance and Effects in the Lung, 16*(4), 341-+. doi: Doi 10.1089/089426803772455622
Mitsakou, C., Helmis, C., & Housiadas, C. (2005). Eulerian modelling of lung deposition with sectional representation of aerosol dynamics. *Journal of Aerosol Science, 36*(1), 75-94. doi: 10.1016/j.jaerosci.2004.08.008
Muir, D. C., Sweetland, K., & Love, R. G. (1970). Inhaled aerosol boluses in man. *Inhaled Part, 1*, 81-90.
Musante, C. J., Schroeter, J. D., Rosati, J. A., Crowder, T. M., Hickey, A. J., & Martonen, T. B. (2002). Factors affecting the deposition of inhaled porous drug particles. *Journal of Pharmaceutical Sciences, 91*(7), 1590-1600. doi: 10.1002/jps.10152
Myojo, T. (1987). Deposition of Fibrous Aerosol in Model Bifurcating Tubes. *Journal of Aerosol Science, 18*(3), 337-&. doi: Doi 10.1016/0021-8502(87)90027-9
Myojo, T. (1990). The Effect of Length and Diameter on the Deposition of Fibrous Aerosol in a Model Lung Bifurcation. *Journal of Aerosol Science, 21*(5), 651-659. doi: Doi 10.1016/0021-8502(90)90120-M
Myojo, T., & Takaya, M. (2001). Estimation of fibrous aerosol deposition in upper bronchi based on experimental data with model bifurcation. *Industrial Health, 39*(2), 141-149. doi: DOI 10.2486/indhealth.39.141
Nahar, K., Gupta, N., Gauvin, R., Absar, S., Patel, B., Gupta, V., . . . Ahsan, F. (2013). In vitro, in vivo and ex vivo models for studying particle deposition and drug absorption of inhaled pharmaceuticals. *Eur J Pharm Sci, 49*(5), 805-818. doi: 10.1016/j.ejps.2013.06.004
Nandiyanto, A. B. D., & Okuyama, K. (2011). Progress in developing spray-drying methods for the production of controlled morphology particles: From the nanometer to submicrometer size ranges. *Advanced Powder Technology, 22*(1), 1-19. doi: DOI 10.1016/j.apt.2010.09.011
NCRP National Council on Radiation Protection., (1997). *Deposition, Retention, and Dosimetry of Inhaled Radioactive Substances: Recommendations of the National Council on Radiation Protection and Measurements*: National Council on Radiation Protection and Measurements.
Newman, S., & Fleming, J. (2011). Challenges in assessing regional distribution of inhaled drug in the human lungs. *Expert Opinion on Drug Delivery, 8*(7), 841-855. doi: Doi 10.1517/17425247.2011.577063
Newman, S. P., Pitcairn, G. R., Hirst, P. H., & Rankin, L. (2003). Radionuclide imaging technologies and their use in evaluating asthma drug deposition in the lungs. *Advanced Drug Delivery Reviews, 55*(7), 851-867. doi: 10.1016/s0169-409x(03)00081-4
Nixon, W., & Egan, M. J. (1987). Modeling Study of Regional Deposition of Inhaled Aerosols with Special Reference to Effects of Ventilation Asymmetry. *Journal of Aerosol Science, 18*(5), 563-579. doi: Doi 10.1016/0021-8502(87)90069-3

Nolan, L. M., Tajber, L., McDonald, B. F., Barham, A. S., Corrigan, O. I., & Healy, A. M. (2009). Excipient-free nanoporous microparticles of budesonide for pulmonary delivery. *European Journal of Pharmaceutical Sciences, 37*(5), 593-602. doi: 10.1016/j.ejps.2009.05.007

Nordlund, M., Belka, M., Kuczaj, A. K., Lizal, F., Jedelsky, J., Elcner, J., . . . Hoeng, J. (2017). Multicomponent aerosol particle deposition in a realistic cast of the human upper respiratory tract. *Inhal Toxicol, 29*(3), 113-125. doi: 10.1080/08958378.2017.1315196

Nowak, N., Kakade, P. P., & Annapragada, A. V. (2003). Computational fluid dynamics simulation of airflow and aerosol deposition in human lungs. *Annals of Biomedical Engineering, 31*(4), 374-390. doi: 10.1114/1.1560632

Oakes, J. M., Breen, E. C., Scadeng, M., Tchantchou, G. S., & Darquenne, C. (2014). MRI-based measurements of aerosol deposition in the lung of healthy and elastase-treated rats. *Journal of Applied Physiology, 116*(12), 1561-1568. doi: 10.1152/japplphysiol.01165.2013

Oakes, J. M., Day, S., Weinstein, S. J., & Robinson, R. J. (2010). Flow Field Analysis in Expanding Healthy and Emphysematous Alveolar Models Using Particle Image Velocimetry. *Journal of Biomechanical Engineering-Transactions of the Asme, 132*(2). doi: Artn 021008
10.1115/1.4000870

Oberdorster, G., Sharp, Z., Atudorei, V., Elder, A., Gelein, R., Kreyling, W., & Cox, C. (2004). Translocation of inhaled ultrafine particles to the brain. *Inhalation Toxicology, 16*(6-7), 437-445. doi: 10.1080/08958370490439597

Oldham, M. J., Phalen, R. F., & Heistracher, T. (2000). Computational fluid dynamic predictions and experimental results for particle deposition in an airway model. *Aerosol Science and Technology, 32*(1), 61-71. doi: Doi 10.1080/027868200303939

Owlcation. (2017). The Upper respiratory tract Retrieved 04.07.2017, 2017, from http://intranet.tdmu.edu.ua/data/kafedra/internal/meds/classes_stud/en/nurse/en/BSN-(4y)/4%20year/fall%20semester/Health%20Alterations%202%20Practicum/11.%20Noninfectious%20problems%20of%20the%20upper%20respiratory%20tract.htm

Patel, B., Gauvin, R., Absar, S., Gupta, V., Gupta, N., Nahar, K., . . . Ahsan, F. (2012). Computational and bioengineered lungs as alternatives to whole animal, isolated organ, and cell-based lung models. *American Journal of Physiology-Lung Cellular and Molecular Physiology, 303*(9), L733-L747. doi: 10.1152/ajplung.00076.2012

Patra, A. L., & Afify, E. M. (1983). An Experimental-Study of Velocity Distribution in a Human-Lung Cast. *Journal of Biomechanical Engineering-Transactions of the Asme, 105*(4), 381-388.

Paz, C., Suarez, E., Concheiro, M., & Porteiro, J. (2017). CFD Transient Simulation of a Breathing Cycle in an Oral-Nasal Extrathoracic Model. *Journal of Applied Fluid Mechanics, 10*(3), 777-784. doi: 10.18869/acadpub.jafm.73.238.25348

Phipps, P. R., Gonda, I., Bailey, D. L., Borham, P., Bautovich, G., & Anderson, S. D. (1989). Comparisons of Planar and Tomographic Gamma Scintigraphy to Measure the Penetration Index of Inhaled Aerosols. *American Review of Respiratory Disease, 139*(6), 1516-1523.

Pich, J. (1972). Theory of gravitational deposition of particles from laminar flows in channels. *Journal of Aerosol Science, 3*(5), 351-361. doi: http://dx.doi.org/10.1016/0021-8502(72)90090-0

Pirozynski, M., & Sosnowski, T. R. (2016). Inhalation devices: from basic science to practical use, innovative vs generic products. *Expert Opinion on Drug Delivery, 13*(11), 1559-1571. doi: 10.1080/17425247.2016.1198774

Raabe, O. G. (1976). *Tracheobronchial geometry: Human, dog, rat, hamster*: U.S. Government Printing Office.

Rahimi-Gorji, M., Gorji, T. B., & Gorji-Bandpy, M. (2016). Details of regional particle deposition and airflow structures in a realistic model of human tracheobronchial airways: two-phase flow simulation. *Computers in Biology and Medicine, 74*, 1-17. doi: 10.1016/j.compbiomed.2016.04.017

Rao, S., & Verkman, A. S. (2000). Analysis of organ physiology in transgenic mice. *American Journal of Physiology-Cell Physiology, 279*(1), C1-C18.

Robinson, R. J., Oldham, M. J., Clinkenbeard, R. E., & Rai, P. (2006). Experimental and numerical smoke carcinogen deposition in a multi-generation human replica tracheobronchial model. *Annals of Biomedical Engineering, 34*(3), 373-383. doi: DOI 10.1007/s10439-005-9049-5

Robinson, R. J., & Yu, C. P. (2001). Deposition of cigarette smoke particles in the human respiratory tract. *Aerosol Science and Technology, 34*(2), 202-215. doi: 10.1080/027868201300034844
Rosenberg, M., Kopelman, I. J., & Talmon, Y. (1990). Factors Affecting Retention in Spray-Drying Microencapsulation of Volatile Materials. *Journal of Agricultural and Food Chemistry, 38*(5), 1288-1294. doi: DOI 10.1021/jf00095a030
Rosner, F. (1984). Maimonides,Moses Treatise on Asthma. *Journal of Asthma, 21*(2), 119-129. doi: Doi 10.3109/02770908409077409
Rostami, A. A. (2009). Computational Modeling of Aerosol Deposition in Respiratory Tract: A Review. *Inhalation Toxicology, 21*(4), 262-290. doi: 10.1080/08958370802448987
Rudolf, G., Gebhart, J., Heyder, J., Scheuch, G., & Stahlhofen, W. (1983). Modeling the Deposition of Aerosol-Particles in the Human Respiratory-Tract. *Journal of Aerosol Science, 14*(3), 188-192. doi: Doi 10.1016/0021-8502(83)90024-1
Rudolf, G., Kobrich, R., & Stahlhofen, W. (1990). Modeling and Algebraic Formulation of Regional Aerosol Deposition in Man. *Journal of Aerosol Science, 21*, S403-S406. doi: Doi 10.1016/0021-8502(90)90266-Z
Russo, J., Robinson, R., & Oldham, M. J. (2008). Effects of cartilage rings on airflow and particle deposition in the trachea and main bronchi. *Med Eng Phys, 30*(5), 581-589. doi: 10.1016/j.medengphy.2007.06.010
Sandeau, J., Katz, I., Fodil, R., Louis, B., Apiou-Sbirlea, G., Caillibotte, G., & Isabey, D. (2010). CFD simulation of particle deposition in a reconstructed human oral extrathoracic airway for air and helium–oxygen mixtures. *Journal of Aerosol Science, 41*(3), 281-294. doi: 10.1016/j.jaerosci.2009.12.001
Shanley, K. T., & Ahmadi, G. (2011). A Numerical Model for Simulating the Motions of Ellipsoidal Fibers Suspended in Low Reynolds Number Shear Flows. *Aerosol Science and Technology, 45*(7), 838-848. doi: 10.1080/02786826.2011.566293
Shanley, K. T., Ahmadi, G., Hopke, P. K., & Cheng, Y.-S. (2016). Simulated airflow and rigid fiber behavior in a realistic nasal airway model. *Particulate Science and Technology*, 1-10. doi: 10.1080/02726351.2016.1208694
Shanley, K. T., Zamankhan, P., Ahmadi, G., Hopke, P. K., & Cheng, Y. S. (2008). Numerical Simulations Investigating the Regional and Overall Deposition Efficiency of the Human Nasal Cavity. *Inhalation Toxicology, 20*(12), 1093-1100. doi: 10.1080/08958370802130379
Shi, H., Kleinstreuer, C., & Zhang, Z. (2006). Laminar airflow and nanoparticle or vapor deposition in a human nasal cavity model. *Journal of Biomechanical Engineering-Transactions of the Asme, 128*(5), 697-706. doi: 10.1115/1.2244574
Shoyele, S. A., & Cawthome, S. (2006). Particle engineering techniques for inhaled biopharmaceuticals. *Advanced Drug Delivery Reviews, 58*(9-10), 1009-1029. doi: DOI 10.1016/j.addr.2006.07.010
Scheckman, J. H., & McMurry, P. H. (2011). Deposition of silica agglomerates in a cast of human lung airways: Enhancement relative to spheres of equal mobility and aerodynamic diameter. *Journal of Aerosol Science, 42*(8), 508-516. doi: 10.1016/j.jaerosci.2011.05.003
Scheuch, G. (1994). Particle Recovery from Human Conducting Airways after Shallow Aerosol Bolus Inhalation. *Journal of Aerosol Science, 25*(5), 957-973. doi: Doi 10.1016/0021-8502(94)90059-0
Scheuch, G., Bennett, W., Borgstrom, L., Clark, A., Dalby, R., Dolovich, M., . . . Newman, S. (2010). Deposition, imaging, and clearance: what remains to be done? *J Aerosol Med Pulm Drug Deliv, 23 Suppl 2*, S39-57. doi: 10.1089/jamp.2010.0839
Schiller-Scotland, C. F., Hlawa, R., & Gebhart, J. (1994). Experimental-Data for Total Deposition in the Respiratory-Tract of Children. *Toxicology Letters, 72*(1-3), 137-144. doi: Doi 10.1016/0378-4274(94)90020-5
Schlesinger, R. B., Bohning, D. E., Chan, T. L., & Lippmann, M. (1977). Particle deposition in a hollow cast of the human tracheobronchial tree. *Journal of Aerosol Science, 8*(6), 429-445. doi: http://dx.doi.org/10.1016/0021-8502(77)90036-2
Schlesinger, R. B., Gurman, J. L., & Lippmann, M. (1982). Particle Deposition within Bronchial Airways - Comparisons Using Constant and Cyclic Inspiratory Flows. *Annals of Occupational Hygiene, 26*(1-4), 47-&. doi: DOI 10.1093/annhyg/26.1.47

Schlesinger, R. B., & Lippmann, M. (1972). Particle Deposition in Casts of Human Upper Tracheobronchial Tree. *American Industrial Hygiene Association Journal, 33*(4), 237-+. doi: Doi 10.1080/0002889728506636

Schmidt, A., Zidowitz, S., Kriete, A., Denhard, T., Krass, S., & Peitgen, H. O. (2004). A digital reference model of the human bronchial tree. *Computerized Medical Imaging and Graphics, 28*(4), 203-211. doi: 10.1016/j.compmedimag.2004.01.001

Schroeter, J. D., Garcia, G. J., & Kimbell, J. S. (2011). Effects of Surface Smoothness on Inertial Particle Deposition in Human Nasal Models. *J Aerosol Sci, 42*(1), 52-63. doi: 10.1016/j.jaerosci.2010.11.002

Schroeter, J. D., Tewksbury, E. W., Wong, B. A., & Kimbell, J. S. (2015). Experimental Measurements and Computational Predictions of Regional Particle Deposition in a Sectional Nasal Model. *Journal of Aerosol Medicine and Pulmonary Drug Delivery, 28*(1), 20-29. doi: 10.1089/jamp.2013.1084

Sinclair, D., & La Mer, V. K. (1949). Light Scattering as a Measure of Particle Size in Aerosols. The Production of Monodisperse Aerosols. *Chemical Reviews, 44*(2), 245-267. doi: 10.1021/cr60138a001

Smith, S., Cheng, U. S., & Yeh, H. C. (2001). Deposition of ultrafine particles in human tracheobronchial airways of adults and children. *Aerosol Science and Technology, 35*(3), 697-709. doi: Doi 10.1080/02786820152546743

Smyth, H. D. C., & Hickey, A. J. (2011). *Controlled pulmonary drug delivery*. New York ; London: Springer.

Soni, B., & Aliabadi, S. (2013). Large-scale CFD simulations of airflow and particle deposition in lung airway. *Computers & Fluids, 88*, 804-812. doi: 10.1016/j.compfluid.2013.06.015

Sood, B. G., Shen, Y. M., Latif, Z., Chen, X. G., Sharp, J., Neelavalli, J., . . . Haacke, E. M. (2008). Aerosol delivery in ventilated newborn pigs: An MRI evaluation. *Pediatric Research, 64*(2), 159-164.

Sosnowski, T. R., Moskal, A., & Gradon, L. (2006). Dynamics of oropharyngeal aerosol transport and deposition with the realistic flow pattern. *Inhalation Toxicology, 18*(10), 773-780. doi: 10.1080/08958370600748737

Stahlhofen, W., Gebhart, J., Heyder, J., & Scheuch, G. (1983). New Regional Deposition Data of the Human Respiratory-Tract. *Journal of Aerosol Science, 14*(3), 186-188. doi: Doi 10.1016/0021-8502(83)90022-8

Stahlhofen, W., Rudolf, G., & James, A. C. (1989). Intercomparison of Experimental Regional Aerosol Deposition Data. *Journal of Aerosol Medicine, 2*(3), 285-308. doi: 10.1089/jam.1989.2.285

Stapleton, K. W., Guentsch, E., Hoskinson, M. K., & Finlay, W. H. (2000). On the suitability of k–ε turbulence modeling for aerosol deposition in the mouth and throat: a comparison with experiment. *Journal of Aerosol Science, 31*(6), 739-749.

Storey-Bishoff, J., Noga, M., & Finlay, W. H. (2008). Deposition of micrometer-sized aerosol particles in infant nasal airway replicas. *Journal of Aerosol Science, 39*(12), 1055-1065. doi: 10.1016/j.jaerosci.2008.07.011

Sturm, R. (2016). Local lung deposition of ultrafine particles in healthy adults: experimental results and theoretical predictions. *Annals of Translational Medicine, 4*(21). doi: ARTN 420
10.21037/atm.2016.11.13

Su, W. C., & Cheng, Y. S. (2005). Deposition of fiber in the human nasal airway. *Aerosol Science and Technology, 39*(9), 888-901. doi: 10.1080/02786820500295685

Su, W. C., & Cheng, Y. S. (2006). Fiber deposition pattern in two human respiratory tract replicas. *Inhalation Toxicology, 18*(10), 749-760. doi: 10.1080/08958370600748513

Su, W. C., & Cheng, Y. S. (2009). Deposition of man-made fibers in human respiratory airway casts. *Journal of Aerosol Science, 40*(3), 270-284. doi: 10.1016/j.jaerosci.2008.11.003

Su, W. C., & Cheng, Y. S. (2015). Estimation of carbon nanotubes deposition in a human respiratory tract replica. *Journal of Aerosol Science, 79*, 72-85. doi: 10.1016/j.jaerosci.2014.09.005

Sussman, R. G., Cohen, B. S., & Lippmann, M. (1991). Asbestos Fiber Deposition in a Human Tracheobronchial Cast. I. Experimental. *Inhalation Toxicology, 3*(2), 145-160. doi: doi:10.3109/08958379109145281

Swift, D. L. (1991). Inspiratory Inertial Deposition of Aerosols in Human Nasal Airway Replicate Casts - Implication for the Proposed Ncrp Lung Model. *Radiation Protection Dosimetry, 38*(1-3), 29-34.

Swift, D. L. (1992). Apparatus and method for measuring regional distribution of therapeutic aerosols and comparing delivery systems. *Journal of Aerosol Science, 23*, 495-498. doi: http://dx.doi.org/10.1016/0021-8502(92)90457-7

Sznitman, J. (2013). Respiratory microflows in the pulmonary acinus. *Journal of Biomechanics, 46*(2), 284-298. doi: 10.1016/j.jbiomech.2012.10.028

Sznitman, J., Heimsch, T., Wildhaber, J. H., Tsuda, A., & Rosgen, T. (2009). Respiratory Flow Phenomena and Gravitational Deposition in a Three-Dimensional Space-Filling Model of the Pulmonary Acinar Tree. *Journal of Biomechanical Engineering-Transactions of the Asme, 131*(3). doi: Artn 031010
10.1115/1.3049481

Takano, H., Nishida, N., Itoh, M., Hyo, N., & Majima, Y. (2006). Inhaled particle deposition in unsteady-state respiratory flow at a numerically constructed model of the human larynx. *Journal of Aerosol Medicine-Deposition Clearance and Effects in the Lung, 19*(3), 314-328. doi: DOI 10.1089/jam.2006.19.314

Tanaka, M., Yamanaka, S., Shirakawa, Y., Shimosaka, A., & Hidaka, J. (2011). Preparation of porous particles by liquid-liquid interfacial crystallization. *Advanced Powder Technology, 22*(1), 125-130. doi: DOI 10.1016/j.apt.2010.09.012

Task Group on Lung Dynamics. (1966). Deposition and retention models for internal dosimetry of the human respiratory tract. Task group on lung dynamics. *Health Phys, 12*(2), 173-207.

Taulbee, D. B., & Yu, C. P. (1975). Theory of Aerosol Deposition in Human Respiratory-Tract. *Journal of Applied Physiology, 38*(1), 77-85.

Taulbee, D. B., Yu, C. P., & Heyder, J. (1978). Aerosol Transport in Human Lung from Analysis of Single Breaths. *Journal of Applied Physiology, 44*(5), 803-812.

Thompson, R. B., & Finlay, W. H. (2012). Using MRI to Measure Aerosol Deposition. *Journal of Aerosol Medicine and Pulmonary Drug Delivery, 25*(2), 55-62. doi: DOI 10.1089/jamp.2011.0897

Tian, L., & Ahmadi, G. (2012). Transport and Deposition of Micro-and Nano-Particles in Human Tracheobronchial Tree by an Asymmetric Multi-Level Bifurcation Model. *The Journal of Computational Multiphase Flows, 4*(2), 159-182. doi: 10.1260/1757-482X.4.2.159

Tian, L., & Ahmadi, G. (2013). Fiber transport and deposition in human upper tracheobronchial airways. *Journal of Aerosol Science, 60*, 1-20. doi: 10.1016/j.jaerosci.2013.02.001

Tian, L., Ahmadi, G., Wang, Z., & Hopke, P. K. (2012). Transport and deposition of ellipsoidal fibers in low Reynolds number flows. *Journal of Aerosol Science, 45*, 1-18. doi: 10.1016/j.jaerosci.2011.09.001

Tian, L., Shang, Y., Chen, R., Bai, R., Chen, C. Y., Inthavong, K., & Tu, J. Y. (2017). A combined experimental and numerical study on upper airway dosimetry of inhaled nanoparticles from an electrical discharge machine shop. *Particle and Fibre Toxicology, 14*. doi: ARTN 24
10.1186/s12989-017-0203-7

Tsuda, A., Henry, F. S., & Butler, J. P. (2008). Gas and aerosol mixing in the acinus. *Respir Physiol Neurobiol, 163*(1-3), 139-149. doi: 10.1016/j.resp.2008.02.010

Tsuda, A., Henry, F. S., & Butler, J. P. (2013). Particle Transport and Deposition: Basic Physics of Particle Kinetics. *Comprehensive Physiology, 3*(4), 1437-1471. doi: 10.1002/cphy.c100085

Van Wijk, A. M., & Patterson, H. S. (1940). The Percentage of Particles of Different Sizes Removed from Dust-Laden Air by Breathing. *Journal of Industrial Hygiene, 22*, 31-35.

Vanbever, R., Mintzes, J., Wang, J., Nice, J., Chen, D., Batycky, R., . . . Edwards, D. (1999). Formulation and physical characterization of large porous particles for inhalation. [Article]. *Pharmaceutical Research, 16*(11), 1735-1742. doi: 10.1023/A:1018910200420

Verbanck, S., Ghorbaniasl, G., Biddiscombe, M. F., Dragojlovic, D., Ricks, N., Lacor, C., . . . Usmani, O. S. (2016). Inhaled Aerosol Distribution in Human Airways: A Scintigraphy-Guided Study in a 3D Printed Model. *Journal of Aerosol Medicine and Pulmonary Drug Delivery, 29*(6), 525-533. doi: 10.1089/jamp.2016.1291

Versteeg, H. K., & Malalasekera, W. (2007). *An introduction to computational fluid dynamics : the finite volume method* (2nd ed. ed.). Harlow: Prentice Hall.
Wang, C.-S. (1975). Gravitational deposition of particles from laminar flows in inclined channels. *Journal of Aerosol Science, 6*(3), 191-204. doi: http://dx.doi.org/10.1016/0021-8502(75)90088-9
Wang, H. C., Sebrie, C., Ruaud, J. P., Guillot, G., Bouazizi-Verdier, K., Willoquet, G., . . . de Rochefort, L. (2016). Aerosol Deposition in the Lungs of Spontaneously Breathing Rats Using Gd-DOTA-Based Contrast Agents and Ultra-Short Echo Time MRI at 1.5 Tesla. *Magnetic Resonance in Medicine, 75*(2), 594-605. doi: 10.1002/mrm.25617
Watkins-Pitchford, W., & Moir, J. (1916). *On the nature of the doubly-refracting particles seen in microscopic sections of silicotic lungs : and an improved method for disclosing siliceous particles in such sections*. Johannesburg: Published by the Institute.
Weers, J., Metzheiser, B., Taylor, G., Warren, S., Meers, P., & Perkins, W. R. (2009). A gamma scintigraphy study to investigate lung deposition and clearance of inhaled amikacin-loaded liposomes in healthy male volunteers. *J Aerosol Med Pulm Drug Deliv, 22*(2), 131-138.
Weibel, E. R. (1963). *Morphometry of the human lung*. Berlin: [s.n.].
Weisz, G. (1995). *The medical mandarins : the French Academy of Medicine in the nineteenth and early twentieth centuries*. New York ; Oxford: Oxford University Press.
Wilson, I. B., & Lamer, V. K. (1948). The Retention of Aerosol Particles in the Human Respiratory Tract as a Function of Particle Radius. *Journal of Industrial Hygiene and Toxicology, 30*(5), 265-280.
Xi, J. X., & Longest, P. W. (2007). Transport and deposition of micro-aerosols in realistic and simplified models of the oral airway. *Annals of Biomedical Engineering, 35*(4), 560-581. doi: DOI 10.1007/s10439-006-9245-y
Xi, J. X., Longest, P. W., & Martonen, T. B. (2008). Effects of the laryngeal jet on nano- and microparticle transport and deposition in an approximate model of the upper tracheobronchial airways. *Journal of Applied Physiology, 104*(6), 1761-1777. doi: 10.1152/japplphysiol.01233.2007
Yamada, Y., Koizumi, A., & Inaba, J. (1998). A new method of casting human respiratory tract for aerosol deposition studies. *Radiation Protection Dosimetry, 79*(1-4), 269-272.
Yeh, H. C., Cuddihy, R. G., Phalen, R. F., & Chang, I. Y. (1996). Comparisons of calculated respiratory tract deposition of particles based on the proposed NCRP model and the new ICRP66 model. *Aerosol Science and Technology, 25*(2), 134-140. doi: 10.1080/02786829608965386
Yeh, H. C., & Schum, G. M. (1980). Models of Human-Lung Airways and Their Application to Inhaled Particle Deposition. *Bulletin of Mathematical Biology, 42*(3), 461-480. doi: Doi 10.1007/Bf02460796
Yeh, H. C., Schum, G. M., & Duggan, M. T. (1979). Anatomic Models of the Tracheobronchial and Pulmonary Regions of the Rat. *Anatomical Record, 195*(3), 483-492. doi: DOI 10.1002/ar.1091950308
Yernault, J. C. (1994). Inhalation-Therapy - a Historical-Perspective. *European Respiratory Review, Vol 4, Review No 18, January 1994*, 65-67.
Yu, C., Chen, S. H., Wang, G., & Wang, Y. (2016). Numerical Analysis of Flow Characteristics for the Normal Human Upper Airway. *Biomedical Engineering-Applications Basis Communications, 28*(2). doi: Artn 1650012
10.4015/S1016237216500125
Yu, C. P., & Cohen, B. S. (1994). Tracheobronchial Airway Deposition of Ultrafine Particles. *Inhaled Particles Vii*, 83-89.
Yu, C. P., & Diu, C. K. (1982). A Probabilistic Model for Intersubject Deposition Variability of Inhaled Particles. *Aerosol Science and Technology, 1*(4), 355-362. doi: 10.1080/02786828208958600
Zamankhan, P., Ahmadi, G., Wang, Z., Hopke, P. K., Cheng, Y.-S., Su, W. C., & Leonard, D. (2006). Airflow and Deposition of Nano-Particles in a Human Nasal Cavity. *Aerosol Science and Technology, 40*(6), 463-476. doi: 10.1080/02786820600660903
Zhang, L., Asgharian, B., & Anjilvel, S. (1996). Inertial and interceptional deposition of fibers in a bifurcating airway. *Journal of Aerosol Medicine-Deposition Clearance and Effects in the Lung, 9*(3), 419-430. doi: DOI 10.1089/jam.1996.9.419

Zhang, L., Asgharian, B., & Anjilvel, S. (1997). Inertial deposition of particles in the human upper airway bifurcations. *Aerosol Science and Technology, 26*(2), 97-110. doi: Doi 10.1080/02786829708965417

Zhang, Y., Finlay, W. H., & Matida, E. A. (2004). Particle deposition measurements and numerical simulation in a highly idealized mouth-throat. *Journal of Aerosol Science, 35*(7), 789-803. doi: 10.1016/j.jaerosci.2003.12.006

Zhang, Z., & Kleinstreuer, C. (2001). Effect of particle inlet distributions on deposition in a triple bifurcation lung airway model. *Journal of Aerosol Medicine-Deposition Clearance and Effects in the Lung, 14*(1), 13-29. doi: Doi 10.1089/08942680152007864

Zhang, Z., & Kleinstreuer, C. (2004). Airflow structures and nano-particle deposition in a human upper airway model. *Journal of Computational Physics, 198*(1), 178-210. doi: 10.1016/j.jcp.2003.11.034

Zhang, Z., Kleinstreuer, C., Donohue, J. F., & Kim, C. S. (2005). Comparison of micro- and nano-size particle depositions in a human upper airway model. *Journal of Aerosol Science, 36*(2), 211-233. doi: 10.1016/j.jaerosci.2004.08.006

Zhang, Z., Kleinstreuer, C., & Kim, C. S. (2001). Flow structure and particle transport in a triple bifurcation airway model. *Journal of Fluids Engineering-Transactions of the Asme, 123*(2), 320-330. doi: Doi 10.1115/1.1359525

Zhang, Z., Kleinstreuer, C., & Kim, C. S. (2008). Airflow and Nanoparticle Deposition in a 16-Generation Tracheobronchial Airway Model. *Annals of Biomedical Engineering, 36*(12), 2095-2110. doi: 10.1007/s10439-008-9583-z

Zhou, Y., & Cheng, Y. (2005). Partical deposition in a cast of human tracheobronchial airways. *Aerosol science and technology, 39,* 492-500.

Zhou, Y., Su, W. C., & Cheng, Y. S. (2007). Fiber deposition in the tracheobronchial region: Experimental measurements. *Inhalation Toxicology, 19*(13), 1071-1078. doi: 10.1080/08958370701626634

Zwartz, G. J., & Guilmette, R. A. (2001). Effect of flow rate on particle deposition in a replica of a human nasal airway. *Inhalation Toxicology, 13*(2), 109-127.

List of publications

Papers published in journals with impact factor

- BĚLKA, M.; LÍZAL, F.; JEDELSKÝ, J.; ŠTARHA, P.; DRUCKMÜLLEROVÁ, H.; JÍCHA, M. Application of image analysis method to detection and counting of glass fibers from filter samples. AEROSOL SCIENCE AND TECHNOLOGY, 2016, vol. 50, no. 4, p. 352-363. ISSN: 0278-6826.
- BĚLKA, M.; LÍZAL, F.; JEDELSKÝ, J.; ELCNER, J.; HOPKE, P.; JÍCHA, M. Deposition of glass fibers in a physically realistic replica of the human respiratory tract. JOURNAL OF AEROSOL SCIENCE, 2017, no. 1, p. 1-15. ISSN: 0021-8502.
- LÍZAL, F.; BĚLKA, M.; ADAM, J.; JEDELSKÝ, J.; JÍCHA, M. A method for in vitro regional aerosol deposition measurement in a model of the human tracheobronchial tree by the positron emission tomography. PROCEEDINGS OF THE INSTITUTION OF MECHANICAL ENGINEERS PART H-JOURNAL OF ENGINEERING IN MEDICINE, 2015, vol. 229, no. 10, p. 750-757. ISSN: 0954-4119.
- NORDLUND, M.; BĚLKA, M.; KUCZAJ, A.; LÍZAL, F.; JEDELSKÝ, J.; ELCNER, J.; JÍCHA, M. Multicomponent aerosol particle deposition in a realistic cast of the human upper respiratory tract. Inhalation Toxicology, 2017, vol. 29, no. 3, p. 113-125. ISSN: 1091-7691.
- FREDERIX, E.; KUCZAJ, A.; NORDLUND, M.; BĚLKA, M.; LÍZAL, F.; JEDELSKÝ, J.; ELCNER, J.; JÍCHA, M.; GEURTS, B. Simulation of size-dependent aerosol deposition in a realistic model of the upper human airways. JOURNAL OF AEROSOL SCIENCE, 2017, vol. 115, no. 1, p. 29-45. ISSN: 0021-8502.

Papers from conference proceedings listed in CPCI Thomson Reuters database or Scopus

- BĚLKA, M.; LÍZAL, F.; JEDELSKÝ, J.; JÍCHA, M. Analysis of fiber deposition using automatic image processing method. In International Conference Experimental Fluid Mechanics 2012 Conference proceedings. EPJ Web of Conferences. FRANCE: E D P SCIENCES, 2013. p. 1-4. ISBN: 978-80-7372-912-7. ISSN: 2100-014X.
- BĚLKA, M.; LIPPAY, J.; LÍZAL, F.; JEDELSKÝ, J.; JÍCHA, M. Comparison of methods for evaluation of aerosol deposition in the model of human lungs. In EPJ Web of Conferences. EPJ Web of Conferences. FRANCE: E D P SCIENCES, 2014. p. 82-85. ISBN: 978-80-260-5375-0. ISSN: 2100-014X.
- BĚLKA, M.; JEDELSKÝ, J.; ZAREMBA, M.; MALÝ, M.; LÍZAL, F. Measurement of Air Flow in Trachea Using Particle Image Velocimetry and Laser-Doppler Anemometry. In Engineering Mechanics 2014. Engineering mechanics 2014. 1. Svratka: 2014. p. 72-75. ISBN: 978-80-214-4871-1. ISSN: 1805-8248.
- BĚLKA, M.; JEDELSKÝ, J.; ELCNER, J. Measurement of Cyclic Flows in Trachea Using PIV and Numerical simulation. In EPJ Web of Conferences. EPJ Web of Conferences. France: EDP Sciences, 2015. p. 1-4. ISSN: 2100-014X.
- BĚLKA, M.; LÍZAL, F.; JEDELSKÝ, J.; JÍCHA, M.; POSPÍŠIL, J. Measurement of an electronic cigarette aerosol size distribution during a puff. In EPJ Web of Conferences. EPJ Web of Conferences. France: EDP SCIENCES, 2017. p. 1-4. ISSN: 2100-014X.

List of symbols and abbreviations

Symbol	Units	Description
A	[m^2]	Total cross-sectional area
A_T	[m^2]	Cumulative cross–sectional area of all airways
A_A	[m^2]	Cumulative cross–sectional area of conductive airways
C_s	[–]	Cunningham slip correction factor
D_a	[m]	Airway diameter
D_p	[m]	Pipe diameter
D_B		Diffusion coefficient
F		Function of bifurcation angle
I	[W]	Intensity of light after it passes a sample
I_0	[W]	Intensity of light before it passes a sample
L	[m]	Characteristic airway diameter
L_a	[m]	Airway length
L_p	[m]	Pipe length
M	[kg·mol^{-1}]	Molar mass
Q	[m^{3}·s^{-1}]	Volumetric flow rate
Q_m	[m^{3}·s^{-1}]	Volumetric flow rate at the mouth
R_a		Air flow resistance
V	[m^3]	Rinsing volume
V_p	[m^3]	Penetration volume
V_T	[m^3]	Tidal volume
c_a		Aerosol concentration
c_m	[mol·l^{-1}]	Molar concentration
d_a	[m]	Aerodynamic equivalent diameter
d_e	[m]	Volume equivalent diameter
d_p	[m]	Particle diameter
g	[m^{2}·s-1]	Gravitational acceleration
k_B		Botzmann's constant
l	[m]	Sample width
m_{dep}	[kg]	Deposited mass
m_p	[kg]	Particle mass
r_a	[m]	Airway radius
v	[m·s^{-1}]	Mean velocity
v_f	[m·s^{-1}]	Fluid velocity
v_p	[m·s^{-1}]	Particle velocity
v_s	[m·s^{-1}]	Settling velocity
δ		Expansion factor
ε		Molar absorption coefficient
η		Dynamic viscosity
λ		Loss coefficient
ρ_p		Particle density
ρ_0		Unit density
χ		Dynamic shape factor

Dimensionless number symbol	Dimensionless number
Kn	Knudsen number
Pe	Peclet number
Re	Reynolds number
Stk	Stokes number
Wo	Womersley number

Abbreviation	Meaning
APS	Aerodynamic particle sizer

CFD	Computational fluid dynamics
CMAD	Count median aerodynamic diameter
COPD	Chronic obstructive pulmonary disease
CT	Computer tomography
DE	Deposition efficiency
DF	Deposition fraction
DEF	Deposition enhancement factor
ERV	Expiratory reserve volume
FE	Filtration efficiency
FPF	Fine particle fraction
FRC	Functional residual capacity
IC	Inspiratory capacity
IRV	Inspiratory reserve volume
MMAD	Mass median aerodynamic diameter
MRI	Magnetic resonance imaging
PET	Positron emission tomography
RV	Residual volume
SEM	Scanning electron microscopy
SPECT	Single–photon–emission computer tomography
SSPD	Small–scale powder disperser
VC	Vital capacity
TDF_a	Total deposition fraction in adults
TLC	Total lung capacity

List of Figures

List of tables